

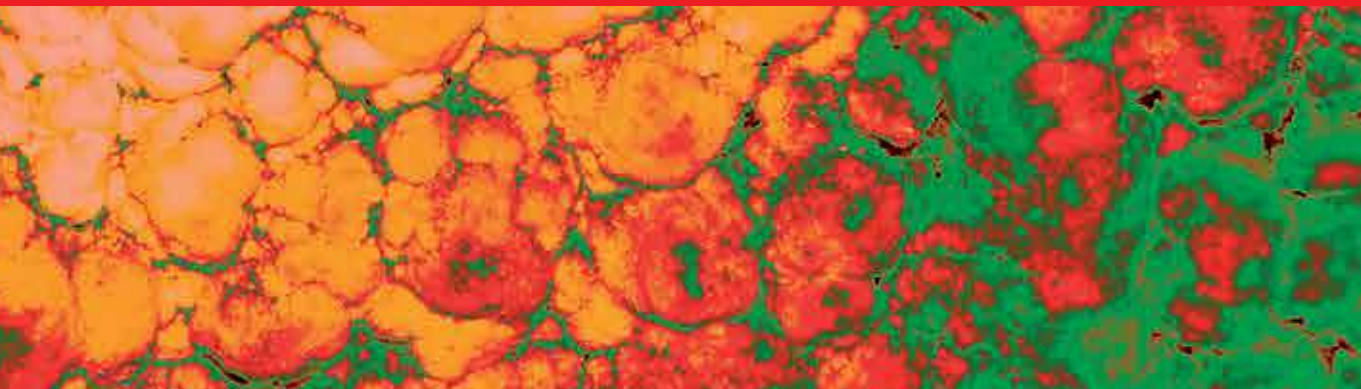


IntechOpen

Infrared Spectroscopy

Principles, Advances, and Applications

Edited by Marwa El-Azazy



Infrared Spectroscopy - Principles, Advances, and Applications

Edited by Marwa El-Azazy

Published in London, United Kingdom



IntechOpen





Supporting open minds since 2005



Infrared Spectroscopy – Principles, Advances, and Applications

<http://dx.doi.org/10.5772/intechopen.73071>

Edited by Marwa El-Azazy

Contributors

Nushaba Gadzhieva, Samuel P. Hernandez-Rivera, Leonardo C. Pacheco-Londoño, John Castro, Nataly J. Galán-Freyte, Amanda M. Figueroa-Navedo, José Ruiz-Caballero, Ricardo Infante-Castillo, Lembe Magwaza, Khayelihle Ncama, Mditshwa Asanda, Tesfay Samson, Patricia Concepcion, Feride Severcan, Ayça Doğan Mollaoğlu, İpek Özyurt, Chayan Mitra, Marwa S. El-Azazy, Amira C. Padilla-Jiménez, Carlos Rios-Velazquez

© The Editor(s) and the Author(s) 2019

The rights of the editor(s) and the author(s) have been asserted in accordance with the Copyright, Designs and Patents Act 1988. All rights to the book as a whole are reserved by INTECHOPEN LIMITED. The book as a whole (compilation) cannot be reproduced, distributed or used for commercial or non-commercial purposes without INTECHOPEN LIMITED's written permission. Enquiries concerning the use of the book should be directed to INTECHOPEN LIMITED rights and permissions department (permissions@intechopen.com).

Violations are liable to prosecution under the governing Copyright Law.



Individual chapters of this publication are distributed under the terms of the Creative Commons Attribution 3.0 Unported License which permits commercial use, distribution and reproduction of the individual chapters, provided the original author(s) and source publication are appropriately acknowledged. If so indicated, certain images may not be included under the Creative Commons license. In such cases users will need to obtain permission from the license holder to reproduce the material. More details and guidelines concerning content reuse and adaptation can be found at <http://www.intechopen.com/copyright-policy.html>.

Notice

Statements and opinions expressed in the chapters are those of the individual contributors and not necessarily those of the editors or publisher. No responsibility is accepted for the accuracy of information contained in the published chapters. The publisher assumes no responsibility for any damage or injury to persons or property arising out of the use of any materials, instructions, methods or ideas contained in the book.

First published in London, United Kingdom, 2019 by IntechOpen

eBook (PDF) Published by IntechOpen, 2019

IntechOpen is the global imprint of INTECHOPEN LIMITED, registered in England and Wales,

registration number: 11086078, The Shard, 25th floor, 32 London Bridge Street

London, SE19SG – United Kingdom

Printed in Croatia

British Library Cataloguing-in-Publication Data

A catalogue record for this book is available from the British Library

Additional hard and PDF copies can be obtained from orders@intechopen.com

Infrared Spectroscopy – Principles, Advances, and Applications

Edited by Marwa El-Azazy

p. cm.

Print ISBN 978-1-78984-968-4

Online ISBN 978-1-78984-969-1

eBook (PDF) ISBN 978-1-83962-064-5

We are IntechOpen, the world's leading publisher of Open Access books Built by scientists, for scientists

4,000+

Open access books available

116,000+

International authors and editors

120M+

Downloads

151

Countries delivered to

Our authors are among the
Top 1%

most cited scientists

12.2%

Contributors from top 500 universities



WEB OF SCIENCE™

Selection of our books indexed in the Book Citation Index
in Web of Science™ Core Collection (BKCI)

Interested in publishing with us?
Contact book.department@intechopen.com

Numbers displayed above are based on latest data collected.
For more information visit www.intechopen.com



Meet the editor



Dr. Marwa El-Azazy is an analytical chemist, experienced educator, and researcher with more than 15 years of teaching experience at several institutions. Her main research interest is construction of sensors (using microfluidic platforms for point-of-care testing of drugs and bioanalytes and ion-selective electrodes), chemometrics and analytical method development, spectroscopic analyses of drugs and pharmaceuticals, synthesis and characterization of nanomaterials, and development of green chemistry approaches for wastewater treatment. Dr. Marwa has a track record of research inputs including more than 20 refereed papers in prestigious international journals, several conference presentations, two book chapters, in addition to several research grants. She serves as a reviewer for a variety of international journals.

Contents

Preface	XIII
Chapter 1 Introductory Chapter: Infrared Spectroscopy - A Synopsis of the Fundamentals and Applications <i>by Marwa El-Azazy</i>	1
Chapter 2 Mid-Infrared Laser Spectroscopy Applications I: Detection of Traces of High Explosives on Reflective and Matte Substrates <i>by Leonardo C. Pacheco-Londoño, John R. Castro-Suarez, Nataly J. Galán-Freyle, Amanda M. Figueroa-Navedo, José L. Ruiz-Caballero, Ricardo Infante-Castillo and Samuel P. Hernández-Rivera</i>	11
Chapter 3 Mid-Infrared Laser Spectroscopy Applications in Process Analytical Technology: Cleaning Validation, Microorganisms, and Active Pharmaceutical Ingredients in Formulations <i>by Leonardo C. Pacheco-Londoño, Nataly J. Galán-Freyle, Amira C. Padilla-Jiménez, John R. Castro-Suarez, Amanda M. Figueroa-Navedo, José L. Ruiz-Caballero, Ricardo Infante-Castillo, Carlos Rios-Velazquez and Samuel P. Hernández-Rivera</i>	35
Chapter 4 Mid-Infrared Spectroscopy and Challenges in Industrial Environment <i>by Chayan Mitra</i>	57
Chapter 5 Applications of Infrared Spectroscopy and Microscopy in Diagnosis of Obesity <i>by Ayca Dogan Mollaoglu, Ipek Ozyurt and Feride Severcan</i>	85
Chapter 6 Application of Visible to Near-Infrared Spectroscopy for Non-Destructive Assessment of Quality Parameters of Fruit <i>by Khayelihle Ncama, Lembe S. Magwaza, Asanda Mditshwa and Samson Z. Tesfay</i>	107
Chapter 7 IR-Spectroscopy of Radiation- Stimulated Processes of Adsorption, Radiolysis, and Hydrogenation on the Surface of Metals in Contact with Hydrocarbons <i>by Nushaba Gadzhieva</i>	125

Chapter 8

Application of Infrared Spectroscopy in Catalysis: Impacts on Catalysts' Selectivity

by Patricia Concepción

147

Preface

Infrared (IR) spectroscopy is a well-established spectroscopic technique that has seen major advances over the past two centuries. Being easy to operate, non-destructive, with a capability of elucidating and quantifying both organic and inorganic materials from different matrices and even in miniature quantities, and offering a *fingerprint* profile for each molecule, makes IR an inestimable analytical technique. The introduction of gratings, interferometers, supercomputers, and the availability of expeditious data analysis approaches together with the growth of IR spectroscopy have paralleled one another. These advances and how they have been greatly reflected in the applications of IR spectroscopy in different realms were enough to justify writing this book.

The material revealed in this book incorporates and blends the fundamentals of IR spectroscopy, the advances assimilated in the field of IR, and a variety of applications: detection of high explosives, biological threats, analysis of pharmaceuticals, monitoring of gas emission and air quality in an industrial environment, early-stage detection of serious health problems like obesity, assessing quality parameters of fruit, study of radiation-stimulated processes of adsorption, radiolysis of hydrocarbons on metal surfaces, radiation hydrogenation of these surfaces, and ideal catalyst development.

From the fundamentals to the applications and throughout the advances, it is our hope that this book will be considered as a reference on IR spectroscopy. The authors of each chapter have tried to appeal to readers from different backgrounds by introducing the basic concepts of every term used.

Finally, I would like to thank all the authors who have contributed to this book by writing a chapter. They are all experts in their fields and have exerted time and effort to make this book a comprehensive, informative piece. Special thanks to the Department of Chemistry and Earth Sciences, Qatar University, Doha, for facilitating my task as editor of this book. I owe much to my son, Yusuf (Y6, QIS, Doha), for his help in creating the diagrams and presentations given in the introductory chapter. Last, but by no means least, I am grateful to my family for all the love, incessant encouragement, and support.

Dr. Marwa El-Azazy

Current Address: Department of Chemistry and Earth Sciences,
College of Arts and Sciences, Qatar University,
Doha, Qatar

Introductory Chapter: Infrared Spectroscopy - A Synopsis of the Fundamentals and Applications

Marwa El-Azazy

1. History and fundamentals

Spectroscopy is a term that describes the interaction of matter with electromagnetic radiation. Several forms of interaction therefore exist: absorption, emission, diffraction, impedance, resonance, and inelastic scattering of radiation. Therefore, and as a big science, spectroscopy is used to characterize/detect matter (atoms, molecules, and nuclei) based on the produced spectra and following their interaction with radiation. The electromagnetic spectrum, and as the word *spectrum* implies, is a range of frequencies of the electromagnetic radiation and the corresponding wavelengths and photon energies [1, 2]. **Figure 1** shows a schematic portrayal of the electromagnetic spectrum, along with the molecular processes that can occur in each region, e.g., rotation (microwave), vibration (infrared), electronic excitation (ultraviolet-visible), and bond breaking and ionization (X-rays).

As shown in **Figure 1**, the sector of the spectrum extending from the nearly 10^{-3} m (microwave) to the 780 nm (visible) wavelength range is labeled as the infrared (IR) region. Extending from the red edge of the visible region to 1 mm on the wavelength scale, IR radiations were first come across by Sir William Herschel in the nineteenth century by sensing the temperature escalation across the visible zone and then from the visible zone to beyond, which was then soon identified as the IR region [3–5]. Akin to the situation in the ultraviolet region, the IR radiations are invisible to the human eye. As shown on the wavelength scale in **Figure 1**, IR radiations appear at a longer wavelength compared to the visible region. Accordingly, and since electromagnetic radiations travel at a constant speed in vacuum which is the speed of light (c , $2.997\,924\,58 \times 10^8$ m s⁻¹), the frequency of IR radiations is therefore lower compared to that of the visible light, applying the formula $\nu = c/\lambda$ where ν = the frequency of light, c = the speed of light, and λ = the wavelength of light. This in turn means that energy associated with the IR radiations is inferior to that of the visible light and greater than that of microwaves, for instance [5–8].

Accordingly, and possessing an energy that can initiate molecular vibrations, IR radiations act by instigating recurring oscillations of the atoms' positions around their bonds, while the entire molecule is in a continual *translational* and *rotational* movement. As the position of a molecule in the space could be outlined by the three Cartesian coordinates: x , y , and z , this molecule would have three degrees of freedom (3 DoF) in terms of its motion. Consequently, and for a nonlinear molecule with N atoms, DoF = $3N$. Normal modes of vibrations for such a molecule can be obtained following the exclusion of the DoF for the translational and rotational

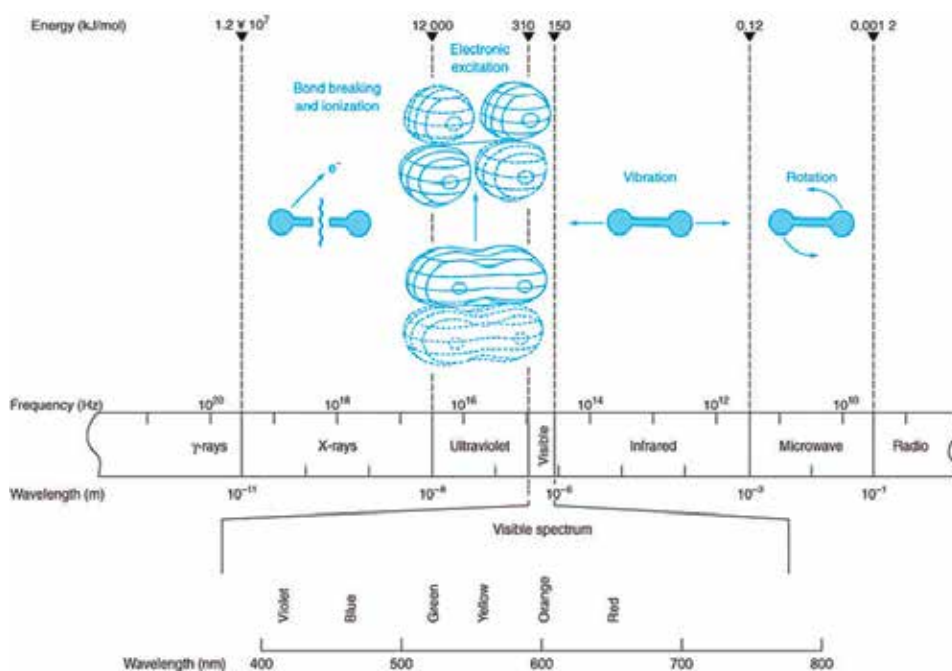


Figure 1.

Schematic portrayal of the electromagnetic spectrum, showing representative molecular processes that occur in each region [2].

motions and are equal to $3N-6$. As the rotation of a linear molecule around the bond axis does not involve a change in energy and hence cannot be observed, the number of internal motions would be $3N-5$ [1, 8–11].

By and large, vibrational spectroscopy is the communal label given to describe measurements involving both infrared (IR) and Raman spectroscopy (RS). As an approach, vibrational spectroscopy is used to measure *molecular* vibrations resulting from absorption of light/photons. Therefore, absorption of energy, E , that matches the vibration frequency, ν , would trigger molecular vibration because of the change in the dipole moment. Both techniques give spectral sketches that express the chemical temperament of a sample.

Two main modes of vibrations are commonly known; *stretching* (where the distance between the two atoms and hence the bond length are affected) and *bending* (where the slant between the two bonds is altered). Further classification of the types of motions would include two stretching modes: *symmetric* (where the two atoms *simultaneously* move toward and away from the central atom) and *anti-symmetric* (where one of the atoms move toward the central atom, while the second moves away from the central atom). Bending vibrations include four types of motions; *rocking* (the two atoms moving in-plane either clockwise or anti-clockwise), *scissoring* (also in-plane, both atoms are simultaneously moving either toward each other or away from each other), *wagging* (out-of-plane, where both atoms simultaneously move like a V sign back and forth), and *twisting* (out-of-plane, where one atom moves forward while the other moves backward), **Figure 2** [10].

Overall, occurrence of vibration of a particular mode, rather than another, is influenced by quite a few considerations. In general, the *mode of vibration* itself is one of the considerations, e.g., bending needs less energy compared to stretching and hence is more feasible. Another concern is the *bond strength*, where a single bond is weaker compared to a double bond, which in turn is weaker than a triple

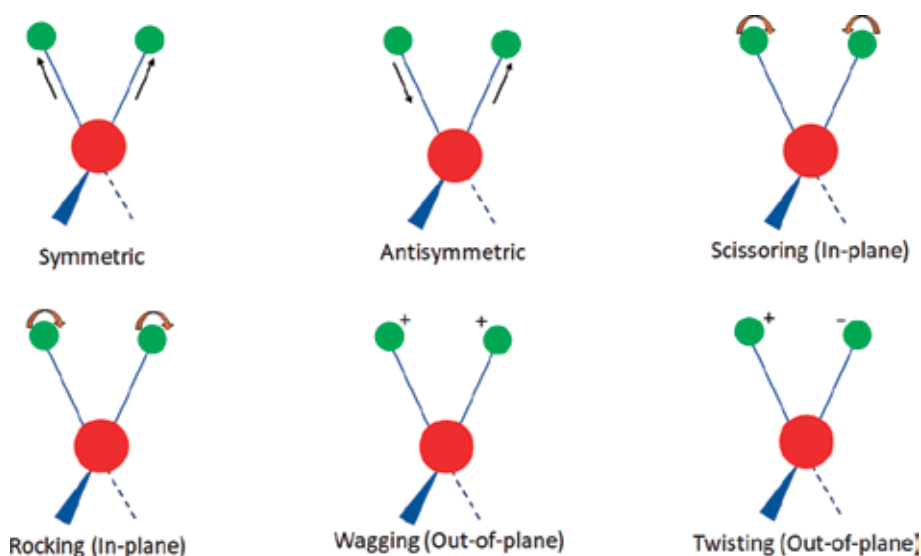


Figure 2.
Modes of molecular vibration.

bond. Therefore, a single bond needs less energy and appears at a lower wavenumber ($\tilde{\nu}$). Mass of the atoms is another consideration, where heavier atoms would vibrate more slowly compared to the light atoms.

2. Advances in IR spectroscopy

Before introducing the reader to the instrumentations and sampling techniques used in the IR region and their impact on the advances in the field of IR spectroscopy, it is crucial to first present the zones of IR.

2.1 Zones of the IR region

Three main zones can be identified in the IR region:

- i. The far-IR (FIR, $400\text{--}10\text{ cm}^{-1}$, $25\text{--}300\text{ }\mu\text{m}$)
- ii. The mid-IR (MIR, $4000\text{--}400\text{ cm}^{-1}$, $2.5\text{--}25\text{ }\mu\text{m}$)
- iii. The near-IR (NIR, $14,000\text{--}4000\text{ cm}^{-1}$, $0.7\text{--}2.5\text{ }\mu\text{m}$)

Ranges given between parentheses are identified on the wavenumber ($\tilde{\nu}$) and wavelength (λ) scales, respectively, **Figure 3** [12]. It is noteworthy to mention that different schemes for the IR division exist depending on the application. For example, a sensor response division scheme classifies the IR region into five zones instead of the three shown above depending on the detector's sensitivity [13–15]. Some classifications add a region of long-wave IR (LWIR) or thermal IR (TIR: $8\text{--}15\text{ }\mu\text{m}$).

The MIR region can be further divided into the *fingerprint* region ($400\text{--}1400\text{ cm}^{-1}$) and the *functional groups*' region ($1400\text{--}4000\text{ cm}^{-1}$). For that reason, the MIR region is the most commonly used where most compounds would have a *signature* absorption/emission in this region.

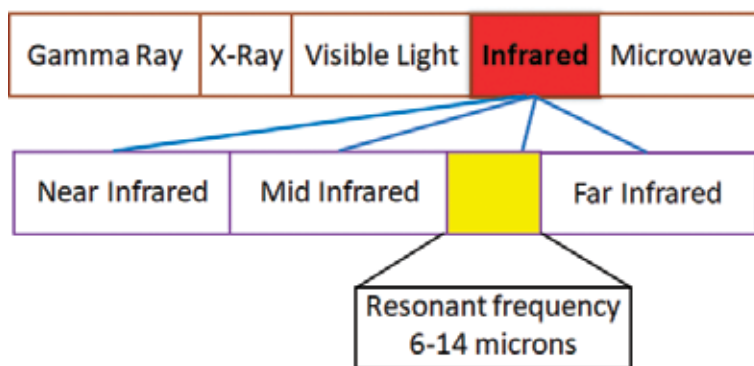


Figure 3. Section from the electromagnetic spectrum showing regions of IR. The diagram is replicated from https://en.wikipedia.org/wiki/Far_infrared#/media/File:Electromagnetic_Far_Infrared.jpg.

Absorption in the NIR region is an outcome of two major processes: *molecular overtones* and *combinations*. For simplification, an *overtone* is a frequency that is higher than the fundamental frequency (lowest frequency). Both frequencies (overtone + fundamental) are known as *harmonic partials*. In simpler words, each fundamental frequency will generate a succession of absorptions at integer multiples of this frequency, and a molecule experiencing an overtone is the one getting excited from the ground state to the second excited state [16]. Consequently, NIR absorptions need higher energy than a fundamental, and few overtones can be observed in this region. On the contrary to overtones arising from a group of fundamental absorptions, combinations, appearing because of the allocation of energy between two or more fundamental MIR bands that get excited simultaneously, are largely seen. Therefore, the NIR region is basically a region of broad peaks with limited use (except for bulk materials keeping in mind that NIR can penetrate much further compared to MIR). Thus, application of multivariate calibration techniques would resolve the complexity of the spectra and help extracting the needed information [16]. Yet, it is noteworthy to mention that each of the three regions (mid-, near-, and far-) has significant applications in different fields as will be seen in the subsequent sections.

2.2 Instrumentations and sampling techniques

In general, this field has seen a major progress especially after grating was first introduced in 1823, and after the first commercial IR spectrometer came to the scene. The conventional IR spectrophotometer, first introduced in the 1940s, was a dispersive instrument. Rudimentary parts of this instrument were a *radiation source*, a *monochromator*, and a *detector*, most frequently in a double-beam setup. Monochromator, the dispersive device, serves to separate the broad spectrum of IR radiations into a continuous sequence of IR bands with resolved frequencies. These instruments work by tracing only a sole frequency at a time. Consequently, a whole spectrum needs a long time to be recorded [6–8, 17, 18]. It was in the 1960s when Fourier transform (FT) instruments came to the scene. The key difference between FT and dispersive instruments was the presence of *interferometers*. The output of the FT-IR instrument is then called an *interferogram*. FT-IR instruments, though were intended to extend the use of IR, had limited applications and were used only for advanced research. This was mainly because of the expensive component electronics and the need for supercomputers to record the generated data. However, after the microelectronic revolution, the capabilities and availability of

these instruments have been greatly improved. In addition to the noticeable speed in acquiring spectra, improved signal to noise ratio, high resolution, accuracy, and reproducibility, FT-IR offers two major pluses over the classical dispersive instruments [6–8, 17–20]:

- i. Multiplex plus: where all frequencies fall on the detector in unison. Therefore, each resolution component is grasped continually, creating a multifaceted spectrum.
- ii. Throughput plus: the presence of gratings and prisms in a dispersive instrument and the need for an ingress slit would decrease the amount of light reaching the detector. Quite the reverse, an interferometer has a large orifice that in turn increases the output.

Samples to be measured with FT-IR or dispersive instruments (*transmission techniques*) need a prior treatment. A solid sample is mixed with potassium bromide, packed together into a compressed disc, and inserted into the pathway of radiation. Liquid samples are placed in special holders or mounted on the surface of a KBR disc. Other sampling techniques, e.g., *reflectance techniques*, however, permit IR radiations to be applied on a larger assortment of sample forms without additional treatment. As their name implies, radiations in these techniques are *reflected* from the sample surface rather than being *transmitted* through it. Reflections might be *total internal*, *specular*, or *diffuse*. Details on speculations of each technique can be summarized as follows and as shown in **Figure 4**:

- i. Total reflection IR or attenuated total reflectance IR (ATR-IR): where light undergoes several internal reflections when passed through an ATR crystal of high refractive index (RI), which in turn is in contact with the sample. The resultant evanescent wave spreads to the sample and infiltrates to a depth that is dependent on a variety of controls such as light wavelength, RI of the crystal and the medium being examined, and incidence angle. An ATR crystal might be made of *Diamond*, *Zinc Selenide (ZnSe)*, *Germanium (Ge)*, or *Silicon (Si)*. The resulting spectrum is analogous to that produced by dispersive instruments especially for thin films [21, 22]. ATR-IR is suitable for a variety of sample forms with no or minimal need for sample preparation. Yet, ATR-IR is less sensitive compared to transmission-based techniques.
- ii. Specular reflection IR spectroscopy (SRS): also known as external reflection IR occurs when light is reflected from a specular surface (mirror-like) at a well-defined angle that is equal to the angle of incidence of IR radiation. Analogous to ATR-IR, thin films' reflectance spectra are like the transmission spectra and are identified as a reflection-absorption mode. For ultrathin films (monomolecular layers), however, using a grazing incidence mode is needed where the path of radiation becomes parallel to the metal surface augmenting the absorption intensity. In general, coupling of an IR spectrophotometer with an optical microscope is known as FT-IR microscopy. Collection of the specular reflection spectrum is performed using such a setup and is commonly known as micro FT-IR [8, 19, 22–24].
- iii. Diffuse reflectance spectroscopy (DRS): this is a combination between internal and external reflections and originates from rough surfaces (*powders*) reflecting light in different directions. Having diffuse reflectance exploited in IR FT spectroscopy is known as DRIFTs [8, 25].

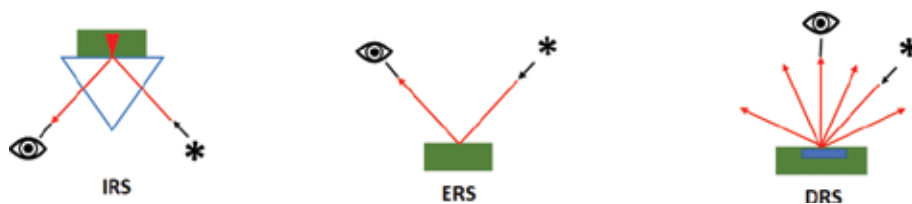


Figure 4.
FT-IR reflection modes.

3. Data treatment in IR spectroscopy

Chemical data encompassed in the MIR spectra exist in peak positions, peak intensities, and peak shape. Therefore, while spectra from MIR can be easily interpreted and information can be easily extracted, the spectra obtained from NIR, however and as previously mentioned, have the absorption bands from the overtones and combinations of fundamental MIR bands and therefore need special treatment to resolve this overlapping. Analysis of data from NIR implementing multivariate data analysis or chemometrics would be a suitable approach. With the advances in data sciences, coupling of IR spectroscopy to chemometrics serves to combine the advantages of both in terms of time, effort, and multicomponent analysis. Application of a certain chemometric method in NIR data analysis would depend greatly on whether the performed analysis is qualitative or quantitative. In general, three approaches are used to examine data from NIR [26–30]:

- i. Arithmetic data pre-processing: this approach helps diminution of the impact of side data and keeps the focus on the main data in a spectrum. Normalization, derivatization, and smoothing are common techniques.
- ii. Classification techniques: mainly used for data obtained from qualitative analysis where samples are congregated based on their spectra. Classification might be *unsupervised* where only the spectra are known for the researcher and no other information is available, or *supervised pattern recognition* where a prior knowledge of samples' categories exists, and spectroscopists would create a classification model then evaluate this model by comparing the predicted values to the actual ones [26, 31, 32]. Principle component analysis (PCA) is a common unsupervised classification approach, while partial least squares discriminant analysis (PLSDA) is a classical supervised classification technique [28, 30].
- iii. Regression methods: used mainly in quantitative analysis. Common approaches include principle component regression (PCR), multi-linear regression (MLR), partial-least squares (PLS), artificial neural network (ANN), and support vector machines (SVMs) [28].

4. What the reader will get from the next chapters

Sampling techniques such as FT-IR and ATR-IR have served in the expansion of IR applications to a variety of matrices. As an established technique that is readily available for researchers and being a cost-effective and non-destructive approach, IR spectroscopy has a realm of applications in different fields. Food analysis, nanoparticle synthesis and characterization, medicine, drug synthesis and analysis, etc. are

among the applications. Yet, being insensitive, and with questionable selectivity, applications of IR are still in a need for further development.

In this introductory chapter, the author (editor) tried to shed light on the fundamentals of IR spectroscopy, advances introduced to the field with the introduction of new sampling techniques, and the common approaches of data analysis. In the following interesting chapters, one can see the IR applications in different fields disclosing themselves to the readers. Authors of every chapter have tried their best to reveal the underlying concepts associated with any of the mentioned applications. The shown assembly of the seven chapters would provide the readers with insights on

- MIR laser spectroscopy sources, especially those applicable in the 3–4 μm wavelength range, e.g., quantum cascade lasers (QCLs).
- Impact of QCLs on the existing spectroscopic schemes. Readers will see the influence of these sources on MIR applications such as detection of weapons of massive destruction, e.g., high explosives (HEs) and biological threats, as well as the analysis of pharmaceutical blends.
- Difficulties encountered in the application of MIR to an industrial environment, e.g. trace gas detection, leak detection, gas emission and monitoring of air quality, and what are the solutions available.
- The competency of FT-IR spectroscopy and micro-spectroscopy in the biomedical research area, with a capability to depict and spot serious health problems, e.g. obesity. Readers will see that FT-IR, employing ATR as a sampling mode and coupled to chemometrics, has greatly impacted the power of IR spectroscopy in terms of detection limits, early-stage detection of disease-induced changes, and inevitability of the obtained results.
- Challenges associated with VIS-NIR applications, with a sample application—such as a non-destructive approach—for assessing quality parameters of fruits and the consequent impact on their nutritional value and the economy at the far end.
- IR spectroscopic studies (reflection-absorption IR spectroscopy) of radiation-stimulated processes of adsorption, radiolysis of hydrocarbons on metal surfaces, and radiation hydrogenation of these surfaces.
- Impact of using IR in developing an ideal catalyst and efficient catalysis process, which in turn would help developing more efficient processes via reduction of energy consumption and the generation of by-products. Readers would get the sequence of such a process through the examples given, e.g., Fischer-Tropsch synthesis, ethylene oligomerization, aniline synthesis, and dehydration of aldoximes to nitriles.
- Coupling of multivariate analysis techniques to both MIR and NIR routines and its influence on the discrimination power, limits of detection and quantification, and data clustering is almost discussed in every chapter.

Finally, I think readers will find this book informative as well as interesting and probably inspiring for further advances in the field. I, therefore, invite the readers to go through the following chapters and see the different applications of IR spectroscopy.

Author details


Marwa El-Azazy^{1,2}

1 Department of Chemistry and Earth Sciences, College of Arts and Sciences, Qatar University, Doha, Qatar

2 Department of Analytical Chemistry, Faculty of Pharmacy, Zagazig University, Zagazig, Egypt

*Address all correspondence to: marwasaid@qu.edu.qa

IntechOpen

© 2018 The Author(s). Licensee IntechOpen. This chapter is distributed under the terms of the Creative Commons Attribution License (<http://creativecommons.org/licenses/by/3.0>), which permits unrestricted use, distribution, and reproduction in any medium, provided the original work is properly cited. 

References

- [1] Hollas JM. *Modern Spectroscopy*. 4th ed. Chichester: John Wiley & Sons, Ltd.; 2004
- [2] Harris DC. *Quantitative Chemical Analysis*. New York, NY: W.H. Freeman and Co; 2007
- [3] Herschel W. Experiments on the refrangibility of the invisible rays of the sun. *Philosophical Transactions of the Royal Society*. 1800;**90**:284
- [4] Maas van der JH. *Basic Infrared Spectroscopy*. 2nd ed. London: Heyden & Son Ltd.; 1972
- [5] Theophanides T, editor. *Introduction to Infrared Spectroscopy—Materials Science, Engineering and Technology*. Rijeka, Croatia: InTech; 2012. Available from: <http://www.intechopen.com/books/infrared-spectroscopy-materials-scienceengineering-and-technology/introduction-to-infrared-spectroscopy>
- [6] Hesse M, Meier HBZ. *Spectroscopic Methods in Organic Chemistry*. 2nd ed. Stuttgart: Georg Thieme Verlag; 2008
- [7] Pavia D, Lampman GKG. *Introduction to Spectroscopy: A Guide for Students of Organic Chemistry*. 3rd ed. Fort Worth, TX: Harcourt College Publishers; 2001
- [8] Monnier GF. A review of infrared spectroscopy in microarchaeology: Methods, applications, and recent trends. *Journal of Archaeological Science: Reports*. 2018;**18**:806-823
- [9] Landau LD, Lifshitz EM. *Mechanics*. 3rd ed. Oxford: Pergamon Press; 1976
- [10] Banwell CN, McCash EM. *Fundamentals of Molecular Spectroscopy*. 4th ed. Berkshire, England: McGraw Hill; 1994
- [11] Atkins PW, de Paula J. *Physical Chemistry*. 8th ed. New York: W. H. Freeman; 2006
- [12] Jaleh B, Fakhri P. Infrared and Fourier transform infrared spectroscopy for nanofillers and their nanocomposites. In: *Spectroscopy of Polymer Nanocomposites*. Netherlands: Elsevier; 2016. pp. 112-129
- [13] ISO 20473:2007. *Optics and Photonics—Spectral Bands*
- [14] Near, Mid and Far-Infrared. NASA IPAC. Archived from the original on 2012-05-29 [Retrieved: 2007-04-04]
- [15] Miller J. *Principles of Infrared Technology: A Practical Guide to the State of the Art*. Van Nostrand Reinhold; New York, NY 10003, USA; 1992
- [16] Balabin RM, Safieva RZ, Lomakina EI. Comparison of linear and nonlinear calibration models based on near infrared (NIR) spectroscopy data for gasoline properties prediction. *Chemometrics and Intelligent Laboratory Systems*. 2007;**88**(2):183-188
- [17] Sherman HC. *Handbook of Instrumental Techniques for Analytical Chemistry*. New Jersey: Prentice Hall; 1997
- [18] Koenig JL. *Infrared and Raman Spectroscopy of Polymers*. Smithers Rapra Technology; 2001
- [19] Griffiths PR, de Haseth JA. *Fourier Transform Infrared Spectrometry*. 2nd ed. Hoboken, New Jersey: John Wiley & Sons; 2007
- [20] Smith BC. *Fundamentals of Fourier Transform Infrared Spectroscopy*. 2nd ed. Boca Raton, FL: CRC Press; 2011
- [21] *FT-IR Spectroscopy—Attenuated Total Reflectance (ATR)*. Perkin Elmer Life and Analytical Sciences. 2005.

- Archived (PDF) from the original on 16 February 2007 [Retrieved: 2007-01-26]
- [22] Mirabella FM Jr. Practical spectroscopy series. In: *Internal Reflection Spectroscopy: Theory and Applications*. New York, USA: Marcel Dekker, Inc.; 1993. pp. 17-52
- [23] Prati S, Sciutto G, Bonacini I, Mazzeo R. New frontiers in application of FTIR microscopy for characterization of cultural heritage materials. *Topics in Current Chemistry*. 2016;**374**(3):26
- [24] Schrader B. *Infrared and Raman Spectroscopy: Methods and Applications*. Weinheim: VCH-Verlag; 1995
- [25] Skoog DA, Holler FJ, Crouch SR. *Principles of Instrumental Analysis*. Vol. 6. Belmont, MA: Brooks/Cole (Cengage Learning); 2007
- [26] Massart DL, Vandeginste BGM, Deming SM, Michotte Y, Kaufmann L. *Chemometrics: A Textbook*. Amsterdam: Elsevier; 2003
- [27] Elazazy MS. In: Sharmin E, Zafar F, editors. *Factorial Design and Machine Learning Strategies: Impacts on Pharmaceutical Analysis, Spectroscopic Analyses*. Rijeka, Croatia: IntechOpen; 2017. Available from: <https://www.intechopen.com/books/spectroscopic-analyses-developments-and-applications/factorial-design-and-machine-learning-strategies-impacts-on-pharmaceutical-analysis>
- [28] Roggo Y, Chalus P, Maurer L, Martinez CL, Edmond A, Jent N. A review of near infrared spectroscopy and chemometrics in pharmaceutical technologies. *Journal of Pharmaceutical and Biomedical Analysis*. 2007;**44**:683-700
- [29] Martens H, Naes T. *Multivariate Calibration*. Chichester: John Wiley & Sons; 1996
- [30] Karoui R, Downey G, Blecker C. Mid-infrared spectroscopy coupled with chemometrics: A tool for the analysis of intact food systems and the exploration of their molecular structure-quality relationships—A review. *Chemical Reviews*. 2010;**110**:6144-6168
- [31] Simon L, Nazmul Karim M. Probabilistic neural networks using Bayesian decision strategies and a modified Gompertz model for growth phase classification in the batch culture of *Bacillus subtilis*. *Biochemical Engineering Journal*. 2001;**7**:41-48
- [32] Marini F, Balestrieri F, Bucci R, Magri AD, Magri AL, Marini D. Supervised pattern recognition to authenticate Italian olive oil varieties. *Chemometrics and Intelligent Laboratory Systems*. 2004;**73**:85-93

Mid-Infrared Laser Spectroscopy Applications I: Detection of Traces of High Explosives on Reflective and Matte Substrates

Leonardo C. Pacheco-Londoño, John R. Castro-Suarez, Nataly J. Galán-Freyle, Amanda M. Figueroa-Navedo, José L. Ruiz-Caballero, Ricardo Infante-Castillo and Samuel P. Hernández-Rivera

Abstract

Mid-infrared (MIR) lasers have revolutionized infrared vibrational spectroscopy, converting an already dominant spectroscopic analysis technique into an even more powerful, easier to use, and quicker turn-around cadre of versatile spectroscopic tools. A selection of applications, revisited under the umbrella of MIR laser-based properties, very high brightness, collimated beams, polarized sources, highly monochromatic tunable sources, and coherent sources, is included. Applications discussed concern enhanced detection, discrimination, and quantification of high explosives (HEs). From reflectance measurements of chemical residues on highly reflective metallic substrates to reflectance measurements of HEs deposited on non-reflective, matte substrates is discussed. Coupling with multivariate analyses (MVA) techniques of Chemometrics allowed near trace detection of HEs, with sharp discrimination from highly MIR absorbing substrates.

Keywords: mid-infrared (MIR) laser spectroscopy, quantum cascade lasers (QCLs), high explosives (HEs), multivariate analyses (MVA), Chemometrics

1. Introduction

Vibrational spectroscopy, in its two main branches: infrared spectroscopy (IRS) and Raman scattering (RS) are used for identifying and quantifying samples in complex matrices because each substance has a unique spectrum in the fingerprint and fundamental vibrations regions of the electromagnetic spectrum and the corresponding Raman shift regions [1–6]. IRS is a well-established discipline within science and technology fields, and it has continuously evolved over the past 200 years [1–3]. Throughout this time, IRS gradually developed all its major modalities: absorption/transmission, reflection, and emission spectroscopies. It has benefited from technological developments in spectral sorting capabilities (gratings instead of prisms; interferometers instead of dispersive spectrometers), improvements in

detection technologies, development of water-resistant optical elements, and in fast processing data analysis: Fourier transformation [1–6]. However, one area that has lagged developments and improvements until very recently has been in excitation sources of infrared spectra. Only thermal sources (globars), which are inherently low power sources been traditionally available for bench and portable systems [3].

Both IRS and RS, in their various modalities, have been shown useful for characterization, detection, identification, and quantification of threat chemicals, among them high explosives (HEs) and homemade explosives (HMEs) [6–18]. In the past 25 years, the techniques have frequently been used in a remote mode to fight terrorist threats establishing the base for the essential countermeasures to inhibit explosives events. Research in areas of interest to security and national defense with a focus on detection of HEs has been reviewed [7–18].

The difference in inherent strength of the photonic mechanisms that enable IRS and RS as the dominant techniques of vibrational molecular spectroscopy limits their capabilities and use in applications of remote detection of threat chemical compounds. IRS being a photonic absorption process is a much stronger mechanism than the inelastic scattering of photons in a Raman event. This fact enables remote infrared spectroscopy (RIRS) with the capability of near trace detection of target chemicals up to tens of meters. On the other hand, RS is supported by important properties of laser technology, which enable remote sensing at distances as long as 1 km, but it is limited to the detection of bulk or semi-bulk amounts of samples (as low as several μg) and small gaseous molecules, due to the weakness of the scattering event [19–26].

The need for developing more powerful mid-infrared (MIR) sources that would allow detection at longer ranges when a target hazardous threat chemical is located on a solid substrate in the form of a residue at trace or near trace level amounts requires the use lasers sources for the task. MIR laser sources were introduced in with the invention of the quantum cascade laser (QCL) [27]. QCLs slowly developed from narrow band operation to widely tunable, multi-diode systems initially producing a few milli Watts of power to current commercial systems, capable of delivering high powers and enabling detection of hazardous chemical compounds remotely [28–34].

QCLs can be used to detect gases and vapors and even high sublimation pressure chemicals, such as triacetone triperoxide (TATP) a cyclic organic peroxide HME. Pentaerythritol tetranitrate (PETN) an aliphatic nitrate ester, 1,3,5-trinitroperhydro-1,3,5-triazine (RDX) an aliphatic nitramine, and 2,4-dinitrotoluene (2,4-DNT) and 2,4,6-trinitrotoluene (TNT) nitroaromatic HEs, have very low sublimation pressures and have been detected as particle residues on substrates using photoacoustic spectroscopy [35–37]. Vapor phase detection of TATP and TNT has also been attained using IRS with adequate results [37, 38]. QCL sources have also been used for remote detection of HEs deposited on solid substrates using reflectance, photoacoustic, and hyperspectral imaging [39–44].

However, previous research in this field has generally centered on the detection of HEs deposited reflective substrates [42]. Only one report addressed the problem of detection of HEs on matte surfaces [44]. The work of Pacific Northwest National Lab researchers in the spectroscopic and angular dependence of MIR diffuse scattering from explosives residues deposited on a painted car door using an external cavity QCL (EC-QCL) was measured laid the foundation for detection of HE on matte surfaces [43]. Intensity dependence on the angle of the source-target-detector in active mode RIRS [45], the dependence of the limit of detection (LOD) on angular position, surface type, and analyte concentration for active mode RIRS using globars, modulated and non-modulated, have also been measured [46].

2. General specifications of scanning QCL spectrometers

The necessity of collimated and coherent light sources in the MIR region is evident by the limitation in the operational distance of RIRS experiments based on thermal sources. Even when coupled to IR telescopes to direct the light source of the substrates containing the target HEs, the energy/area of these systems can greatly benefit from a monochromatic, coherent, collimated and polarized source: a laser. The development of lasers with the ability to emit radiation in the 3–12 μm ($833\text{--}3330\text{ cm}^{-1}$) spectroscopic range has advanced dramatically with the development lasers [27, 47, 48]. MIR laser spectroscopy offers the possibility to detect threat chemicals, both in the vapor phase (high sublimation pressure HEs, such as TATP) as well as traces deposited on substrates. A remote detection scheme for low vapor pressure nitroexplosives was described by Bauer et al. [36] QCLs are highly suitable for compact and rugged sensor devices used for security and defense applications.

Block Engineering (BE; Southborough, MA, USA) developed a scanning QCL pre-dispersive spectrometer (LaserScan™) operating in the 6–12 μm ($830\text{--}1670\text{ cm}^{-1}$) spectral range. This QCL spectrometer offers some key advantages over other established technologies in developing the applications discussed in this contribution, namely:

1. Speed: very fast scanning and inspection of surfaces due to the use of a large 2–4-mm beam spot, long remote distance and high pulse rate lasers.
2. Ease of use: the system uses a collimated beam with fixed optics that allows operating at a convenient, safe remote minimum distance of 1–2 m.
3. Detection of multiple threat chemicals: including HEs, HMEs, mixes, formulations, and essentially any substance that has a spectral feature in the range 6–12 μm .
4. Detection of all states of substances: liquids, gases, and vapors, in addition to its current capacity of surface detection.
5. Personnel safety: non-focusing laser beam operating in the 6–12 μm spectral region avoids eye safety issues.
6. High sensitivity measurements: high-power laser source enables detection of low chemical concentrations on surfaces: 1–15 $\mu\text{g}/\text{cm}^2$ (0.01–0.15 g/m^2) and bulk materials.

This LaserScan™ spectroscopic system was designed for detection of surface contaminants. The system can acquire reflectance spectra of films and deposits of chemicals on reflective substrates. The initial stage of development of applications of MIR lasers involved validation experiments aimed at evaluating the performance of the QCL LaserScan™ in the goal of detecting HEs on metal surfaces. Some of the results obtained with the QCL LaserScan™ system and corresponding FTIR reference (Ref) spectra are shown in **Figure 1**.

There are operational parameters worth discussing in some detail. Two aligning He:Ne lasers can be turned on to focus the invisible MIR laser beam of the spectrometer. The unit was designed for short focal length work, and the two He:Ne beams converge at the focal length of $15 \pm 3\text{ cm}$. Since these units were designed to operate in reflectance mode, smooth reflective metal substrates, such as Al, stainless

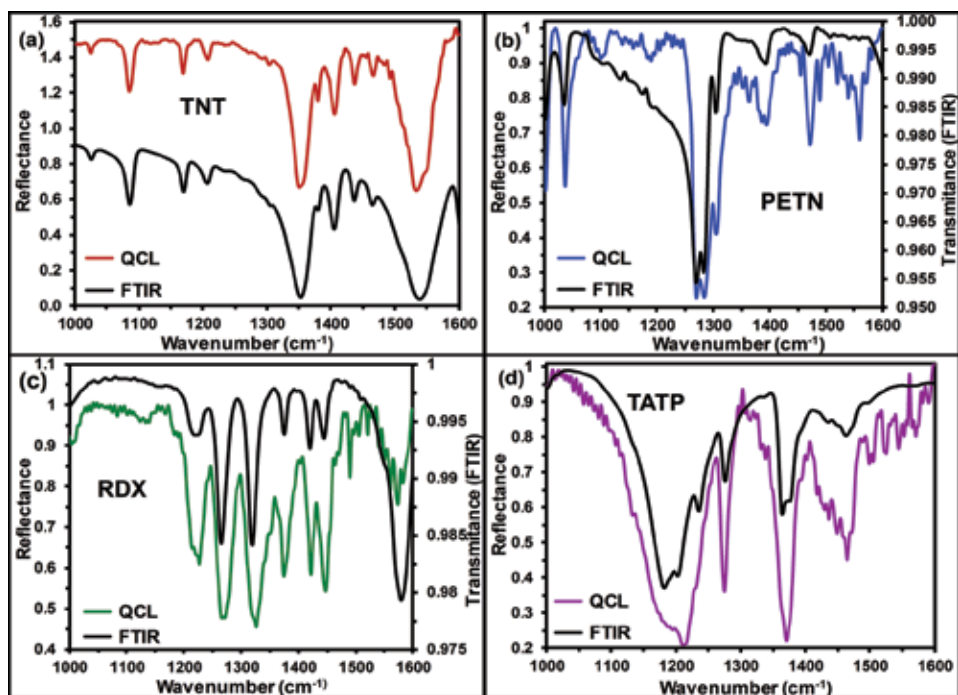


Figure 1. QCL and FTIR (reference) spectra of HEs on reflective Al plates: (a) TNT, (b) PETN, (c) RDX and (d) TATP.

steel (SS), gold, etc., were used for the initial experiments. However, defocusing the MIR laser beam was required when measuring the spectra of chemicals deposited on highly reflective metallic surfaces since the specular radiation collected in back reflection mode saturated the detector. Alternatively, tilting the metallic substrate to 9–10° avoided detector saturation. The reflectance spectra measured with QCL and FTIR (reference) of (a) TNT, (b) PETN, (c) RDX and (d) TATP are shown in **Figure 1**. The MIR laser spectra were collected on a smooth aluminum (Al) substrate. These spectra, as well as other acquired, serve the purpose of validating the proposed technique for detection of neat HEs, mixtures, and formulations, and HME and their chemical precursors. The MIR laser spectra were acquired at open-air conditions. Thus, water vapor lines can be observed for some of the spectra, particularly for TATP samples, which are rapidly sublimating even at room temperature. In other cases, the inherent strength of the MIR signatures of the HEs makes the water vapor lines imperceptible.

3. MIR laser spectroscopy detection of HE on matte substrates

A MIR laser spectrometer was used to acquire reflectance spectra of HEs coatings on matte, low reflectivity substrates such as travel bags (TB; polyester), cardboard (CB), and wood (W). Various deposition methods including smearing, partial immersion, spin coating, and air spray were used for transferring the HEs to the substrates used in the study. The HEs used included nitroaromatic explosive (TNT), aliphatic nitrate ester (PETN), and aliphatic nitramine (RDX). Multivariate analysis (MVA) algorithms were used to analyze the data. Partial least squares (PLS) regression analysis was applied to correlate the intensity of the reflectance bands to the surface loadings of the HE deposited on the substrates. Moreover,

discriminant analysis (DA) combined with PLS (PLS-DA) to identify similarities of HEs and to discriminate spectral features of one type of HE from other types of HEs and substrates [49–51]. The data was pre-treated with Chemometrics algorithms to prepare the reflectance spectra of the explosives deposited on the matte surfaces studied. The results demonstrated that the MIR laser spectroscopy method presented can be used for detection and discrimination of HEs on non-reflective substrates when a supervised model has been previously constructed or when a reference spectrum of the neat substrate can be acquired to be subtracted from the HE/substrate spectrum. Low surface loadings ($1\text{--}15\ \mu\text{g}/\text{cm}^2$) of HEs were used in the investigation.

3.1 Spectral analysis

Reflectance spectra of selected HEs deposited on matte substrates used for the investigation were acquired using the LaserScan™. The MIR region, where fundamental modes of vibration of HEs are located ($1000\text{--}1600\ \text{cm}^{-1}$), such as the symmetric and asymmetric NO_2 modes, was scanned. Representative QCL reflectance spectra of HEs/substrates are illustrated in **Figure 2**. Spectra of HE/Al have been included as reference spectra to help in the assignment of the vibrational markers of the HEs on the non-reflective substrates. Distinctive vibrational signatures of TNT, PETN, and RDX are illustrated in **Figure 2a**. These spectra evidence the reflective nature of the metallic substrate. Tentative assignments for TNT include CH_3 deformation ($1024\ \text{cm}^{-1}$), C–H ring in-plane bending ($1086\ \text{cm}^{-1}$), nitro groups symmetric stretching ($1350\ \text{cm}^{-1}$) and NO_2 asymmetric stretching ($1551\ \text{cm}^{-1}$) [52]. PETN vibrational signatures included CO stretching ($1003\ \text{cm}^{-1}$), NO_2 rocking ($1038\ \text{cm}^{-1}$), ONO_2 rocking ($1272\ \text{cm}^{-1}$), NO_2 stretching ($1285\ \text{cm}^{-1}$) and NO_2

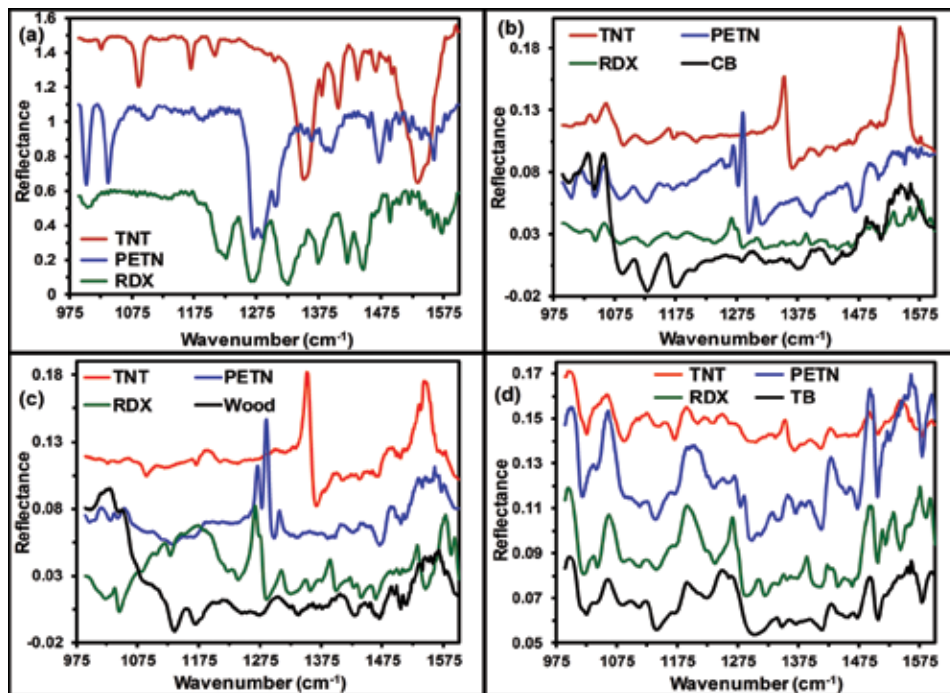


Figure 2. QCL spectra of HEs on substrates studied: (a) Al, reference reflective substrate; (b) CB; (c) wood (W); and (d) TB. Surface concentrations were kept constant at $\sim 15\ \mu\text{g}/\text{cm}^2$ for comparison purposes. Reflectance spectra of matte substrates are included to denote the extent of spectroscopic intrusion.

rocking (1306 cm^{-1}) [53, 54]. Vibrational markers for RDX included N–N and ring stretching (997 cm^{-1}), C–N stretching (1220 cm^{-1}), NO_2 stretching (1270 cm^{-1}), N–N stretching (1310 cm^{-1}), H–C–N asymmetric bending (1420 and 1445 cm^{-1}) and N–O asymmetric stretching (1570 cm^{-1}) [55, 56]. The HEs signatures detected agree well with literature values. The QCL spectroscopic features of the NO_2 group markers from the HEs deposited on the matte substrates used in the investigation differed slightly from those of HEs/Al. When the HEs were deposited on matte surfaces, the vibrational markers were inverted with respect to the corresponding markers of HEs deposited on reflective substrates. Suter et al. also described the same effect when studying the QCL reflectance spectra of TNT deposited on a painted car door [43].

The reflectance of a material is a measure of its capacity to reflect incident light. It is mainly based on: the portion of the incident radiation reflected from the material surface of and the incident power of the radiation at a given wavenumber interval. It is customary to represent reflectance spectra as the ratio of the reflected MIR light from the sample surfaces to the reflected MIR light from the reference surface (Al plate). This is called the relative reflectance. When the HEs were deposited on metallic substrates, such as Al, the intensity of the reflected light was lower in the spectral region where the HEs have MIR signals. This generated “downward” peaks because of the light power loss at the MIR active band location when calculating the relative reflectance spectrum (**Figure 2a**). For samples with HEs deposited on low matte surfaces (such as TB, CB, W) alterations in the optical characteristics of the surfaces took place such that the intensities of the light reflected from the HE/surface combinations was higher in the spectral locations in which the HEs have MIR peaks, generating inverted or “upward” signals.

3.2 Chemometrics analyses

Two MVA routines were used to analyze the laser reflectance spectra: principal component analysis (PCA) and partial least squares (PLS). PCA was employed to classify similarities in a spectral data set, and PLS was used to find the best correlation between the MIR signatures and the surface concentration of the HEs. MVA routines used were highly efficient in achieving the objectives of this research. MVA pre-treatment routines were applied to the QCL reflectance spectra of HEs/substrates combinations. Chemometrics routines used to enhance the detection of target HEs deposited on TB, and CB required only first derivative (1st dvt) and mean centering (MC) as preprocessing routines. W substrates were more challenging for generating efficient PCA models and required a third pre-treatment of the data: standard normal variate (SNV) transformation to achieve discrimination of the HEs from the substrates. Classification according to the type of HE was also attained. A general PCA model of TNT, PETN, and RDX on TB, CB, and W enabled the discrimination - even in the presence of highly MIR absorbing and complex matrices. A total of 12 principal components (PCs) were required to capture a variance of 80%. Hence, MIR laser spectroscopy was shown useful in the detection of HEs on matte surfaces. When coupled with powerful Chemometrics routines, such as PCA, the technique was successful in discriminating the HEs from the highly interfering substrates investigated. Some of the results using PCA models were: **Figure 3a** shows PCA for HE/TB; **Figure 3b** shows the PCA regression model for TNT, PETN, RDX on TB, CB, W (grand model: all HEs/all substrates).

PLS models were highly efficient in predicting the surface loadings of the HEs on the matte surfaces with eight latent variables (LVs) obtaining values of the correlation coefficients (R^2) higher than 0.9. This validates that the developed

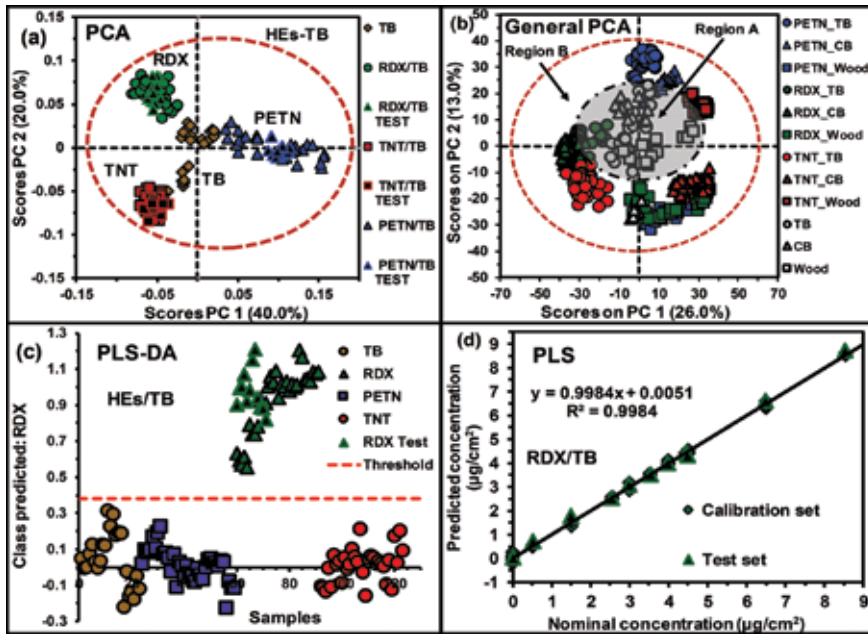


Figure 3. (a) PCA model for QCL detection of HE/TB; (b) general PCA regression model for QCL spectra of HE/substrates. The dotted red closed curve represents a 95% confidence level. (c) Class prediction of HE on TB using PLS-DA; (d) PLS predicted vs. nominal surface concentration of RDX/TB with a correlation coefficient (R^2) of 0.9984.

methodology can be used for the detection of HEs on highly MIR absorbing matte substrates. **Figure 3c** shows an example the resulting from the discrimination of a matte substrate (TB) using the developed PLS-DA models. Discrimination of each HE from the others and the substrate are illustrated in the figure as an example. Four LVs were used to obtain the best MVA classification model with high sensitivity (see **Table 1**), for the data sets of calibration, cross-validation, and prediction. The total variance accounted for was 87.8%, which is sufficiently effective for a good classification of the predicted spectroscopic set on TB. For the Chemometrics cluster analysis of HEs/TB, six LVs were used to retain 80% of the variance of the spectral data. As shown in the score plot in **Figure 3d**, two LVs that captured 60% of

Substrate	Explosive	LV	R^2 CV	R^2 Pred	RMSECV ($\mu\text{g}/\text{cm}^2$)	RMSEP ($\mu\text{g}/\text{cm}^2$)
TB	PETN	8	0.998	0.999	0.12	0.09
	RDX	8	0.996	0.998	0.17	0.13
	TNT	8	0.973	0.971	0.48	0.41
CB	PETN	7	0.980	0.985	0.56	0.41
	RDX	8	0.980	0.987	0.61	0.40
	TNT	8	0.945	0.993	1.06	0.47
Wood	PETN	5	0.989	0.996	0.43	0.29
	RDX	8	0.984	0.985	0.46	0.39
	TNT	9	0.918	0.982	1.03	0.45

Table 1. PLS parameters of calibrations for QCL spectra of HEs deposited on substrates.

the variance was enough to attain a very good classification and to discriminate the HEs from the non-reflective surfaces. Spectra from the prediction sets: RDX-Test, TNT-Test, and PETN-Test were all well grouped according to chemical properties with spectra from the calibration sets.

Figure 4 shows some of the HE/substrates surface concentration profiles generated and an illustration of how obtaining difference spectra can easily result in analytes identification. Similar spectra were used to prepare surface concentration profiles in preparation to perform quantitative Chemometrics runs. A sample set consisting of nine surface concentration profiles, three-HEs \times three-substrates (plus three replicas of each combination), was assembled. Non dosed, clean Al substrates were used as background. **Figure 4a** shows some of the RDX spectra recorded on W substrates. **Figure 4b** shows spectra for TNT on CB at various surface concentrations. **Figure 4c** shows measured QCL reflectance spectra for PETN on wood. The QCL-based methodology proposed for detecting HEs on matte substrates does not necessitate the use of MVA for identifying the HEs. As shown in **Figure 4d**, a reflectance spectrum of the substrate (CB) was compared to the corresponding spectrum of PETN/CB to obtain a difference spectrum: PETN/CB-CB. Examining the MIR laser transfectance spectrum of PETN/Al reveals that several of the vibrational markers of the aliphatic nitrate ester can be readily identified by simple comparison with the reference MIR laser spectrum. Thus, the only prerequisite for the application of this type of remote detection experiment is to acquire a MIR laser spectrum of a non-HE coated part of the substrate surface.

3.3 Conclusions

A MIR laser spectroscopic system allowed the detection of HEs on matte substrates at low substrate loadings on three types non-reflective substrates

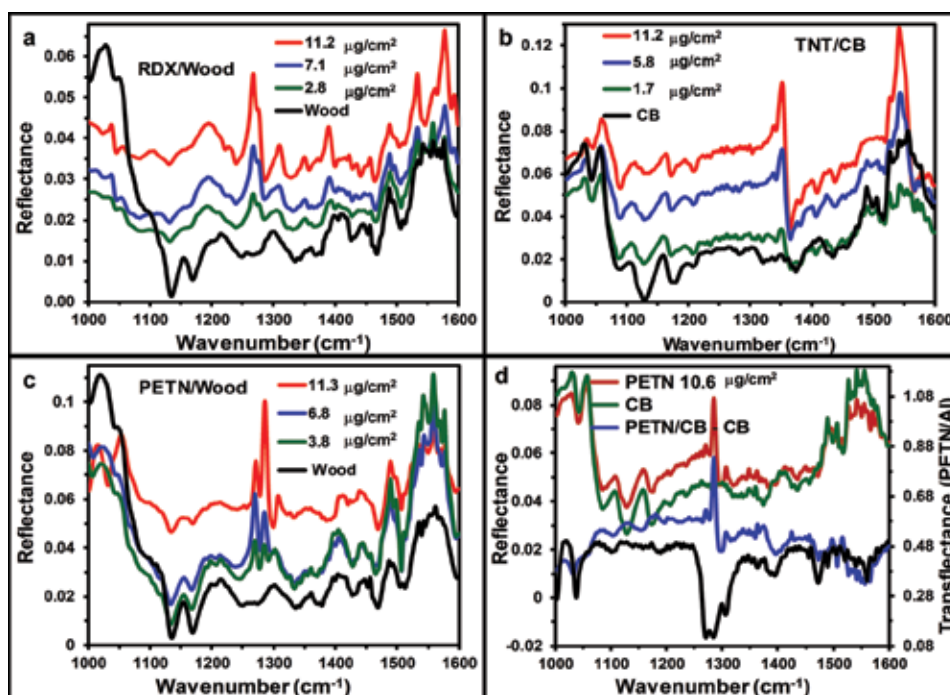


Figure 4. Surface concentration profiles for: (a) RDX/W; (b) TNT/CB; (c) PETN/W; (d) difference spectrum: PETN/CB-CB and QCL transfectance spectrum PETN/Al (Ref).

investigated: TB, CB, and W. Spectral appearance of analytes deposited on substrates depend markedly on the optical properties of the substrate, namely the reflectivity of the surface. For metallic surfaces such as Al and SS, the reflectance spectra are similar to the transmission spectra of the analytes. For non-reflective substrates such as the ones used in this study, transfection spectra are observed that are similar to reflectance spectra with distorted band shapes, where NO₂ group bands dominate. Spectral identification using spectral correlation algorithms are generally insufficient for identifying the analytes when present as surface contaminants on strong MIR absorbing substrates. Nevertheless, MVA routines were adequately robust to attain the objectives of this research. The MVA routines used to identify the target HEs and to discriminate HEs from other HEs and the matte substrates serving as hosts for the explosives deposited on them required only the 1st dvt and MC as pretreatment algorithms for the spectroscopic data. Creating proficient PLS-DA models for W substrates was a much harder challenge, pre-processing a third step (SNV) to achieve the sought discrimination on W surfaces. Furthermore, classifications based on HEs were also achieved. A generalized PLS-DA model involving all HEs on all substrates permitted the discrimination even in the presence of strongly MIR absorbing and matte matrices, although the model relied on 12 LVs to capture a variance of 80%.

MIR laser spectroscopy was proven valuable for developing fast detection methods for detection of HEs on matte substrates. When HE is present on low reflectivity, high MIR absorbing surfaces coupling with MVA routines such as PLS and PLS-DA, identification and efficient discrimination of the HEs from the matte substrates was achieved. Moreover, when a reference spectrum of the matte surface can be obtained previous to obtaining the HE/surface reflectance spectrum, then the HE can be readily identified from a single spectroscopic measurement. Chemometrics routines can be used to create a more statistically sound methodology. PLS models were capable of predicting the surface loadings of explosives on substrates investigated using eight LVs or less to obtain regression coefficients squared values >0.9 [44, 57].

4. MIR laser spectroscopy assisted by classical least squares

Remote sensing using IRS depends on the range: observer-target distance. Other important factors to consider are the angle between source-target-detector and the reflectivity of the target. In the search for attaining higher return signals in back reflection mode, a QCL spectrometer was used to determine the presence of HE on cotton and other fabrics. The identification of vibrational signals was generated by a simple spectral comparison using classical least squares (CLS) in the minimization of the difference between real spectra (RS) and calculated spectra (CS). The models used for obtaining CS were based on linear combinations of HE spectra, cotton spectra, and biases. The QCL spectrometer was equipped with a 3" diam. Convex ZnSe lens, which had three purposes: to focus the MIR light beam on the sample at 15 cm, to collect the reflected light, and to direct the light onto an internal MCT detector. Wavenumber precision and accuracy were 0.2 and 0.5 cm⁻¹, respectively. The optimum reflectance measurements were obtained at 15 ± 3 cm.

Experiments considering binary, ternary, and quaternary combinations of components such as cotton (and other fibers), TNT, RDX, and PETN were performed. The parameters calculated for the linear combination of the calculated spectrum were used to generate a discriminant analysis to determine the sensibility and specificity. Also, the extracted spectral signals of several amounts of RDX ($m_{\text{RDX}} \geq 0.02$ mg) deposited on the cotton substrates were used to calculate the

LOD value from the calculated S/Ns, which were determined from several spectra of cotton with different amounts of RDX in decreasing order until the S/N was ~ 3 . Several DA schemes were successful in distinguishing the HE signals from those of the fabric substrates, but identification of HEs on cotton fabrics was achieved without the MVA used for discrimination.

The HEs samples were deposited on cotton and other fabrics by direct download of the solid. Two types of procedures were used for HE deposition. First, an amount of HE was deposited on glass, then the fabrics substrates were placed in contact with the HE/glass, and the HE was forced to be transferred using a thumb-print. In the second procedure, a metallic tip was pressed against a deposit of HE, and small quantities (particles) of the HE were transferred to the tip. Then these particles were deposited onto the fabrics. The fabrics were weighted before and after the transfer of the HEs to know the quantities deposited. Mass measurements were done using two scales. The first scale used for depositions of 3–0.1 mg, had a precision of ± 0.1 mg. The second scale (thermogravimetric analysis scale) used for deposition of HE samples of masses ≤ 0.1 mg, had a precision of ± 0.01 μg .

CLS can be considered as the transition between univariate and multivariate procedures of analysis. It is the most used regression method in academic environments since it is based on the Beer-Lambert–Bouguer linear relationship between the absorbance of a chemical species in a mixture of a solute and solvent, the path length of the light through the cell containing the mixture and the molar concentration of the species. Its familiarity among practitioners and students is based on the fact that for dilute solutions, it is directly applicable to quantitative spectral analyses [58].

CLS analysis can be easily extended to multi-component systems, where a wide range of peaks of several components in a mix is involved in the study. Typically, comprehensive information of the discrete constituents in the matrix studied is essential. This requirement is the greatest limitation of the regression analysis algorithm. Thus, the spectrum of each of the neat component as well as the spectrum of the mix is required to be able to estimate the spectral portion of each constituent in the mix. This is correct only when pure constituents are involved. The intensity at any wavenumber can be treated as a linear arrangement of the intensities of each constituent in the mix. The technique also estimates the portion of each spectrum constituent in the spectrum of the mix by minimizing the sum of the squares of the errors. Typically, this is equal to or linearly related to the percentage in the mix.

Two components, three components, and four components mixes were made from the four (4) constituents in the calibration set: three explosives: TNT, RDX, PETN, and the substrates: cotton, synthetic fabric or a mixed fabric. CLS analysis was coupled to QCL reflectance measurements of the four components and their mixes with the objective of developing a methodology for fast detection and discrimination analysis HE on fabrics. A simple technique for visualization of the data and interpretation of the models is presented. PLS-DA-based analysis requires the generation of independent models for each fabric type. This makes this MVA routine very hard to adapt to field detection of HEs. In the proposed CLS application, adapting the models to field work requires adding the spectra of new HEs or new substrates types to the database.

QCL diffuse reflectance spectra of all components and mixes were acquired using a rough gold substrate as background reference. Reflectance units (R) were converted to $[-\log(R)]$ to be used in the Chemometrics analysis of the data. **Figure 5** contains typical spectra obtained for the HEs and the fabrics. Normalization of the spectral data was achieved using SNV as preprocessing algorithm, applied to the whole spectroscopic range studied to remove the baseline drifts caused by scattering based on variations in particle size of the analytes (HEs) and the morphology of the substrates.

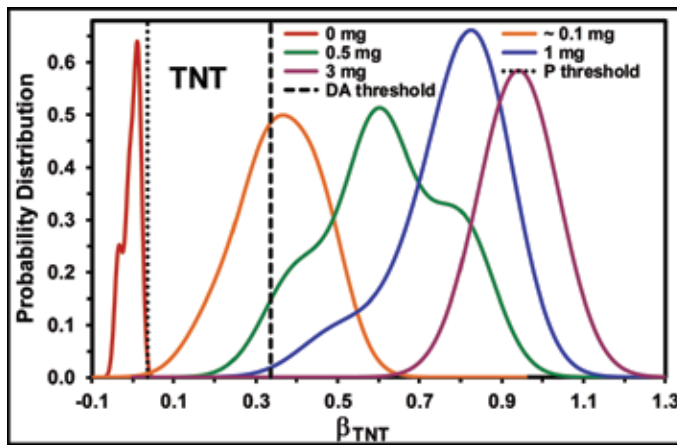


Figure 5.
 Kernel probability distribution of the $\hat{\beta}_{\text{TNT}}$ parameter for TNT/cotton binary mix.

4.1 Statistical models

Spectra were acquired in SPC file format for spectroscopy (Thermo-Galactic Grams/AI™, Thermo-Fisher Scientific, Inc., Waltham, MA, USA) and analyzed using a CLS algorithm coded in Matlab™ (The MathWorks, Inc., Natick, MA, USA). PLS Toolbox v. 8.1 (Eigenvector Research, Inc., Manson, WA, USA) was used to generate the matrices for other MVA. Other statistical routines were implemented using Statgraphics Centurion XV software, version 15.2.05. (Statpoint Technologies, Inc. Warrenton, VA, USA). The linear model based on CLS can be described by [58].

$$f(\varphi_j, \hat{\beta}_j)_i = \hat{\beta}_0 + \hat{\beta}_1 \varphi_1(\omega_i) + \dots + \hat{\beta}_j \varphi_j(\omega_i) \quad (1)$$

Here, $(\varphi_j, \hat{\beta}_j)_i$ represents the i th intensity, normalized, of the spectrum with intensities calculated in $[-\log(R)]$ units, from a mix of several constituents (j); $\varphi_j(\omega_i)$ is the intensity at each wavenumber (ω_i) of the net spectrum belonging to the j component, and $\hat{\beta}_j$ is a parameter that indicates the portion of the spectrum of a given constituent in the spectrum of the mix. It has been assumed that there are no interactions among the components in the mix leading to chemical bonds. If present, these interactions would result in changes in intensities, shifts of band locations and formation or loss of vibrational bands due to the chemical bonds formed. Thus, at least to first order, the contributions to a given intensity are additive. The $\hat{\beta}_j$ were estimated by computing the minimum value of the square of the difference between the real (RS) and the calculated spectra (CS) according to:

$$d_i = y_i - \hat{f}(\varphi_j, \hat{\beta}_j)_i \quad (2)$$

The minimum of the sum of the squares of the residuals (d_i) with respect to $\hat{\beta}_j$ can be obtained by calculating the first-order partial derivatives with respect to $\hat{\beta}_j$, equating them to zero and calculating the values for $\hat{\beta}_j$. This leads to a set of “ n ” parameters, which represent “ n ” partial-derivative equations:

$$\frac{\partial d^2}{\partial \hat{\beta}_j} = -2 \sum_i d_i \frac{\partial f(\hat{\varphi}_j, \hat{\beta}_j)_i}{\partial \hat{\beta}_j} = 0, \quad j = 1, 2, \dots, n \quad (3)$$

The signals of interest for each constituent of the mix can be extracted from the model. For instance, for constituent 1, the extracted spectrum ($\hat{\psi}$) is

$$\hat{\psi}_{1(\omega_i)} = y_i - \hat{\beta}_0 - \hat{\beta}_2 \varphi_2(\omega_i) - \dots - \hat{\beta}_j \varphi_j(\omega_i) \quad (4)$$

Three types of CLS models were created, according to the constituents in the mix: 2, 3, and 4-constituent models. One of the binary models consisted only in spectra of the fabric and one of the HEs. Thus, Eq. (1) now becomes:

$$f_{cotton}^{HE} = \hat{\beta}_0 + \hat{\beta}_{cotton} \varphi_{cotton}(\omega_i) + \hat{\beta}_{HE} \varphi_{HE}(\omega_i) \quad (5)$$

A total of 12 samples containing surface loadings of HEs in the range of 0.1–3 mg were prepared. The $\hat{\beta}_{HE}$ values were calculated from five replicate spectra acquired at various positions on the surface for the various sample concentrations, resulting in a total of 60 spectra. Probability distributions were then predicted. P-models for each of the HE/substrate binary combinations were generated. The p-values of the models were used as decision thresholds. These values were determined by using the projected average value (\bar{x}) of $\hat{\beta}_{HEM}$ for the cotton fabric substrates (controls) and standard deviations (s_d) according to:

$$p = \bar{x} + 3.28 \cdot s_d \quad (6)$$

From the definition of the LOD, the random error was estimated at 5% [42–44]. This implies that there is a high probability that non-dosed substrates were below the threshold. To obtain good discrimination typical spectra of the fabric substrates were required to be present in the database. As shown in **Table 2**, the models generated were characterized with high selectivity and sensitivity for the HEs in the range of 0.1–3 mg. The CLS-based model was compared with a discriminant analysis (DA) model. **Table 2** contains the results, where the value of $\hat{\beta}_{HE}$ was used to create a model for discrimination. The difference between the CLS model and the DA model is in the calibration. The CLS model required a spectrum of the substrate (cotton) without the presence of HEs (no HE) and with the reflectance spectra of the HEs (no substrate). There is no need to include HEs/substrates spectra. **Figure 5** shows the estimation of the probability for TNT in the range of 0.1–3 mg vs. $\hat{\beta}_{TNT}$.

The spectra for the two-component models for the HEs are shown in **Figure 6a–c**. In each of these graphs, the spectra with ~0.1 mg of the HE/cotton fabric substrates are shown in blue. Predicted spectra from Eq. (5) are in red. Reference spectra for the powder form of the HEs (“Ref”) and cotton fabric substrates are in black and orange, respectively. The HE/cotton spectra with the cotton fabric spectra subtracted using Eq. (5) are in green. The two-components model that consists of cotton fabric and RDX spectra is shown as an example. The equation used was based on Eq. (5):

$$f_{cotton}^{RDX} = \hat{\beta}_0 + \hat{\beta}_{cotton} \varphi_{cotton}(\omega_i) + \hat{\beta}_{RDX} \varphi_{RDX}(\omega_i) \quad (7)$$

The equation for three-components models (cotton, TNT, RDX) following Eq. (1) is:

$$f_{cotton}^{TNT+RDX} = \hat{\beta}_0 + \hat{\beta}_{cotton} \varphi_{cotton}(\omega_i) + \hat{\beta}_{TNT} \varphi_{TNT}(\omega_i) + \hat{\beta}_{RDX} \varphi_{RDX}(\omega_i) \quad (8)$$

Three components mixes were composed of TNT, RDX, and fabric substrates. The sample set included 12 samples each in the range of 0.1–3 mg of 100% TNT and % RDX (24 samples) and 134 samples of binary mixtures of 50% TNT/RDX in the

Component	CLS model		Discriminant model		
	Sensitivity	Specificity	Sensitivity	Specificity	
	Binary		Binary		
Cotton	100%	100%	100%	89%	
TNT	100%	100%	89%	100%	
Cotton	100%	100%	100%	85%	
RDX	100%	100%	85%	100%	
Cotton	100%	100%	100%	95%	
PETN	100%	100%	95%	100%	
		Ternary		Ternary	
Cotton	100%	100%	100%	86%	
TNT	100%	97%	94%	100%	
RDX	99%	88%	91%	100%	
HEM	100%	100%	86%	100%	
		Quaternary		Quaternary	
Cotton	100%	100%	100%	88%	
TNT	89%	94%	86%	90%	
RDX	95%	84%	86%	100%	
PETN	99%	67%	86%	91%	
HEM	100%	100%	88%	100%	

Table 2.
 Sensitivity and specificity values for CLS and DA models.

range of 0.5–3 mg deposited on cotton fabric. These were treated in the same way as for binary mixes. The values of $\hat{\beta}_{TNT}$ and $\hat{\beta}_{RDX}$ were estimated and the distribution plot for each sample from Eq. (8).

Quaternary mixes containing TNT, RDX, PETN, and fabrics can be described by:

$$f_{cotton}^{HEs} = \hat{\beta}_0 + \hat{\beta}_{cotton} \varphi_{cotton}(\omega_i) + \hat{\beta}_{TNT} \varphi_{TNT}(\omega_i) + \hat{\beta}_{RDX} \varphi_{RDX}(\omega_i) + \hat{\beta}_{PETN} \varphi_{PETN}(\omega_i) \quad (9)$$

Four components mixes were similar to three-component mixes with the addition of PETN. A total of 252 samples of 100% TNT, RDX, and PETN in the mass range of 0.1 to 3 mg and 50% mixes of TNT/RDX, TNT/PETN, PETN/RDX, and 33.3% mixes of TNT/PETN/RDX, each in the range of 0.5–3 mg were transferred onto cotton substrates. The values for $\hat{\beta}_{TNT}$, $\hat{\beta}_{RDX}$, and $\hat{\beta}_{PETN}$ for the mixes were estimated together with their distribution plot for each sample from Eq. (9). **Table 2** contains the calculated values for the sensitivity and specificity. Comparison of reference spectra of HE and a spectrum for the quaternary mixture TNT-RDX-PETN/cotton is illustrated in **Figure 6d**.

A DA was done with the purpose of evaluating the discriminating capacity of the β parameters. Discriminating functions (F1, F2, and F3) were obtained. The functions captured nearly all the statistically pertinent information of the DA, contributing to 95.3% of the discrimination. Eigenvalues for the discriminant functions were highly significant ($p < 0.0001$). **Table 3** shows the values for the canonical correlation coefficient, which is indicative of the efficiency for discriminating new samples, the functions showed excellent capabilities for determining group differences: 93% (F1), 87% (F2), and 77% (F3). F3 was not as effective as the other two

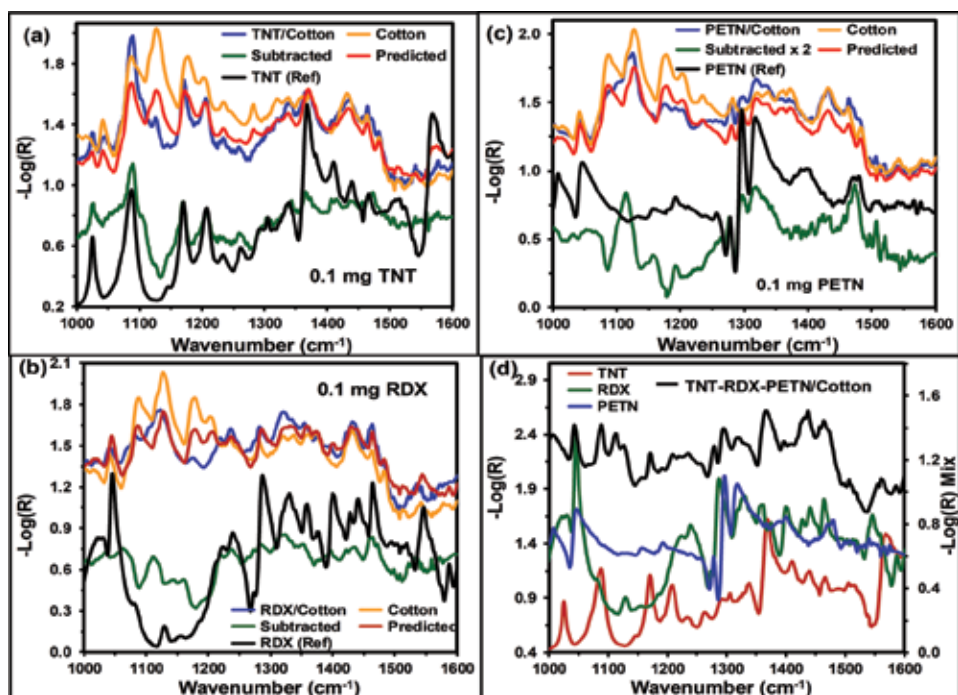


Figure 6. (a–c) Spectra of ~ 0.1 mg of HE/cotton (blue); predicted spectra from Eq. (5) (red traces); cotton spectra (orange); subtraction of the cotton spectra from HE/cotton spectra calculated using Eq. (4) (green); reference HE spectra (black); (d) comparison of reference spectra of HE and a spectrum for the quaternary mixture: TNT-RDX-PETN/cotton.

	Discriminant analysis		
Discriminant function	1	2	3
Eigenvalue	6.2	3.2	0.5
Relative %	63%	32%	5%
Canonical correlation	0.93	0.87	0.56
Wilks Lambda	0.02	0.16	0.68
Chi-squared	901.9	431.7	90.6
p value	<0.0001	<0.0001	<0.0001

Table 3. Values of statistical parameters of functions derived from the $\hat{\beta}_{HE}$ parameters.

DA functions. The value for the LOD was calculated from various spectra of RDX at low surface loadings (<0.1 mg). The RDX vibrational signatures were assigned and Eq. (4) was applied to the laser reflectance spectra. Then S/Ns were calculated for two signals (1040 and 1463 cm^{-1}). An S/N of 3 represented a mass of 22 ± 6 μg . According to the IUPAC definition, this is the LOD. Other methods for calculating the LOD lead to values ranging from 15 to 58 μg RDX.

4.2 Tests with other substrates

Other fabrics were tested as substrates (5 in total). These included 100%, cotton (white T-shirt), 100% polyester, 65% polyester/35% cotton, 45% polyester/55% cotton, and 84% polyester/16% SpandexTM. Spectra for the clean substrates (no HEs)

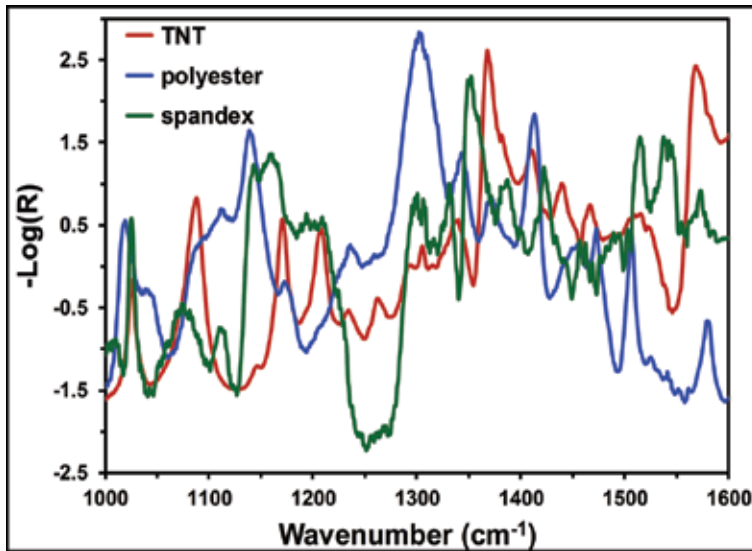


Figure 7. QCL reflectance spectra of components used in the additional tests of the proposed methodology based on CLS: TNT, polyester and Spandex™.

and spectra of substrates dosed with TNT were acquired. **Figure 7** shows the MIR laser spectra of TNT, polyester, and Spandex™ used for the three additional models generated. First, a two-component model was generated with TNT as HE, based on Eq. (5). This model consisted of a spectrum for blue jeans cotton and a spectrum of TNT. **Table 4** contains the information resulting from the study. All substrates containing TNT were predicted correctly. Nevertheless, some of the samples containing polyester and Spandex™ (no TNT) were predicted as having TNT, i.e., as false positives. Except for the samples of white cotton substrates, $\hat{\beta}_{TNT}$ values were high, since the model previously incorporated a spectrum of cotton from blue jeans. High $\hat{\beta}_{TNT}$ values were predicted for samples with low amounts of TNT (~0.1 mg). This was unexpected since $\hat{\beta}_{TNT}$ values should have been low. In spectra of samples of polyester and spandex polymer substrates the result can be explained based on the fact that these substrates have intense peaks in the same spectral range as TNT.

Spectra of cotton, polyester, and TNT were used to build another model. Then the spectrum of polyester was included in the model resulting in samples with this substrate were correctly predicted with values of $\hat{\beta}_{TNT}$ close to zero. Samples of Spandex™ substrate were incorrectly classified. A third model was created by adding the spectrum of Spandex™ to the second model. This resulted in a correct classification of all samples. Moreover, samples with low amounts of TNT (~0.1 mg) had a low value of $\hat{\beta}_{TNT}$ (**Table 4**). This further confirms the hypothesis in order to have a good prediction ability for CLS models developed it is important to include the spectra of all components, including spectra of neat substrates. For practical identification of HEs on fabrics in defense and security applications, the database to be built must contain the spectrum of the target HE, as well as the spectra for the substrate and the other components in the matrix. Moreover, this important result leads to the conclusion that the model is forward adaptive, both to “new” HEs and “new” substrates.

4.3 Conclusions

Reconceptualization of CLS procedure in combination MIR laser spectroscopy resulted in a protocol for detection of HEs in mixes. The ability of the MIR laser

Sample	Model1 ($\hat{\beta}_{TNT}$)	Model2 ($\hat{\beta}_{TNT}$)	Model3 ($\hat{\beta}_{TNT}$)
White cotton	-0.05 ± 0.01	-0.07 ± 0.01	-0.06 ± 0.01
Polyester	0.15 ± 0.05	-0.01 ± 0.03	0.00 ± 0.02
65% polyester 35% cotton	0.15 ± 0.03	-0.05 ± 0.03	-0.01 ± 0.03
45% polyester 55% cotton	0.04 ± 0.04	-0.03 ± 0.03	-0.07 ± 0.03
84% polyester 16% spandex	0.31 ± 0.03	0.17 ± 0.03	0 ± 0.03
2 mg TNT 65% polyester 35% cotton	0.83 ± 0.04	0.78 ± 0.04	0.68 ± 0.05
0.5 mg TNT 65% polyester 35% cotton	0.5 ± 0.1	0.4 ± 0.1	0.3 ± 0.1
2 mg TNT 45% polyester 55% cotton	0.72 ± 0.08	0.67 ± 0.09	0.58 ± 0.09
0.5 mg TNT 45% polyester 55% cotton	0.38 ± 0.02	0.31 ± 0.02	0.27 ± 0.03
4 mg TNT on 84% polyester 16% spandex	0.9 ± 0.1	0.9 ± 0.1	0.9 ± 0.1
2 mg TNT on 84% polyester 16% spandex	0.3 ± 0.1	0.3 ± 0.2	0.5 ± 0.2
0.8 mg TNT on 84% polyester 16% spandex	0.3 ± 0.2	0.2 ± 0.2	0.3 ± 0.2
0.5 mg TNT on 84% polyester 16% spandex	0.4 ± 0.1	0.3 ± 0.1	0.2 ± 0.2
~0.1 mg TNT on 84% polyester 16% spandex	0.25 ± 0.01	0.12 ± 0.01	0.05 ± 0.01

Table 4. Prediction of $\hat{\beta}_{TNT}$ parameters for the three models developed for additional fabrics.

spectroscopy assisted by CLS for detection of 1, 2, and 3 HEs in solid mixes deposited on non-reflective surfaces, such as cotton, polyester and spandex fabrics, was demonstrated. Moreover, the adaptive learning ability of the models based on CLS was also demonstrated by performing discrimination with the spectra corresponding to the different substrate where the HE detection would occur. This important feature of the CLS models was demonstrated by adding spectra of five other substrates (fabrics) to the database. Neat substrates (no analyte present) and substrates containing TNT were investigated. For models that did not contain the spectra of the fabric substrate, false positives were obtained resulting in detection failure for samples with HEs. Thus, for the methodology to work, the model must be fed with the spectra for the fabric substrates and HEs.

RDX signals ($m_{RDX} > 0.02$ mg) on cotton fabrics were used to calculate the LOD. Values of S/N calculated from the spectra of cotton fabrics dosed with decreasing masses of RDX until $S/N \approx 3$ resulted in a LOD of 15–33 μg , depending on the spectroscopic signal used. Comparisons of dosed RDX mass with the fraction predicted led to linear fits which were also used to calculate LOD values based on the uncertainty of the blank and the slope of the fit. The LOD value resulting from this procedure was of 58 μg . Another way of calculating the LOD used an interpolation of the p-value threshold for low RDX dosage resulted in a value of 40 μg . This is probably the most representative value of the method LOD [59].

The minimum limit of quantification (LOQ) of surface concentrations was based on experiments performed on three-components mixes of RDX/PETN/cotton. The LOQ value for RDX was 10%. Vibrational markers for PETN and RDX could be readily observed for all samples except at 5% RDX (lowest concentration). Successful detection of RDX on cotton in the 10% RDX/90% PETN mix on cotton was achieved using the presented procedure.

Coupling of CLS to QCL reflectance data of analyte residues on fabrics enable a fast and efficient discrimination procedure providing an improved understanding and visualization of analyte/substrate reflectance signals. Since there is a nonlinear

dependence between the spectrum of the mix and the spectra of the neat components, quantification of HE/fabric is not easily achieved. However, this situation does not affect HEs detection on fabrics for all the cases studied. Further studies are required to determine if QCL-CLS detection of HE can be done on other matte substrates, particularly in the presence of interferents and other contaminants [57, 60].

5. Summary

MIR laser spectroscopy is a powerful spectroscopic analysis technique that has recently achieved significant acceptance in many fields of science and technology. When the reflectance spectra excited by a QCL system is coupled to the powerful MVA routines of Chemometrics, the results obtained are even further reaching, regarding the discriminating power, the LOD and LOQ, and the clustering of similar data and separation of dissimilar data of not easily correlated spectroscopic information. A selection of several applications of MIR laser spectroscopy has been presented that concentrating on the detection of HEs. The near and far future of the technique is as bright as the MIR lasers that shine on samples to enable design and development of new applications as well as revisiting other well established spectroscopic tools under highly enhanced conditions.

Acknowledgements

This material is based upon work supported by the U.S. Department of Homeland Security, Science and Technology Directorate, Office of University Programs, under Grant Award 2013-ST-061-ED0001. The views and conclusions contained in this document are those of the authors and should not be interpreted as necessarily representing the official policies, either expressed or implied, of the U.S. Department of Homeland Security. Parts of the work were supported by the U.S. DoD, Agreement Number: W911NF-11-1-0152.

Author details

Leonardo C. Pacheco-Londoño^{1,2}, John R. Castro-Suarez^{1,3}, Nataly J. Galán-Freyle^{1,2}, Amanda M. Figueroa-Navedo¹, José L. Ruiz-Caballero¹, Ricardo Infante-Castillo^{1,4} and Samuel P. Hernández-Rivera^{1*}

1 Department of Chemistry, ALERT DHS Center of Excellence, University of Puerto Rico-Mayagüez, Mayagüez, PR, USA


2 School of Basic and Biomedical Sciences, Universidad Simón Bolívar, Barranquilla, Colombia

3 Antonio de Arévalo Technological Foundation, TECNAR, Cartagena, Colombia

4 Department of Physics-Chemistry, University of Puerto Rico, Arecibo, PR, USA

*Address all correspondence to: samuel.hernandez3@upr.edu

IntechOpen

© 2018 The Author(s). Licensee IntechOpen. This chapter is distributed under the terms of the Creative Commons Attribution License (<http://creativecommons.org/licenses/by/3.0>), which permits unrestricted use, distribution, and reproduction in any medium, provided the original work is properly cited. 

References

- [1] Schraeder B. Early history of vibrational spectroscopy. In: Schrader B, editor. *Infrared and Raman Spectroscopy: Methods and Applications*. Weinheim, Germany (New York, NY): VCH; 1995. ISBN: 3-527-26446-9
- [2] Sheppard N. The historical development of experimental techniques in vibrational spectroscopy. In: Chalmers JM, Griffiths PR, editors. *Handbook of Vibrational Spectroscopy*. Vol. 1. West Sussex England: Wiley, Chichester; 2002. 1 p. ISBN: 978-0-471-98847-2
- [3] Griffiths PR. Introduction to vibrational spectroscopy. In: Chalmers JM, Griffiths PR, editors. *Handbook of Vibrational Spectroscopy*. Vol. 1. Chichester, West Sussex, England: Wiley; 2002. 33 p. ISBN: 978-0-471-98847-2
- [4] Griffiths PR, de Haseth JA. *Fourier Transform Infrared Spectrometry*. 2nd ed. Hoboken, NJ: John Wiley & Sons, Inc.; 2007. ISBN: 978-0-471-19404-0
- [5] Larkin P. *Infrared and Raman Spectroscopy: Principles and Spectral Interpretation*. 2nd ed. Waltham, MA, USA: Elsevier; 2018. ISBN: 978-0-12-804162-8
- [6] Yinon J, Zitrin S. *Modern Methods and Applications in Analysis of Explosives*. Chichester, UK: John Wiley & Sons Ltd; 1996. ISBN: 978-0-471-96562-6
- [7] Castro-Suarez JR, Ortiz-Rivera W, Galán-Freyre N, Figueroa-Navedo A, Pacheco-Londoño LC, Hernández-Rivera SP. *Multivariate Analysis in Vibrational Spectroscopy of Highly Energetic Materials and Chemical Warfare Agents Simulants*. DOI: 10.5772/54104
- [8] Valim de Freitas L, Barbosa Rodrigues de Freitas AP. *Multivariate Analysis in Management, Engineering and the Sciences*. Rijeka, Croatia: InTech; 2013. DOI: 10.5772/3301. ISBN: 978-953-51-0921-1
- [9] Steinfeldt JI, Wormhoudt J. Explosives detection: A challenge for physical chemistry. *Annual Review of Physical Chemistry*. 1998;49:203-232. DOI: 0066-426X/98/1001-0203
- [10] Committee on the Review of Existing and Potential Standoff Explosives Detection Techniques, Existing and Potential Standoff Explosives Detection Techniques. Washington, DC: National Research Council, National Academy of Sciences Committee; 2004. DOI: 10.17226/10998
- [11] Parmenter JE. The challenge of standoff explosives detection. In: *Proceedings of the 38th Annual International Carnahan Conference on Security Technology*. New York, NY: IEEE; 2004. pp. 355-358
- [12] Schubert H, Rimski-Korsakov A. Stand-off detection of suicide-bombers and mobile subjects. In: *Proceedings of the NATO Advanced Research Workshop on Stand-off Detection of Suicide Bombers and Mobile Subjects, NATO Security through Science Series B: Physics and Biophysics*, Pfinztal, Germany. Germany: Springer; 2005
- [13] Moore DS. Instrumentation for trace detection of high explosives. *The Review of Scientific Instruments*. 2004;75:2499-2512. DOI: 10.1063/1.1771493
- [14] Moore DS. Recent advances in trace explosives detection instrumentation. *Sensing and Imaging*. 2009;8(1):9-38. DOI: 10.1007/s11220-007-0029-8

- [15] Marshall M, Oxley JC. Aspects of Explosives Detection. Amsterdam, The Netherlands: Elsevier; 2009. ISBN: 978-0-12-374533-0
- [16] Caygill JS, Davis F, Higson SPJ. Current trends in explosive. *Talanta*. 2012;**88**:14-29. DOI: 10.1016/j.talanta.2011.11.043
- [17] Tourné M. Developments in explosives characterization and detection. *Journal of Forensic Research*. 2013;**S12**:1-10. DOI: 10.4172/2157-7145.S12-002
- [18] Fountain AW III, Christesen SD, Moon RP, Guicheteau JA. Recent advances and remaining challenges for the spectroscopic detection of explosive threats. *Applied Spectroscopy*. 2014;**68**(8):795. DOI: 10.1366/14-07560
- [19] Carter JC, Angel SM, Lawrence-Snyder M, Scaffidi J, Whipple RE, Reynolds JG. Standoff detection of high explosive materials at 50 meters in ambient light conditions using a small Raman instrument. *Applied Spectroscopy*. 2005;**59**(6):769-775. DOI: 10.1366/0003702054280612
- [20] Ortiz-Rivera W, Pacheco-Londoño LC, Castro-Suarez JR, Félix-Rivera H, Hernandez-Rivera SP. Vibrational spectroscopy standoff detection of threat chemicals. *Proceedings of SPIE*. 2011;**8031**(803129):803129-803110. DOI: 10.1117/12.884433
- [21] Moros J, Lorenzo JA, Novotný K, Laserna JJ. Fundamentals of stand-off Raman scattering spectroscopy for explosive fingerprinting. *Journal of Raman Spectroscopy*. 2013;**44**(1): 121-130. DOI: 10.1002/jrs.4138
- [22] Wallin S, Pettersson A, Östmark H, Hobro A. Laser-based standoff detection of explosives: A critical review. *Analytical and Bioanalytical Chemistry*. 2009;**395**(2):259-274. DOI: 10.1007/s00216-009-2844-3
- [23] Galán-Freyte NJ, Pacheco-Londoño LC, Figueroa-Navedo AM, Hernandez-Rivera SP. Standoff detection of highly energetic materials using laser-induced thermal excitation of infrared emission. *Applied Spectroscopy*. 2015;**69**(5):535-544. DOI: 10.1366/14-07501
- [24] Castro-Suarez JR, Pacheco-Londoño LC, Vélez-Reyes M, Diem M, Tague TJ, Hernandez-Rivera SP. FT-IR standoff detection of thermally excited emissions of trinitrotoluene (TNT) deposited on aluminum substrates. *Applied Spectroscopy*. 2013;**67**(2):181-186. DOI: 10.1366/11-06229
- [25] Pacheco-Londoño LC, Ortiz-Rivera W, Primera-Pedrozo OM, Hernández-Rivera SP. Vibrational spectroscopy standoff detection of explosives. *Analytical and Bioanalytical Chemistry*. 2009;**395**(2):323-335. DOI: 10.1007/s00216-009-2954-y
- [26] Pettersson A, Johansson I, Wallin S, Nordberg M, Östmark H. Near real-time standoff detection of explosives in a realistic outdoor environment at 55 m distance. *Propellants, Explosives, Pyrotechnics*. 2009;**34**(4):297-306. DOI: 10.1002/prop.200800055
- [27] Faist J, Capasso F, Sivco DL, Sirtori C, Hutchinson A, Cho AY. Quantum cascade laser. *Science*. 1994;**264**(5158):553-556. DOI: 10.1126/science.264.5158.553
- [28] Faist J, Capasso F, Sirtori C, Sivco DL, Baillargeon JN, Hutchinson AL, et al. High power mid-infrared ($\lambda \sim 5 \mu\text{m}$) quantum cascade lasers operating above room temperature. *Applied Physics Letters*. 1996;**68**(26):3680-3682. DOI: 10.1063/1.115741
- [29] Capasso F, Gmachl C, Paiella R, Tredicucci A, Hutchinson AL, Sivco DL, et al. New frontiers in quantum cascade lasers and applications. *IEEE Journal of Selected Topics in Quantum Electronics*. 2000;**6**:931. DOI: 10.1109/2944.902142

- [30] Gmachl C, Capasso F, Sivco DL, Cho AY. Recent progress in quantum cascade lasers and applications. *Reports on Progress in Physics*. 2001;**64**:1533. DOI: 10.1088/0034-4885/64/11/204
- [31] Beck M, Hofstetter D, Aellen T, Faist J, Oesterle U, Ilegems M, et al. Continuous wave operation of a mid-infrared semiconductor laser at room temperature. *Science*. 2002;**295**(5553):301-305. DOI: 10.1126/science.1066408
- [32] Mizaikoff B, Lendl B. Sensor systems based on mid-infrared transparent fibers. In: Chalmers JM, Griffiths PR, editors. *Handbook of Vibrational Spectroscopy*. Vol. 2. Chichester, West Sussex, England: Wiley; 2002. ISBN: 978-0-471-98847-2
- [33] Razeghi M. High-performance InP-based mid-IR quantum cascade lasers. *IEEE Journal of Selected Topics in Quantum Electronics*. 2009;**15**:941. DOI: 10.1109/JSTQE.2008.2006764
- [34] Razeghi M. High-power high-wall plug efficiency mid-infrared quantum cascade lasers based on InP/GaInAs/InAlAs material system. *Proceedings of SPIE*. 2009;**7230**:723011. DOI: 10.1117/12.813923
- [35] Pushkarsky MB, Dunayevskiy IG, Prasanna M, Tsekoun AG, Go R, Patel CKN. High sensitivity detection of TNT. *Proceedings of the National Academy of Sciences of the United States of America*. 2006;**103**(52):19630-19634. DOI: 10.1073/pnas.0609789104
- [36] Patel CKN. Laser based In-situ and standoff detection of chemical warfare agents and explosives. *Proceedings of SPIE*. 2009;**7484**:748402-1-78401-14. DOI: 10.1117/12.835883
- [37] Bauer C, Willer U, Schade W. Use of quantum cascade lasers for detection of explosives: Progress and challenges. *Optical Engineering*. 2010;**49**(11):111126-111126-7. DOI: 10.1117/1.3498771
- [38] Pacheco-Londoño LC, Castro-Suarez JR, Hernández-Rivera SP. Detection of nitroaromatic and peroxide explosives in air using infrared spectroscopy: QCL and FTIR. *Advanced Optical Technologies*. 2013;**2013**:8 p. Article ID: 532670. DOI: 10.1155/2013/532670
- [39] Van Neste CW, Senesac LR, Thundat T. Standoff spectroscopy of surface adsorbed chemicals. *Analytical Chemistry*. 2009;**81**:1952-1956. DOI: 10.1021/ac802364e
- [40] Hildebrand J, Herbst J, Wöllenstein J, Lambrecht A. Explosive detection using infrared laser spectroscopy. *Proceedings of SPIE*. 2009;**7222**:72220B. DOI: 10.1117/12.808976
- [41] Fuchs F, Hugger S, Kinzer M, Aidam R, Bronner W, Losch R, et al. Imaging standoff detection of explosives using widely tunable mid infrared quantum cascade lasers. *Optical Engineering*. 2010;**49**(11):111127-111127-8. DOI: 10.1117/1.3506195
- [42] Deutsch ER, Kotidis P, Zhu N, Goyal AK, Ye J, Mazurenko A, et al. Active and passive infrared spectroscopy for the detection of environmental threats. *Proceedings of SPIE*. 2014;**9106**:91060A-9. DOI: 10.1117/12.2058544
- [43] Suter JD, Bernacki B, Phillips MC. Spectral and angular dependence of mid-infrared diffuse scattering from explosives residues for standoff detection using external cavity quantum cascade lasers. *Applied Physics B: Lasers and Optics*. 2012;**108**(4):965-974. DOI: 10.1007/s00340-012-5134-2
- [44] Castro-Suarez JR, Pollock YS, Hernández-Rivera SP. Explosives detection using quantum cascade

- laser spectroscopy. Proceedings of SPIE. 2013;**8710**:871010. DOI: 10.1117/12.2016037
- [45] Pacheco-Londoño LC, Castro-Suarez JR, Aparicio-Bolaños J, Hernández-Rivera SP. Angular dependence of source-target-detector in active mode standoff infrared detection. Proceedings of SPIE. 2013;**8711**:8711081-8711086. DOI: 10.1117/12.2016153
- [46] Ortega-Zúñiga CA, Galán-Freyre NY, Castro-Suarez JR, Aparicio-Bolaños J, Pacheco-Londoño LC, Hernández-Rivera SP. Dependence of detection limits on angular alignment, substrate type and surface concentration in active mode standoff IR. Proceedings of SPIE. 2013;**8734**:87340R-1-87340R-8. DOI: 10.1117/12.2016196
- [47] Castro-Suarez JR, Pacheco-Londoño LC, Aparicio-Bolaño J, Hernandez-Rivera SP. Active mode remote infrared spectroscopy detection of TNT and PETN on aluminum substrates. Journal of Spectroscopy. 2017;**2017**:2730371
- [48] Figueroa-Navedo AM, Galán-Freyre NJ, Pacheco-Londoño LC, SP H-R. Chemometrics enhanced laser induced thermal emission detection of PETN and RDX. Journal of Chemometrics. 2015;**29**:329-337
- [49] Barker M, Rayens W. Partial least squares for discrimination. Journal of Chemometrics. 2003;**17**(3):166-173. DOI: 10.1002/cem.785
- [50] Brereton RG. Chemometrics for Pattern Recognition. Chichester, England. The Atrium, Southern Gate: John Wiley & Sons Ltd.; 2009. ISBN: 978-0-470-98725-4
- [51] Ballabio D, Consonni V. Classification tools in chemistry. Part 1: linear models. PLS-DA. Analytical Methods. 2013;**5**(16):3790-3798. DOI: 10.1039/C3AY40582F
- [52] Clarkson J Smith WE, Batchelder DN, Smith DA, Coats AM. A theoretical study of the structure and vibrations of 2,4,6-trinitrotoluene. Journal of Molecular Structure. 2003;**648**(3):203-214. DOI: 10.1016/S0022-2860(0e3)00024-3
- [53] Perger WF, Zhao J, Winey JM, Gupta YM. First-principles study of pentaerythritol tetranitrate single crystals under high pressure: Vibrational properties. Chemical Physics Letters. 2006;**428**(4):394-399. DOI: 10.1016/j.cplett.2006.07.046
- [54] Prasad RL, Prasad R, Bhar GC, Thakur SN. Photoacoustic spectra and modes of vibration of TNT and RDX at CO₂ laser wavelengths. Spectrochimica Acta, Part A: Molecular and Biomolecular Spectroscopy. 2002;**58**(14):3093-3102. DOI: 10.1016/S1386-1425(02)00071-9
- [55] Karpowicz RJ, Brill TB. Comparison of the molecular structure of hexahydro-1, 3,5-trinitro-s-triazine in the vapor, solution, and solid phases. The Journal of Physical Chemistry. 1984;**88**(3):348-352. DOI: 10.1021/j150647a005
- [56] Infante-Castillo R, Pacheco-Londoño L, Hernández-Rivera SP. Vibrational spectra and structure of RDX and its ¹³C- and ¹⁵N-labeled derivatives: A theoretical and experimental study. Spectrochimica Acta A. 2010;**76**(2):137-141. DOI: 10.1016/j.saa.2010.02.051
- [57] Castro-Suarez JR, Hidalgo-Santiago M, Hernández-Rivera SP. Detection of highly energetic materials on non-reflective substrates using quantum cascade laser spectroscopy. Applied Spectroscopy. 2015;**69**(9):1023-1035. DOI: 10.1366/14-07626
- [58] Gallagher NB, Blake TA, Gassman PL, Shaver JM, Windig W. Multivariate curve resolution applied

to infrared reflection measurements of soil contaminated with an organophosphorus analyte. *Applied Spectroscopy*. 2006;**60**(7):713-722. DOI: 0003-7028/06/6007-0713\$2.00/0

[59] Long GL, Winefordner JD. Limit of detection: A closer look at the IUPAC definition. *Analytical Chemistry*. 1983;**55**(07):712A-724A. DOI: 10.1021/ac00258a724

[60] Pacheco-Londoño LC, Aparicio-Bolaño J, Galán-Freyle NJ, Román-Ospino AD, Ruiz-Caballero JL, Hernández-Rivera SP. Classical least squares-assisted mid-infrared (MIR) laser spectroscopy detection of high explosives on fabrics. *Journal of Applied Spectroscopy*. 2018 (The online version). DOI: 10.1177/0003702818780414

Mid-Infrared Laser Spectroscopy Applications in Process Analytical Technology: Cleaning Validation, Microorganisms, and Active Pharmaceutical Ingredients in Formulations

Leonardo C. Pacheco-Londoño, Nataly J. Galán-Freyte, Amira C. Padilla-Jiménez, John R. Castro-Suarez, Amanda M. Figueroa-Navedo, José L. Ruiz-Caballero, Ricardo Infante-Castillo, Carlos Rios-Velazquez and Samuel P. Hernández-Rivera

Abstract

Mid-infrared (MIR) lasers are very high-brightness energy sources that are replacing conventional thermal sources (globars) in many infrared spectroscopy (IRS) techniques. Although not all laser properties have been exploited in depth, properties such as collimation, polarization, high brightness, and very high resolution have contributed to recast IRS tools. Applications of MIR laser spectroscopy to process analytical technology (PAT) are numerous and important. As an example, a compact grazing angle probe mount has allowed coupling to a MIR quantum cascade laser (QCL), enabling reflectance-absorbance infrared spectroscopy (RAIRS) measurements. This methodology, coupled to powerful multivariable analysis (MVA) routines of chemometrics and fast Fourier transform (FFT) preprocessing of the data resulted in very low limits of detection of active pharmaceutical ingredients (APIs) and high explosives (HEs) reaching trace levels. This methodology can be used to measure concentrations of surface contaminants for validation of cleanliness of pharmaceutical and biotechnology processing batch reactors and other manufacturing vessels. Another application discussed concerns the enhanced detection of microorganisms that can be encountered in pharmaceutical and biotechnology plants as contaminants and that could also be used as weapons of mass destruction in biological warfare. In the last application discussed, the concentration of APIs in formulations was determined by MIR laser spectroscopy and was cross validated with high-performance liquid chromatography.

Keywords: mid-infrared (MIR) laser spectroscopy, grazing angle probe (GAP), reflectance-absorption infrared spectroscopy (RAIRS), active pharmaceutical ingredients (API), pharmaceutical cleaning validation, microorganisms

1. QCL-grazing angle reflectance-absorbance IR spectroscopy

A variety of optical sensing methods can be used for the detection of chemical contaminant residues on surfaces. These methods include QCL spectroscopy, Raman, FTIR, remote infrared spectroscopy (RIRS), and laser-induced thermal excitation (LITE) of infrared emission, among others [1–17]. Fast trace detection of chemical and biological threat agents on contaminated surfaces with high selectivity and specificity is fundamental in the prevention of terrorist attacks and rapid performance and execution of security protocols. Ideally, analyte sensing on surfaces would be a rapid, in situ, low-cost, portable, highly sensitive, and able to discriminate between components. A new setup with multi-reflection passes by a grazing angle probe (GAP) using a QCL source was employed to improve in situ detection of organic contaminants on a surface. This new prototype reduced the time analysis and improved the spectral S/N.

MIR spectroscopy operating at the grazing angle of incidence ($\sim 80\text{--}82^\circ$ from the surface normal) is the most sensitive optical absorption technique available for measuring low chemical concentrations on surfaces such as metals [9, 18]. Under these conditions, reflection-absorption infrared spectroscopy (RAIRS) can be performed for optically thin samples. The technique can measure low concentrations of chemical compounds deposited on substrate surfaces, such as metals, glasses, and plastics [19–23]. LODs from 10 to 50 ng/cm² of a single analyte have been obtained [24]. Because of the above, this technique allows for the analysis of monolayers on surfaces. However, the low absorbance shown by monolayers requires longer analysis times (from 5 to 120 min of integration) to obtain spectra with good signal to noise ratios (S/N). The integration time can be reduced by multiple reflection pass systems or by increasing the power of the laser source. Both alternatives improve the absorbance of the sample. However, multiple reflections involve the loss of light by phenomena such as scattering due to the substrates where the target analytes reside, sample physical properties, and mirror imperfections. The divergence of the MIR beam and absorption by the substrate, samples, and mirrors are also factors that lead to signal losses.

Therefore, the main objective was to evaluate the QCL-GAP in back-reflection mode, which is suggested as a viable method to validate detection of explosives on metallic surfaces. A QCL-GAP was designed to obtain measurements in the lab. Reflectance spectra of RDX samples deposited on aluminum (Al) plates were obtained for a remote sensing modality.

Also, GAP-IRS can be used outside the confinement of the sample compartment, making it available for fieldwork. FTIR fiber optic-coupled grazing angle probe-reflection-absorption infrared spectroscopy (FOC-GAP-RAIRS) using a thermal excitation source (globar) has been investigated before to develop techniques for detection of HE residues on substrates [23, 25, 26]. The methodology can be used in situ to detect nanograms of the target compounds. Samples with surface concentrations (C_s) ranging from micrograms/cm² to nanograms/cm² of explosives (DNT, TNT, PETN, nitroglycerine (NG) and triacetone triperoxide (TATP)) have been studied on SS plates with excellent results yielding 10–100× LODs for HEs than for active pharmaceutical ingredients (APIs), for which the setup was originally developed [25, 26]. The main objective of this study was to design, develop and test a grazing angle probe (GAP) mount for coupling to MIR QCL spectrometer

(QCL-GAP) as a viable tool to develop methodologies for detection of chemicals and microorganisms on surfaces at trace level quantities within the framework of homeland security applications. The QCL-GAP was designed to obtain measurements in the laboratory and the field. Back-reflection spectra of RDX samples deposited on SS plates outside the sample compartment were remote.

1.1 Optical system

A QCL source and a compact mount with mirrors fixed near the grazing angle ($\sim 82^\circ$ from surface normal) were carefully coupled to improve detection, increase the S/N and reduce the time of analysis without saturating the MCT detector. A general view of the complete optical configuration of this novel system is shown in **Figure 1**. The beam was focused and expanded by a lens (ZnSe, 3 in. diameter) in the vertical direction. Next, the light was reflected by a mirror at 49° of the surface, deflecting the light at an angle of 8° with respect to the surface or 82° with respect to the surface normal, forming an elliptical beam spot on the surface. The axial size of the ellipse was $d \times [d/(\sin(8^\circ))]$. For example, for $d = 4 \text{ mm}$, the axis of the ellipse was $4 \times [4/(\sin(8^\circ))] = 4 \times 29 \text{ mm}^2$. The light was returned by a plane mirror ($\sim 82^\circ$) to the same surface producing a slightly larger image at the same position.

The QCL spectrometer has inherent limitations related to the instrument design in which the MIR detector is located within the spectrometer so that the system operates only collecting the back-reflected light. The results on the detection of explosives residues on SS plates with the setup illustrated in **Figure 2** are highly promising: 73 pg./cm^2 for RDX. This value is $\sim 102\text{--}103$ times lower than currently reported LOD values for these explosives. In the next-generation design, the MIR

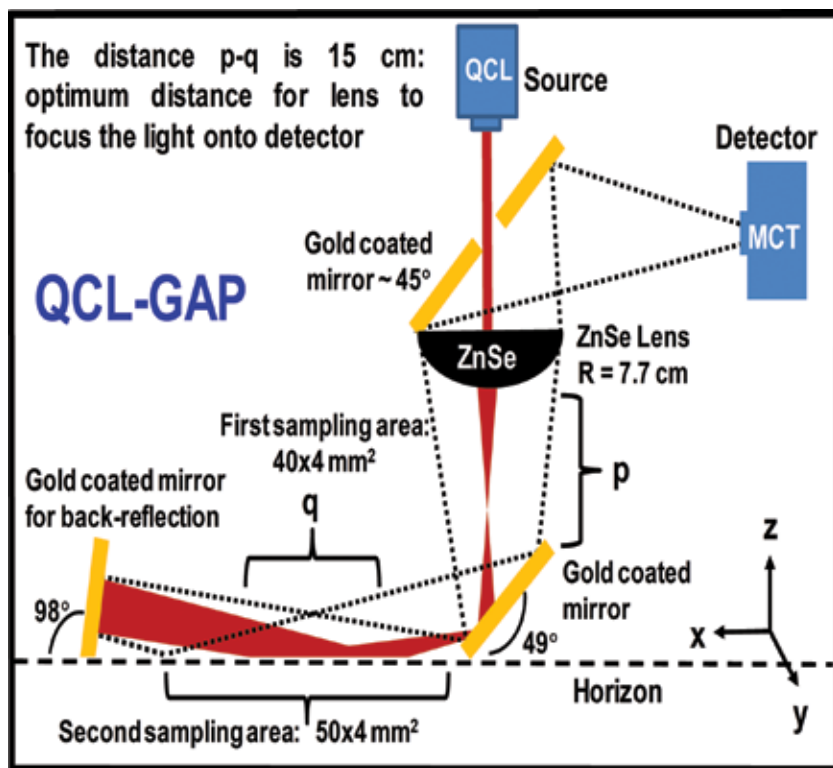


Figure 1.
Optical layout for coupling a MIR laser to the GAP.

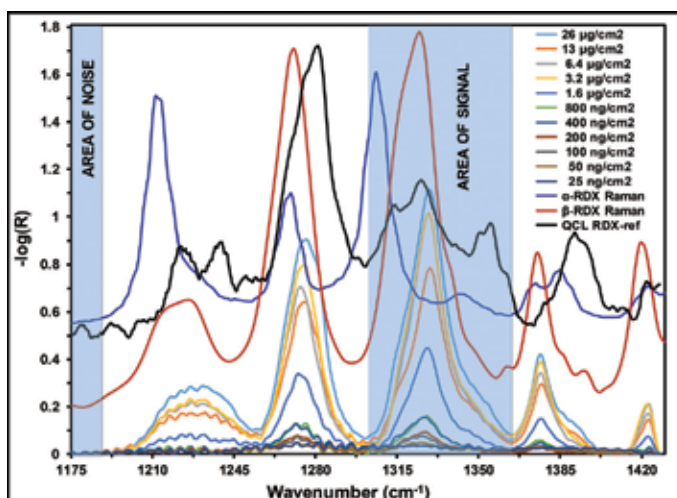


Figure 2.
QCL-GAP reflectance spectra of RDX at various C_s .

detector will be placed at the plane of the second gold-coated mirror and placed at $\sim 82^\circ$ from the surface normal. The extrapolated value of the LOD can be obtained by plotting the S/N versus the reciprocal of the surface concentration (CS) to the value of ≈ 3 [26].

1.2 Removal of QCL-GAP interference fringes of RAIRS spectra

The proposition of using a QCL-GAP setup was evaluated for monolayer analysis of HE residues. PCA and PLS multivariate routines of chemometrics were employed to verify the effect of preprocessing options for the MIR RAIRS spectra obtained. When the optical system was well aligned, interference patterns were obtained that initially were considered problems that masked the spectroscopic information. Moreover, the observed patterns were modified when the surface had an analyte deposited on it. A fast Fourier transform (FFT) analysis was applied to determine if the interferences could be handled by FFT preprocessing for discrimination and quantification analysis using multivariate analysis (MVA). FFT is an algorithm that transforms a function from the time domain to the frequency domain and conversely. The resulting transformation is a complex function. In complex notation, the domain contains one signal made up of N complex points. Each of these complex points is composed of two parts, the real part and the imaginary part. In this case, FFT was carried out to find the frequencies of the interference patterns. This transformation was used for discrimination using PLS-DA and for quantification using PLS. Both PLS and PLS-DA are supervised methods in which the data are reduced to linear combinations containing the information to generate discrimination for PLS-DA or quantification for PLS.

Figure 3a shows the spectra of substrate clean (SS); the SS with the analyte loadings, ~ 16 ng/cm² RDX on SS and ~ 20 ng/cm² irbesartan (IRBS) on SS; and an active pharmaceutical ingredient (API) an angiotensin II receptor and active component of AVAPRO® used as a potential chemical interferant. The figure also includes the reference spectra for RDX and IRBS acquired with a conventional diffuse-reflection system for bulk samples (90° with respect to the surface normal). **Figure 3b** shows a schematic diagram on how the interference patterns can be formed on the spectra of the substrate clean and with the analyte loading. These patterns are due to the interference by multiple reflections in the system. The

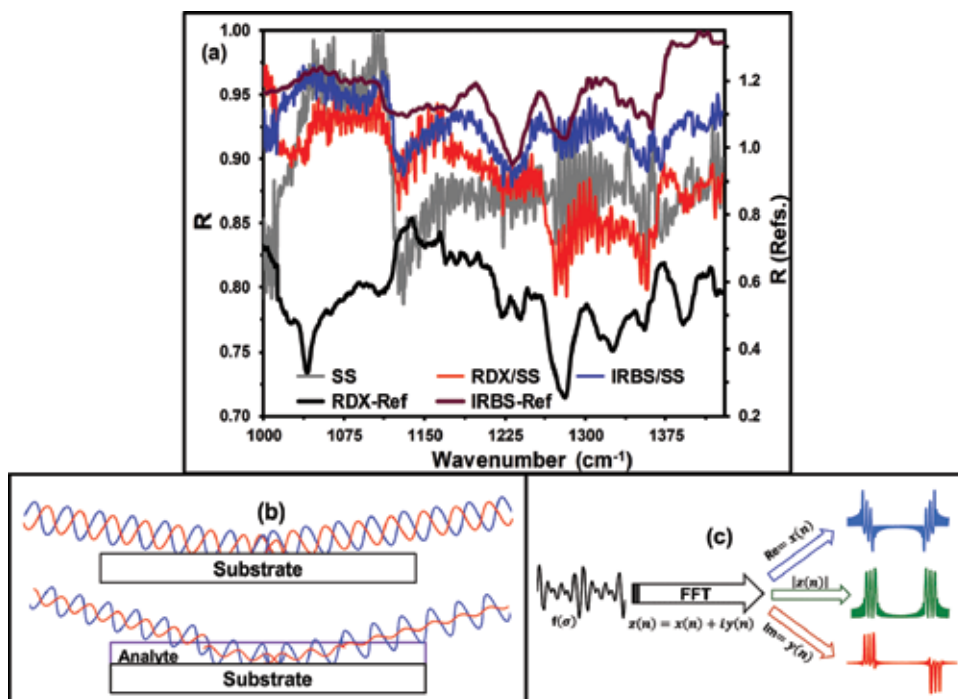


Figure 3. Comparison of spectra of clean SS substrate, reference QCL reflection spectra for RDX/SS ($\sim 16 \text{ ng/cm}^2$) and IRBS/SS ($\sim 20 \text{ ng/cm}^2$) showing details of the band patterns of the analytes, overlapped by the interference fringes; (b) diagram illustrating the formation of the interference patterns; (c) schematic of applying the FFT to the QCL reflectance spectra.

variation of interference patterns depending on whether the substrate is clean or loaded with the analyte can also be noticed. **Figure 3c** illustrates how the FFT is applied to the RAIRS spectra. In the RDX spectra, some signals were observed with difficulties such as NO_2 symmetric stretch at 1275 cm^{-1} and N-N symmetric stretch at 1352 cm^{-1} [27, 28]. Multiple reflections are generated by semitransparent analytes when low concentrations are deposited. This interaction of the light with the surface causes a modification of the interference patterns depending on the analyte and the concentration deposited. Transformation of the data with FFT preprocessing produces a complex function consisting of an imaginary part (Im), a real part (Re), and the magnitude of the function expressed as the absolute value of $z(n)$. These parameters were used for MVA to build robust models.

Figure 4a–c show the spectra transformation for substrate SS clean (none) and SS contaminant with RDX IRBS. The FFT shows each frequency or modes that generated the interferences in the spectra. A detailed analysis of **Figure 4a–c** demonstrates that modes for RDX and IRBS are similar to clean SS and differ in small modifications of these modes. These small modifications are due to the nature of the layer, shown as absorbance, homogeneity, refractive index, particle size, and layer thickness. The Re function has a mode with a higher intensity than the other modes. This mode should be the principal interference which is generated between the lens and the mirror in back reflection. Each transformation and other preprocessing were used for a principal component analysis (PCA) to verify the differences between the analytes and the clean surface. A complete separation of spectra without analytes, with RDX and IRBS, was archived with the real part Re of FFT. The loadings for the analysis are shown in **Figure 4d**. Two components were necessary for a complete separation with Re FFT preprocessing.

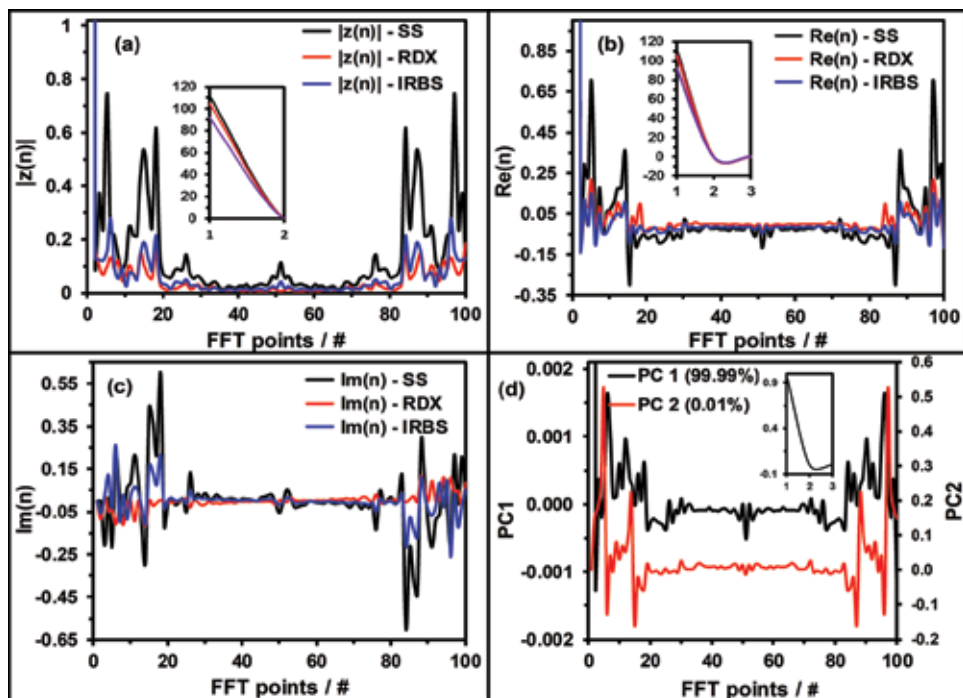


Figure 4. FFT preprocessing: (a) $|z(n)|$, (b) $Re(FFT)$, (c) $Im(FFT)$, and (d) loadings for PC1 and PC2 for PCA using $Re(FFT)$.

In comparison to other parameters of FFT and other preprocessing algorithms, the separation was not complete. The preprocessing used were SNV, first derivative (FD), second derivative (SD), extended scatter correction (EMSC), multiplicative signal correction (MSC), Im, and $|z(n)|$. **Figure 5a–d** show the correlation between the scores of PC1 and PC2 for the SNV, $|z(n)|$, Im, and Re. A visualization of the separation between the classes using Re is clear and complete; the maximum separation was achieved with PC2.

PLS-DA was employed using $Re(FFT)$ as a preprocessing routine. The complete analysis was done to measure the discriminant capacity. The number of points in FFT was changed to select the better resolution for the analysis. The sensitivity and specificity for leave-one-out cross validation (LOOCV) were also calculated for a different number of points for FFT. The PLS-DA model performance was evaluated through parameters of the confusion matrix such as sensitivity and specificity of the validation. The validation was initially evaluated regarding LOOCV. The sensitivity can be defined as the samples predicted as belonging to a class divided by the total samples in that class, and the specificity is the samples predicted as not belonging to the class divided by the total samples not belonging to that class. The sensitivity and specificity were calculated according to Eqs. 1 and 2:

$$\text{Sensitivity} = (TP)/(TP + FN) \quad (1)$$

$$\text{Specificity} = (TN)/(TN + FP) \quad (2)$$

Here TP, FN, TN, and FP represent the number of true positives, false negatives, true negatives, and false positives, respectively. The best models were generated using 75 and 100 number of points for the FFT preprocessing steps. These models

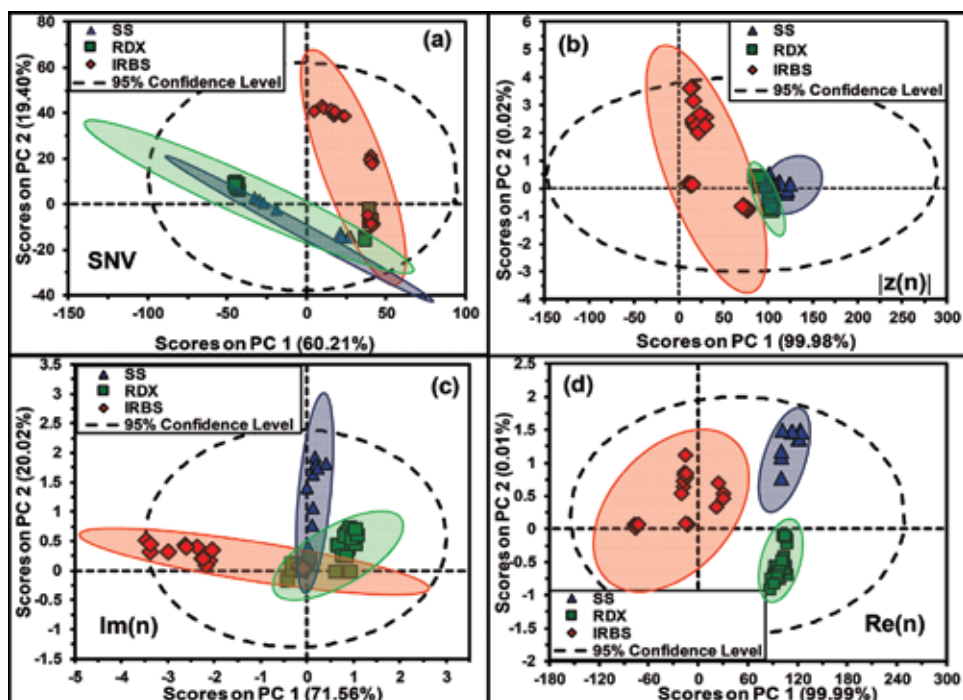


Figure 5. PCA with preprocessing (a) SNV; (b) $|z(n)|$, (c) $Re(FFT)$, (d) $Im(FFT)$.

# points	Sensitivity (CV)			Specificity (CV)		
	SS	RDX/SS	IRBS/SS	SS	RDX/SS	IRBS/SS
10	0.900	0.893	0.708	0.885	0.765	0.737
20	1.000	1.000	0.958	1.000	1.000	0.974
50	1.000	1.000	1.000	1.000	1.000	0.947
75	1.000	1.000	1.000	1.000	1.000	1.000
100	1.000	1.000	1.000	1.000	1.000	1.000
200	1.000	1.000	1.000	0.962	1.000	1.000
500	1.000	1.000	1.000	0.904	1.000	1.000
750	0.900	1.000	0.833	0.885	0.912	0.912
1000	1.000	0.893	0.792	0.885	1.000	0.737

Table 1. Leave one out cross-validation (LOOCV) sensitivity/specificity for two latent variables. The best models were generated using 75 and 100 number of points for the FFT preprocessing.

correspond to very high sensitivity and specificity values. Parameters for CV for all models are shown in **Table 1** in which only two LVs were used. A model for quantification for RDX was generated [29–31].

1.3 Conclusions

A compact GAP designed to be interfaced to a QCL-based spectrometer has been described. The unit enables RAIRS measurements in the MIR under conditions of a polarized, coherent, collimated, and high-brightness laser source. The new hyphenated technique has been used in analysis surface contaminants in two broad

area applications: pharma/biotech reactor cleaning validation and HE detection for defense and security applications. Interference back-reflection patterns were observed that initially hindered the successful application of the technique. A preprocessing algorithm based on FFT was implemented in MATLAB and successfully tested. Three derived functions were used: the absolute value of the complex function of the FFT ($|z(n)|$), the imaginary part of the FFT complex function ($\text{Im}(n)$), and the real part of the complex function of the FFT ($\text{Re}(n)$).

Optimization of preprocessing was obtained upon evaluation of preprocessing models for quantitative and qualitative analysis. PLS quantification models and PCA qualitative models improved by using $\text{Re}(n)$, allowing complete separation of three classes: clean substrates (SS), HE/substrates (RDX/SS), and active API/substrates (IRBS/SS). The values for the sensitivity and specificity were 1.000 for both RDX and IRBS. These results were attained using 75/100 pts. FFT preprocessing. The QCL-GAP back-reflection setup described herein can provide the basis for developing methodologies for high specificity and sensitivity results for monolayer analysis using RAIRS. These results will have a far-reaching impact on cleaning validation, defense/security, and other applications involving monolayer analysis.

2. MIR laser detection and discrimination of microorganisms

Driven by an imperative need to develop quick and precise methods for detection of biological warfare agents (BWAs), MIR laser spectroscopy study of selected microorganisms was undertaken. *Escherichia coli* (*Ec*) can be detected using electrochemical immunosensors, immobilized probes and solid-phase microextraction followed by GC-MS, which can also be used to detect other microorganisms. All these methods and others currently available are laborious and costly and comprise many preparation steps or selective pre-enrichment [32–39]. Though identification/discrimination of bacterial spores with FTIR has been reported, this contribution proposes the application of MIR laser spectroscopy for identification and discrimination of bacteria residing on reflective and matte surfaces [34, 35].

Bacillus thuringiensis (*Bt*) is a Gram-positive bacterium that forms spores that are highly chemoresistant and also tolerate high temperatures in their dormant state. *Bt* was selected as a simulant for BWAs based on its resemblances with *Bacillus anthracis* (anthrax), a well-known BWA. *Staphylococcus epidermidis* (*Se*) is a Gram-positive coccus that can be found usually on human skin. *Ec* is a Gram-negative bacteria affiliated to the family *Enterobacteriaceae*. *Ec* is a coliform that can be found in intestines of warm-blooded animals. Thus, the presence of *Ec* is associated with fecal contamination.

Several materials, including SS, CB, TB, glass, and W, were used as substrates for depositing the samples. Since the spectroscopic information of bacteria mainly consists of signature contributions from all the cell components, the reflectance spectra show the molecular compositions of the cells in general. Other IRS studies have focused the problem of detecting, identifying, and discriminating bacteria from the substrates they reside on using chemometric methods [36–40]. The methodology used in this work involves obtaining the MIR laser-enhanced reflectance spectra under high-brightness conditions. Certified bacterial strains of *Bt* (ATCC #35646), *Ec* (ATCC #8789), and *Se* (ATCC #2228) were acquired from the Microbial Biotechnology and Bioprospecting Lab at the Department of Biology at the University of Puerto Rico-Mayagüez campus. The microorganisms were selected based on their resemblance to real-world BWA simulants.

QCL spectra of microorganisms were used to identify the molecular vibrational markers in the biosamples. These vibrational signatures contain data on the

biochemical composition of microorganisms and of the molecules of which they composed [38]. Some of the cell wall components are different for Gram-positive and Gram-negative bacteria. On the one hand, Gram-positive bacteria have a denser and stiffer peptidoglycan coating that amounts from 40 to 80% more of the cell wall (by weight) than in Gram-negative bacteria. Also, Gram-positive bacteria contain teichoic acids that are covalently attached to peptidoglycan. Gram-negative cells do not contain teichoic acids. In contrast, they contain lipoproteins that are covalently attached to the peptidoglycan in the cell walls. Gram-negative bacteria have an external membrane outside the peptidoglycan layer that contains phospholipids in the interior and lipopolysaccharides in the exterior [23]. Each bacterial species has a unique MIR fingerprint spectrum due to the stretching and bending vibrations of its molecular bonds or protein functional groups (including nucleic acids, lipids, sugars, and lipopolysaccharides), as illustrated by the reference spectra presented in **Figure 6** [40, 41]. MIR FTIR reference spectra of *Bt*, *Ec*, and *Se* are illustrated in **Figure 6**. Reference spectra were obtained in IR absorption using the Bruker Optics bench microspectrometer IFS66/v/S.

Representative QCL spectra of the microorganisms deposited on SS are shown in **Figure 7**. A total of 245 experiments are reported out of the 836 carried out. An experiment consisted of 15 replicate spectroscopic acquisitions for each bacterium/substrate arrangement. The spectral signatures were observed on the SS coupons, particularly in the fingerprint region, because of the highly MIR reflectivity of these surfaces. Tentative band assignments were based on a comparison of reported values. However, it was difficult to distinguish the different classes of species/surface arrangements studied based on the raw MIR spectral data due to the high degree of band overlapping. Thus, MVA routines were useful in handling the large dataset generated and facilitating the spectroscopic analysis. Vector normalization (VN) was used for data preprocessing before statistical analyses. Similar effects were found for the matte (nonreflective) substrates, although the classification and discrimination required more robust MVA routines and pretreatments. **Table 2** shows the classification obtained between groups of bacteria on different surfaces using PCA. Bold values represent percentages of the discrimination predicted within a correctly classified group. Selecting 10–15 QCL reflectance spectra of samples from each bacterium on each of the substrate (225 spectra) led to generate other PCA models.

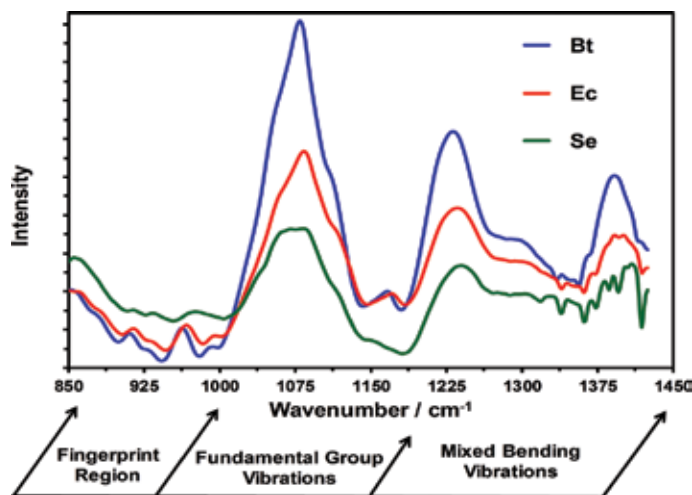


Figure 6.
Reference MIR reflectance spectra of *Bt*, *Ec*, and *Se* in the spectral region studied.

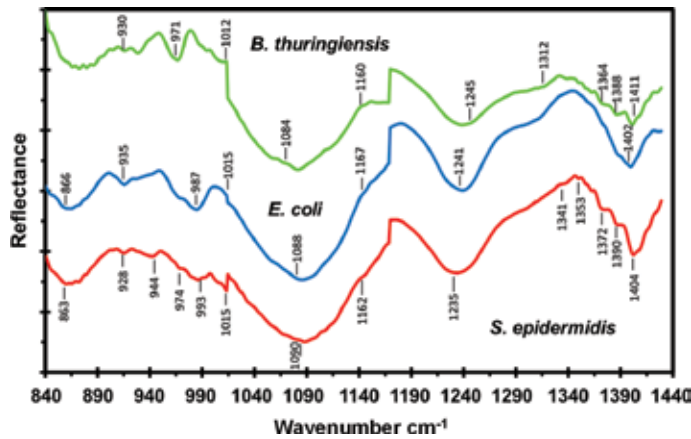


Figure 7. QCL reflectance spectra of *Bt*, *Ec*, and *Se* deposited on SS at room temperature.

Discrimination	Group size	Predicted discrimination			
		<i>Bt</i>	<i>Ec</i>	<i>Se</i>	Substrates
<i>Bt</i>	75	45 (60%)	18 (24%)	8 (11%)	4 (5%)
<i>Ec</i>	77	3 (4%)	64 (83%)	9 (12%)	1 (1%)
<i>Se</i>	75	14 (19%)	3 (4%)	50 (67%)	8 (11%)
Substrates	18	3 (17%)	4 (22%)	0 (0%)	11 (61%)

Percentage of cases correctly classified: 69.4%

Table 2. Classification between groups of bacteria (*Bt*), (*Ec*), and (*Se*) on various substrates.

Spectra were pretreated by applying first dvt and MC algorithms to all bacterium/substrate combination spectra. SNV pretreatment had to be applied to the data involving the use of W substrates. A PCA model for MIR laser spectra of *Bt*, *Ec*, and *Se* deposited on the surfaces studied was generated, and the variance captured by the PCs was analyzed for each surface type. Score plot (PC-3 vs. PC-1) for TB is shown in **Figure 8a**. A relatively poor separation between the datasets of the bacteria was observed. PC-1 (53% variance) versus PC-2 (14% variance) was correlated with the differences among the microorganisms. **Figure 8b** illustrates the grouping of spectra according to PC-3 (10% variance) versus PC-2 (14% variance). In total, 60% of the *Bt* samples were classified as *Ec*, while 93% of the *Ec* and *Se* and 100% spectra were correctly classified. The score plots did not show a class separation between the three types of microorganisms on the matte substrate (TB). Nonetheless, these plots only represent only portions of the data variance (14 and 53%, respectively).

PLS-DA was used as a classification methodology for differentiating between the bacterial species on the five matte substrates studied. In PLS-DA, the estimated experimental percentage of the correctly classified samples determines the sensitivity of the model. Moreover, the estimated experimental percentage of the samples that are rejected by the other classes in the model gives information on the specificity of the model. Therefore, in a perfect class model, the sensitivity and specificity have values of 1 or 100%. A total of 225 spectra corresponding to 15 spectra for of

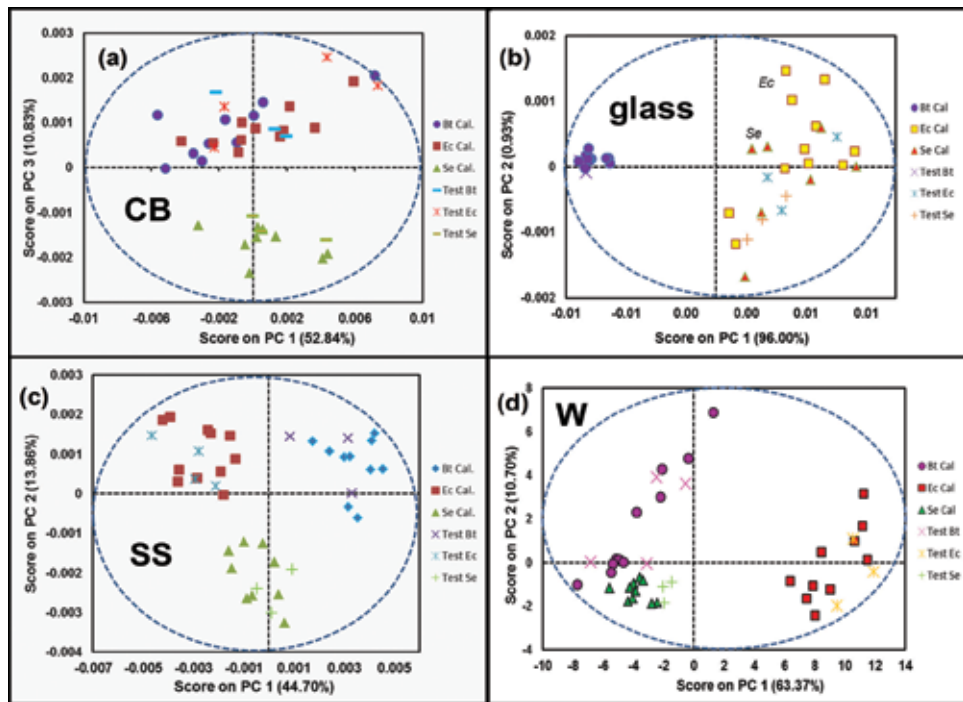


Figure 8.
 PC-2 vs. PC-1 for the PCA models of Bt, Ec and Se spectra on: (a) CB; (b) glass for (a); (c) SS; (d) W.

each bacterium/surface arrangement were analyzed. Spectroscopic data were organized into two sets. About 75% of the reflectance spectra were randomly selected as the training set for the calibration and cross validation. The remaining 25% of the data comprised an external test set. The spectral windows used for the chemometric runs were 848–1012, 1022–1170, and 1173–1400 cm^{-1} . Then data were preprocessed by smoothing before applying the first dvt.

A cross validation procedure using Venetian blinds with 10 splits was carried out. A classification model using this procedure was applied to 90% of the data. Then, the other 10% of the data was separated for the validation dataset to determine the accuracy of the models. The QCL spectra were pretreated by smoothing and taking the first derivative to improve the visualization of the spectra. The discrimination models for the bacteria/substrates are shown in **Figure 9** for bacterial species deposited on TB. These illustrate the predicted (PRED) cross validation (CV) of classes for each sample (PLS-DA plot). The results obtained demonstrate that the use of QCL spectroscopy (840–1440 cm^{-1}) coupled to MVA-PCA and PLS-DA are suitable for discriminating between microorganisms (*Bt*, *Ec*, and *Se*) on several surfaces, including on reflective, matte substrates.

MIR laser spectroscopy was very effective for detecting microorganisms on various surfaces. When coupled to MVA, the combined methodology provided a quick response and efficient discrimination from the matte substrates. The methodology could be used to identify biofilms deposited on substrates, providing quick and precise analyses for national defense and security applications and for quality control purposes in industrial scenarios, when nondestructive analytical methods are preferred. Identification and discrimination of microorganisms from the acquired MIR laser reflectance spectra were attained with PCA and PLS-DA. In general, PLS-DA performed significantly better than PCA in the analyses of the bacteria studied [40, 41].

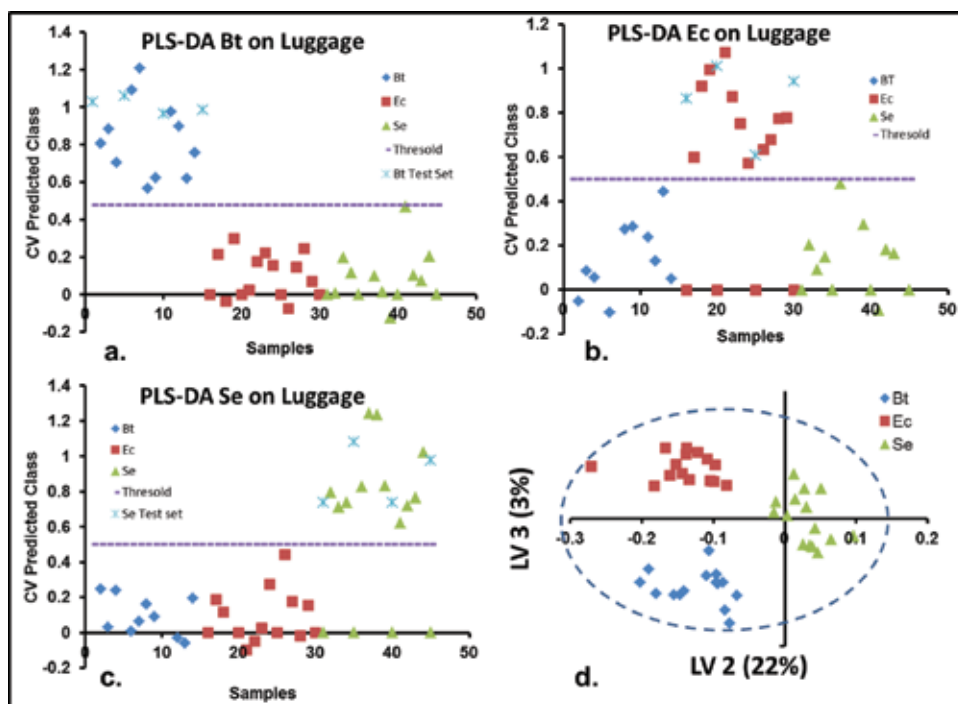


Figure 9. PLS-DA plots for discriminating bacteria on luggage. Cross validation (CV) and prediction (PRED) of: (a) Bt/TB; (b) Se/TB; (c) Ec/TB; (d) variance accounted for (%) by LV 2 and LV 3 used in the model.

3. MIR laser spectroscopy analysis of pharma formulations

The Beer–Lambert–Bouguer law is a relationship between the attenuation of radiant flux, the path length of the light traversing the media (l ; m), and the molar concentration of the absorbing species (c ; mol·dm⁻³). At a fixed frequency or in small frequency interval, this relationship is characterized by the absorptivity or molar attenuation coefficient (ϵ ; m²·mol⁻¹) of the material or components in a mixture. In the near-infrared (NIR) region, intrinsically small values of ϵ make spectrometric measurements ideal for monitoring online industrial procedures because light travels a long way in the media or can be reflected off the sample [42]. Corresponding ϵ values in the MIR region are much higher [43]. Thus, the main difficulties of using the MIR region for online industrial applications are the thickness of the samples, the concentrations of the samples, or both. For non-thin or dilute samples, radiation in the MIR is almost totally attenuated by the samples, and the light back-reflected by the detector is very little. Thus, diffuse reflectance measurements in the MIR lead to low intensities and accordingly to low S/N values. This makes the MIR inappropriate for online applications of monitoring industrial processes.

The main objective of this work was to investigate if MIR laser spectroscopy could be used to develop a remotely sensed method for quantitative analysis of APIs in pharmaceutical blends. A QCL spectrometer was used to collect the reflectance from powder samples. Provided that the API has a high ϵ value when a MIR laser is used to excite the spectra, much more light would be reflected resulting in high S/N values. This study concluded that accuracies and precisions obtained using MIR laser spectroscopy are comparable to NIR spectroscopy [44, 45], Raman spectroscopy [46, 47], and attenuated total reflection (ATR) infrared spectroscopy [48]. Other process analytical technology (PAT) applications of MIR laser spectroscopy

are cleaning validation of pharmaceutical and biotechnology industrial batch reactors and other processing equipment [19], determination of API levels in tablets and formulations [49, 50], and vibrational circular dichroism [51].

3.1 Experimental details

Ibuprofen (IBP) and excipients, lactose monohydrate (54.25–74.25%), microcrystalline cellulose (25%), colloidal silicon dioxide (0.25%), and magnesium stearate (0.5%), were mixed concentrations from 0 to 21% (w/w); 21 compositions were prepared together with various samples of the control (0% API). Sample mixing was conducted by using a shaker/mixer. After initial mixing, the samples were ground in a mortar and pestle and remixed. QCL reflectance spectra of 21 powder mixtures and control were acquired on various locations on the sample surfaces. The parameters of the MIR laser spectrometer were 1.5 s scan time, the average power was 0.5–10 mW, and the spectral range was 600 cm^{-1} . Reference spectra for all chemicals were acquired in a model IFS 66v/S bench interferometer (FTIR, Bruker Optics, Billerica, MA, USA). This system had a cryo-cooled MCT detector and a KBr beam splitter. Reference spectra were acquired in transmission mode at a resolution of 4 cm^{-1} using 32 scans at 10 kHz scan velocity.

Cross validation experiments were carried out using the industry standard method based on high-performance liquid chromatography (HPLC) on a model 1100 Agilent Technologies system (Santa Clara, CA, USA). The system was equipped with a diode array UV-VIS detector. A C18 HPLC column was used for the chromatographic experiments. Ultrapure water adjusted to pH of 2.5 with HPO_3 , and acetonitrile (40/60, v/v) was used as mobile phase at a flow rate of 1.0 mL/min. Analyte detection was carried out in the UV at an excitation wavelength of 214 nm [52].

3.2 Results

The measured reflectance spectra were converted to the Kubelka-Munk (K-M) function. The main criterion to use the K-M transformation was that the intensity values obtained for the samples were very low [53]. For the chemometric analyses, a preprocessing step consisting of VN was used in the full spectral range to remove baseline shifts produced by scattering of the MIR light. These shifts are typically caused by variations in particle sizes of the crystalline components of the mixtures. VN involves calculating the average intensity first. Then, the average value of the intensities was subtracted from each spectrum. Subsequently, the sum of the intensities squared was calculated, and each spectrum was divided by the square root of this value. VN operates on each spectrum. This preprocessing step worked better than other pretreatment steps applied: MC, constant offset elimination (OFFSET), straight-line subtraction (SLS), minimum-maximum normalization (MIN-MAX), multiplicative scattering correction (MSC), and first and second dvt.

The control spectra were similar to the spectrum of the formulation containing a composition of 20% API. The differences observed were based on the fact that the excipients used to prepare the formulations contained many vibrational bands in the spectral region studied. A spectrum consisting of the difference between the 20% IBP formulation and the control (DIFF) was obtained and used to identify the vibrational markers of IBP in the formulations (**Figure 10a**). The IBP reflectance spectrum acquired by MIR laser (IBP-QCL) was compared to the corresponding FTIR spectrum (IBP-FTIR) to establish the exactness of the method. Vibrational signals corresponding to IBP were identified, establishing a good agreement between reflectance spectra obtained by IBP-QCL and IBP-FTIR. A slight shift of $+4\text{ cm}^{-1}$ for IBP-QCL relative to DIFF was observed for the band at 1303 cm^{-1} .

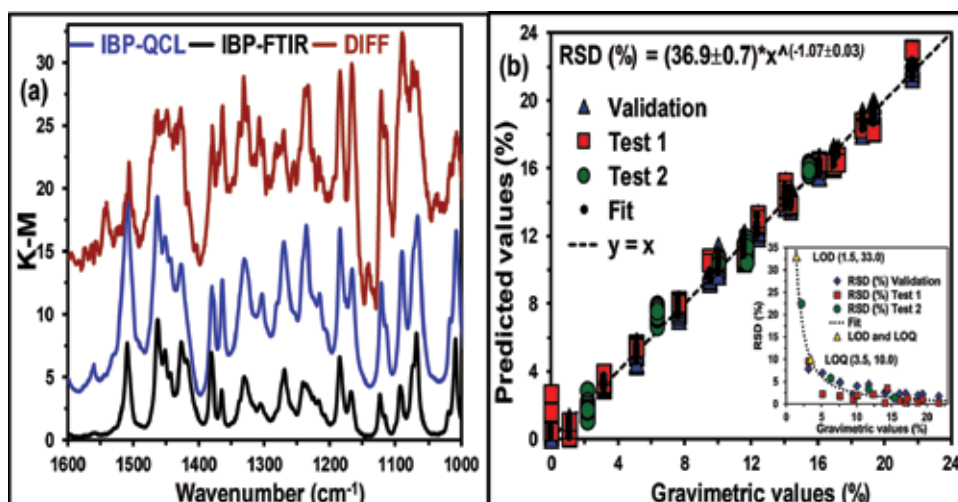


Figure 10.

(a) QCL, FTIR spectra of 20% IBP, FT-IR, and difference spectrum (DIFF) between the QCL spectrum of the 20% IBP formulation and control (placebo). PRED values vs. reference gravimetric values for the PLS model. Inset: power fit of various relative standard deviation values versus gravimetric values used to extrapolate values of LOD and LOQ.

Low-intensity signals were noticed in the DIFF spectrum at 1142, 1255, 1293, and 1540 cm⁻¹. Thus, though API-matrix interactions were weak and did not affect the shape or position of the spectral markers of the API for the bands observed, the technique is sensitive enough to detect these weak interactions. Because the controls did not contain API and the excipients amounts were kept at the same levels as the samples with API, these were about 25% higher in concentration in the controls. The spectral profile of the various constituents in the control mixture at this substantial concentration change cannot be entirely compensated when applying a non-weighted spectral subtraction.

Values for the statistical parameters of the PLS model are included in **Table 3**. The root-mean-square error of estimation (RMSEE) and relative standard error (RSE) were used to estimate the exactness of the PLS-based models [54]. Spectra were acquired at various locations on the surface of the sample, 20 spectra/sample in total. The calibration and internal validation set consisted of 16 of these spectra. The external validation set, used for testing the model, consisted of the remaining four spectra. The resulting forecasted error was labeled RMSEP1. This procedure was repeated for each composition. The robustness of the model was verified by preparing five formulations with compositions different from those of the calibration set and predicting their concentration values. Another prediction error was calculated by the average of the differences between the nominal (gravimetric) value and the value predicted by the PLS model. This error was designated as RMSEP2.

The optimum model was generated by narrowing the spectral range. This was done by first using the complete spectroscopic window, then dividing the full range into equal spectral subregions, and so forth. The optimum arrangement of subregions was determined by starting with 10 subregions and sequentially excluding 1 subregion, each time determining the value of the RMSECV. The process continued until the values for RMSECV did not reduce any further. The region from 990 to 1295 cm⁻¹ was selected as the best for the PLS modeling. The values achieved for RMSEE and RMSECV were comparable and small compared to the composition range of the experiments (0–21%) as per the values of RSE and RSCV of 2.3 and 3.1%, respectively, indicating the percentage of error in the model and

Parameter	Value	Parameter	Value
R ²	0.998	LOD%	1
R ² -CV	0.996	LOQ%	3
RMSEE (%)	0.3	RPD-Fit	21.3
RMSECV (%)	0.41	RPD-CV	15.5
RMSEP (%)*	0.7	RSD-R (%)	0.5
RMSEP1 (%)	0.54	RSD-H (%)	2.7
RMSEP2 (%)	0.82	RSD-REP (%)	5.4
RSE	2.3%	SEN	0.0063
RSP2	7.0%	LV	4
RSP-HPLC	1.3%	Bias	-0.002

*Error calculation used data of RMSEP1 and RMSEP2

Table 3.
 Values of relevant parameters for calculating the figures of merit of the PLS models.

the prediction capability, respectively. Challenging the model with new samples resulted in an RSE value increased to 6.5%, including the sample preparation errors. The bias, which is the average of the predicted values by cross validation, provides information on systematic errors. Since this value was small (**Table 3**), no significant deviations were attributed to the preparation of samples.

The very good linearity of the calibration model as can be evidenced by the value of the correlation coefficient squared (R²). This means that the percentage of variance of the reference gravimetric values that are reproduced in the PLS regression is high (**Table 3**). This is also evident in **Figure 10b**: plot of prediction values (%) versus reference values (%) for the samples in calibrations, cross validations, and tests. Black dots represent fitted dataset for the calibration. Blue triangles symbolize cross validation dataset. Red squares represent the first test set; the second test set is shown in green circles. The ideal model ($y = x$), in which all the predicted values are equal to the reference values through the whole data interval, is represented by a dotted line. **Figure 10b** shows low dispersion of the data about the ideal model ($y = x$) for predicted values of calibrations, cross validations, and tests.

Finally, the most debatable figure of merit in the PLS analysis is the LOD [54–56]. The RSD was calculated for each mix from the predicted concentrations by cross validation and testing. A plot of the precision in terms of the RSD values versus nominal reference values was obtained. According to IUPAC recommendations [57–62], a power fit was applied, and the values for the LOD and the limit of quantification (LOQ) were obtained by the interpolation of the concentration for 33.3% of RSD and 10% of RSD, respectively [63]. LOD found was 1% of API, and the RSD was maintained below 5% for concentrations >5% (see inset of **Figure 10b**). This result suggests a good value for the LOD and a low uncertainty for the analytical quantification. These values are comparable to methodologies based on NIR and Raman spectroscopy measurements.

An evaluation between the proposed MIR laser spectroscopy methodology and the industry standard HPLC method was done. For the comparison study, a sample set of three formulations in the range of 0–20% was prepared, and the sample compositions were verified by HPLC and contrasted with the values obtained by the MIR laser spectroscopy methodology proposed (**Table 4**). A relative standard error of prediction for HPLC (RSP-HPLC) was obtained using the gravimetric values. The value obtained for RSP-HPLC was lower than other RSP values, but as can be

% weight	% HPLC	% PLS-QCL
14.4 ± 0.1	14.63 ± 0.03	14.4 ± 0.4
9.9 ± 0.1	10.07 ± 0.02	10.1 ± 0.3
4.48 ± 0.09	4.58 ± 0.03	4.5 ± 0.4

Table 4.
Prediction of IBP Composition (w/w%) by HPC and QCL.

observed in **Table 4**, the predicted concentration values (% composition, API) were very close to the gravimetric values and the HPLC predicted values. Thus, this cross validation experiment points to the robustness of the MIR laser methodology proposed.

3.3 Conclusions

QCL spectroscopy was used to acquire spectra of API in lab-prepared pharmaceutical formulations. MIR laser spectra of formulations were acquired outside the sample compartment, at 15 cm, in diffuse reflectance in the range of 1000–1600 cm^{-1} . Because of the convoluted MIR spectra of the formulations, the quantification had to be handled using PLS. The MVA method was shown to be capable of achieving good exactness and precision at forecasting the API compositions in the lab-made formulations. Significant effectiveness obtained for the model is indicative of a high analytical sensitivity equivalence (0.05% API), good repeatability (2.7%), and good reproducibility (5.4%). All these qualities allowed achieving a LOD of 1%. Furthermore, the proposed procedure is characterized by high specificity, high sensitivity, fast response, and sufficiently high accuracy and precision.

The proposed protocol is a demonstration that MIR laser spectroscopy can be used for off-line monitoring of APIs in pharmaceutical formulations. Further work in this area could lead to the next phase, where MIR laser spectroscopy combined with MVA routines of chemometrics possibly will be used to challenge results obtained by online supervision of manufacturing pharmaceutical and biotechnology processes. This would provide real-time data to control systems in continuous manufacturing practices (CMP) in agreement with modern PAT tendencies.

4. Summary

MIR laser spectroscopy has been demonstrated as a highly adaptable spectroscopic method for recasting traditional MIR spectroscopic techniques, such as absorption, reflectance, transmission, emission, and RAIRS, under the high-brightness conditions that a collimated, polarized, coherent laser source provides. When MIR laser-excited reflectance spectra are coupled to chemometric algorithms for classification, discrimination, and quantification, much lower LOD and LOQ values were obtained for the target chemical/biological agent simulants. A selection of several applications of MIR laser spectroscopy has been presented. These applications cover from the coupling a MIR laser to a compact grazing angle probe for trace detection of chemical and biological threat agents, experiments for detection of microorganisms, and PAT applications such as cleaning validation of batch reactors in pharmaceutical and biotechnology manufacturing plants and quantification of APIs in pharmaceutical formulations.

Acknowledgements

This material is based upon work supported by the US Department of Homeland Security, Science and Technology Directorate, Office of University Programs, under Grant Award 2013-ST-061-ED0001. The views and conclusions contained in this document are those of the authors and should not be interpreted as necessarily representing the official policies, either expressed or implied, of the US Department of Homeland Security. The parts of the work were supported by the US Department of Defense, Agreement Number: W911NF-11-1-0152.

Author details

Leonardo C. Pacheco-Londoño^{1,2}, Nataly J. Galán-Freyle^{1,2},
Amira C. Padilla-Jiménez^{1,3}, John R. Castro-Suarez^{1,4},
Amanda M. Figueroa-Navedo¹, José L. Ruiz-Caballero¹, Ricardo Infante-Castillo^{1,5},
Carlos Rios-Velazquez⁶ and Samuel P. Hernández-Rivera^{1*}

1 Department of Chemistry, University of Puerto Rico-Mayagüez, ALERT DHS Center of Excellence, Mayagüez, Puerto Rico, USA

2 School of Basic and Biomedical Sciences, University of Simón Bolívar, Barranquilla, Colombia

3 Department of Chemistry, University of Córdoba, Water Resources, Pesticides, and Heavy Metals Research Group, “GIAMP”, Montería, Colombia


4 Antonio de Arévalo Technological Foundation, TECNAR, Cartagena, Colombia

5 Department of Physics-Chemistry, University of Puerto Rico, Arecibo, Puerto Rico, USA

6 Department of Biology, University of Puerto Rico, Mayagüez, Puerto Rico, USA

*Address all correspondence to: samuel.hernandez3@upr.edu

IntechOpen

© 2018 The Author(s). Licensee IntechOpen. This chapter is distributed under the terms of the Creative Commons Attribution License (<http://creativecommons.org/licenses/by/3.0>), which permits unrestricted use, distribution, and reproduction in any medium, provided the original work is properly cited. 

References

- [1] Caygill JS, Davis F, Higson SPJ. Current Trends in Explosive. *Talanta*. 2012;**88**:14-29. DOI: 10.1016/j.talanta.2011.11.043
- [2] Galán-Freyre NJ, Pacheco-Londoño LC, Figueroa-Navedo AM, Hernández-Rivera SP. Standoff detection of highly energetic materials using laser-induced thermal excitation of infrared emission. *Applied Spectroscopy*. 2015;**69**(5):535-544. DOI: 10.1366/14-07501
- [3] Castro-Suarez JR, Pacheco-Londoño LC, Vélez-Reyes M, Diem M, Tague TJ, Hernández-Rivera SP. FT-IR standoff detection of thermally excited emissions of trinitrotoluene (TNT) deposited on aluminum substrates. *Applied Spectroscopy*. 2013;**67**(2):181-186. DOI: 10.1366/11-06229
- [4] Pacheco-Londoño LC, Ortiz-Rivera W, Primera-Pedrozo OM, Hernández-Rivera SP. Vibrational spectroscopy standoff detection of explosives. *Analytical and Bioanalytical Chemistry*. 2009;**395**(2):323-335. DOI: 10.1007/s00216-009-2954-y
- [5] Pettersson A, Johansson I, Wallin S, Nordberg M, Östmark H. Near real-time standoff detection of explosives in a realistic outdoor environment at 55 m distance. *Propellants, Explosives, Pyrotechnics*. 2009;**34**(4):297-306. DOI: 10.1002/prop.200800055
- [6] Pacheco-Londoño LC, Castro-Suarez JR, Hernández-Rivera SP. Detection of nitroaromatic and peroxide explosives in air using infrared spectroscopy: QCL and FTIR. *Advances in Optical Technologies*. 2013;**2013**(8):532670. DOI: 10.1155/2013/532670
- [7] Van Neste CW, Senesac LR, Thundat T. Standoff spectroscopy of surface adsorbed chemicals. *Analytical Chemistry*. 2009;**81**:1952-1956. DOI: 10.1021/ac802364e
- [8] Hildebrand J, Herbst J, Wöllenstein J, Lambrecht A. Explosive detection using infrared laser spectroscopy. *Proceedings of SPIE*. 2009;**7222**:72220B. DOI: 10.1117/12.808976
- [9] Fuchs F, Hugger S, Kinzer M, Aidam R, Bronner W, Losch R, et al. Imaging standoff detection of explosives using widely tunable mid infrared quantum cascade lasers. *Optical Engineering*. 2010;**49**(11):111127-111128. DOI: 10.1117/1.3506195
- [10] Deutsch ER, Kotidis P, Zhu N, Goyal AK, Ye J, Mazurenko A, et al. Active and passive infrared spectroscopy for the detection of environmental threats. *Proceedings of SPIE*. 2014;**9106**:91060A-9. DOI: 10.1117/12.2058544
- [11] Suter JD, Bernacki B, Phillips MC. Spectral and angular dependence of mid-infrared diffuse scattering from explosives residues for standoff detection using external cavity quantum cascade lasers. *Applied Physics B: Lasers and Optics*. 2012;**108**(4):965-974. DOI: 10.1007/s00340-012-5134-2
- [12] Castro-Suarez JR, Pollock YS, Hernández-Rivera SP. Explosives detection using quantum cascade laser spectroscopy. *Proceedings of SPIE*. 2013;**8710**:871010. DOI: 10.1117/12.2016037
- [13] Castro-Suarez JR, Hidalgo-Santiago M, Hernández-Rivera SP. Detection of highly energetic materials on non-reflective substrates using quantum cascade laser spectroscopy. *Applied Spectroscopy*. 2015;**69**(9):1023-1035. DOI: 10.1366/14-07626
- [14] Pacheco-Londoño LC, Castro-Suarez JR, Aparicio-Bolaños J, Hernández-Rivera SP. Angular dependence of source-target-detector in active mode standoff infrared

- detection. *Proceedings of SPIE*. 2013;**8711**:8711081-8711086. DOI: 10.1117/12.2016153
- [15] Ortega-Zúñiga CA, Galán-Freyle NY, Castro-Suarez JR, Aparicio-Bolaños J, Pacheco-Londoño LC, Hernández-Rivera SP. Dependence of detection limits on angular alignment, substrate type and surface concentration in active mode standoff IR. *Proceedings of SPIE*. 2013;**8734**:87340R-1-87340R-8. DOI: 10.1117/12.2016196
- [16] Castro-Suarez JR, Pacheco-Londoño LC, Aparicio-Bolaño J, Hernandez-Rivera SP. Active mode remote infrared spectroscopy detection of TNT and PETN on aluminum substrates. *Journal of Spectroscopy*. 2017;**2017**:2730371
- [17] Figueroa-Navedo AM, Galán-Freyle NJ, Pacheco-Londoño LC, Hernández-Rivera SP. Chemometrics enhanced laser induced thermal emission detection of PETN and RDX. *Journal of Chemometrics*. 2015;**29**:329-337
- [18] Griffiths PR, de Haseth JA. *Fourier Transform Infrared Spectrometry*. 2nd ed. Hoboken, NJ: John Wiley & Sons, Inc.; 2007. ISBN: 978-0-471-19404-0
- [19] Mehta NK, Goenaga-Polo J, Hernández-Rivera SP, Hernández D, Thomson MA, Melling PJ. Development of an in situ spectroscopic method for cleaning validation using mid-IR fiber-optics. *BioPharm*. 2002;**15**:36-42
- [20] Hamilton ML, Persto BB, Harland PW, Williamson BE, Thomson MA, Melling PJ. Grazing-angle fiber-optic IRRAS for in situ cleaning validation. *Organic Process Research and Development*. 2005;**9**(3):337-343
- [21] Hvozدارa L, Pennington N, Kraft M, Karlowatz M, Mizaiakoff B. Quantum cascade lasers for mid-infrared spectroscopy. *Vibrational Spectroscopy*. 2002;**30**:53-58
- [22] Unemura J. Reflection-absorption spectroscopy of thin films on metallic substrates. In: Chalmers JM, Griffiths PR, editors. *Handbook of Vibrational Spectroscopy*. Vol. 1. Chichester, West Sussex, England: Wiley; 2002. 33 p. ISBN: 978-0-471-98847-2
- [23] Galán-Freyle NJ, Figueroa-Navedo AM, Pacheco-Londoño LC, Ruiz-Caballero JL, Hernández-Rivera SP. Removal of quantum cascade grazing angle probe interference fringes in applications of cleaning validation and detection of explosives using Fast Fourier Transform preprocessing algorithm. *Journal of Chemometrics*, submitted
- [24] Moore DS. Instrumentation for trace detection of high explosives. *The Review of Scientific Instruments*. 2004;**75**:2499-2512. DOI: 10.1063/1.1771493
- [25] Moore DS. Recent advances in trace explosives detection instrumentation. *Sensing and Imaging*. 2009;**8**(1):9-38. DOI: 10.1007/s11220-007-0029-8
- [26] Long GL, Winefordner JD. Limit of detection: A closer look at the IUPAC definition. *Analytical Chemistry*. 1983;**55**(07):712A-724A. DOI: 10.1021/ac00258a724
- [27] Karpowicz RJ, Brill TB. Comparison of the molecular structure of hexahydro-1,3,5-trinitro-s-triazine in the vapor, solution, and solid phases. *The Journal of Physical Chemistry*. 1984;**88**(3):348-352. DOI: 10.1021/j150647a005
- [28] Infante-Castillo R, Pacheco-Londoño L, Hernández-Rivera SP. Vibrational spectra and structure of RDX and its ¹³C- and ¹⁵N-labeled derivatives: A theoretical and experimental study. *Spectrochimica Acta A*. 2010;**76**(2):137-141. DOI: 10.1016/j.saa.2010.02.051
- [29] Barker M, Rayens W. Partial least squares for discrimination. *Journal of*

- Chemometrics. 2003;**17**(3):166-173. DOI: 10.1002/cem.785
- [30] Brereton RG. Chemometrics for Pattern Recognition. Chichester, England. The Atrium, Southern Gate: John Wiley & Sons Ltd.; 2009. ISBN 978-0-470-98725-4
- [31] Ballabio D, Consonni V. Classification tools in chemistry. Part 1: Linear models. PLS-DA. Analytical Methods. **2013**, **5**(16):3790-3798. DOI: 10.1039/C3AY40582F
- [32] Zhao G, Xing F, Deng S. A disposable amperometric enzyme immunosensors for rapid detection of vibrio parahaemolyticus in food based on agarose/nano-Au membrane and screen-printed electrode. Electrochemistry Communications. 2007;**9**:1263-1268. DOI: 10.1016/j.elecom.2007.01.036
- [33] Wu VCH, Chen S, Lin CS. Real-time detection of *Escherichia coli* O157:H7 sequences using a circulating-flow system of quartz crystal microbalance. Biosensors and Bioelectronics. 2007;**22**:2967-2975. DOI: 10.1016/j.bios.2006.12.016
- [34] Siripatrawan U, Harte BR. Solid phase microextraction/gas chromatography/mass spectrometry integrated with chemometrics for detection of *Salmonella typhimurium* contamination in a packaged fresh vegetable. Analytica Chimica Acta. 2007;**581**:63-70. DOI: 10.1016/j.aca.2006.08.007
- [35] Naumann D. Infrared spectroscopy in microbiology. In: Meyers RA, editor. Encyclopedia of Analytical Chemistry. Chichester, UK: John Wiley & Sons; 2000. pp. 102-131. DOI: 10.1002/9780470027318.a0117
- [36] Félix-Rivera H, González R, Rodríguez GD, Primera-Pedrozo OM, Ríos-Velázquez C, Hernández- Rivera SP. Improving SERS detection of *Bacillus thuringiensis* using silver nanoparticles reduced with hydroxylamine and with citrate capped borohydride. International Journal of Spectroscopy. 2011;**2011**:9. DOI: 10.1155/2011/989504
- [37] Primera-Pedrozo OM, Jerez-Rozo JI, De La Cruz-Montoya E, Luna-Pineda T, Pacheco-Londoño LC, Hernández-Rivera SP. Nanotechnology-based detection of explosives and biological agents simulants. IEEE Sensors Journal. 2008;**8**(6):963. DOI: 10.1109/JSEN.2008.923936
- [38] Hans-Ulrich G, Yan B, editors. Infrared and Raman Spectroscopy of Biological Materials. Practical Spectroscopy Series. Vol. 24. New York: Marcel Dekker, Inc.; 2001
- [39] Samuels AC, Snyder AP, Amant DS, Emge DK, Minter J, Campbell M, et al. Classification of select category A and B bacteria by Fourier transform infrared spectroscopy. Proceedings of SPIE. 2008;**6954**:695413. DOI: 10.1117/12.767292
- [40] Padilla-Jiménez AC, Ortiz-Rivera W, Castro-Suarez JR, Ríos-Velázquez C, Vázquez-Ayala I, Hernández-Rivera SP. Microorganisms detection on substrates using QCL spectroscopy. Proceedings of SPIE. 2013;**8710**:871019-1-871019-12. DOI: 10.1117/12.2016099
- [41] Padilla-Jiménez AC, Ortiz-Rivera W, Ríos-Velázquez C, Vázquez-Ayala I, Hernández-Rivera SP. Detection and discrimination of microorganisms on various substrates with QCL spectroscopy. Optical Engineering. 2014;**53**(6):061611-1-061611-10. DOI: 10.1117/1.OE.53.6.061611
- [42] Drury MA. Applications for mid-IR spectroscopy in the pharmaceutical process environment. Spectroscopy. 2004;**19**(2):60-63
- [43] Févotte G. In situ Raman spectroscopy for in-line control of

pharmaceutical crystallization and solids elaboration processes: A review. *Chemical Engineering Research and Design*. 2007;**85**(7):906-920

[44] Roggo Y, Chalus P, Maurer L, Lema-Martinez C, Edmond A, Jent N. A review of near infrared spectroscopy and chemometrics in pharmaceutical technologies. *Journal of Pharmaceutical and Biomedical Analysis*. 2007;**44**(3):683-700

[45] Wang X, Fu Q, Sheng J, Yang X, Jia J, Du W. Construction of a universal quantitative model for ibuprofen sustained-release capsules from different manufacturers using near-infrared diffuse reflection spectroscopy. *Vibrational Spectroscopy*. 2010;**53**(2):214-217

[46] Pestaner JP, Mullick FG, Centeno JA. Characterization of acetaminophen: Molecular microanalysis with Raman microprobe spectroscopy. *Journal of Forensic Sciences*. 1996;**41**(6):1060-1063

[47] Kachrimanis K, Braun DE, Griesser UJ. Quantitative analysis of paracetamol polymorphs in powder mixtures by FT-Raman spectroscopy and PLS regression. *Journal of Pharmaceutical and Biomedical Analysis*. 2007;**43**(2):407-412

[48] Chan KLA, Hammond SV, Kazarian SG. Applications of attenuated total reflection infrared spectroscopic imaging to pharmaceutical formulations. *Analytical Chemistry*. 2003;**75**(9):2140-2146

[49] Henson MJ, Zhang L. Drug characterization in low dosage pharmaceutical tablets using Raman microscopic mapping. *Applied Spectroscopy*. 2006;**60**(11):1247-1255

[50] Thakral NK, Ragoonanan V, Suryanarayanan R. Quantification, mechanism, and mitigation of active

ingredient phase transformation in tablets. *Molecular Pharmaceutics*. 2013;**10**(8):3128-3136

[51] Lüdeke S, Pfeifer M, Fischer P. Quantum-cascade laser-based vibrational circular dichroism. *Journal of the American Chemical Society*. 2011;**133**(15):5704-5707

[52] Alsirawan MB, Mohammad MA, Alkasmi B, Alhareth K, El-Hammadi M. Development and validation of a simple HPLC method for the determination of ibuprofen sticking onto punch faces. *Journal of Pharmacy and Pharmaceutical Sciences*. 2013;**5**(4):227-231

[53] Kubelka P. New contributions to the optics of intensely light-scattering materials: Part I. *Journal of the Optical Society of America*. 1948;**38**(5):448-448

[54] Blanco M, Bautista M, Alcalá M. Preparing calibration sets for use in pharmaceutical analysis by NIR spectroscopy. *Journal of Pharmaceutical Sciences*. 2008;**97**(3):1236-1245

[55] Olivieri AC, Faber NM, Ferré J, Boqué R, Kalivas JH, Mark H. Uncertainty estimation and figures of merit for multivariate calibration (IUPAC Technical Report). *Pure and Applied Chemistry*. 2006;**78**(3):633

[56] Allegrini F, Olivieri AC. Analytical figures of merit for partial least-squares coupled to residual multilinearization. *Analytical Chemistry*. 2012;**84**(24):10823-10830

[57] Ostra M, Ubide M, Vidal M, Zuriarrain J. Detection limit estimator for multivariate calibration by an extension of the IUPAC recommendations for univariate methods. *The Analyst*. 2008;**133**(4):532-539

[58] Boqué R, Faber NM, Rius FX. Detection limits in classical

multivariate calibration models.

Analytica Chimica Acta.

2000;**423**(1):41-49

[59] Boqué R, Rius FX. Multivariate detection limits estimators.

Chemometrics and Intelligent

Laboratory Systems. 1996;**32**(1):11-23

[60] Faber K, Kowalski BR. Improved estimation of the limit of detection in multivariate calibration. *Fresenius Journal of Analytical Chemistry*.

1997;**357**(7):789-795

[61] Bauer G, Wegscheider W, Ortner H. Limits of detection in multivariate calibration. *Fresenius Journal of Analytical Chemistry*.

1991;**340**(3):135-139

[62] Thomsen V, Schatzlein D, Mercurio D. Limits of detection in spectroscopy. *Spectroscopy*.

2003;**18**(12):112-114

[63] Galán-Freyte NJ, Pacheco-Londoño LC, Román-Ospino AD, Hernández-Rivera SP. Applications of quantum cascade laser spectroscopy in the analysis of pharmaceutical formulations. *Applied Spectroscopy*.

2017;**70**(9):1511-1519

Mid-Infrared Spectroscopy and Challenges in Industrial Environment

Chayan Mitra

Abstract

In recent years, Mid-Infrared spectroscopy has garnered lot of attention from researchers and industries due to the availability of industrial grade room temperature Intra-band and Quantum Cascade Lasers. These lasers are repeatable in their performance and along with Near-Infrared Lasers, it has opened the entire Infra-red spectral band for industrial applications. This enabled widespread applications of tunable laser absorption spectroscopy for real-time, in-situ and non-invasive gas sensing. Though several spectroscopy techniques are currently available, Mid-Infrared Absorption Spectroscopy offers us a unique advantage of measurement of trace gas concentrations of few gases which has very weak transitions in Near-Infrared region. The objectives of this chapter are to discuss about the spectroscopy technique commonly used for Mid-Infrared Lasers, a comparative study with other techniques, noise and some challenges remaining for industrial applications.

Keywords: mid-infrared, Quantum Cascade Laser, absorption spectroscopy, near-infrared, spectroscopy

1. Introduction

1.1 General introduction

The Power Generation industry, one of the growth engines for a nation, today face a unique challenge of market volatility and uncertainty. The industry needs to depend on a diverse set of fuel mix and ensure reliable delivery of power while providing asset level visibility (state of asset performance in real-time). It has to provide electricity to over 1 billion people globally for stable growth while ensuring reduced environmental footprint and improved efficiency. The requirement for real-time demand adjustments in response to supply conditions requires integration of real-time measurements, predictability and operational process optimization. This in-turn requires smarter combination of monitoring devices and analytics. The successful transformation depends largely on merger of physical and digital technologies. Real-time, non-invasive and in-situ sensing technologies are the main connects with the network of assets providing powerful data driven insights – a single unified automation architecture for the utility operators and owners.

Apart from air pollution control, emission measurement provides a deeper insight and characterization of a combustion process and control. There are two distinct categories of emission species from a power plant. CO_2 , H_2O , N_2 and O_2 are the major species of emission and are present in percent concentrations, whereas, NO_x , CO , SO_x , Unburned Hydrocarbons (UHC) and Particulate Matters (PMs) constitutes the minor species and are present in parts per million (ppm) concentrations [1, 2]. Nitrogen oxide (NO_x), carbon monoxide (CO) and sulfur oxide (SO_x) the three most important anthropogenic air pollutants are formed during the combustion process in power generation industry (gas fired, coal fired and oil fired). The emission levels from outlet of the treatment systems is important as it outlines few key parameters for selecting flue gas monitoring systems based on the target application: Measurement range, Measurement uncertainty and accuracy, Purpose of measurement and Interfering species.

Spectroscopy-based system is one of the most versatile technologies available for real-time, non-invasive and accurate measurement of trace gases in a combustion environment or a complex gas mixture.

In a spectroscopic measurement system, one down-selects a target molecular transition (based on a “selection” criteria) of the gas species for analyzing the line strength, line shape (and effect of gas temperature and pressure) and estimation of concentration of the species in the gas mixture. Accurate information about the transition will provide users symptoms of any machine/process health issues, possible causes (when evaluated along with operating parameters), possible consequences (impact on service schedules) and possible mitigation methods. Like any measurement system we have the challenge of mitigation of systematic errors (biases) and random errors (white noise). Systematic errors or biases tend to shift the result (the target molecular transition) to one side. This is particularly important as a molecular transition of any gas species is always closely stacked along with the transitions of moisture (a common product from any combustion process). An error in this case will lead to merger of multiple transitions (or targeting a wrong transition!). Proper laser tuning is probably the most critical step in minimizing this error. Random errors are mostly contributed by noise from the detector circuit ($1/f$ noise, generation-recombination noise and Johnson noise), fluctuations in background radiations (above $3\ \mu\text{m}$). These errors can be minimized but cannot be avoided.

1.2 Near-infrared absorption spectroscopy and challenges

Near-Infrared (Near-IR) (wavelength range: visible to $\sim 3\ \mu\text{m}$) Tunable Diode Laser Absorption Spectroscopy (TDLAS) is a promising technology for real-time trace gas detection without intruding the flow field. This has applications in multiple fields like, environment monitoring, medical diagnostics, defense and law enforcement. TDLAS technique using Near-IR laser at room temperature monitors the overtones of the molecular transitions which have much weaker line strength than the fundamental transitions [3].

Scanned wavelength Direct absorption spectroscopy (DAS) typically involves irradiating the sample with a laser whose wavelength is periodically changed across a fixed range that is larger than the range at which the gas absorbs. The output intensity is measured as a function of wavelength. **Figure 1a**, shows a schematic of DAS. In DAS, the measured output is a dip in intensity at the absorption wavelength of the sample. This becomes difficult for samples with weak absorption lines, or very low gas concentrations (in which the change in fractional absorbance can be as low as 10^{-5}), where one needs to measure a very small change in intensity riding on a large background intensity.

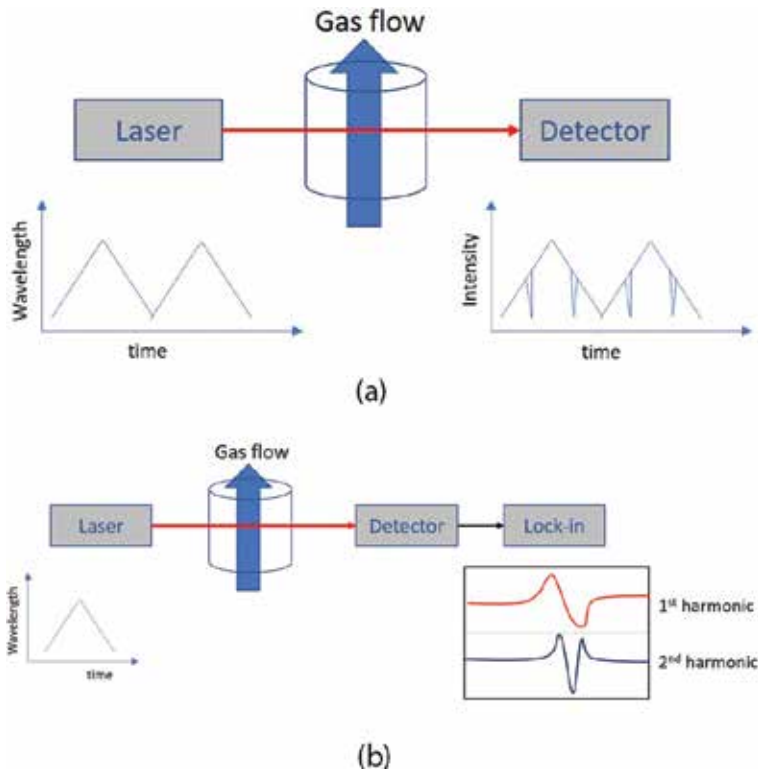


Figure 1. (a) Schematic representation of scanned wavelength direct absorption spectroscopy (DAS). (b) Schematic representation of wavelength modulation spectroscopy (WMS).

Wavelength Modulation Spectroscopy (WMS) or second harmonic detection is a way of increasing the sensitivity of absorption spectroscopy. It involves modulating the laser wavelength and detecting the signal at the second harmonic of the modulation frequency. **Figure 1b** shows a schematic of WMS technique. The benefits of using WMS as opposed to DAS are:

- increased sensitivity,
- insensitivity to interfering species that have broad absorption features in the region of interest,
- Insensitivity to input intensity fluctuations,
- Insensitivity to vibrations.

In WMS, the input wavelength is simultaneously scanned (ramp or triangular waveforms are typically used) and modulated with a sinusoidal waveform. The output intensity is demodulated at the modulation frequency (for first harmonic) and at twice the modulation frequency (for second harmonic). The gas concentration is calculated from the amplitude of the second harmonic signal.

Due to weaker line-strengths and therefore low absorption coefficients of gas species in Near-IR region, absorption spectroscopy in Near-IR has limitations in presence of complex gas mixtures, high pressure and high temperature environment. Availability of industrial grade Interband Cascade Lasers (ICLs) and Quantum Cascade Lasers (QCLs) has enabled application of TDLAS at Mid-Infrared

(Mid-IR) for an accurate and real-time measurement of trace gas content at high temperature in a complex gas mixture environment.

1.3 Enablers of Mid-IR spectroscopy

The first generation QCLs (Quantum Cascade Lasers) operated only in pulsed mode and at ~ 90 K temperature. Significant advancements in epitaxial layer growth processes using Molecular Beam Epitaxy (MBE) and Metallorganic Chemical Vapor Deposition (MOCVD) technologies, bandgap engineering opened the Mid-IR spectral region (wavelength range: 3–24 μm). Subsequently, the continuous single-mode tunability of the QCLs were achieved using tuning schemes like active and simultaneous tuning of grating angles, external cavity length and optical length of the laser chip (drive current tuning and or chip temperature tuning) [4–7].

Gas detection and measurement at trace concentration levels like ppbv (parts per billion in volume) and sub-ppbv or pptv (parts per trillion in volume) requires targeting of strong fundamental roto-vibrational transitions (and hence large absorption coefficient) of the molecules of gas species in the Mid-IR spectral region [8]. Availability of compact, solid-state, high performance and low dissipation single-mode QCLs (Example: Output power 25 mW at 2226 cm^{-1} , dissipated power 1 W [9]) enabled cost-effective usage in several industrial applications without the constraint of heavy packaging in the measurement system. Apart from the QCLs, improvement in detector technology using multi-stage Peltier cooled HgCdTe (Mercury Cadmium Telluride or MCT) Mid-Wavelength Infrared (MWLIR) and Long Wavelength Infrared (LWIR) detectors paved way for stable, fast response (time constant $\tau < 2\text{ ns}$ [10]) and low noise detection in the entire Mid-IR spectral range (upto $\approx 13\text{ }\mu\text{m}$) [11, 12].

To isolate the QCL devices from any kind of inadvertent exposure to high temperature of the process gas, ease of servicing of the laser modules and ensuring Gaussian beam delivery, Chalcogenide glass (ChGs), Fluoride glass, Sapphire and Silver Halide fibers were initially used for the transmission of Mid-IR lasers as it has wide optical transmission windows in the IR region. A major challenge with the fibers was their brittle nature and laser feedback due to back reflections from the fiber end which reduces signal-to-noise ratio [13, 14]. Last decade has witnessed rapid development of low-loss Hollow Core Waveguides (HCW) for transmission of the Mid-IR beams from the QCLs [15–19]. These are essentially a glass capillary tube with dielectric/metallic structure deposited inside the bore of the tube. Apart from possessing high coupling efficiencies ($>95\%$) and high-power handling capabilities, the hollow core waveguides propagate single-mode [20].

Beam divergence, astigmatism are some of the common challenges one needs to address for all practical applications of Mid-IR spectroscopy [21]. In case of multiple gas species detection, beams from multiple QCL sources are combined along with a red laser (this will be discussed later in Section 4.3). A reflecting beam expander with silver mirror (Wavelength: 450 nm–20 μm , for example *see Thorlabs Product Catalog* [22]) is typically used in these cases. A reflective beam reducing optics is similarly used at the detection end to avoid the chromatic aberrations.

As mentioned previously, the wavelength tuning of QCLs consists of two methods: (1) temperature tuning, (2) injection current tuning. Temperature tuning is slow process and generally used for coarse and slow frequency sweeps [23–25]. Wavelength change through injection current tuning is a much faster process with bandwidth $>100\text{ KHz}$. In this case, the tuning range is much narrower with a significant change in emitted optical power [26, 27]. In modulation spectroscopy techniques, the current modulation sometimes leads to a residual amplitude modulation (RAM) as there is significant change in optical power with injection current.

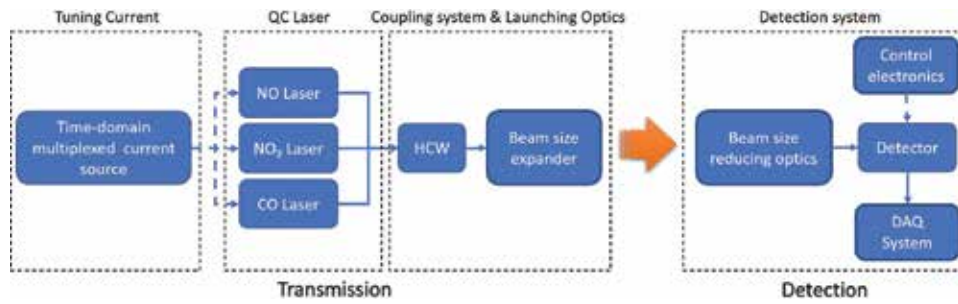


Figure 2. A simplified schematic representation of the Mid-IR spectroscopy system (HCW: hollow core waveguides; DAQ: data acquisition; QC: quantum cascade).

This leads to some distortions in the harmonics of absorption spectra (asymmetry in the $2f$ spectra) [25]. This requires low noise laser current controllers to minimize linewidth, drift and jitter [21, 28]. It should be remembered that commonly used laser diode drivers cannot be used for QCLs due to the compliance voltage which is in the range of 5–15 V.

A simplified schematic of the Mid-IR spectroscopy system is shown in **Figure 2**.

2. Spectroscopy

2.1 Spectroscopic databases and transition lines

As discussed in the introductory section proper down-selection of the roto-vibrational transition lines is a critical part of the process for ensuring accuracy of the measurement system. Several spectroscopic databases, like HITRAN (*High Resolution Transmission*) Molecular Absorption Database [29], HITEMP (*High Temperature Molecular Spectroscopic Database*) [30], GEISA (*Gestion et Etude des Informations Spectroscopiques Atmospheriques*) Spectroscopic Database [31], PNNL (*Pacific Northwest National Laboratory*) Vapor Phase Infrared Spectral Library [32], ATMOS (*Atmospheric Trace Molecule Spectroscopy*) Database [33], NIST (*National Institute of Standards and Technology*) Infrared Spectroscopy Database [34], BT2 (*A high accuracy computed water line list*) Spectroscopic list [35] and CDSDB (*Carbon Dioxide Spectroscopic Databank*) [36] exists for analyzing the spectroscopic parameters and simulate the transmission spectra. As Mid-IR spectroscopy for industrial applications is the recurrent theme of this chapter, the focus will be on the dominant roto-vibrational transitions in the Mid-IR region for those gas species playing a major role in industrial applications. A summary of rotational-vibration bands and their line-strengths for anthropogenic pollutants NO, NO₂, CO, SO₂ and a major interfering gas (H₂O) in the Mid-IR region is given in **Table 1**.

Table 1 also contains the absorbance values for the gases at temperature (T) = 300 K, Pressure (P) = 1 atm, Length (L) = 100 cm and gas mole-fraction (X) = 1, computed using *SpectraPlot* [41] tool. The line-strength and hence absorbance for H₂O in Mid-IR (ν_1 , ν_2 and ν_3) is almost an order of magnitude higher than in the Near-IR ($\nu_1 + \nu_2$, $\nu_2 + \nu_3$, and $3\nu_2$).

An overview of the roto-vibrational spectra of the above gases in Near-IR and Mid-IR region is shown in **Figure 3**.

It can be noticed that the Mid-IR spectra contains the fundamental vibration modes for H₂O. H₂O has very strong bands in both Near-IR and Mid-IR region and

Gas species	Mode	Wave number (cm ⁻¹)	Line-strength (cm ⁻² /atm)	Absorbance	Ref.
H ₂ O	ν_2	1594.746	1.723×10^{-1}	12	[37, 41]
	$2\nu_2$	3151.629	2.172×10^{-3}	0.18	
	ν_1	3657.629	2.665	1.8×10^2	
	ν_3	3755.928	2.773×10^{-2}	64	
	$3\nu_2$	4666.790	1.961×10^{-2}	0.00013	
	$(\nu_1 + \nu_2)$	5234.976	8.004×10^{-2}	7.0	
	$(\nu_2 + \nu_3)$	5331.267	2.380×10^{-1}	18	
CO	$\Delta\nu = 2 - 1$	2115.625	9.213	4.3×10^3	[38, 41]
	$\Delta\nu = 1 - 0$	2145.999	7.374×10^{-4}	36	
	$\Delta\nu = 3 - 1$	4204.664	3.778×10^{-2}	0.43	
	$\Delta\nu = 2 - 0$	4260.063	2.866×10^{-6}	0.012	
SO ₂	ν_2	517.75	1.635×10^{-2}	45	[38, 39, 41]
	ν_1	1155.920	1.033×10^{-1}	98	
	ν_3	1360.791	5.119×10^{-1}	2×10^3	
	$(\nu_1 + \nu_2 + \nu_3) - \nu_2$	2492.444	2.019×10^{-2}	27	
	$(\nu_1 + \nu_3)$	2498.444	1.334×10^{-2}	38	
NO ₂	ν_2	741.599	7.862×10^{-3}	28	[38, 41]
	$2\nu_2$	1490.77	1.430×10^{-4}	0.35	
	ν_3	1616.152	9.861×10^{-1}	2.4×10^3	
	$(\nu_2 + \nu_3) - \nu_2$	1605.497	2.478	3.8×10^3	
	$\nu_1 + 2\nu_2$	2805.512	7.041×10^{-6}	0.0089	
	$(\nu_1 + \nu_2 + \nu_3) - \nu_2$	2898.193	8.516×10^{-2}	1.5×10^2	
	$\nu_1 + \nu_3$	2906.069	4.967×10^{-2}	89	
NO	$\Delta\nu = 1 - 0$	(1875.959)	3.179×10^{-2}	2.7×10^2	[40, 41]
	$\Delta\nu = 2 - 1$	1875.898	1.908×10^{-2}	5.0×10^2	
	$\Delta\nu = 2 - 0$	3723.526	2.476×10^{-3}	6.1	
	$\Delta\nu = 1 - 0$	1678.184	1.207×10^{-5}	0.00028	
	$\Delta\nu = 2 - 1$	(1846.568)	4.177×10^{-1}	1.3×10^3	

Table 1.

Summary of some major roto-vibrational spectra for anthropogenic pollutants in Mid-IR spectral region.

careful line selection strategy needs to be adopted for accurate spectral analysis of the target gases.

2.2 Selection of transitions

The study of the spectroscopic properties and down-selection of proper transition for the target gas species is extremely important as the sensitivity and accuracy of the gas species measurement in a gas sensor depends primarily on the line selection process. It is the first step towards designing an accurate sensor. The basic criteria for the selection of a transition are existence of strong absorbance and minimal spectral interference from other combustion products (like water vapor). For example, consider the NO₂ transitions in **Table 1**. The transitions at around

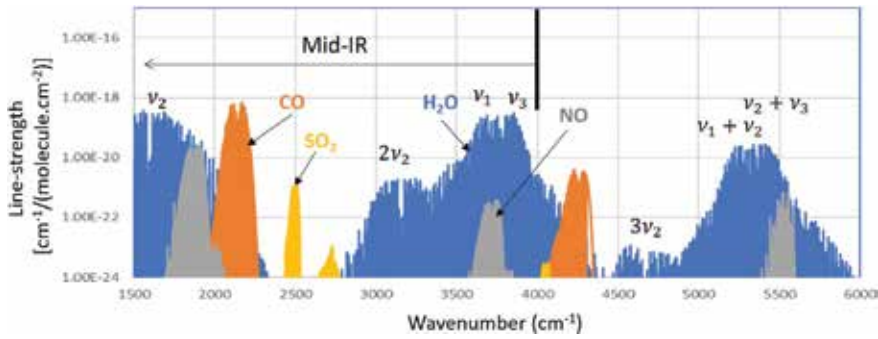


Figure 3. Roto-vibrational spectra of H₂O, NO, CO and SO₂ in NIR and Mid-IR region simulated using spectral data from HITRAN database [29].

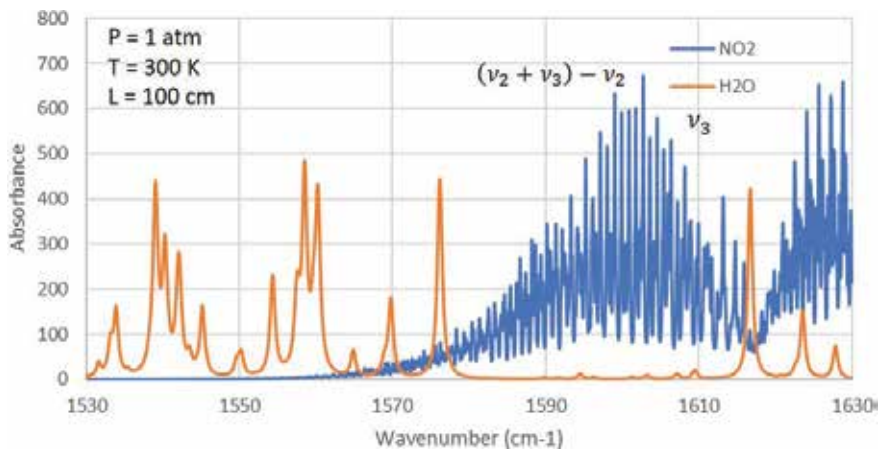


Figure 4. Roto-vibrational spectra of H₂O and NO₂ in Mid-IR region simulated using spectral data from HITRAN database and SpectraPlot tool.

1600 cm⁻¹ are the strongest among all the transitions highlighted for NO₂. In most industrial applications, water vapor is the major interfering species. A simulation study using *SpectraPlot* [41] tool for NO₂ (mole-fraction = 0.1) and H₂O (mole-fraction = 0.8) is shown in **Figure 4**.

Figure 4 shows strong absorption band of NO₂ in 1600 cm⁻¹ region with a well-defined and less-structured water vapor spectrum. This is particularly important as it allows the use of wavelength modulation spectroscopy technique to properly differentiate the spectral features of NO₂ and H₂O completely removing the interferences.

2.3 Absorption spectroscopy: basics and models

The theory of laser absorption spectroscopy has been widely discussed in several literatures in details [42–44]. Some of the key equations will be highlighted here to set the stage for further discussions.

The basic equation relating the incident laser intensity and transmitted laser intensity through a gas medium is given by Beer-Lambert's law

$$\left(I_r/I_0\right)_\nu = \exp(-\alpha_\nu L) \quad (1)$$

Here α_ν denotes the spectral absorbance (also given in **Table 1**) at frequency ν (cm^{-1}). It can also be written as

$$\alpha_\nu = \frac{1}{L} \log(I_0/I_T)_\nu = \sum_j P n x_{abs} S_j(T) \phi(\nu, T, P, x_{abs})_j L \quad (2)$$

The spectral absorbance depends on specific gas properties like mole-fraction (x_{abs}), number density of gas (n) in ($\text{molecules}/\text{cm}^3$), line-strength ($S_j(T)$) and line-shape function $\phi(\nu, T, P, x_{abs})_j$ for a specific quantum transition j . The path-length of the laser (interaction length of the laser through the gas sample) is L (cm). In the above equation, T and P are temperature (K) and pressure (atm) respectively. The transition line-shape function is a key parameter which depends on the ν, T, P and the x_{abs} . Various factors like limited lifetime of the energy levels involved in the transition, thermal motion of the molecules broaden the absorption lines and results in a statistical distribution of frequencies around a center frequency of the transition (ν_0). These line-shape functions are mostly symmetric in nature except for those in complex systems (large molecules) [45]. **Table 2** gives the summary of different line-shape models used in absorption spectroscopy (irrespective of whether it is Near-IR or Mid-IR).

From **Table 2**, we can see that the Doppler broadening has strong ν dependence and weak T (temperature) and m (molecular weight of the gas species) dependence. On the other hand, the Lorentzian profile changes with the life-time of the transition state. Doppler broadening is the dominant factor at low pressure and pressure induced shift (Δ) dominates at higher pressure. Apart from the usual Gaussian, Lorentzian and Voigt distributions (which are symmetric distributions), an Asymmetric model is also highlighted in the table. In a multi-peak fitting scenario, degree of overlap, number of non-resolved bands in the profile under study and base-line position are the critical parameters which drives the accuracy of curve fits [47, 48].

The models are developed to provide a ‘best fit’ to the experimental data and to quantify the parameters of interest as described in **Table 2**. Derived using theoretical equations, the parameters provide us specific physical interpretation of the underlying process. The ‘Sum of Squared Residuals’ (Sum of Squared Residuals: square of the difference between a model estimate and the corresponding data point) is often used for estimating the measurement error [49]. At very low-

	Lineshape model	FWHM, Parameters	Mechanism and Ref.
Gaussian	$G(\nu) = \frac{A}{\gamma_0} \sqrt{\frac{4\ln 2}{\pi}} \exp\left[-4\ln 2 \left(\frac{\nu-\nu_0}{\gamma_0}\right)^2\right]$	$\gamma_0 = 2\nu_0 \sqrt{\frac{2\ln 2k_B T}{mc^2}}$ γ_0	Doppler broadening [45]
Lorentz	$L(\nu) = \frac{2A/\pi\gamma_L}{1+4[(\nu-\nu_0-\Delta)/\gamma_L]^2}$	$\gamma_L = 1/(4\pi\tau)$ γ_L, Δ	Radiation damping, collision broadening [45]
Pseudo-voigt	$V(\nu) = L(\nu) \otimes G(\nu)$ $V(\nu - \nu_0) = \int_{-\infty}^{\infty} G(\nu' - \nu_0)L(\nu - \nu')d\nu'$	Parameters: $\gamma_0, \gamma_L, \Delta$	Convolution of Gaussian & Lorentzian [45, 46]
Asymmetry	$A(\nu) = \frac{2\gamma_0}{1+\exp[a(\nu-\nu_0)]}$	$a < 0, \nu_0 \rightarrow$ higher wavenumbers $a > 0, \nu_0 \rightarrow$ lower wavenumbers	Complex molecules in Mid-IR [45]

FWHM: full width at half maximum.

Table 2. Summary of line-shape models used for spectral analysis in absorption spectroscopy along with the parameters characterizing the profiles.

pressure regime (<20 Pa), the Voigt distribution fit of the profile does not reproduce accurately the observed spectral line shape of the gas species. ‘W-shaped’ residuals have been observed in these cases [50]. Galatry profiles (for soft collisions) and Rautian profiles (for hard collisions) have been developed to minimize the observed residuals [51, 52].

The ‘fit’ of the models to the experimental data becomes extremely critical when we try to estimate the gas concentration with ppbv (parts per billion in volume) or pptv (parts per trillion in volume) accuracy levels (in 3σ scales). This will be discussed in detail in Section 3.

2.4 Absorption spectroscopy: effect of temperature

In most real-world applications, it is desirable to measure the gas species concentration at elevated temperatures. Temperature dependency of line-strength and line-shape leads to complications in species concentration estimation in combustion gas flow field. A thorough understanding of ‘fit’ of the models (described in Section 2.3) with the acquired spectra at higher temperatures is important, as it lowers the accuracy levels of the species concentrations.

The temperature dependency of line-strength of a transition is given by Eq. (3):

$$S(T) = S(T_0) \frac{Q(T_0)T_0}{Q(T)T} \left[1 - \exp\left(\frac{hc\nu_0}{k_B T}\right) \right] \left[1 - \exp\left(\frac{hc\nu_0}{k_B T_0}\right) \right]^{-1} \exp\left[\frac{-hcE''}{k_B} \left(\frac{1}{T} - \frac{1}{T_0}\right)\right] \quad (3)$$

where k_B (Boltzman’s constant), c (speed of light), h (Plank’s constant) are the constant terms and ν_0 is the line-center frequency, E'' is the lower energy state and Q is the partition function. Eq. (3) is given in terms of reference temperature T_0 (296 K) [41, 53].

The accuracy of line-strength and absorbance depends on the accurate knowledge of high temperature partition function $Q(T)$ as shown in Eq. (3). HITEMP database [30] has been developed (based on direct numerical diagonalization, wave function and electric dipole-moment function calculations) to estimate the line-strengths of five species H_2O , CO_2 , CO , NO and OH . A summary of absorbances of H_2O , CO , NO and NO_2 at elevated temperatures are given in **Table 3**.

The condition at 900 K is the typical case one would likely get in a combustion environment. The absorbances for H_2O , CO and NO has been estimated using HITEMP 2010 and *Spectraplot* tool [30, 41]. Absorbance for NO_2 has been estimated using HITRAN 2012 and *Spectraplot* [41, 55]. An experimental determination of broadening parameters γ_0 and temperature-dependent exponent, n , for NO_2 - N_2 and NO_2 - Ar has been discussed in detail in Ref. [54]. The broadening coefficients and the temperature dependent exponent for NO_2 depends on the species it collides with. In the case of the collision partner, lighter the molecule larger the optical collision diameter and *vice-versa*. The wavenumbers were selected based on the availability of lasers and detectors from different suppliers.

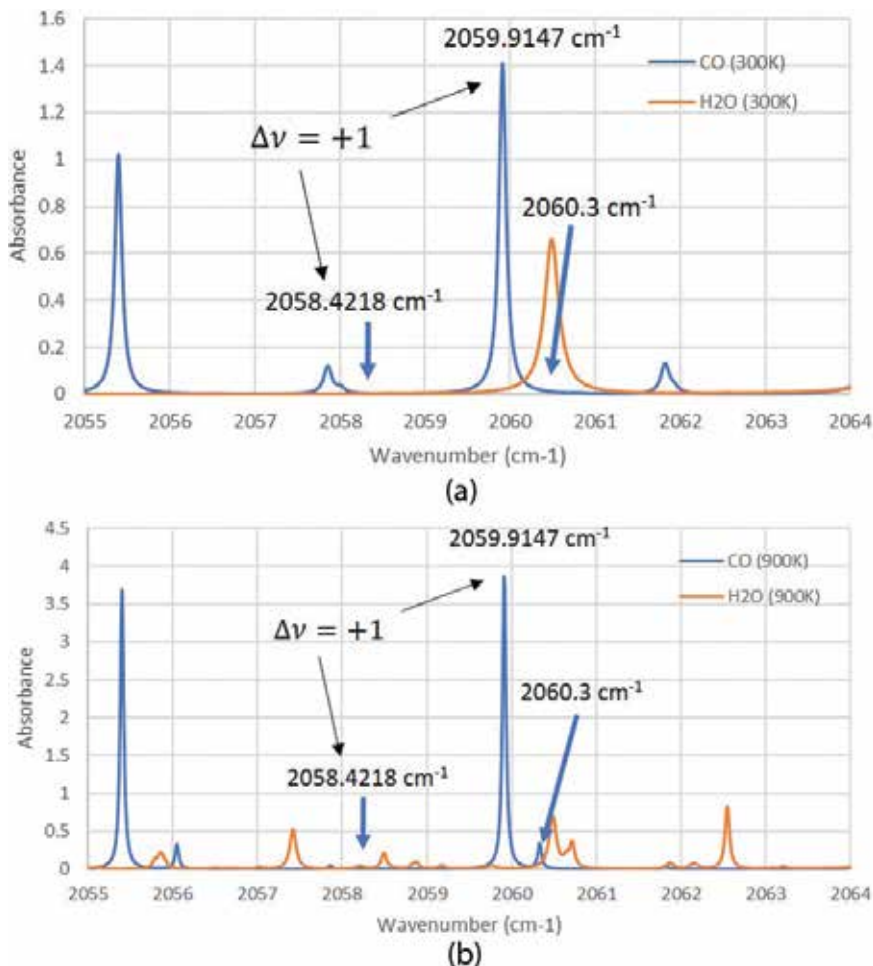
A HITRAN simulation of CO line at two different temperatures (300 and 900 K) for 2059.91 cm^{-1} ($E'' = 806.4\text{ cm}^{-1}$) line using *Spectraplot* tool is given in **Figure 4**.

From **Figure 5**, we can see that at 300 K, the CO transition lines at 2058.4 cm^{-1} (corresponding to $\Delta\nu = +1$) and 2060.3 cm^{-1} are not at all visible [56]. There is a single well-defined water transition at 2060.5 cm^{-1} . The leading edge of the water line overlaps with the trailing edge of the CO line. At 900 K, the line-width of the CO line decrease with an increased absorbance with an appearance of a smaller and well-resolved transition at 2060.3 cm^{-1} ($E'' = 2543.1\text{ cm}^{-1}$). The similar effect is also seen for the water transition line at 2060.5 cm^{-1} .

Gas species	Frequency (cm ⁻¹)	Line strength (cm ⁻² /Atm)	Absorbance			References
			300 K	600 K	900 K	
H ₂ O	2060.48	8.272 × 10 ⁻⁴	0.65	0.94	0.7	HITEMP 2010, SpectraPlot [30, 41]
CO	2013.35	1.118 × 10 ⁻⁵	0.02	0.62	1.20	
	2059.91	8.753 × 10 ⁻⁴	1.4	3.6	3.7	
NO	1927.27	1.183 × 10 ⁻⁴	1.0	1.3	1.0	
	1929.03	1.828 × 10 ⁻⁴	1.6	1.7	1.2	
NO ₂	1599.01	2.324 × 10 ⁻³	16	6	2.3	HITRAN 2012, SpectraPlot [29, 41, 54, 55]
	1599.91	2.802 × 10 ⁻³	15	5	1.8	
	1600.08	1.014 × 10 ⁻⁵	2	0.77		

Table 3.

Variation of absorbance at different temperatures with conditions as mole-fractions ($x_{\text{Gas}} = 0.001$, $x_{\text{H}_2\text{O}} = 0.08$), path-length (L) = 250 cm, pressure (P) = 1 atm, balance N_2 .


Figure 5.

(a) HITRAN simulation using Spectraplot tool of a CO and a water transition line at 300 K, (b) HITEMP simulation using Spectraplot tool of a CO and a water transition line at 900 K.

Considering the two transitions at 2059.91 and 2060.3 cm^{-1} , we can infer the gas temperature from the ratio of absorbances at both the transitions of CO. The ratio of absorbances is shown in Eq. (4):

$$\left(\frac{\alpha_{\nu_1}}{\alpha_{\nu_2}}\right) = \frac{S_A(T) \phi(\nu_1, T, P, x_{abs})}{S_B(T) \phi(\nu_2, T, P, x_{abs})} = R(T) \quad (4)$$

The temperature sensitivity is given by

$$\left|\frac{dR/R}{dT/T}\right| \approx \left(\frac{hc}{k_B}\right) \left|\frac{E''_{\nu_1} - E''_{\nu_2}}{T}\right| \quad (5)$$

The E''_{ν_1} and E''_{ν_2} are the lower energy states of the two transitions of the CO lines as indicated in **Figure 5(b)**. The sensitivity depends strongly on the difference in the lower energy states of the transitions. A detailed analysis on this is given in the Refs. [57, 58] by Spearrin et al. and Zhou et al. respectively.

2.5 Absorption spectroscopy: techniques

Two categories of laser-based absorption techniques are available for measurement of trace gas species concentration: direct absorption spectroscopy (DAS) and wavelength modulation spectroscopy (WMS). These techniques are further subdivided into two categories based on fixed wavelength and scanned wavelength techniques. Though these techniques were initially developed for spectroscopy in the Near-IR spectral region, it has found widespread application in Mid-IR spectroscopy.

2.5.1 Direct absorption spectroscopy

In direct absorption spectroscopy, the laser wavelength is tuned such that it is resonant with the absorption transition of interest of the gas species. Fixed wavelength direct absorption spectroscopy is rarely used as it contains very limited spectral information and non-absorbing losses (scattering, vibrations, beam-steering) are negligible. In case of scanned-wavelength direct absorption spectroscopy (SW-DAS), the laser injection current is tuned to scan across an absorption transition of interest and the trace gas species properties are estimated using Eq. (2). In this case, the laser frequency tuning range is $\approx 0.1\text{--}10 \text{ cm}^{-1}$. *Hyperspectral direct-absorption spectroscopy* techniques exist for range greater than 10 cm^{-1} .

2.5.2 Wavelength modulation spectroscopy

In a complex gas mixture, like in case of combustion gas or in natural gas, one of the major challenge is to identify an absorption line of the trace gas species isolated from background gases. Also, at elevated temperature, the Boltzmann distribution results in redistribution of molecules among energy states thereby increasing the relative strength of absorption of the far wings of the fundamental bands. This increases the chances of overlap of the trace gas spectra with the background gases. To address this challenge, Wavelength Modulation Spectroscopy (WMS) technique of detection of trace gas has been developed to estimate the concentration in presence of complex background gas mixtures (e.g. CO₂, H₂O, Hydrocarbons).

Several literatures exist discussing the details of the WMS technique [42, 43, 53]. In brief, the harmonics (nf or n^{th} -derivative) of the wavelength modulation

provides several answers to the absorption spectra of the trace gas. The second-harmonic (WMS-2f) is used for trace gas species concentration estimation when the absorbance is quite low. In WMS-2f/1f technique, the WMS-2f signal is normalized with the 1f signal to minimize the non-absorption losses like, beam-steering, scattering, window fouling. This is particularly useful in using the laser-based technique for a robust trace gas species measurement in an industrial environment.

In fixed-WMS, the injection current modulation is used to modulate the laser's wavelength on an absorption transition of interest. Whereas, in case of scanned-WMS, the laser's wavelength modulation is accompanied by a minor amplitude wavelength scan to resolve the peak of the WMS-2f signal normalized with 1f.

Optimization of the modulation depth parameter (a_m) is a critical requirement for an enhanced signal-to-noise ratio (SNR) of the measurement system. The modulation depth parameter is defined in Eqs. (6), (7) as:

$$\nu(t) = \bar{\nu} + \nu_m(t) + \nu_s(t) \quad (6)$$

$$\nu(t) = \bar{\nu} + a_m \cos(2\pi f_m t + \varphi_m) + a_s(2\pi f_s t + \varphi_s) \quad (7)$$

In WMS model, the tuning frequency is a superposition of laser scanning and modulation terms around a mean optical frequency ($\bar{\nu}$). This is a combination of high-frequency modulation (f_m) and a low frequency scan (f_s). In the above equation, a_m (cm^{-1}) and a_s (cm^{-1}) are the modulation depth and scan depth respectively. φ_m and φ_s are the temporal phases of optical frequency tuning [54]. The 2f signal increases with increase in modulation depth and slowly starts to saturate [59]. The initial point of the saturation is considered as the optimal modulation depth for the measurement process. The optimal modulation depth varies with different trace gas species.

2.6 Absorption spectroscopy in Mid-IR

Wavelength modulation Spectroscopy scheme discussed above is widely used in Mid-IR region. The suitability and subsequent modification of the technique depends largely on the knowledge of spectral features of the target gas and its variations with local operating conditions. In Mid-IR region, the transitions of single gas species are sometimes severely convoluted. This requires characterizations of all the components of transition parameters for accurately modeling the profiles [54].

This becomes further complicated during the detection of trace gas in presence of strong spectral interference from species like water. In these cases, one also must consider the effect on sensitivity of the WMS-2f signal due to fluctuations in interference by the interfering species. An optimization method to be used in this case has been discussed in detail by Sur et al. in Ref. [54].

3. Measurement challenges in Mid-IR

For any measurement system, noise, repeatability and reproducibility plays an important role in determining three critical points: (1) factors influencing the measurement process, (2) whether measurement system variability is small compared to process variability and (3) the capability of measurement system to distinguish between parts (or *part-to-part* variation). "*Part-to-part*" variation in the present case will be variations in industrial processes. For any laser-based measurement system, noise and repeatability are the major contributors of measurement errors.

Reproducibility is the variability in measurement system due to differences in operators and cannot be considered in this case.

The availability of industrial grade QCLs for trace gas measurement has enabled sub-ppm and sub-ppb level measurement. The measurement error due to noise and repeatability play an extremely crucial role as we go down to the low concentration and high specificity measurement regime. Various factors like, $1/f$ -noise, pressure (P) and temperature (T) effects, etalon effect contribute to the measurement system noise. Wavelength stability of successive scans leads to short- and long-term drifts in measurement which is mostly a repeatability challenge with the system.

3.1 Noise

In Direct Absorption Spectroscopy (DAS) technique, the noise is usually dominated by $1/f$ -noise of the laser source. This limits the lowest detectable limit to a higher value. Development of high frequency modulation techniques, substantially reduced the $1/f$ -noise in the TDLAS technique. This was further improved by using Mid-IR spectral region for measurement purpose.

Figure 6 gives an overview of the noise regimes and the contributing factors in a laser-based technique.

As discussed above, the $1/f$ -noise is the primary contributor in Section 1, due to the laser source. In Section 2, the gas pressure and temperature are the major factors contributing the deviations from Voigt-only distribution fit (giving the distinct “W-shape” residuals for the best fit) [60].

The detection limit of a trace gas species is calculated as [61, 62],

$$\Delta x_{\text{species}} = \frac{\Delta V_{\text{residual}}}{V_{\text{Peak}}(\nu_0)} \quad (8)$$

In the above equation, $\Delta V_{\text{residual}}$ corresponds to the 3σ of the fit residual and $V_{\text{Peak}}(\nu_0)$ corresponds to the peak absorption of the Voigt distribution fit at ν_0 . This can be further reduced by averaging over N samples as [63]:

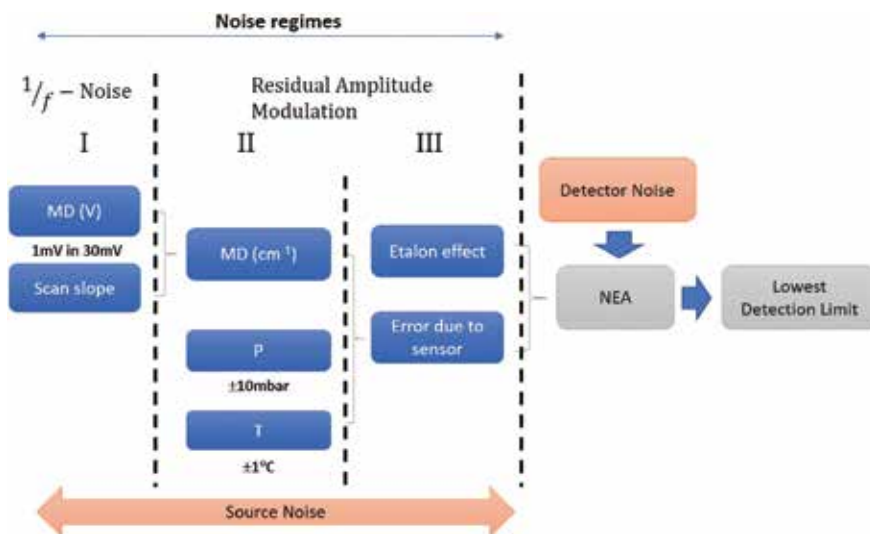


Figure 6. Noise regimes at various sections of the measurement system and the contributing factors to the overall error budget.

$$\langle \Delta V_{residual} \rangle = \frac{1}{N} \sqrt{(\Delta V_{residual})^2} \quad (9)$$

$$\langle \Delta x_{species} \rangle = \frac{\langle \Delta V_{residual} \rangle}{V_{Peak}(V_0)} \quad (10)$$

Another important contributor of the noise are the Etalon fringes due to non-uniform transmission through optical windows, lens [64]. This appear as oscillations in $2f$ signals. The transmittance of laser through two windows with the distance between the windows as L is given by:

$$T = 1 - R = \frac{1}{1 + F \sin^2\left(\frac{\delta}{2}\right)} \quad (11)$$

Where F is the coefficient of finesse, given as, $F = \frac{4R}{(1-R)^2}$ and $\delta = \frac{2\pi}{\lambda} nL \cos \theta$. Here R is the reflectance of the optical components. For Mid-IR applications, ZnSe windows are usually used which has $T = 0.7$ for 2.0–14 μm region.

The Normalized Noise Equivalent Absorbance (NNEA) is calculated using Eq. (12):

$$NNEA = \alpha_{min} P \sqrt{t} \quad (12)$$

In the above equation α_{min} is the noise equivalent absorption coefficient (cm^{-1}), P is the incident optical power (W) and t is the measured time (s).

A summary of optical techniques and their normalized noise equivalent absorbance is given in **Table 4**.

3.2 Repeatability and Allan variance

Another important source of measurement error in spectroscopic systems is the repeatability of the measurement process. In trace level measurement, integration

Measurement technique	NNEA ($\text{Wcm}^{-1} \text{Hz}^{-1/2}$)	Spectral region (cm^{-1})	Ref.
Open path tunable diode laser absorption spectroscopy	6.32×10^{-8}	3778–3780	[65]
	6×10^{-9} – 8.419×10^{-11}	1246–1250	[66]
	2.0×10^{-13}	9397–9399	[67]
Cavity ring down spectroscopy	4.25×10^{-14}	6135–6369	[68]
	3.0×10^{-16}	6350–6380	[69]
	2.0×10^{-15}	6472–6693	[70]
Cavity enhanced spectroscopy	6.0×10^{-14}	6490–6555	[71]
	2.2×10^{-9}	6525–6529	[72]
Tunable diode laser photo-acoustic spectroscopy	5.19×10^{-10}	4038.8–4039	[73]
	1.2×10^{-7}	2310–2313	[74]
	3.2×10^{-10}	2310–2313	[75]

NNEA: normalized noise equivalent absorbance.

Table 4. Summary of optical techniques for trace gas concentration measurement using laser absorption in both near IR and Mid-IR spectral region and its normalized noise equivalent absorbance.

time of the measurement or time-binning is an important parameter that helps us to study the repeatability of the system when laser frequency stability is a factor (not the systematic errors). The bandwidth of the measurement system becomes critical when one tries to measure multiple trace gases in a single measurement system.

Allan variance is defined as [76]:

$$\sigma_y^2(\tau) = \frac{1}{2\tau^2} \langle (\Delta^2 x)^2 \rangle = \frac{1}{2} \langle (\Delta y)^2 \rangle \quad (13)$$

and the deviation is given as

$$\sigma_y(\tau) = \sqrt{\sigma_y^2(\tau)} \quad (14)$$

A good discussion on using of Allan deviation for calibration of laser absorption spectrometer using QCLs is given in Ref. [77] by Smith et al. Optimization of sampling rates plays a major role in enabling high sensitivity measurement of QCL-based laser absorption spectrometers.

4. Enablers for industrial application

Some of the challenges of using Quantum Cascade Lasers for industrial applications have already been highlighted in previous sections in a different context. Few those challenges along with some new ones will be discussed here to avoid the desultoriness.

4.1 Window materials

Some of the common window materials used for Mid-IR applications are Sapphire, Calcium Fluoride (CaF_2), Barium Fluoride (BaF_2), Magnesium Fluoride (MgF_2) and Zinc Selenide (ZnSe). The transmittance from un-coated wedged windows (wedge angle: 30 ± 10 arcmin) is shown in **Figure 7**.

Though CaF_2 and BaF_2 can transmit over a broad wavelength range (around 10–14 μm), it is not suitable for combustion or high temperature applications in

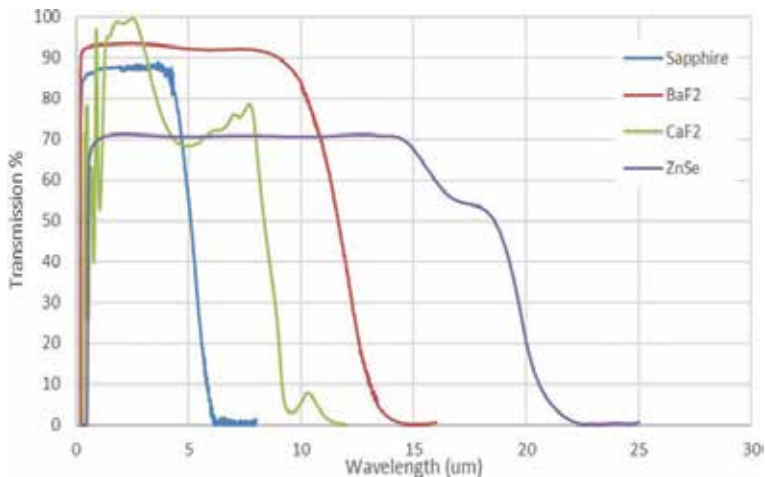


Figure 7. Transmission % from wedged windows of Sapphire, CaF_2 , BaF_2 and ZnSe with wavelength (μm). Data Source: Thorlabs catalog for optical windows [78].

presence of moisture. These materials are extremely hygroscopic and degrade in presence of moisture. Due to their large thermal expansion coefficients they are not suitable for combustion applications. ZnSe has much broader transmittance and has lower thermal expansion than the fluoride crystals. Sapphire is the most suitable material for high temperature and high-pressure combustion applications but it has a lower transmittance window compared to the Fluoride crystals and ZnSe (upto 4.0 μm). Careful selection of windows is required keeping in cognizant the following parameters: application conditions (temperature, pressure), gas species, etalon effects. A summary of the properties for the window materials is given in **Table 5**.

4.2 Optical fibers

It is always desirable in an industrial application to isolate the lasers from the operating environment to protect the lasers. Several types of fiber cables exist for delivery of Mid-IR laser beams. A summary of optical fibers available for Mid-IR range is given in **Table 6**.

The wavelength range covered by hollow core waveguides is widest among all the fibers available for Mid-IR laser beam transmission.

Window material	Refractive index range	Wavelength range (μm)	Thermal expansion coeff. ($^{\circ}\text{C}$)	Melting point ($^{\circ}\text{C}$)
SAPPHIRE	1.9–1.62	0.2–5.0	5.3×10^{-6}	1800
Calcium fluoride	1.58–1.3	0.2–10	18.85×10^{-6}	1418
Barium fluoride	1.65–1.3	0.2–15	18.4×10^{-6}	1368
Magnesium fluoride	1.43–1.3	0.2–6.7	13.7×10^{-6}	1255
Zinc selenide	2.75–2.35	0.5–16	7.1×10^{-6}	1520

Data Source: Thorlabs catalog for optical windows [78].

Table 5. Summary of optical and thermal properties of some common window materials used for Mid-IR applications.

Fiber type	Attenuation (dB/m)	Core diameter (μm)	Wavelength range (μm)	Ref
Zirconium (IV) fluoride	0.20	100, 200, 400	1.5–3.7	[79]
Zirconium (iv) fluoride	0.25	600	2.0–3.5	[79]
Indium (iii) fluoride	0.45	100	1.0–4.5	[79]
Hollow core waveguides	0.10	700	3.0–14	[17]
Hollow core waveguides	<1.0	300	7.6–11	[15]
Chalcogenide (as-s type)	0.12 (0.6)	100	2–3.5 (4.0)	[80]
Chalcogenide (As-se type)	0.2 (0.5)	100	2–8 (4.5)	[80]

Table 6. Mid-IR optical fibers with core diameters, attenuation and wavelength range.

4.3 Alignment of optics

For all practical applications, the laser beams need to remain in continuous alignment with the detector during all operational conditions. As discussed in Section 2.4, $1f$ -normalization of WMS- $2f$ is used to reject the background emissions (beam-steering, transmission losses due to dust particle scattering, window fouling) that vary much slowly with respect to $1f$. But for coarse alignment of the beam (due to thermal misalignment, etc.) one needs to use a different technique for automatic misalignment correction. In this case, a 633 nm laser is multiplexed with the Mid-IR lasers and transmitted through the gas flow path. The transmitted beam is demultiplexed and a quadrant photodetector is used as the position sensitive detector. The technique has been discussed in detail in Ref. [81] by Mitra et al.

4.4 Multi-wavelength detection

Simultaneous detection of multiple gases in combustion process is an unique challenge for a spectroscopy-based measurement. For example, one needs to measure NO, NO₂, CO, O₂ and H₂O simultaneously in the combustion gas mixture. This implies multiplexing of Mid-IR and Near-IR wavelengths for measurement. The demultiplexing process involves using CaF₂ (1–6 μm) or ZnSe (1–12 μm/7–14 μm) beam splitters to separate the Mid-IR and Near-IR beams [82].

Sequencing the laser operation and the detection is the key factor for the optimizing the sensor performance when we have multiple source and single detector. Mukherjee et al. [83] discussed about using scanning galvanometer to switch between the lasers (in <1 s) for multispecies trace gas detection. Time-division multiplexing (TDM) method has been reported by Dong et al. [84] where a stepper motor coupled to detectors were used for measurement of multiple gases.

For process control applications, the measurement time is usually between 1–10s. As highlighted in Section 3.2, optimization of integration time is required for each species to minimize the noise and drifts while carrying out all the measurements within the time window required for process control applications. A hybrid approach of wavelength and frequency multiplexing needs to be developed in accordance to the process requirement.

4.5 Calibration-free measurement

For all on-site measurements, periodic calibration of the measurement process is required for accurate estimation of concentration. Usually, a certified standard gas mixture in fiber-coupled gas cell is used for the calibration purpose [85]. A detailed calibration process steps have been discussed by Werle et al. in Ref. [86]. The “Zero” reading of the sensor is established using Nitrogen, Synthetic Air or local clean ambient air. Pre-mixed calibration gases of various concentrations are used for sensor “span” calibration. The “dynamic” calibration is finally carried out using a known test gas with the full sensor system in operational condition.

Presently most of the commercially available TDL-based sensors contains fiber coupled gas cells of high concentrations (also known as reference cell) of the target gas. A part of the laser beam is transmitted through the cell and used for line-locking of the transmitted beam. In this technique, a prudent selection of spectral region is required which is isolated from any neighboring transitions. Though in Mid-IR spectroscopy there is a good chance of locating these transitions, the implementation is quite challenging in applications which require trace level measurement in complex gas mixtures.

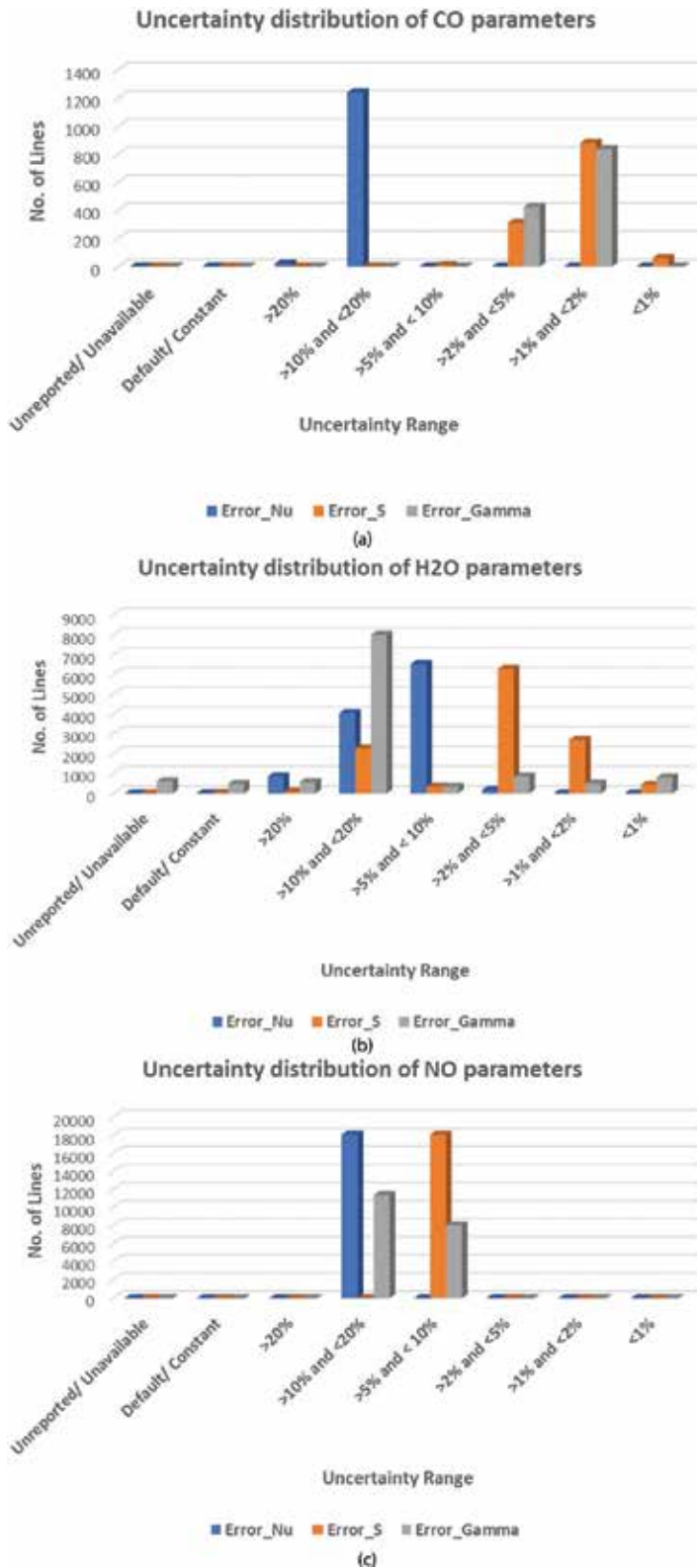


Figure 8. Uncertainty distribution of ν_0 , S and γ_{air} for (a) CO ($1900\text{--}2300\text{ cm}^{-1}$), (b) H₂O ($1500\text{--}2300\text{ cm}^{-1}$) and (c) NO ($1600\text{--}2200\text{ cm}^{-1}$).

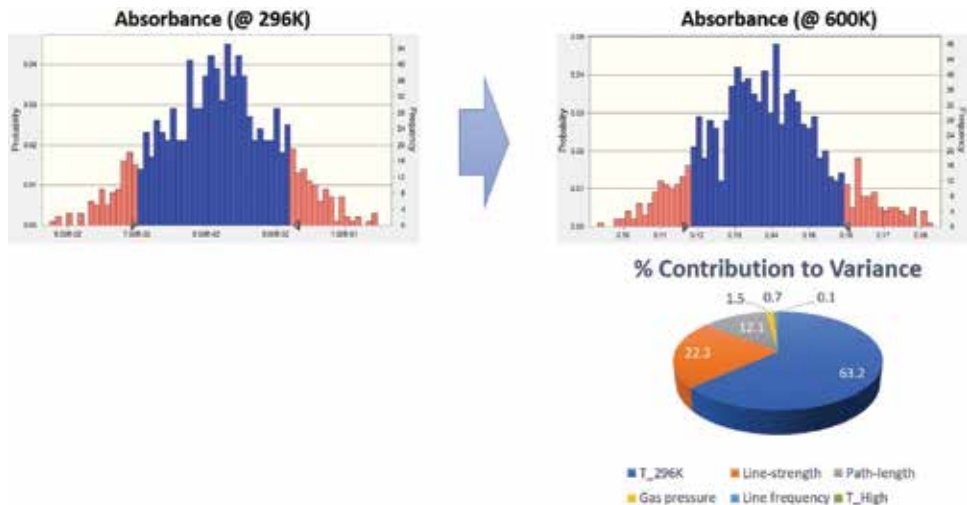


Figure 9. Monte-Carlo simulation of absorbance at 296 and 600 K with percentage contribution to variance.

There are broadly two versions of “Calibration-free” WMS technique reported in literatures. The first version discusses about using residual amplitude modulation (RAM) from the $1f$ signal for normalizing the incident laser intensity [87–89]. Like above, in this case too, the spectral region of interest should be well isolated from neighboring transitions. This limits the application in high gas pressure regime as the line broadening might blend the neighboring transitions. In addition to this, incident laser intensity fluctuations due to high vibrations, window fouling, beam steering are some of the major challenges for implementations of this technique.

In the second version of the “calibration free” technique, the WMS- $2f/1f$ signal obtained from actual measurement is compared against a model WMS- $2f/1f$ signal developed using laser tuning parameters and transition parameters used in the absorption feature under probe. The model is continuously updated based on the process parameters (T, P and gas concentration). A detailed explanation of the technique has been discussed by Rieker et al. and Sun et al. in Refs. [90, 91]. The same approach can be used for QCL-based measurements.

One of the major challenge with above method is the uncertainties with HITRAN spectral line parameters. **Figure 8** shows the uncertainty distributions for CO, NO and H₂O spectral parameters in the Mid-IR region [92].

It becomes a key to understand the impact of these uncertainties of the line parameters on absorbance and concentration estimation when measuring trace gas levels. Using the above details, a Monte-Carlo simulation was carried out to check the percentage contribution to variance at 600 K (**Figure 9**).

Figure 9 shows that in general the absorbance distribution (with 80% confidence interval) remains Gaussian at both 296 and 600 K temperatures. The major contribution for variance is due to variations from errors in measurement of temperature 296 K (63%) and uncertainties in line-strength (22%).

5. Conclusions

Since its discovery in 1994 by Capasso et al. [93], Quantum Cascade Lasers has come of age from being a laboratory tool to industrial application. It has opened the Mid-IR spectral region for industrial usage. Maturation of near-IR TDLAS

techniques over last 20 years and its applications using QCLs have opened a new vista for trace gas sensing for efficiency of combustion processes, environmental sensing for leak detection, emission and air quality monitoring. It also enabled explosives, chemicals and bio-hazard detection for law enforcement and defense agencies.

5.1 Takeaways

Availability of Mid-IR spectral region and improvements in WMS measurement scheme has enabled our ability to measure, CO, CO₂, NO, NO₂ accurately. Availability of High Heat Load (HHL) packages for QCLs, HCWs and robust detectors with multi-stage cooling, auto-alignment and calibration-free techniques has led to the application of QCLs in combustion process monitoring and controls.

5.2 Opportunities

Two broad categories of challenges remain to be addressed by Mid-IR spectroscopy.

First, the accuracy of spectroscopy databases in Mid-IR spectral region needs to be improved for high temperature applications. Only five species are covered in HITEMP (H₂O, CO, CO₂, NO, OH). High temperature parameters are based on quantum mechanical computations with uncertainties ranging from 5–20% and that limits the sensitivity of the measurement. Accurate HITEMP database is required for other combustion gases like NO₂, SO₂ and hydrocarbons.


Second, a major drawback with the Mid-IR fibers (HCWs) is their bending loss [17]. Also, the length of the HCWs available is not more than 1 m without significant transmission loss (<1 dB/m). For true remote application we need to have fibers >10 m. The Mid-IR lasers with improved performance and stability without additional cooling mechanisms are required for a robust sensor system.

Author details

Chayan Mitra
Environment Control Systems, Steam Power Systems, GE Power India Ltd.,
Noida, India

*Address all correspondence to: chayanmitra@yahoo.com

IntechOpen

© 2018 The Author(s). Licensee IntechOpen. This chapter is distributed under the terms of the Creative Commons Attribution License (<http://creativecommons.org/licenses/by/3.0>), which permits unrestricted use, distribution, and reproduction in any medium, provided the original work is properly cited. 

References

- [1] Purgert B, Shingledecker J. Update on U.S. DOE/OCDO advanced ultrasupercritical (A-USC) steam boiler and turbine consortium. EPRI, DOE-FE Cross-Cutting Review Meeting; 2015
- [2] GE Power. Powering the Future with Gas Power Systems: Offering 2018. USA: GEPower Offering; 2018
- [3] Wang J, Maiorov M, Baer DS, Garbuzov DZ, Connolly JC, Hanson RK. In-situ combustion measurements of CO with diode-laser absorption near 2.3 μm . *Applied Optics*. 2000;**39**(30): 5579-5589. DOI: 10.1364/AO.39.005579
- [4] Gmachl C, Capasso F, Sivco DL, Cho AY. Recent progress in quantum cascade lasers and applications. *Reports on Progress in Physics*. 2001;**64**(11):1533. DOI: 10.1088/0034-4885/64/11/204
- [5] Curl RF, Capasso F, Gmachl C, Kosterev AA, McManus B, Lewicki R, et al. Quantum cascade lasers in chemical physics. *Chemical Physics Letters*. 2010;**487**:1-18. DOI: 10.1016/j.cplett.2009.12.073
- [6] Wysocki G, Curl RF, Tittel FK, Maulini R, Bulliard JM, Faist J. Widely tunable mode-hop free external cavity quantum cascade laser for high resolution spectroscopic applications. *Applied Physics B*. 2005;**81**(6):769-777. DOI: 10.1007/s00340-005-1965-4
- [7] Meng B, Wang QJ. Broadly tunable single-mode mid-infrared quantum cascade lasers. *Journal of Optics*. 2015; **17**(2):023001. DOI: 10.1088/2040-8978/17/2/023001
- [8] Kosterev A, Wysocki G, Bakhirkin Y, So S, Lewicki R, Fraser M, et al. Application of quantum cascade lasers to trace gas analysis. *Applied Physics B: Lasers and Optics*. 2008;**90**:165-176. DOI: 10.1007/s00340-007-2846-9
- [9] Bismuto A, Blaser S, Terazzi R, Gresch T, Muller A. High performance, low dissipation quantum cascade lasers across the mid-IR range. *Optics Express*. 2015;**23**(5):5477-5484. DOI: 10.1364/OE.23.005477
- [10] VIGO Systems S.A. Catalogue; 2017
- [11] Piotrowski A, Piotrowski J, Gawron W, Pawluczyk J, Pedzinska M. Extension of usable spectral range of Peltier cooled photodetectors. *Acta Physica Polonica A*. 2009;**116**:S-52, S-55
- [12] Norton P. HgCdTe infrared detectors. *Opto-Electronics Review*. 2002;**10**(3):159-174
- [13] Krishnaswami K, Qiao H, Bernacki BE, Anheier N. Characterization of single-mode chalcogenide optical fiber for mid-infrared applications. *Proceedings of SPIE*. 2009;**7325**:73250Z. DOI: 10.1117/12.818184
- [14] Tao G, Abouraddy A. Advances in infrared fibers. *Proceedings of SPIE*. 2015;**9485**:94850K. DOI: 10.1117/12.2176403
- [15] Patimisco P, Sampaolo A, Mihai L, Giglio M, Kriesel J, Sporea D, et al. Low-loss coupling of quantum cascade lasers into hollow-core waveguides with single mode output in the 3.7–7.6 μm spectral range. *Sensors*. 2016;**16**(533):1-11. DOI: 10.3390/s16040533
- [16] Sampaolo A, Patimisco P, Kriesel JM, Tittel FK, Scamarcio G, Spagnolo V. Single mode operation with mid-IR hollow fibers in the range 5.1-10.5 μm . *Optics Express*. 2015;**23**(1):195-204. DOI: 10.1364/OE.23.000195
- [17] Kriesel JM, Gat N, Bernacki BE, Erikson RL, Cannon BD, Myers TL, et al. Hollow Core Fiber optics for mid-wave and long-wave infrared

- spectroscopy. Proceedings of SPIE. 2011; 8018-8031. DOI: 10.1117/12.882840
- [18] Kriesel J, Gat N, Bernacki B, Myers T, Bledt C, Harrington J. Fiber Delivery of Mid-IR lasers. SPIE Newsroom (Defense & Security); 2011. DOI: 10.1117/2.1201108.003794
- [19] Harrington JA, Bledt CM, Kriesel JM. Hollow waveguides for the transmission of quantum cascade laser (QCL) energy for spectroscopic applications. Proceedings of SPIE. 2011; **7894**:789414. DOI: 10.1117/12.881548
- [20] Patimisco P, Spagnolo V, Vitiello MS, Tredicucci A, Scamarcio G, Bledt CM, et al. Coupling external cavity mid-IR quantum cascade lasers with low loss hollow metallic/dielectric waveguides. Applied Physics B. 2012; **108**(2):255-260. DOI: 10.1007/s00340-012-4891-2
- [21] Tittel FK, Richter D, Fried A. Mid-infrared laser applications in spectroscopy. Topics in Applied Physics: Solid State Mid-Infrared Laser Sources. 2003;**89**:445-516. DOI: 10.1007/3-540-36491-9
- [22] THORLABS. Reflective Optical Beam Expander. Product Catalogue
- [23] Sergechev I, Maulini R, Bismuto A, Blaser S, Gresch T, Bidaux Y, et al. All-electrical frequency noise reduction and linewidth narrowing in quantum cascade lasers. Optics Letters. 2014; **39**(22):6411-6414. DOI: 10.1364/OL.39.006411
- [24] Gurell K, Schilt S, Bismuto A, Bidaux Y, Tardy C, Blaser S, Gresch T, Sudmeyer T. Characterization of a new frequency tuning and modulation mechanism for spectroscopy in a quantum cascade laser. OSA Technical Digest: CLEO. 2016; Applications of Semiconductor Lasers: Ath1J.2. DOI: 10.1364/CLEO_AT.2016.ATH1J.2
- [25] Gürell K, Schilt S, Bismuto A, Bidaux Y, Tardy C, Blaser S, et al. Frequency tuning and modulation of a quantum cascade laser with an integrated resistive heater. Photonics. 2016;**3**(3):47-59. DOI: 10.3390/photonics3030047
- [26] Nanoplus Nanosystems and Technologies GmbH. 5265.0nm DFB Laser. Product Specification; 2017
- [27] Bidaux Y, Bismuto A, Tardy C, Terazzi R, Gresch T, Blaser S, et al. Extended and quasi-continuous tuning of quantum cascade lasers using superstructure gratings and integrated heaters. Applied Physics Letters. 2015; **107**(22):221108. DOI: 10.1063/1.4936931
- [28] Wavelength Electronics. QCL OEM Series QC Laser Driver. Product Datasheet and Operating Guide; 2016. pp. 1-23
- [29] Gordon IE, Rothman LS, Hill C, Kochanov RV, Tan Y, Bernath PF, et al. The HITRAN 2016 molecular spectroscopic database. Journal of Quantitative Spectroscopy and Radiative Transfer. 2017;**203**:3-69. DOI: 10.1016/j.jqsrt.2017.06.038
- [30] Rothman LS, Gordon IE, Barber RJ, Dothe H, Gamache RR, Goldman A, et al. HITEMP, the high temperature molecular spectroscopic database. Journal of Quantitative Spectroscopy and Radiative Transfer. 2010;**111**: 2139-2150. DOI: 10.1016/j.jqsrt.2010.05.001
- [31] Jacquinet-Husson N, Armante R, Scott NA, Chedin A, Crepeau L, Boutammine C, et al. The 2015 edition of the GEISA spectroscopic database. Journal of Molecular Spectroscopy. 2016;**327**:31-72. DOI: 10.1016/j.jms.2016.06.007
- [32] Sharpe SW, Johnson TJ, Sams RL, Chu PM, Rhoderick GC, Johnson PA. Gas-phase databases for quantitative

- infrared spectroscopy. *Applied Spectroscopy*. 2004;**58**(12):1452-1461. DOI: 10.1366/0003702042641281
- [33] Brown LR, Gunson MR, Toth RA, Irion FW, Rinsland CP, Goldman A. 1995 atmospheric trace molecule spectroscopy (ATMOS) linelist. *Applied Optics*. 1996;**35**(16):2828-2848. DOI: 10.1364/AO.35.002828
- [34] Chu PM, Guenther FR, Rhoderick GC, Lafferty WJ. The NIST quantitative infrared database. *Journal of Research of the National Institute of Standards and Technology*. 1999;**104**(1):59-81. DOI: 10.6028/jres.104.004
- [35] Barber RJ, Tennyson J, Harris GJ, Tolchenov RN. A high-accuracy computed water line list. *Monthly Notices of the Royal Astronomical Society*. 2006;**368**(3):1087-1094. DOI: 10.1111/j.1365-2966.2006.10184.x
- [36] Tashkun SA, Perevalov VI. CDS-4000: High-resolution, high-temperature carbon dioxide spectroscopic databank. *Journal of Quantitative Spectroscopy and Radiative Transfer*. 2011;**112**(9):1403-1410. DOI: 10.1016/j.jqsrt.2011.03.005
- [37] Tennyson J, Bernath PF, Brown LR, Campargue A, Csaszar AG, Daumont L, et al. IUPAC critical evaluation of the rotational-vibrational spectra of water vapor, part III: Energy levels and transition wavenumbers for H₂(16)O. *Journal of Quantitative Spectroscopy and Radiative Transfer*. 2013;**117**:29-58. DOI: 10.1016/j.jqsrt.2012.10.002
- [38] Rothman LS, Gamache RR, Tipping RH, Rinsland CP, Smith MAH, Chris Benner D. The HITRAN molecular database: Editions of 1991 and 1992. *Journal of Quantitative Spectroscopy and Radiation Transfer*. 1992;**48**(5-6):469-507. DOI: 10.1016/0022-4073(92)90115-K
- [39] Rothman LS, Rinsland CP, Goldman A, Massie ST, Edwards DP, Flaud J-M. The HITRAN molecular spectroscopic database and HAWKS (HITRAN atmospheric workstation): 1996 edition. *Journal of Quantitative Spectroscopy and Radiative Transfer*. 1998;**60**(5):665-710. DOI: 10.1016/S0022-4073(98)00078-8
- [40] Goldman A, Brown LR, Schoenfeld WG, Spencer MN, Chackerian C Jr, Giver LP, et al. Nitric oxide line parameters: Review of 1996 HITRAN update and new results. *Journal of Quantitative Spectroscopy and Radiative Transfer*. 1998;**60**(5):825-838. DOI: 10.1016/S0022-4073(98)00085-5
- [41] Goldenstein CS, Miller VA, Spearrin RM, Strand CL. Spectra Plot.com: Integrated spectroscopic modeling of atomic and molecular gases. *Journal of Quantitative Spectroscopy & Radiative Transfer*. 2017;**200**:249-257. DOI: 10.1016/j.jqsrt.2017.06.007
- [42] Mitchell Spearrin R. Mid-infrared laser absorption spectroscopy for carbon oxides in harsh environments. Doctoral Thesis. Stanford University; 2014
- [43] Sur R. Development of robust TDLAS sensors for combustion products at high pressure and temperature in energy systems. Doctoral Thesis. Stanford University; 2014
- [44] Hanson RK, Spearrin RM, Goldenstein CS. *Spectroscopy and Optical Diagnostics for Gases*. 1st ed. USA: Springer; 2016. DOI: 10.1007/978-3-319-23252-2
- [45] Stancik AL, Brauns EB. A simple asymmetric lineshape for fitting infrared absorption spectra. *Vibrational Spectroscopy*. 2008;**47**(1):66-69. DOI: 10.1016/j.vibspec.2008.02.009
- [46] Belfhal A. The shape of spectral lines: Widths and equivalent widths of the Voigt profile. *Optic*

- Communication. 2000;**177**(1-6): 111-118. DOI: 10.1016/S0030-4018(00)00564-2
- [47] Tennyson J, Bernath PF, Campargue A, Csaszar AG, Daumont L, Gamache RR, et al. Recommended isolated-line profile for representing high-resolution spectroscopic transitions (IUPAC technical report). *Pure and Applied Chemistry*. 2014;**86**(12):1931-1943. DOI: 10.1515/pac-2014-0208
- [48] Vandeginste BGM, De Galan L. Critical evaluation of curve fitting in infrared spectrometry. *Analytical Chemistry*. 1975;**47**(13):2124-2132. DOI: 10.1021/ac60363a029
- [49] Draper NR, Smith H. *Applied Regression Analysis*. 3rd ed. John Wiley & Sons, Inc; 2014. 736 p. DOI: 10.1002/9781118625590
- [50] Birk M, Wagner G. Voigt profile introduces optical Stre depth dependent systematic errors – Detected in high resolution laboratory spectra of water. *Journal of Quantitative Spectroscopy and Radiative Transfer*. 2016;**170**: 159-168. DOI: 10.1016/j.jqsrt.2015.11.008
- [51] Claveau C, Henry A, Hurtmans D, Valentin A. Narrowing and broadening parameters of H₂O lines perturbed by he, ne, Ar, Kr and nitrogen in the spectral range 1850-2140cm⁻¹. *Journal of Quantitative Spectroscopy and Radiative Transfer*. 2001;**68**(3):273-298. DOI: 10.1016/S0022-4073(00)00025-X
- [52] Varghese PL, Hanson RK. Collisional narrowing effects on spectral line shapes measured at high resolution. *Applied Optics*. 1984;**23**(14):2376-2385. DOI: 10.1364/AO.23.002376
- [53] Schultz I. Practical applications of laser absorption spectroscopy for aeroengine testing. Doctoral Thesis. Stanford University; 2014
- [54] Sur R, Peng WY, Strand C, Spearrin RM, Jefferies JB, Hanson RK, et al. Mid-infrared laser absorption spectroscopy of NO₂ at elevated temperatures. *Journal of Quantitative Spectroscopy and Radiative Transfer*. 2017;**187**: 364-374. DOI: 10.1016/j.jqsrt.2016.10.016
- [55] Rothman LS, Gordon IE, Babikov Y, Barbe A, Chris Benner D, Bernath PF, et al. The HITRAN 2012 molecular spectroscopic database. *Journal of Quantitative Spectroscopy and Radiative Transfer*. 2013;**130**:4-50. DOI: 10.1016/j.jqsrt.2013.07.002
- [56] Goorvitch D. Infrared CO line list for the X1 sigma (+) state. *The Astrophysical Journal Supplement Series*. 1994;**95**(2):535-552. DOI: 10.1086/192110
- [57] Spearrin RM, Ren W, Jeffries JB, Hanson RK. Multi-band infrared CO₂ absorption sensor for sensitive temperature and species measurements in high-temperature gases. *Applied Physics B*. 2014;**116**(4):855-865. DOI: 10.1007/s00340-014-5772-7
- [58] Zhou X, Liu X, Jeffries JB, Hanson RK. Development of a sensor for temperature and water concentration in combustion gases using a single tunable diode laser. *Measurement Science and Technology*. 2003;**14**(8):1459-1468. DOI: 10.1088/0957-0233/14/8/335
- [59] Sharma R, Mitra C, Tilak V. Diode laser-based trace detection of hydrogen-sulfide at 2646.3 nm and hydrocarbon spectral interference effects. *Optical Engineering*. 2016;**55**(3):037106-1-037106-6. DOI: 10.1117/1.OE.55.3.037106
- [60] Truong G-W, Anstie JD, May EF, Stace TM, Luiten AN. Accurate lineshape spectroscopy and the Boltzman constant. *Nature Communications*. 2015;**6**(8345):1-6. DOI: 10.1038/ncomms9345

- [61] Telle HH, Urena AG. *Laser Spectroscopy and Laser Imaging - an Introduction*. 1st ed. USA: CRC Press (Taylor & Francis Group); 2018
- [62] Sharma R, Mitra C, Maity S, Tilak V, Liu X, Kowal A, Tao C. System and Method for Measuring Concentration of a Trace Gas in a Gas Mixture. United States Patent Application Publication. 2017; US 2017/0003218 A1
- [63] Nagapriya KS, Sinha S, Prashanth R, Poonacha S, Chaudhry G, Bhattacharya A, et al. Laser calorimetry spectroscopy for ppm-level dissolved gas detection and analysis. *Scientific Reports*. 2017;7: 42917. DOI: 10.1038/srep42917
- [64] Cao J-n, Wang Z, Zhang K-k, Yang R, Wang Y. Etalon effects analysis in tunable diode laser absorption spectroscopy gas concentration detection system based on wavelength modulation spectroscopy. In: 2010 Symposium on Photonics and Optoelectronics (SOPO 2010) Proceedings; 19-21 June 2010; Chengdu, China. IEEE; 2010. DOI: 10.1109/SOPO.2010.5504036
- [65] Frish MB. Current and emerging laser sensors for greenhouse gas detection and monitoring. *Spectroscopy*. 2014;29(7)
- [66] Moser H, Polz W, Waclawek JP, Ofner J, Lendl B. Implementation of a quantum cascade laser-based gas sensor prototype for sub-ppmv H₂S measurements in a petrochemical process gas stream. *Analytical and Bioanalytical Chemistry*. 2017;409(3): 729-739. DOI: 10.1007/s00216-016-9923-z
- [67] Spence TG, Harb CC, Paldus BA, Zare RN, Willke B, Byer RL. A laser-locked cavity ring-down spectrometer employing an analog detection scheme. *The Review of Scientific Instruments*. 2000;71(2):347-353. DOI: 10.1063/1.1150206
- [68] Long DA, Truong G-W, van Zee RD, Plusquellic DF, Hodges JT. Frequency-agile, rapid scanning spectroscopy: Absorption sensitivity of 2×10^{-12} cm⁻¹ Hz^{-1/2} with a tunable diode laser. *Applied Physics B*. 2014;114(4):489-495. DOI: 10.1007/s00340-013-5548-5
- [69] Long DA, Fleisher AJ, Wójtewicz S, Hodges JT. Quantum-noise-limited cavity ring-down spectroscopy. *Applied Physics B*. 2014;115(2):149-153. DOI: 10.1007/s00340-014-5808-z
- [70] Axner O, Ehlers P, Foltynowicz A, Silander I, Wang J. NICE-OHMS—Frequency modulation cavity-enhanced spectroscopy—Principles and performance. In: Gagliardi G, Loock HP, editors. *Cavity-Enhanced Spectroscopy and Sensing*. Springer Series in Optical Sciences ed. Berlin, Heidelberg: Springer-Verlag; 2014. pp. 211-251. DOI: 10.1007/978-3-642-40003-2_6
- [71] Kasyutich VL, Sigrist MW. Characterisation of the potential of frequency modulation and optical feedback locking for cavity-enhanced absorption spectroscopy. *Applied Physics B*. 2013;111(3):341-349. DOI: 10.1007/s00340-013-5338-0
- [72] Webber ME, Pushkarsky M, Patel CKN. Fiber-amplifier-enhanced photoacoustic spectroscopy with near-infrared tunable diode lasers. *Applied Optics*. 2003;42(12):2119-2126. DOI: 10.1364/AO.42.002119
- [73] Tomberg T, Vainio M, Hieta T, Halonen L. Sub-parts-per-trillion level sensitivity in trace gas detection by cantilever-enhanced photoacoustic spectroscopy. *Scientific Reports*. 2018;8: 1848. DOI: 10.1038/s41598-018-20087-9
- [74] Kosterev AA, Bakhrkin YA, Curl RF, Tittel FK. Quartz-enhanced photoacoustic spectroscopy. *Optics Letters*. 2002;27(21):1902-1904. DOI: 10.1364/OL.27.001902

- [75] Patimisco P, Borri S, Scamarcio G, Spagnolo V, Galli I, Giusfedi G, et al. Cavity and quartz enhanced photo-acoustic mid-IR sensor. In: Razeghi M, Tournié E, Brown GJ, editors. *Quantum Sensing and Nanophotonic Devices XI* (Proc. of SPIE - 8993). SPIE; 2014. pp. 899321-1-899321-8. DOI: 10.1117/12.2042246
- [76] Allan DW, Ashby N, Hodge CC. *The Science of Time-keeping*. Hewlett Packard Application Note 1289; 1997, USA. Hewlett-Packard Company Copyright © 1997 5965-7984E. pp. 1-88
- [77] Smith CJ, Wang W, Wysocki G. Real-time calibration of laser absorption spectrometer using spectral correlation performed with an in-line gas cell. *Optics Express*. 2013;**21**(19):22488-22503. DOI: 10.1364/OE.21.022488
- [78] THORLABS. *Optical Windows*. Product Catalogue
- [79] THORLABS. *Mid-Infrared Optical Fibers*. Product Catalogue
- [80] Lafond C, Couillard J-F, Delarosbil J-L, Sylvain F, de Sandro P. Recent improvements on mid-IR chalcogenide optical fibers. In: Andresen BF, Fulop GF, Hanson CM, Norton PR, editors. *Infrared Technology and Applications XL* (Proc. SPIE Vol. 9070). SPIE; 2014. p. 90701C (7 Pages). DOI: 10.1117/12.2050488
- [81] Mitra C, Sharma R. Diode laser-based sensor for extreme harsh environment data acquisition. In: Viskup R, editor. *High Energy and Short Pulse Lasers*. 1st ed. Croatia: InTech; 2016. pp. 393-415. DOI: 10.5772/63971
- [82] Mitra C, Joshi ND, Tilak V, Smith GR, Fung E, Sharma R, et al. *Gas Detector and Method of Detection*. United States Patent. 2016; US9500580B1
- [83] Mukherjee A, Prasanna M, Lane M, Go R, Dunayevskiy I, Tsekoun A, et al. *Optically multiplexed multi-gas detection using quantum cascade laser photoacoustic spectroscopy*. *Applied Optics*. 2008;**47**(27):4884-4887. DOI: 10.1364/AO.47.004884
- [84] Dong M, Zheng C, Miao S, Zhang Y, Du Q, Wang Y, et al. *Development and measurements of a mid-infrared multi-gas sensor system for CO, CO2 and CH4 detection*. *Sensors*. 2017;**17**(10): 2221-2235. DOI: 10.3390/s17102221
- [85] Swann WS, Gilbert SL. *Accuracy limits for simple molecular absorption based wavelength references*. In: Williams PA, Day GW, editors. *Symposium on Optical Fiber Measurements: Technical Digest*. NIST Special Publication 1024; 2004. pp. 15-17
- [86] Werle PW, Mazzinghi P, D'Amato F, De Rosa M, Maurer K, Slemr F. *Signal processing and calibration procedures for in-situ diode laser absorption spectroscopy*. *Spectrochimica Acta Part A*. 2004;**60**(8-9):1685-1705. DOI: 10.1016/j.saa.2003.10.013
- [87] Rieker GB. *Wavelength-modulation spectroscopy for measurements of gas temperature and concentration in harsh environments*. Doctoral Thesis. Stanford University; 2009
- [88] Duffin K, McGettrick AJ, Johnstone W, Stewart G, Moodie DG. *Tunable diode-laser spectroscopy with wavelength modulation: A calibration-free approach to the recovery of absolute gas absorption line shapes*. *Journal of Lightwave Technology*. 2007; **25**(10):3114-3125. DOI: 10.1109/JLT.2007.904937
- [89] McGettrick AJ, Duffin K, Johnstone W, Stewart G, Moodie DG. *Tunable diode laser spectroscopy with wavelength modulation: A phasor*

decomposition method for calibration-free measurements of gas concentration and pressure. *Journal of Lightwave Technology*. 2008;**26**(4):432-440. DOI: 10.1109/JLT.2007.912519

[90] Rieker GB, Jeffries JB, Hanson RK. Calibration-free wavelength-modulation spectroscopy for measurements of gas temperature and concentration in harsh environments. *Applied Optics*. 2009;**48**(29):5546-5560. DOI: 10.1364/AO.48.005546

[91] Sun K, Chao X, Sur R, Goldenstein CS, Jeffries JB, Hanson RK. Analysis of calibration-free wavelength-scanned wavelength modulation spectroscopy for practical gas sensing using tunable diode lasers. *Measurement Science and Technology*. 2013;**24**(12):125203-125215. DOI: 10.1088/0957-0233/24/12/125203

[92] Rothman LS, Jacquemart D, Barbe A, Benner DC, Birk M, Brown LR, et al. The HITRAN 2004 molecular spectroscopic database. *Journal of Quantitative Spectroscopy and Radiative Transfer*. 2005;**96**(2):139-204. DOI: 10.1016/j.jqsrt.2004.10.008

[93] Faist J, Capasso F, Sivco DL, Sirtori C, Hutchinson AL, Cho AY. Quantum cascade laser. *Science*. 1994;**264**(5158):553-556. DOI: 10.1126/science.264.5158.553

Applications of Infrared Spectroscopy and Microscopy in Diagnosis of Obesity

Ayca Dogan Mollaoglu, Ipek Ozyurt and Feride Severcan

Abstract

Infrared (IR) spectroscopy is a vibrational spectroscopic technique based on the absorption of infrared radiation by matters that excite vibrations of molecular bonds. It is a powerful method for investigating structural, functional, and compositional changes in biomolecules, cells, and tissues. In recent years, scientific researchers have continued to increase the performance of this technique on clinical cases such as cancers and metabolic disorders. Obesity is one of the main factors that increases the risk of many diseases and contributes to functional disabilities in tissues such as adipose, liver, and muscle. Applications of IR spectroscopic techniques allow identifying molecular changes due to obesity, to understand the molecular mechanism of the disease, to identify specific spectral biomarkers that can be used in diagnosis. In addition, these spectral biomarkers can be used to identify the appropriate drugs and their doses for treatment. In this chapter, applications of IR spectroscopic and microscopic techniques to the characterization and understanding the obesity metabolism will be presented. The discriminatory power of these techniques in diagnosis of obesity will be discussed. In future, these novel approaches will shed light on the internal diagnosis of obesity in clinical application.

Keywords: infrared, spectroscopy, imaging, obesity, adipose tissue, characterization, diagnosis, metabolic disorders

1. Introduction

Biospectroscopy is an analytical multistep process, including sample preparation, spectral acquisition, pre-processing, and computational analysis. Each of these steps plays a critical role for performing experiments accurately in order to obtain reliable results [1]. Since each molecule will have its own unique vibrational characteristics, each molecule possesses a unique IR spectrum. Based on this fact, vibrational spectroscopy has been considered as a golden tool in the characterization of molecular structure. Spectrum as a reflection of molecular structure of sample includes series of peaks/bands with unique characteristic properties such as band position, band width, and band intensity/area. These properties can be used for obtaining functional group information or monitoring molecules in different conditions such as disease states. Disease states are able to induce changes in molecular composition, concentration, structure, and function of biomolecules,

which are directly reflected in the vibrational spectral bands, and therefore, they can be evaluated by using vibrational spectroscopy techniques [2]. Vibrational spectroscopy includes Raman spectroscopy, IR spectroscopy, and Tera Hertz (THz) spectroscopy. IR spectroscopy consists of far, mid, and near IR spectroscopy. Vibrational spectroscopy has been applied widely in biological and medical area. Since, this analytical technique provides qualitative and quantitative information as a rapid, accurate, noninvasive, cost-effective, and operator-independent for identification of the spectral differences arising from pathological or environmental conditions. Here in this chapter, we will discuss the mid and near IR spectroscopy in obesity research.

Obesity is resulted from a chronic imbalance between the level of energy intake and consumption causing extreme weight gain. The prevalence of obesity has increased drastically in recent decades and reached global epidemic dimensions [3, 4]. Unhealthy diet habits, reduced physical activity together with modern lifestyle, urbanization, genetic predisposition, and aging cause an obesity-promoting (obesigenic) environment and contribute to the higher prevalence of these diseases across all age groups [5]. A state of excessive accumulation of body fat results in simultaneous development of a number of metabolic pathologies including insulin resistance, glucose intolerance, diabetes mellitus, hypertension, dyslipidemia, stroke, fatty liver disease, coronary heart diseases, cancer, and metabolic diseases [6–8]. Both genetic and environmental factors contribute to the development of metabolic complications, which result in a significant health and economic burden. Together with excess health care expenditure, obesity also causes decrease in the productivity as a result of lost work days, mortality, and permanent disability [9–11]. Taking into consideration the nonhealth impacts and health risks associated with obesity, there is an urgent need for early diagnosis and treatment of this global burden.

A series of methods have been proposed to define and characterize obesity. Body Mass Index (BMI, also called Quetelet's Index, in kg/m^2) is used widely that is calculated as body weight in kilogram divided by the body height in meters squared. According to this metric, the grading of body fatness can be classified as overweight (BMI: 25–30 kg/m^2), obese (BMI: 30–40 kg/m^2), and morbidly obese (BMI > 40 kg/m^2) [12]. The waist circumference (WC) is also used to monitor central obesity and measured at a level midway between the lowest rib and the iliac crest. The risk of diseases is determined according to cutoff values of 102 cm (40 in) for men and 88 cm (35 in) for females (WHO). Due to its technical problems such as the difficulty in determining bony prominences, this method identifies obesity risk poorly. The dual energy X-ray absorptiometry (DEXA) or magnetic resonance imaging (MRI) have been also used to measure fat pad size and body fat distribution as more reliable techniques [13], however, they are expensive and inaccessible. Other techniques include skinfold thickness, dual energy X-ray absorptiometry, bioelectrical impedance, plethysmography, underwater weighing, computed tomography, and near-IR interactance. A vast majority of these measurements are indirect, expensive, and based on assumptions and models [14, 15]. IR spectroscopy presents the great power in the biomedical research area due to mentioned advantages above, high sensitivity and ease application, Furthermore, IR spectroscopy is concerned as a high throughput technique that is very practical to quantify the alteration of structure, function, composition and distribution, of biologically relevant components in samples.

In this chapter, after mentioning about the basis of IR spectroscopy and microscopy, the sample preparation techniques, spectral analysis methods together with the chemometric tools used in IR spectroscopy, the topic of obesity will be given briefly. Then, how IR spectroscopy can be applied to characterization and diagnosis of obesity will be discussed in detail. Finally, the future direction of the field will be mentioned.

2. Infrared spectroscopy and microscopy in obesity research

2.1 Basis of IR spectroscopy and microscopy

Spectroscopy is based on the interactions between matter (sample analyzed) and energy from the portion of electromagnetic spectrum. IR spectroscopy is one of the most important analytical techniques that almost all type of samples such as liquids, solutions, pastes, powders, gases, and surfaces can all be studied. IR spectrometers have been commercially available since the 1940s [16]. The most significant advance in IR spectroscopy is the introduction of Fourier-transform methodology into the spectrometers. This instrument employs an interferometer and exploits the well-established mathematical process of Fourier-transformation. Fourier-transform infrared (FTIR) spectroscopy allows us to study the samples in its aqueous environment. It has dramatically improved the quality of IR spectra and minimized the time required to obtain data [17]. In addition, with constant improvements in computers, and coupling with microscope to the system, IR spectroscopy has made further great strides. In this section, the basic ideas and definitions associated with IR spectroscopy and microscopy will be described.

2.1.1 IR spectroscopy

IR spectroscopy is a technique based on the study of absorption of IR radiation, which causes transition between vibrational energy states in the molecule. When the applied IR energy is equal to the energy difference between vibrational states, absorption of IR radiation takes place and a peak is observed. If absorbed energy is plotted as a function of wavenumber, an IR spectrum is observed. IR spectroscopy products measure the transition between stretching vibrations (symmetrical and anti-symmetrical types) and bending vibrations. IR spectrum of a chemical substance is a fingerprint of a molecule for its identification.

2.1.2 IR microscopy

IR microscopy, also called as IR microspectroscopy, is a type of light microscopy. It uses a source that transmits IR wavelengths of light to view an image of the sample. An IR microscope has reflective optics that allows the microscope to cover the entire spectral range of IR light. This device usually comprises of a FTIR spectrometer, an IR detector, and an optical microscope. The IR detector may detect IR light at a single point, a linear array or a focal plane array to view different sections of the sample. This allows both spatial and spectral information about the sample structure to be collected. In FTIR microscopy, the microscope sits above the FTIR sampling compartment. Infrared radiation from the spectrometer is focused onto a sample placed on a standard microscope x–y stage. After passing through the sample, the IR beam is collected by an objective that produces an image of the sample within the point of the microscope [18]. A variable aperture is placed in this image plane. After that, another condenser focuses the radiation on MCT detector. Also, there are glass objectives in order to allow visual view of the sample. In addition, the microscope can be converted from transmission mode to reflectance mode by switching mirrors in the optical train.

3. Experimental sampling protocol of IR spectroscopy and microscopy

The sample preparation methods are chosen according to the size, nature, and condition of the specimen. Particular technique/accessory that is used also plays

an important role for sample preparation. Moreover, useful accessories, such as temperature controller systems and the attenuated total reflectance (ATR) mode are available to increase the fields of applications of FTIR spectroscopy and microscopy. Some popular sampling techniques and accessories will be discussed below.

3.1 IR spectroscopy

3.1.1 Transmission IR spectroscopy methods

Transmission spectroscopy is the oldest and most straightforward method that based upon the absorption of IR radiation at specific wavelengths as it passes through a sample, which can be in liquid and solid samples [17]. Protein in solution and membrane studies are only performed using this method [19].

3.1.1.1 Liquid samples

Various techniques are available for sampling of liquids. For example, fixed-path length-sealed cells are useful for volatile liquids, but cannot be taken apart for cleaning. On the other hand, semi-permanent cells are removable so that the windows can easily be cleaned. Usually, the spacer is made of polytetrafluoroethylene (PTFE, Teflon) with a variety of thickness is used. If quantitative analysis of a sample is required, it is necessary to use a cell of known path length [20, 21]. An important consideration in the choice of IR cells is the type of window material. The material must be transparent to the incident IR radiation and normally alkali halides are used in transmission methods [20, 22, 23]. The cheapest material is sodium chloride (NaCl), but other commonly used materials are potassium bromide (KBr), calcium fluoride (CaF₂) [24], and barium fluoride (BaF₂). A drop of liquid is sandwiched, using suitable spacer, between two IR windows that are then mounted in a cell holder. Before producing an IR sample in solution, a suitable solvent must be chosen. The other factors while choosing solvent are that it should be as nonpolar as possible to minimize solute–solvent interactions; and it should not strongly absorb IR radiation.

3.1.1.2 Solid samples

Alkali halide disk method is one of the most favorable methods to examine solid samples. In order to apply this technique, a solid sample is mixed with a dry alkali halide powder. Then, mixture is ground with an agate mortar and subjected to a pressure of 10 ton in⁻² ($1.575 \times 10^5 \text{ kg m}^{-2}$) in an evacuated die. This sinters the mixture and produces clear transparent disks. The most commonly used alkali halide is KBr, which is completely transparent in the MID-IR region [18]. The ratio of the sample to alkali halide is important; generally, sample to halide ratio is chosen as 1:100. The disk thickness is important; thin disks are fragile and difficult to handle, while thick disks transmit too little radiation. If the crystal size of the sample is too large, excessive scattering of radiation results, especially at high wavenumbers (this is known as the Christiansen effect) [25]. In that case, further grinding is required. Drying process is applied to remove the bulk water from the samples. However, bound water or inter-bilayer water still exists in the biological systems [26]. The presence of bound water molecules is not only required for the structural stability of the lipid bilayer [27], but also to control the dynamics and structure of lipid bilayer phases [28] and proteins [29, 30]. In KBr pellet technique, since the system is not exactly in its natural aqueous environment, some alterations in macromolecular structure may occur. Therefore, only relative information can be deduced. The KBr

pellet technique has been extensively used to study a variety of biological systems in dry stated [31, 32].

3.1.2 Reflectance infrared spectroscopy method

ATR spectroscopy utilizes the phenomenon of total internal reflection. When a beam of radiation enters a crystal, if the angle of incidence at the interface between the sample and crystal is greater than the critical angle, incident radiation will undergo total internal reflection [33]. The crystals used in ATR cells are made from materials that have low solubility in water and are of a very high refractive index. Such materials include Diamond, zinc selenide (ZnSe), germanium (Ge), silicon (Si), and thallium/iodide.

Besides aqueous samples, dry samples, homogeneous soft tissues, or hard tissues can also be studied with the ATR-IR spectroscopy by directly placing a small portion of the sample on the crystal and then applying the same pressure to all the samples. The applied pressure should allow until the strongest spectral bands to appear with an intensity extending beyond 70% T, and care should be given to provide uniform contact of the sample with crystal. ATR is accepted to require little or no sample preparation, and is one of the most versatile sampling techniques.

3.2 IR microscopy

FTIR microspectroscopy provides the opportunity to investigate heterogeneous biological tissues without any prior chemical or physical process like dyeing. In recent years, there have been considerable advances in FTIR microscopy by reaching sample size at the order of microns. During sample preparation for FTIR microspectroscopy, tissue sections can either be directly obtained using a cryotome or be initially embedded into different kinds of embedding media and then cryo-sectioned. Different kinds of embedding media can be used for soft and hard tissues. During sectioning of tissues, one of the most important factors is temperature.

3.2.1 Soft tissues

The infiltration and embedding medium for soft tissues is paraffin. However, for the evaluation of certain proteins or other cellular components, routine formaldehyde fixation and paraffin-based histology are not suitable. In these situations, sections should be embedded in optimum cutting temperature (OCT) medium and cryo-sectioned to retain the most sensitive and undisrupted insight into tissue architecture. Bubble formation should be avoided while applying OCT media. After embedding in a material, generally, 6–10 micron tissue sections are obtained [34, 35]. Finally, tissue samples are thaw-mounted on IR-transparent CaF₂ or BaF₂ windows for IR mapping and data processing [36].

3.2.2 Hard tissues

Hard tissues are first exposed to different concentrations of ethanol, methyl methacrylate, and benzoyl peroxide for fixation and infiltration, and then are embedded into polyethylene methyl methacrylate (PMMA) along with a polymerization accelerator [37]. After the embedding procedure, 2-micron tissue sections are obtained with a cryotome [38, 39] and tissue samples are thaw-mounted on IR-transparent CaF₂ or BaF₂ windows for IR mapping and data processing.

4. Data analysis of IR spectroscopy and microscopy

4.1 Preprocessing methods

Preprocessing is essential to extract the relevant chemical information by applying chemometric techniques to remove baseline deviations, to normalize sample to the same thickness/quantity of material, and to reduce noise or contaminants. It is also useful to sort out bad quality spectra (spectra showing signs of saturation, spectra that are too weak, spectra that are too distorted) and remove outliers. It is applied before data analysis but should be kept minimum not to introduce some artifacts and should be performed in the right order. First, visual inspection of the spectra should be done to remove bad quality spectra. If there is a distortion in the spectral bands that may be encountered in cell studies, Mie scattering correction should be performed. Then, smoothing is applied if necessary and baseline correction is applied before normalization and derivatives [1].

Multiple methods exist to perform baseline correction. Offset correction can be applied by putting the lowest point to zero and linear baseline correction can be applied by subtracting a linear baseline as shown in **Figure 1** or polynomial baseline correction may be preferred by subtracting a polynomial baseline of required order.

Normalization is the mathematical function to set all the spectra to the same norm and scale. It is mandatory to correct differences in spectral intensity that arises from heterogeneity in sample thickness or inaccuracies in positioning. It should be performed before any scaling or other preprocessing steps, but after baseline correction. Common normalization methods are min-max and vector normalization. In min-max normalization, the minimum and the maximum intensities of the whole spectrum are scaled to zero and one, respectively. In vector normalization, the sum of all intensity values squared of normalized mean-centered spectrum is equal to 1. Derivatives are used for finding precise peak positions, which are mostly computed by a Savitzky-Golay filter. There are several orders of derivative; first order is according to slope of the peak and second order is according to curvature radius. Smoothing is used to reduce noise in data. However, smoothing also induces distortion in peak shape and may erase small peaks and shoulders [40].

4.2 Data analysis

The band positions and bandwidths of the spectral bands are measured from the center of weight ($0.80 \times$ peak height position). The position of the spectral bands

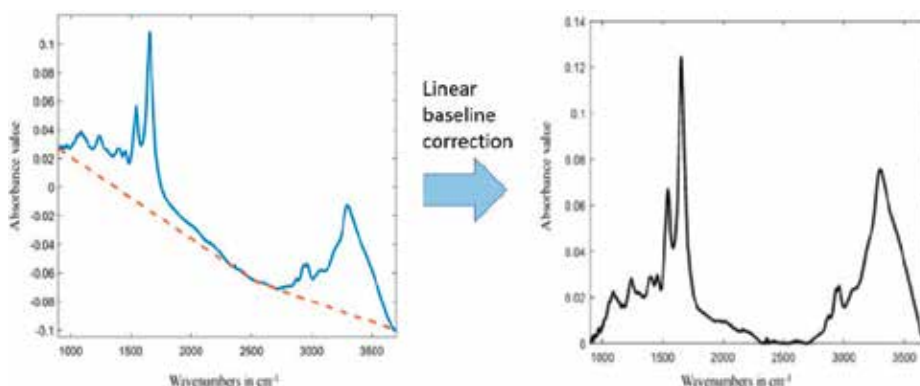


Figure 1. Representation of a spectrum before (left) and after (right) linear baseline correction.

allows us to do band assignments. The bandwidth of the CH₂ stretching bands gives lipid fluidity information. The shift in the positions of the bands gives structural information. For example, the shift in the position of CH₂ symmetric and anti-symmetric bands monitors lipid order/disorder, which gives information about the flexibility of the lipid acyl chains [20, 24]. The shift in the position of the C=O stretching and the PO₂⁻ anti-symmetric double stretching bands gives information about hydration status of these functional groups [20, 24]. The shift in the position of the amide I band and ratio of the amide I to amide II give information about the variations in protein secondary structure [22]. According to Beer–Lambert law, the signal intensity or more accurately the area under the bands gives concentration information. In order to remove any artifact that arise from the thickness of the sample, generally in cell and tissue studies, area ratios of the specific bands are used [41, 42]. In membrane studies, since the OH stretching bands (3400–3200 cm⁻¹ and 1800–1500 cm⁻¹) due to the buffer, these bands overlap with the bands of interest. Therefore, the spectrum of the buffer is subtracted from the spectrum of liposomes at corresponding temperatures. The subtraction process is performed until the bulk water located around 2100 cm⁻¹ is flattened using the spectrometer's software program. The detailed analyses are performed from the subtracted native spectra.

4.3 Chemometrics

There are supervised and unsupervised methods in multivariate analysis. Compared to unsupervised methods (simple clustering methods), supervised methods (classification and identification methods) can be used to train a model to create classes or in order to predict the class of unknown samples. Because they are supervised methods, there is a need for cross-validation and independent validation dataset. Since there is no application of supervised methods to obesity yet, only unsupervised methods will be discussed here.

4.3.1 Principle component analysis (PCA)

PCA is an unsupervised analysis method based on the decomposition of variance in a new multidimensional space. It is a well-known technique for reducing the dimensionality of multivariate data while preserving most of the variance [43]. This technique can reduce a large scale of spectra to a point in a space by using linear transformation. PCA can be used to define groups based on spectral similarity/variance as classification method. PCA can cluster spectra by similarity, detects outliers, finds correlations between variables and can decorrelate different sources of variability as a data exploration method. Each PC describes the spectral variability among samples in decreasing order. Thus, the first principle component, i.e., PC1, expresses most of the variance in the data; PC2 expresses the second largest variance in the data and so on [44]. Furthermore, PCA is capable to obtain loadings plots to identify the main contributory variables (i.e., wavenumbers) that determine the discriminating wavenumbers throughout the IR spectrum.

4.3.2 Hierarchical cluster analysis (HCA)

Among the different methods used in cluster analysis, generally Ward's algorithm together with Euclidian distances is used to construct the dendrograms, which gives one of the best predictions [45]. In this method, the two spectra with the highest similarity (i.e., spectra with the smallest spectral distance) are merged

into a cluster and then the distances between this cluster and all other spectra are calculated. This process continues until the two spectra (spectrum/spectrum or spectrum/cluster or cluster/cluster) are merged into a new cluster. This procedure is repeated until only one big cluster is left. Different from other methods, Ward's algorithm tries to find as homogeneous groups as possible. By the way, HCA builds the hierarchical tree of dissimilarity between data points that is called dendrogram. Well-known parameters of clinical studies such as sensitivity and specificity can be used to describe the performance of the methods in disease diagnosis. Explanation of sensitivity, specificity, positive (true and false), and negative (true and false) values can be found in Severcan et al. [22].

5. Obesity

Stability of body fat is key point to maintain metabolic homeostasis. Excess amount of energy is stored in the form of triglycerides in the lipid droplets of adipocytes and result in the increase in the number of adipocyte (hyperplasia) or enlargement in the size of adipocytes (hypertrophy). Adipose tissue depots are classified into white adipose tissue (WAT) and brown adipose tissue (BAT), each of them has unique structure and function. They differ in their degree of vascularization and innervation. BAT is rich in protein content and mitochondria than that of WAT. Brown adipose tissue (BAT) is highly specialized in thermogenesis and maintaining body temperature [46]. WAT is involved in the regulation of energy homeostasis, body thermal insulation and present active endocrine organ functions via production and secretion of adipokines such as leptin, adiponectin, IL6, IL10, TNF α , etc. Both tissues are capable to store triglycerides [47]. White adipose tissue has been organized in different anatomical location as visceral white adipose tissue (VAT) and subcutaneous white adipose tissue (SCAT). VAT has higher amount of plasminogen activator inhibitor-1 (PAI-1), IL6 and higher expression of glucocorticoid, androgen, AT $_1$ and beta-3 adrenergic receptor than in the subcutaneous tissue. The products of VAT are driven to the liver via portal vein system, affecting its function. SCAT possesses higher concentrations of leptin and adiponectin. The secretions of SCAT are released into the general circulation [48]. Therefore, WAT paves the way for different metabolic diseases and presents great detrimental effect to human health [49, 50].

Adipose tissue responds to excess triglycerides accumulation by inducing an immune response. Excessive fat accumulation results in changes in cellular and structural remodeling processes and causes alterations in the endocrine and metabolic systems. This inflammatory state is associated with increased accumulation of macrophages in adipose tissues along with the production of inflammatory cytokines and their secretion into the circulation (e.g., adiponectin, leptin, resistin, IL6, IL10, TNF α , macrophage migration inhibitory factor [51], and components of the renin-angiotensin system [52]). These cytokines mediate inflammation or play an active role in immune and inflammatory responses to obesity. Increased circulating levels of inflammatory markers are associated with obesity-related pathologies. For example, TNF α and IL6 contribute to the induction of insulin resistance [53] and are associated with increased glucose levels and altered lipid metabolism [54, 55]. Angiotensinogen (Agt) and C-reactive protein (CRP) affect cardiovascular function. Plasminogen activator inhibitor 1 (PAI1) causes impaired fibrinolysis and promotes atherosclerosis [56, 57]. These associations are affected by adipose tissue distributions. In the literature, visceral adipose tissue has been implicated as a major risk factor for insulin resistance, type 2 diabetes [48, 58], cardiovascular disease [59], stroke [60], and metabolic syndrome [61]. Therefore, visceral fat is thought to be the more dangerous

adipose tissue. The liver is the major organ of lipid metabolism and can store lipids, which could lead to fatty liver syndrome. Fatty liver, itself, stimulates a local subacute inflammatory state by production of inflammatory mediators such as TNF α or IL-6 that contribute to hepatic and systemic insulin resistance [62].

Obesity-induced inflammation is emerged as a result of change in the cytokine profile, in particular, decrease in adiponectin and increase in leptin levels, mitochondrial dysfunction, accelerated adipocyte death and endoplasmic reticulum (ER) stress. Specific signaling pathways, such as Jun N-terminal kinase, I κ B kinase β /nuclear factor κ -light-chain-enhancer of activated B cells, inositol requiring kinase 1, pancreatic ER kinase, activating transcription factor 6, etc., also are contributed to inflammatory state [63]. Endoplasmic reticulum is a major site for protein and for lipid synthesis. In the ER, proteins are folded into their native confirmation and undergo posttranslational modifications, which are important for their structure and activity. In the case of nutrition overload, function of ER is impaired, protein folding is disturbed, ER stress develops and activates a signaling network called the unfolded protein response (UPR) to restore ER homeostasis [64, 65]. It is known that ER stress is linked with obesity-related pathologies including insulin resistance, type 2 diabetes, hypertension, and nonalcoholic fatty liver disease [5, 65, 66]. Consequently, adipose tissue serves as a main site for activation of the inflammatory response in obesity.

6. Application of IR spectroscopy and microscopy in obesity research

Biological samples contain biochemical substances such as lipids, proteins, carbohydrates, proteins, and nucleic acids, and these biomolecules have their unique vibrational fingerprints. Therefore, disease-induced changes in the position, bandwidth, signal intensity, and area of the spectral bands of the system of interest, can be monitored by IR spectroscopy. In current chapter, the applications of IR (mid and near), spectroscopic and microspectroscopic techniques in obesity research will be discussed in detail.

Recent studies pointed out the importance of adipose tissue in diagnosis and treatment of obesity and obesity related diseases. Therefore, adipose tissues draw attraction in obesity research. **Figure 2** shows a representative IR spectrum of a human adipose tissue. This spectrum is quite complex and contains several bands, which arise from different functional groups belonging to biomolecules of the system. The relevant band assignments of the bands are given in **Table 1** [67, 68].

It is known that obesity constitutively results in storage of triglycerides in different adipose tissues [2]. A recent article discussed the potential of ATR-FTIR spectroscopy to monitor obesity from the triglyceride spectral band located around 1730 cm^{-1} [43]. In this study, hierarchical cluster analysis (HCA) and principal component analysis (PCA) were applied to the spectra of triglyceride bands of subcutaneous (SCAT) and visceral (VAT) adipose tissues. The adipose tissue samples were obtained from 10 weeks old male control (DBA/2 J) ($n = 6$) and four different obese BFMI mice lines ($n = 6$ per group). As seen from **Figure 3**, successful discrimination of the obese, obesity-related insulin resistant and control groups was achieved with high sensitivity and specificity. Based on the spectral differences, the results revealed the power of FTIR spectroscopy coupled with chemometric in internal diagnosis of abdominal obesity. This work also indicated that SCAT and VAT were affected from obesity at different rates and ATR-FTIR spectroscopy coupled with chemometric analysis could sensitively differentiate these effects of obesity in adipose tissues. In conclusion, the VAT and especially, the SCAT samples can be easily examined by ATR-FTIR spectroscopy coupled with

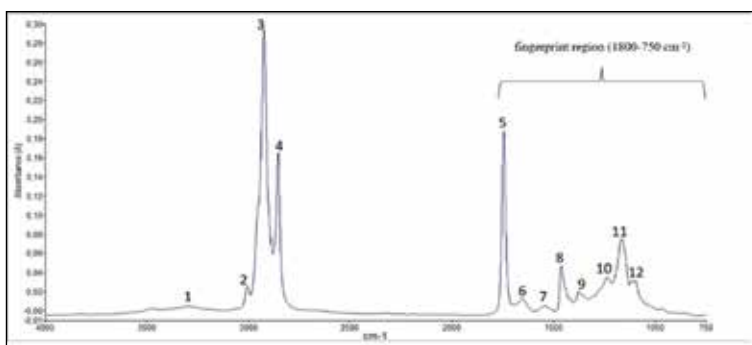


Figure 2. A representative baseline corrected normalized FTIR spectrum of a human adipose tissue in the 4000–750 cm^{-1} region.

chemometrics in human studies and this combined technique will shed light on the internal diagnosis of obesity in medical research [43].

In the other study of the same group, lipid profiles in terms of the content and structure of skeletal muscle and adipose tissues were determined to understand better the characteristics of juvenile-onset spontaneous obesity without high fat diet induction. Biomolecular content, concentration, and structure were determined by ATR-FTIR spectroscopy. The muscle (longissimus, quadriceps) and adipose (inguinal, gonadal) tissues of 10-week-old male DBA/2 J and Berlin Fat Mouse inbred (BFMI) lines (BFMI856, BFMI860, BFMI861) fed with a standard breeding diet were used. Spectral differences indicated differences in lipid structure and content of BFMI lines, which may originate from different insulin

Band number	Band position (cm^{-1})	Definition of band assignment	References
1	3290	N–H and O–H symmetric stretching: mainly N–H stretching (amide A) of proteins with the little contribution from O–H stretching of polysaccharides, carbohydrates and water	[67]
2	3006	Olefinic = CH stretching vibration: unsaturated lipids, cholesterol esters	[68]
3	2924	CH_2 anti-symmetric stretching: mainly lipids, with some contribution from proteins, carbohydrates, nucleic acids	[68]
4	2854	CH_2 symmetric stretching: mainly lipids, with some contribution from proteins, carbohydrates, nucleic acids	[68]
5	1744	Carbonyl C–O stretch: triglycerides	[68]
6	1654	Amide I (protein C–O stretching)	[67]
7	1547	Amide II (protein N–H bend, C–N stretch)	[67]
8	1469	CH_2 bending of the acyl chains of lipids	[67]
9	1375	C–N Stretching	[67]
10	1238	Asymmetric PO_2 stretching	[67]
11	1164	C–O stretching (in normal tissue)	[67]
12	1100	Stretching PO_2 symmetric (phosphate II)	[67]

Table 1. General band assignment of the FTIR spectrum of an adipose tissue.

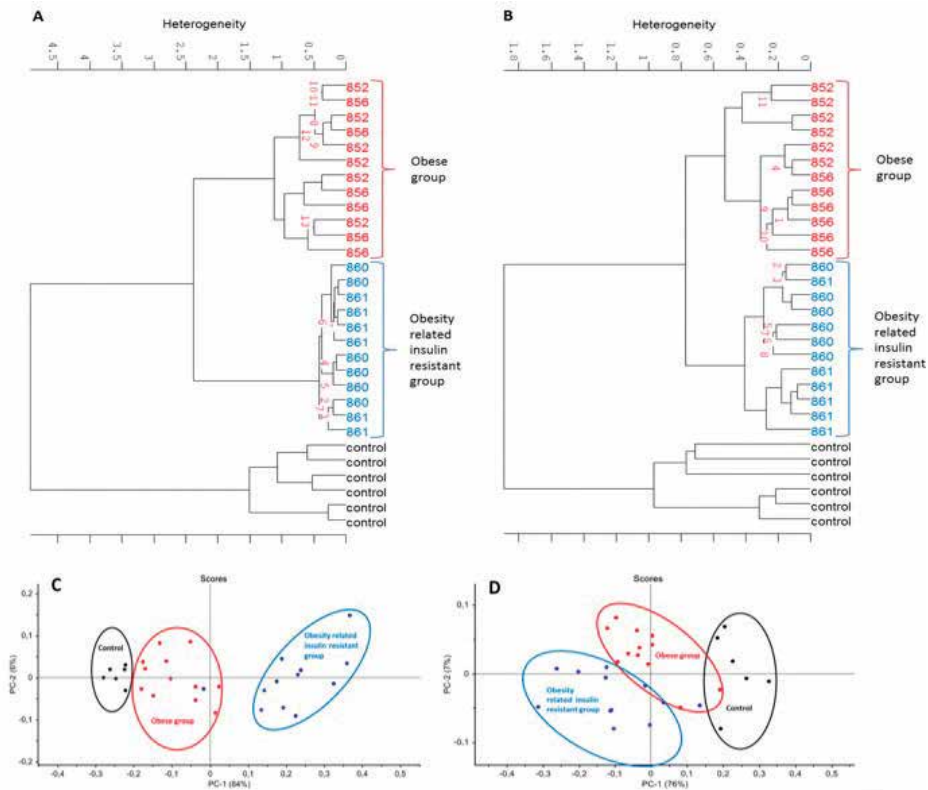


Figure 3. Hierarchical clustering of control, obese and obesity related insulin resistant groups in SCAT (A) and VAT (B) in the $1770\text{--}1720\text{ cm}^{-2}$ spectral region. Control group (black), obese group (BFMI 852–856) (red), obesity related insulin resistant group (BFMI 860–861) (blue). PC1 versus PC2 scores plot of the second derivative vector normalized spectra in the same range of SCAT (C) and VAT (D). Control group (black), obese group (BFMI 852–856) (red), obesity related insulin resistant group (BFMI 860–861) (blue).

sensitivity levels of the lines. This makes them promising animal models for spontaneous obesity. The referred study will shed light to the understanding of the generation of insulin resistance in obesity without high fat diet induction [69]. A recent FTIR microspectroscopic study of the same group aimed to characterize and compare VAT and SCAT in terms of macromolecular content and investigate transdifferentiation between white and brown adipocytes [34]. In order to achieve this, the gonadal (visceral) and inguinal (subcutaneous) adipose tissues of male BFMI lines, which are spontaneously obese were studied. The prominent increase in the lipid/protein ratio (**Figure 4**), accompanied with a decrease of UCP1 protein content might be due to the transdifferentiation of brown adipocytes to white adipocytes in obese groups. When the amount of BAT was decreased, lower unsaturation/saturation ratio, qualitatively longer hydrocarbon acyl chain length of lipids and higher amount of triglycerides were obtained in both adipose tissues of mice lines as seen in **Figure 4**. The results also showed that SCAT was more prone to obesity-induced structural changes than VAT. This could originate from it possessing a lower amount of brown adipose tissue. The current study clearly revealed the power of FTIR microspectroscopy in the precise determination of obesity-induced structural and functional changes in inguinal and gonadal adipose tissue of mice lines [34].

In another obesity research [68], which targets to identify specific gene loci, regulating obesity in BXD recombinant inbred (RI) strains of mice, ATR-FTIR

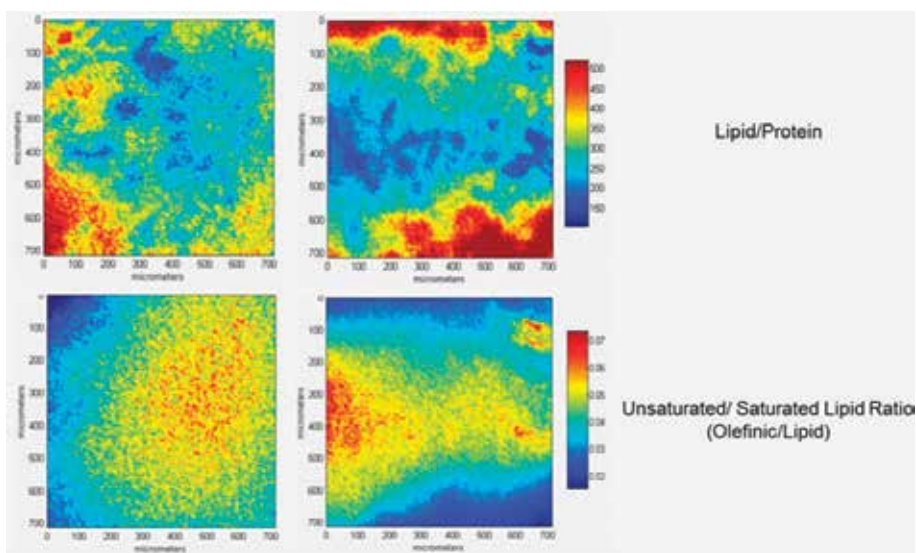


Figure 4.

The representative spectral maps of lipid/protein and olefinic/protein ratios belong to the inguinal adipose tissue of control (left side) and obese (right side) male mice lines. The absorbance in the spectral maps was represented in color-coded images, where low absorption was represented in blue and high absorption was represented in red color. (Adapted from [34], with permission from Royal Society of Chemistry).

spectroscopy was performed as a novel phenotyping tool. The epididymal adipose tissue, liver, and muscle of 29 BXD recombinant inbred mouse strains fed with high fat diet were used to analyze the role of white adipose tissue as a mediator of inflammation. The content of total fat, unsaturated fat, lipid to protein ratio, and collagen and collagen integrity were measured in tissue of interest and the results of IR analysis were revealed differences in the biomolecular composition of adipose and liver tissues among high fat diet-fed BXD RI strains that reflect genetic variation. *Rsd2*, which may modulate lipid droplet contents and lipid biosynthesis, and *Colec11*, which may play a role in apoptotic cell clearance and maintenance of adipose tissue were suggested as potential quantitative trait candidate genes. This study showed the efficiency and suitability of ATR-FTIR spectroscopy to identify quantitative trait loci (QTLs) that influence various traits and heightened the power of gene mapping studies.

Bortolotto et al. [70] determined the total content of trans fatty acids (TFA) in subcutaneous, retroperitoneal, and visceral fat of morbidly obese and nonobese patients subjected to bariatric surgery or plastic and abdominal surgery. TFA were measured by FTIR-ATR spectroscopy. TFA content in all adipose tissues analyzed was higher than reported in other countries. They showed more TFA in VAT than in other abdominal fat (subcutaneous and retroperitoneal) stores. The TFA depot in visceral fat was higher than other fatty tissues for morbidly obese and nonobese patients. Gazi et al. [71] demonstrated lipid-specific translocation between adipocytes and tumor cells and the use of FTIR microspectroscopy to characterize various biomolecular features of a single adipocyte without the requirement for cell isolation and lipid extraction. Stimulating increased thermogenic activity in adipose tissue is an important biological target for obesity treatment. Aboualazadeh et al. [72] investigated the biochemical changes caused by cold exposure using FTIR imaging technique in the brown and subcutaneous white adipose tissues (BAT and s-WAT) of 6-week-old C57BL/6 mice exposed to different temperatures for 10 days. Protein to lipid ratio, calculated from the ratio of the integrated area from 1600 to 1700 cm^{-1} (amide I) to the integrated area from 2830 to 2980 cm^{-1} (saturated

lipids), was increased as temperature decreased. The degree of unsaturation was obtained from the ratio of the integrated area of unsaturated lipids (2992–3020 cm^{-1}) to the integrated area of saturated lipids (2830–2980 cm^{-1}), showed stepwise decreases going from colder-exposed to warmer-exposed BAT. Complementary ^1H NMR measurements confirmed the findings from this ratio in BAT. PCA analysis successfully operated to groups. This study revealed that, FTIR imaging is a promising technique to quantify cold-induced biochemical changes in BAT and s-WAT in a label-free manner [72].

Nonalcoholic fatty liver disease (NAFLD) is a frequent lesion associated with obesity, diabetes, and the metabolic syndrome. The potential of mid-IR fiber evanescent wave spectroscopy was used as a minimum-invasive method for evaluating the liver status during NAFLD. In the study, 75 mice were subjected to a control, high-fat or high-fat-high carbohydrate diets. The mid-IR spectra were acquired from serum, and then analyzed to develop a predictive model of the steatosis level. Animals subjected to enriched diets were obese. The relationship between the spectroscopy-predicted and observed levels of steatosis, expressed as percentages of the liver biopsy area, was not linear. The data suggest that mid-IR spectroscopy combined with statistical analysis allows identifying serum mid-IR signatures that reflect the liver status during NAFLD [73]. In another work [74], the potential of FTIR microspectroscopy for grading steatosis on frozen tissue sections was evaluated. The use of the bright IR source emitted by synchrotron radiation (SR) allowed the investigation of the biochemical composition at cellular level. PCA method was applied to spectral data. The results showed that the progression of steatosis corresponds not only to the accumulation of lipids but also to significant changes in the qualitative composition of the tissue. Indeed, as the grade of steatosis was lowered, a decrease in glycogen content with a concomitant increase in lipids was observed in comparison to normal liver. Intermediate steatosis exhibited an increase in glycogen amount and major changes in lipids, with a significant contribution of esterified fatty acids with elongated carbon chains and unsaturated lipids. These features were more pronounced in a high grade of steatosis. The dramatic biochemical changes occurred in the nonsteatotic part of the tissue, suggested that the whole tissue reflects the grade of steatosis [74].

Obesity might alter the electric activity in brain areas triggering appetite and craving. In a recent study, electrical activity was induced by transcranial direct current brain stimulation (tDCS). FTIR spectroscopy and synchrotron X-ray fluorescence (SRXRF) microprobe techniques show that brain areas implicated appetite control, upon experimental treatment by either anodal-type tDCS (atDCS) or cathodal-type tDCS (ctDCS). The C-H stretching, amide I-IV, and PO_4^{2-} anti-symmetric stretching regions were investigated. The most dramatic lipid-related changes were found for $\gamma_{\text{as}}(\text{CH}_2)$ at 2930 cm^{-1} , whereas the protein secondary changes occurred at the amide I band, for α -helix and β -sheet located at 1660 and 1630 cm^{-1} , respectively. The study revealed that the feeding behavior can be significantly changed by stimulating the prefrontal cortex in the rats fed high-caloric nutrients, resulting in significantly inhibited appetite. Both, atDCS and ctDCS produced significant molecular changes involving qualitative and structural properties of lipids, whereas atDCS induced more significant effect on protein secondary structure in all the brain areas investigated [75].

Alterations in dietary fatty acid composition can influence the regulation of metabolism in adipose tissue. Bizeau et al. [76] studied the effect of dietary fatty acid composition on lipolysis. The rats were fed with diets containing menhaden oil (MO) or coconut oil (CO) for 4 weeks. FTIR spectroscopy was used to examine the effect of altered plasma membrane fatty acid composition on membrane physical properties. The results of this study suggested that membrane order is not responsible for the lower rate of lipolysis in animals fed

coconut oil when both variables are measured at 37°C. In another recent study, rats fed with a high-fat diet were treated with resistant starch (RS), chitosan oligosaccharide (COS), and a combination of these complexes with the aim of determining their effect on controlling blood glucose levels and improving insulin resistance. Cross-linking between RS and COS was confirmed by FTIR spectroscopy analysis. For COS analysis, in IR spectroscopy, the absorption peak at 3416.33 cm⁻¹ belonged to O-H and N-H stretching vibrations, 2922.80 cm⁻¹ corresponding to a C-H stretching vibration, and 1566.70 cm⁻¹ originated from -NH₂ absorption peak were used. The RS spectra showed an absorption band at 3416.50 cm⁻¹, (O-H stretching) and 2926.85 cm⁻¹ by C-H stretching vibration. A new absorption peak at 1560.88 cm⁻¹ appeared in the COS-RS complex spectra, and the shape of typical absorption peaks for starch from 1180 to 953 cm⁻¹ also changed. The results suggested that the consumption of COS-RS complexes exerted a more efficient recovery of insulin sensitivity compared to individual treatments [77]. Herbal supplements are currently available as a safer alternative to manage obesity. Many chemical drugs on the market are designed to prevent or manage obesity whose high cost, low efficacy, and multiple side effects limit their use. El-Menshawe et al. [78] evaluated nano lipo-vesicles phytosomal thermogel of Soybean [*Glycine max* (L.) Merrill], for its anti-obesity action on body weight gain, adipose tissue size, and lipid profile data by FTIR spectroscopy. Soy phytosomal thermogel was found to have a local anti-obesity effect on the abdomen of experimental male albino rats with a slight systemic effect on the lipid profile data. In another study, FTIR spectroscopy was used to determine physio-chemical properties of pectin extracted from the apple pomace that was proposed to inhibit pancreatic lipase (steapsin). The study showed the extracted pectin has potential use in the anti-obesity formulations [79]. Dunkhunthod et al. [80] used FTIR microspectroscopy coupled with chemometrics to monitor and discriminate biomolecular changes due to the anti-adipogenesis effect of baicalein on adipogenesis in 3 T3-L1 cells. The signal intensity and the integrated areas of glycogen and carbohydrate of baicalein-treated 3T3-L1 adipocytes were found to be significantly less than the untreated 3 T3-L1 adipocytes. The intensity ratio of the CH₂ to CH₃ anti-symmetric stretches, which the acyl chain length of phospholipids, and the ratio CH₂ asymmetric stretch/amide I, which represents the lipid/protein ratio, was significantly less for the baicalein-treated cells than for the untreated cells. The findings provided evidence for the development of IR biochemical obesity markers and showed the potential of FTIR microspectroscopy in the evaluation of the effectiveness of the drug in the treatment of obese patients [33].

7. Conclusion and future directions

FTIR spectroscopy is a rapid, very sensitive, cost-effective, and easy-use technique. Especially in ATR mode, samples are directly put on the crystal without any sample preparation step. In addition, results are not dependent on the operator but to computational analyses of the spectra. This property gives an important advantage to this technique. Furthermore, FTIR spectra may give information about the disease-induced changes at very early stage, earlier than they become visible. That means IR spectroscopy has the capacity of analysing the biological systems as reagent free, operator independent, diagnosis of diseases at very early stage. It also allows the detection of lower concentrations of biological components ranging from biomolecules, membranes, cells, tissues, and body fluids. With these state-of-the-art technology, IR spectroscopy coupled with chemometric tools have taken part in the field

of biomedicine especially in determination of disease-induced spectral biomarkers, disease diagnosis, and treatment-oriented monitoring in clinical investigations.

The IR spectroscopy results of the animal studies on adipose tissues can be transferred to medical research to be used in the diagnosis of obesity. Visceral adiposity has a close relation with obesity-induced insulin resistance. This effect of obesity on the VAT highly correlates with the SCAT. Since the SCAT is more accessible than the VAT for medical interventions, this type of adipose tissue can be used preferably in biopsies and bariatric operations [43]. In recent years, since BAT have been proposed as a potential therapeutic target for obesity and related metabolic diseases, targeting BAT, thermogenesis and monitoring BAT metabolism might hold a possible therapeutic potential for these metabolic diseases. Recent innovations in spectroscopy and microspectroscopy contributed to evaluation, characterization, and differentiation of the obesity. However, application of IR spectroscopy to obesity research is quite limited so far. There are several issues in obesity area that need to be clarified. For example, the mechanism of the protective role of fatty acids, the effect of macrophage localization and origin to induce inflammation in adipose tissue and ER stress induced response of different organs such as liver, adipose tissue, anti-obesity effect of diets, therapeutic effect of drug, structural characterization of obese human membranes, tissues and organs are still not exactly known and further researches are required. In terms of structural studies, there is no information yet in the literature about obesity-induced protein structural changes. Furthermore, supervised analysis methods have not been applied to IR spectra yet for the obesity differentiation. Promising new experimental tools and models will help for elucidating remaining questions related to obesity and may be critical for the development of the new therapeutic strategies.

Conflicts of interest

The authors report no financial conflicts of interest. The authors are only responsible for the content and writing of this chapter.

Author details

Ayca Dogan Mollaoglu^{1,2}, Ipek Ozyurt^{2,3} and Feride Severcan^{2,3*}

1 Department of Physiology, Faculty of Medicine, Altinbas University, Istanbul, Turkey

2 Graduate Program in Biomedical Sciences, Institute of Health Sciences, Altinbas University, Istanbul, Turkey

3 Department of Biophysics, Faculty of Medicine, Altinbas University, Istanbul, Turkey

*Address all correspondence to: feride.severcan@altinbas.edu.tr

IntechOpen

© 2018 The Author(s). Licensee IntechOpen. This chapter is distributed under the terms of the Creative Commons Attribution License (<http://creativecommons.org/licenses/by/3.0>), which permits unrestricted use, distribution, and reproduction in any medium, provided the original work is properly cited. 

References

- [1] Severcan F, Haris PI. *Vibrational Spectroscopy in Diagnosis and Screening*. Amsterdam: IOS Press; 2012. pp. 12-52. DOI: 10.3233/BSI-130036
- [2] Baloglu FK, Severcan F. Characterization and differentiation of adipose tissue by spectroscopic and spectral imaging techniques. In: Szablewski L, editor. *Adipose Tissue*. Rijeka, Croatia: InTechOpen; 2018. DOI: 10.5772/intechopen.75156
- [3] Maiano C, Hue O, Morin AJ, et al. Prevalence of overweight and obesity among children and adolescents with intellectual disabilities: A systematic review and meta-analysis. *Obesity Reviews*. 2016;**17**:599-611. DOI: 10.1111/obr.12408
- [4] Zylke JW, Bauchner H. The unrelenting challenge of obesity. *Journal of the American Medical Association*. 2016;**315**:2277-2278. DOI: 10.1001/jama.2016.6190
- [5] Kevin NK, Vinicius FC, Rodrigo C, et al. Molecular events linking oxidative stress and inflammation to insulin resistance and β -cell dysfunction. *Oxidative Medicine and Cellular Longevity*. 2015;**2015**:181643. DOI: 10.1155/2015/181643
- [6] Afshin A, Forouzanfar MH, Reitsma MB, et al. Health effects of overweight and obesity in 195 countries over 25 years. *The New England Journal of Medicine*. 2017;**377**:13-27. DOI: 10.1056/NEJMoa1614362
- [7] Jacome-Sosa MM, Parks EJ. Fatty acid sources and their fluxes as they contribute to plasma triglyceride concentrations and fatty liver in humans. *Current Opinion in Lipidology*. 2014;**25**:213-220. DOI: 10.1097/MOL.0000000000000080
- [8] Hubler MJ, Kennedy AJ. Role of lipids in the metabolism and activation of immune cells. *The Journal of Nutritional Biochemistry*. 2016;**34**:1-7. DOI: 10.1016/j.jnutbio.2015.11.002
- [9] Andreyeva T, Sturm R, Ringel JS. Moderate and severe obesity have large differences in health care costs. *Obesity Research*. 2004;**12**:1936-1943. DOI: 10.1038/oby.2004.243
- [10] Dee A, Kearns K, O'Neill C, et al. The direct and indirect costs of both overweight and obesity: A systematic review. *BMC Research Notes*. 2014;**7**:242. DOI: 10.1186/1756-0500-7-242
- [11] Tremmel M, Gerdtham UG, Nilsson PM, et al. Economic burden of obesity: A systematic literature review. *International Journal of Environmental Research and Public Health*. 2017;**14**(4):435
- [12] Falagas ME, Kompoti M. Obesity and infection. *The Lancet Infectious Diseases*. 2006;**6**:438e46. DOI: 10.1016/S1473-3099(06)70523-0
- [13] Seabolt LA, Welch EB, Silver HJ. Imaging methods for analyzing body composition in human obesity and cardiometabolic disease. *Annals of the New York Academy of Sciences*. 2015;**1353**:41-59. DOI: 10.1111/nyas.12842
- [14] Azizian H, Kramer JK, Heymsfield SB, et al. Fourier transform near infrared spectroscopy: A newly developed, non-invasive method to measure body fat: Non-invasive body fat content measurement using FT-NIR. *Lipids*. 2008;**43**(1):97-103. DOI: 10.1007/s11745-007-3121-x
- [15] Bernhard AB, Santo MA, Scabim VM, et al. Body composition

- evaluation in severe obesity: A critical review. *Advances in Obesity, Weight Management & Control*. 2016;**4**(6):00113. DOI: 10.15406/aowmc.2016.04.00113
- [16] Stuart B. *Infrared Spectroscopy: Fundamentals and Applications*. England: John Wiley & Sons; 2004. pp. 15-44. DOI: 10.1002/0470011149
- [17] Griffiths PR, Haseth JA. *Fourier Transform Infrared Spectrometry*. 2nd ed. New York: Wiley; 1986. pp. 1240-1241. DOI: 10.1002/bbpc.19860901224
- [18] Stuart B. *Analytical Techniques in Materials Conservation*. Chichester: Wiley; 2007. p. 113. DOI: 10.1002/9780470060520
- [19] Severcan F, Haris P. Fourier transform infrared spectroscopy suggests unfolding of loop structures precedes complete unfolding of pig citrate synthase. *Biopolymers*. 2003;**69**:440-447. DOI: 10.1002/bip.10392
- [20] Severcan F, Sahin I, Kazanci N. Melatonin strongly interacts with zwitterionic model membranes-evidence from Fourier transform infrared spectroscopy and differential scanning calorimetry. *Biochimica et Biophysica Acta (BBA) - Biomembranes*. 2005;**1668**:215-222. DOI: 10.1016/j.bbamem.2004.12.009
- [21] Kazanci N, Severcan F. Concentration dependent different action of tamoxifen on membrane fluidity. *Bioscience Reports*. 2007;**27**(4-5):247-255. DOI: 10.1007/s10540-007-9050-3
- [22] Severcan F, Bozkurt O, Gurbanov R, et al. FT-IR spectroscopy in diagnosis of diabetes in rat animal model. *Journal of Biophotonics*. 2010;**3**:621-631. DOI: 10.1002/jbio.201000016
- [23] Cakmak G, Zorlu F, Severcan M, et al. Screening of protective effect of amifostine on radiation-induced structural and functional variations in rat liver microsomal membranes by FT-IR spectroscopy. *Analytical Chemistry*. 2011;**83**(7):2438-2444. DOI: 10.1021/ac102043p
- [24] Korkmaz F, Severcan F. Effect of progesterone on DPPC membrane: Evidence for lateral phase separation and inverse action in lipid dynamics. *Archives of Biochemistry and Biophysics*. 2005;**440**:141-147. DOI: 10.1016/j.abb.2005.06.013
- [25] Prost R. The influence of the Christiansen effect on I.R. spectra of powders. *Clays and Clay Minerals*. 1973;**21**:363-368
- [26] Oetjen GW, Haseley P. *Freeze-Drying*. 2nd ed. Weinheim: Wiley-VCH Verlag GmbH & Co. KGaA; 2004. DOI: 10.1002/9783527612482.ch5
- [27] Schneider AS, Middaugh CR, Oldewurtel MD. Normal and abnormal red cell membranes. *Journal of Supramolecular Structure*. 1979;**10**: 265-275. DOI: 10.1002/jss.400070405
- [28] Nimtz G. Magic numbers of water molecules bound between lipid bilayers. *Physica Scripta*. 1986;**13**:172-177. DOI: 10.1088/0031-8949
- [29] Quicoho FA. Intermolecular cross-linking of a protein in the crystalline state: Carboxypeptidase-A. *Biochemistry*. 1989;**52**:833-839. DOI: 10.1073/pnas.52.3.833
- [30] Kuhn LA, Siani MA, Pique ME, et al. The interdependence of protein surface topography and bound water molecules revealed by surface accessibility and fractal density measures. *Journal of Molecular Biology*. 1992;**228**:13-22. DOI: 10.1016/0022-2836(92)90487-5

- [31] Cakmak G, Togan I, Severcan F. 17 β -estradiol induced compositional, structural and functional changes on rainbow trout liver, revealed by FTIR spectroscopy: A comparative study with nonylphenol. *Aquatic Toxicology*. 2006;**77**(1):53-63. DOI: 10.1016/j.aquatox.2005.10.015
- [32] Akkas SB, Severcan M, Yilmaz O, et al. Effects of lipoic acid supplementation on rat brain tissue: An FTIR and neural network study. *Food Chemistry*. 2007;**105**(3):1281-1288. DOI: 10.1016/j.foodchem.2007.03.015
- [33] Hoboken NJ. Characterization Analysis of Polymers. New Jersey: Wiley-Interscience; 2008. p. 97. DOI: 10.1021/ja801591j
- [34] Baloglu FK, Ustaoglu SG, Heise S, et al. FTIR imaging of structural changes in visceral and subcutaneous adiposity and brown to white adipocyte trans differentiation. *The Analyst*. 2015;**140**(7):2205-2214. DOI: 10.1039/c4an02008a
- [35] Ustaoglu SG, Evis Z, Ilbay G, et al. Side-effects of convulsive seizures and anti-seizure therapy on bone in a rat model of epilepsy. *Applied Spectroscopy*. 2017;**72**(5):689-705. DOI: 10.1177/0003702817734617
- [36] Toyran N, Lasch P, Naumann D, et al. Early alterations in myocardia and vessels of the diabetic rat heart: An FTIR microspectroscopic study. *The Biochemical Journal*. 2006;**397**(3):427-436. DOI: 10.1042/BJ20060171
- [37] Aparicio S, Doty SB, Camacho NP, et al. Optimal methods for processing mineralized tissues for Fourier transform infrared microspectroscopy. *Calcified Tissue International*. 2002;**70**(5):422-429. DOI: 10.1007/s00223-001-1016-z
- [38] Erben RG. Embedding of bone samples in methylmethacrylate: An improved method suitable for bone histomorphometry, histochemistry, and immunohistochemistry. *The Journal of Histochemistry and Cytochemistry*. 1997;**45**(2):307-313. DOI: 10.1177/002215549704500215
- [39] Garip S, Sahin D, Severcan F. Epileptic seizure-induced structural and functional changes in rat femur and tibia bone tissues: A Fourier transform infrared imaging study. *Journal of Biomedical Optics*. 2013;**18**(11):111409. DOI: 10.1117/1.JBO.18.11.111409
- [40] Feuerstein D, Parker KH, Boutelle MG. Practical methods for noise removal: Applications to spikes, nonstationary quasi-periodic noise, and baseline drift. *Analytical Chemistry*. 2009;**81**:4987-4994. DOI: 10.1021/ac900161x
- [41] Cakmak G, Miller LM, Zorlu F, et al. Amifostine, a radioprotectant agent, protects rat brain tissue lipids against ionizing radiation induced damage: An FTIR microspectroscopic imaging study. *Archives of Biochemistry and Biophysics*. 2012;**520**:67-73. DOI: 10.1016/j.abb.2012.02.012
- [42] Turker S, Ilbay G, Severcan M, et al. The investigation of compositional, structural and dynamical changes of PTZ-induced seizures on a rat brain by FTIR spectroscopy. *Analytical Chemistry*. 2014;**86**(3):1395-1403. DOI: 10.1021/ac402992j
- [43] Baloglu FK, Baloglu O, Heise S, et al. Triglyceride dependent differentiation of obesity in adipose tissues by FTIR spectroscopy coupled with chemometrics. *Journal of Biophotonics*. 2017;**10**(10):1345-1355. DOI: 10.1002/jbio.201600223
- [44] Demir P, Onde S, Severcan F. Phylogeny of cultivated and wild wheat species using ATR-FTIR spectroscopy. *Spectrochimica Acta Part A: Molecular and Biomolecular Spectroscopy*.

2015;**135**:757-763. DOI: 10.1016/j.saa.2014.07.025

[45] Lasch P, Haensch W, Naumann D, et al. Imaging of colorectal adenocarcinoma using FT-IR microspectroscopy and cluster analysis. *Biochimica et Biophysica Acta*. 2004;**1688**:176-178. DOI: 10.1016/j.bbadis.2003.12.006

[46] Pellegrinelli V, Carobbio S, Vidal-Puig A. Adipose tissue plasticity: How fat depots respond differently to pathophysiological cues. *Diabetologia*. 2016;**59**:1075-1088

[47] Giarola M, Guella G, Mariotto G, et al. Vibrational and structural investigations on adipose tissues. *Philosophical Magazine*. 2008;**88**:33-35. DOI: 10.1080/14786430802585141

[48] Tarasiuk A, Mosińska P, Fichna J. The mechanisms linking obesity to colon cancer: An overview. *Obesity Research & Clinical Practice*. 2018;**12**:251-259. DOI: 10.1016/j.orcp.2018.01.005

[49] Dutheil F, Gordon BA, Naughton G, et al. Cardiovascular risk of adipokines: A review. *The Journal of International Medical Research*. 2018;**46**(6):2082-2095. DOI: 10.1177/0300060517706578

[50] Grigoraş A, Amalinei C, Balan RA, et al. Adipocytes spectrum—From homeostasia to obesity and its associated pathology. *Annals of Anatomy*. 2018;**3**:102-120. DOI: 10.1016/j.aanat.2018.06.004

[51] Fain JN, Madan AK, Hiler ML, et al. Comparison of the release of adipokines by adipose tissue, adipose tissue matrix, and adipocytes from visceral and subcutaneous abdominal adipose tissues of obese humans. *Endocrinology*. 2004;**145**(5):2273-2282. DOI: 10.1210/en.2003-1336

[52] Engeli S, Schling P, Gorzelniak K, et al. The adipose-tissue renin-angiotensin-aldosterone system: Role in the metabolic syndrome? *The International Journal of Biochemistry & Cell Biology*. 2003;**35**:807-825. DOI: 10.1016/S1357-2725(02)00311-4

[53] Ruan H, Lodish HF. Insulin resistance in adipose tissue: Direct and indirect effects of tumor necrosis factor- α . *Cytokine & Growth Factor Reviews*. 2003;**14**:447-455. DOI: 10.1016/S1359-6101(03)00052-2

[54] Arner P. The adipocyte in insulin resistance: Key molecules and the impact of the thiazolidinediones. *Trends in Endocrinology and Metabolism*. 2003;**14**:137-145. DOI: 10.1016/S1043-2760(03)00024-9

[55] Rotter V, Nagaev I, Smith U. Interleukin-6 (IL-6) induces insulin resistance in 3T3-L1 adipocytes and is, like IL-8 and tumor necrosis factor- α , overexpressed in human fat cells from insulin-resistant subjects. *The Journal of Biological Chemistry*. 2003;**278**:45777-45784. DOI: 10.1074/jbc.M301977200

[56] Mavri A, Alessi MC, Juhan-Vague I. Hypofibrinolysis in the insulin resistance syndrome: Implication in cardiovascular diseases. *Journal of Internal Medicine*. 2004;**255**:448-456. DOI: 10.1046/j.1365-2796.2003.01288.x

[57] Thogersen AM, Jansson JH, Boman K, et al. High plasminogen activator inhibitor and tissue plasminogen activator levels in plasma precede a first acute myocardial infarction in both men and women: Evidence for the fibrinolytic system as an independent primary risk factor. *Circulation*. 1998;**98**:2241-2247. DOI: 10.1161/circ.98.21.2241

- [58] Cnop M, Lindchild MJ, Vidal J, et al. The concurrent accumulation of intra-abdominal and subcutaneous fat explains the association between insulin resistance and plasma leptin concentrations: Distinct metabolic effects of two fat compartments. *Diabetes*. 2002;**51**:1005-1015. DOI: 10.2337/diabetes.51.4.1005
- [59] HC MG Jr, McMahan CA, Herderick EE, et al. Obesity accelerates the progression of coronary atherosclerosis in young men. *Circulation*. 2002;**105**:2712-2718. DOI: 10.1161/01.CIR.0000018121.67607.CE
- [60] Suk SH, Sacco RL, Boden-Albala B, et al. Abdominal obesity and risk of ischemic stroke: The northern Manhattan stroke study. *Stroke*. 2003;**34**:1586-1592. DOI: 10.1161/01.STR.0000075294.98582.2F
- [61] Wajchenberg BL. Subcutaneous and visceral adipose tissue: Their relation to the metabolic syndrome. *Endocrine Reviews*. 2000;**21**:697-738. DOI: 10.1210/edrv.21.6.0415
- [62] Parekh S, Anania FA. Abnormal lipid and glucose metabolism in obesity: Implications for nonalcoholic fatty liver disease. *Gastroenterology*. 2007;**132**:2191-2207. DOI: 10.1053/j.gastro.2007.03.055
- [63] Karalis KP, Giannogonas P, Kodela E, et al. Mechanisms of obesity and related pathology: Linking immune responses to metabolic stress. *The FEBS Journal*. 2009;**276**:5747-5754. DOI: 10.1111/j.1742-4658.2009.07304.x
- [64] Ariyasu D, Yoshida H, Hasegawa Y. Endoplasmic reticulum (ER) stress and endocrine disorders. *International Journal of Molecular Sciences*. 2017;**18**(2):382. DOI: 10.3390/ijms18020382
- [65] Ozcan U, Qiong Cao Q, Yilmaz E, et al. Endoplasmic reticulum stress links obesity, insulin action, and type 2 diabetes. *Science*. 2004;**306**:457-461. DOI: 10.1126/science.1103160
- [66] Boden G. Obesity and free fatty acids. *Endocrinology and Metabolism Clinics of North America*. 2008;**37**(3):635-646. DOI: 10.1016/j.ecl.2008.06.007
- [67] Movasaghi Z, Rehman S, Rehman I. Fourier transform infrared (FTIR) spectroscopy of biological tissues. *Applied Spectroscopy Reviews*. 2008;**43**(2):134-179. DOI: 10.1080/05704920701829043
- [68] Dogan A, Lasch P, Neuschl C, et al. ATR-FTIR spectroscopy reveals genomic loci regulating the tissue response in high fat diet fed BXD recombinant inbred mouse strains. *BMC Genomics*. 2013;**14**:386. DOI: 10.1186/1471-2164-14-386
- [69] Sen I, Bozkurt O, Aras E, et al. Lipid profiles of adipose and muscle tissues in mouse models of juvenile onset of obesity without high fat diet induction: A Fourier transform infrared (FTIR) spectroscopic study. *Applied Spectroscopy*. 2015;**69**(6):679-688. DOI: 10.1366/14-07443
- [70] Bortolotto JW, Reis C, Ferreira A, et al. Higher content of trans fatty acids in abdominal visceral fat of morbidly obese individuals undergoing bariatric surgery compared to non-obese subjects. *Obesity Surgery*. 2005;**15**(9):1265-1270. DOI: 10.1381/096089205774512375
- [71] Gazi E, Gardner P, Lockyer NP, et al. Direct evidence of lipid translocation between adipocytes and prostate cancer cells with imaging FTIR microspectroscopy. *Journal of Lipid Research*. 2007;**48**(8):1846-1856. DOI: 10.1194/jlr.M700131-JLR200

- [72] Aboualizadeh E, Carmichael OT, He P, et al. Quantifying biochemical alterations in brown and subcutaneous white adipose tissues of mice using fourier transform infrared widefield imaging. *Frontiers in Endocrinology*. 2017;**8**:121. DOI: 10.3389/fendo.2017.00121
- [73] Le Corvec M, Allain C, Lardjane S, et al. Mid-infrared fibre evanescent wave spectroscopy of serum allows fingerprinting of the hepatic metabolic status in mice. *The Analyst*. 2016;**141**(22):6259-6269. DOI: 10.1039/c6an00136j
- [74] Peng CY, Chiappini F, Kascakova S, et al. Vibrational signatures to discriminate liver steatosis grades. *The Analyst*. 2015;**140**(4):1107-1118. DOI: 10.1039/c4an01679c
- [75] Surowka AD, Ziomber A, Czyzycki M, et al. Molecular and elemental effects underlying the biochemical action of transcranial direct current stimulation (tDCS) in appetite control. *Spectrochimica Acta Part A-Molecular and Biomolecular Spectroscopy*. 2018;**195**:199-209. DOI: 10.1016/j.saa.2018.01.061
- [76] Bizeau ME, Solano JM, Hazel JR. Menhaden oil feeding increases lipolysis without changing plasma membrane order in isolated rat adipocytes. *Nutrition Research*. 2000;**20**(11):1633-1644. DOI: 10.1016/S0271-5317(00)00245-1
- [77] Wang JX, Si X, Shang WT, et al. Effect of single or combined administration of resistant starch and chitosan oligosaccharides on insulin resistance in rats fed with a high-fat diet. *Starch-Starke*. 2017;**69**:7-8. DOI: 10.1002/star.201600209
- [78] El-Menshawe SF, Ali AA, Rabeh MA, et al. Nanosized soy phytosome-based thermogel as topical anti-obesity formulation: An approach for acceptable level of evidence of an effective novel herbal weight loss product. *International Journal of Nanomedicine*. 2018;**13**:307-318. DOI: 10.2147/IJN.S153429
- [79] Kumar A, Chauhan GS. Extraction and characterization of pectin from apple pomace and its evaluation as lipase (steapsin) inhibitor. *Carbohydrate Polymers*. 2000;**82**(2):454-459. DOI: 10.1016/j.carbpol.2010.05.001
- [80] Dunkhunthod B, Thumanu K, Eumkeb G. Application of FTIR microspectroscopy for monitoring and discrimination of the anti-adipogenesis activity of baicalein in 3T3-L1 adipocytes. *Vibrational Spectroscopy*. 2017;**89**:92-101. DOI: 10.1016/j.vibspec.2017.01.006

Application of Visible to Near-Infrared Spectroscopy for Non-Destructive Assessment of Quality Parameters of Fruit

Khayelihle Ncama, Lembe S. Magwaza, Asanda Mditshwa and Samson Z. Tesfay

Abstract

The accuracy and robustness of prediction models are very important to the successful commercial application of visible to near-infrared spectroscopy (Vis-NIRS) on fruit. The difference in physiological characteristics of fruit is very wide, which necessitates variance in the type of spectrometers applied to collect spectral data, pre-processing of the collected data and chemometric techniques used to develop robust models. Relevant practices of data collection, processing and the development of models are a challenge because of the required knowledge of fruit physiology in addition to the Vis-NIRS expertise of a researcher. This chapter deals with the application of Vis-NIRS on fruit by discussing commonly used spectrometers, data chemometric treatment and common models developed for assessing quality of specific types of fruit. The chapter intends to create an overview of commonly used techniques for guiding general users of these techniques. Current status, gaps and future perspectives of the application of Vis-NIRS on fruit are also discussed for challenging researchers who are experts in this research field.

Keywords: near-infrared spectroscopy (NIRS), chemometrics, multivariate data, fruit quality

1. Introduction

The quality of fruits is produced in the orchard or garden and only maintained during postharvest storage [1]. This necessitates accurate determination of the optimal harvest time and a deeper understanding of physiological changes occurring in fresh fruit during storage. The main goal of postharvest management is to delay senescence by reducing the ripening processes and other physiological processes such as respiration [2]. The quality of fruit at commercial consignments is commonly assessed using techniques such as reflectometer-based determination of total soluble solutes (TSS), fruit mass or firmness tests [3]. The fruits selected as samples for assessment of parameters such as juice TSS are wasted because after they are destructed they cannot be returned to the batch. Therefore, the quantity sent by a farmer does not reach the destined market in its original quantity. Moreover, the

fruits taken as samples may not properly represent the actual status of the batch. The challenge of sample size is significant in huge farms that require a large number of representative samples. It is also known that fruits from the same batch, same tree and the same branch of a tree are likely to differ in quantities of their quality parameters. It is therefore necessary to find non-destructive alternative techniques that can be used to analyse the entire batch without losing any samples.

Techniques such as mass and firmness determinations do not destruct sample fruit. However, most fruits are very perishable and develop bruises if they experience successive external impact [4, 5]. Moreover, the physical parameters such as mass and firmness cannot be associated to organoleptic qualities with accuracy. A big fruit does not warrant a better taste than a small fruit. Therefore, the elevated purchase price of big fruit based on mass is not a justified technique for customers. The firmness tests can be used to determine the level of ripeness and associated with the edibility of climacteric fruit such as avocado and mango. However, the firmness cannot be directly associated to flavour because flavour is determined by the levels of certain biochemical compounds that should be analysed from the consumed fruit part. It is for these reasons that application of spectrometers is necessary since they can analyse quantities of biochemical compounds without excessive contact with a fruit. Spectrometers can be a very useful tool for growers who want to non-destructively determine fruit parameters that are used to track optimal time of harvesting. Application of hand-held spectrometers on hanging fruit can eliminate the estimation of harvest time using few samples that sometimes do not fully represent the entire orchard [6, 7]. Moreover, they preserve the sample fruit that would be wasted if destructive methods were used. In postharvest storage, visible and near-infrared spectroscopy (Vis-NIRS) can be applied in various forms where fruit would be passed under a radiation chamber and be analysed for physical, chemical and organoleptic properties whilst rolling on sorting belts [8]. The Vis-NIRS holds many advantages over destructive or contact techniques. Analyses of every fruit in a batch, mechanised precision that lasts longer than human effort and reduction of fruit waste as a result of specified management are among major benefits that can be obtained from Vis-NIRS applications.

2. Spectrometers commonly applied in acquisition of spectra from fruit

The trade names may differ from one supplier to the other. However, the type of spectrometers commonly used can be properly categorised based on their operation mode. Vis-NIRS operates in three common modes: the reflectance, transmittance and interactance (diffuse reflectance) modes [9]. Reflectance is the most common mode of acquiring spectra from fresh fruit. Although it can be associated with the type of spectrometers commonly available, it is also a less restricted mode compared to others. Other modes such as transmittance would require that the radiation passes through the sample fruit which is sometimes inefficient because radiation may not reach the other side of a fruit due to disturbances such as a stone, seeds or hollow spaces inside the fruit. Hereon, the common spectrometers applied on specific fruit types will be reviewed and associated with the botanic characteristics of the fruit.

2.1 Stone (drupe) fruits

Stone fruit, also called drupe fruit, is an indehiscent fruit characterised by a thin sheet as exocarp, fleshy mesocarps and a hard endocarp. The hard endocarp usually contains a single seed and is referred to as a stone because of its high firmness [10]. Examples of drupe fruit are peaches, nectarines, plums, lychees, mangoes, avocados

and cherries. Application of Vis-NIRS on stone fruit for assessing organoleptic parameters requires awareness about the stone that can interfere with radiation. As a result, most researchers would avoid using spectrometers that use transmittance mode as most radiation is likely to be deflected or absorbed by the stone inside the fruit. Spectrometers working on reflectance and interactance modes are the most relevant methods if the analysis is not associated with a stone [11]. The choice of a spectrometer can depend on the assessed fruit quality. Transmittance mode would be appropriate if the objective is to analyse the size or hardness of the stone.

The appropriateness of reflectance mode is achieved when the spectra are collected for assessing parameters in the mesocarp. Assuming that the number of streams illuminated by the spectrometer (n) is 4, **Figure 1** illustrates the assumption of radiation paths the radiation can pass through if the hypothetical radiation is applied in three different modes. One, three or one of the four arrays reaches the sensor if a transmittance, reflectance or interactance mode is used, respectively.

2.2 Berry or aggregate fruits

Botanically, a berry or aggregate fruit is made up of more than one seed containing fruitlets produced from a single ovary [12]. Common examples include citrus, banana, pineapples, cucumber, tomatoes and grapes. The term berry fruit is commonly used to refer to small pulpy fruit with thin coat-like exocarp tissues covering the fleshy edible mesocarp. Examples of fleshy berries are strawberries, raspberries, mulberries, blackberries, blueberries, redcurrants and blackcurrants. The main factor of consideration in application of Vis-NIRS on aggregate fruit is that the fruit is formed as a combination of smaller fruit which can vary in biochemical composition [13]. The uneven ripeness of berry fruit is significant on vine fruit such as grapes, which may necessitate the use of spectrometers that consider each fruit in the bunch as a single fruit. Any mode of spectrometer can be used on aggregate fruit. This is due to their fleshy internal structure and few or tiny seeds interfering with the radiation passing through the fruit. However, the important consideration is that the size of the radiation source is fully covered and the fruit size can enable passage of radiation from the source to the detector if the transmittance mode is used. Lammertyn et al. [14] investigated the distance that a light beam can penetrate into the fruit. The authors found that there was a wavelength-dependent effect that showed that the regions in 700–900 and 900–1900 nm reach around 4 and 2–3 mm,

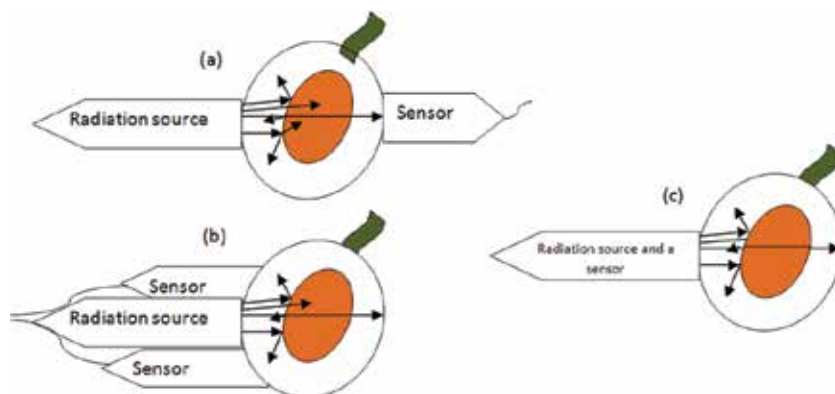


Figure 1.

The assumption of possible radiation pathways inside a stone fruit. (a) Is the transmittance mode, (b) is the illustration of reflectance mode and (c) is the interactance mode and their ability to obtain the required information from only the mesocarp of the fruit.

respectively, which showed that a more intensified illumination was required to obtain a penetration of greater depth if the transmittance spectrum was required.

2.3 Pome fruit

Pome fruit are characterised by a thin exocarp, edible mesocarp and a soft endocarp. Their seeds are in the part called an endocarp or a pit which is relatively harder than the edible mesocarp but softer than the endocarp of stone fruit [15, 16]. Common examples of pome fruit are apples, pears, cotoneaster, crataegus (hawthorn and mayhaw), loquat, medlar, pyracantha, toyon, quince, rowan and white-beam fruit. Application of Vis-NIRS on pome fruit can be in any form depending on the objective of the assessment. The hardness of endocarp can be used as a measure of maturity of pome fruit [17, 18]. If maturity is assessed, the endocarp is not considered as interference in the transmittance mode which requires radiation to pass through the fruit. However, the endocarp is likely to differ from one fruit to another irrespective of common characteristics such as maturity stage or size. Two fruits of the same maturity stage and the same size may have a different number of seeds. Using transmittance mode can reduce the assessment accuracy when the quality parameters of interest are in the mesocarp.

3. Chemometric treatment of spectral data obtained from fruit

Most spectrometers acquire a full visible to near infrared radiation spectra ranging from 450 to 2500 nm. However, theory suggests that organic components with concentrations higher than 0.1% in fruit have their particular range on the visible or near-infrared wavelengths that result to their best reflection [9]. As such, most researchers always select specific ranges where the analysed compound is likely to respond. However, some fruit quality parameters may be best reflected by the entire spectra [19]. The use of the full spectral range is somehow superior to using specific ranges since it provides a wide source of reference points along the spectrum. The general steps of chemometric analysis applied to spectral data collected from fruit are (i) selecting the wavelength range, (ii) pre-processing raw data to derivatives, (iii) calibrating prediction models and (iv) validating the performance of the developed models on independent external test set. Based on the objective of the study, a researcher can either develop quantitative or qualitative models.

The necessary results that authors show are after validation. The most important model parameters of reference are correlation coefficient (R^2) and the root mean squared error of prediction (RMSEP). A good model is selected based on high R^2 value and low RMSEP value which are the main parameters of consideration, although there are other parameters such as the ratio of performance deviation (RPD) and bias. RPD is widely used as a reference parameter of the performance of prediction models. However, there is lack of information on how was the system developed, and the relationship between the R^2 values and RPD values is in exponential form, whilst it should be linear if both values can be used as references to judge models' accuracy [20]. Therefore, the most necessary parameter is the R^2 value because of its simplicity and a traceable statistical development of its relevance. The R^2 values range from 0 (poor model) to 1 (best model), and anything in between can be related to its proximity to the mentioned extremes. The RPD values cannot be simplified to that level of stating the maximum and minimum values. Several authors refer to Chang et al. [21] who invented the three quality categories of model reliability: excellent models ($RPD > 2$), fair models ($1.4 < RPD < 2$) and non-reliable models ($RPD < 1.4$). However, those authors did not give any statistical basis of the mentioned thresholds.

3.1 Quantitative models

Quantitative Vis-NIRS models are those that estimate the exact quantity of a physical or biochemical compound. They hold a higher advantage in the assessment of quality parameters that cannot be categorised into distinct groups but characterised by a continuous range. Partial least square (PLS) regression (PLSR) is arguably the most used quantitative model by researchers. In PLS models, an orthogonal basis of latent variables is constructed one by one in such a way that they are oriented along directions of maximal covariance between the spectral matrix and the response value [22]. The technique was introduced by Herman Wold in 1975 as an improved modification to overcome collinearity of multiple linear regressions [23]. A unique feature of basic PLS regression is its simplicity. The basic PLS method consists of a series of simple least square optimisation called nonlinear iterative partial least squares NIPALS; [24]. The PLS technique also accounts for noisy and redundant spectral variables and can analyse more than one chemical variables at once.

The majority of recent research reports are based on its different manipulations. As a result, models such as interval partial least squares (iPLS), interval successive projection algorithm (iSPA-PLS), moving window partial least squares (MWPLS) and other PLS modifications were introduced or reinvented in the last decade [25–27]. The PLS modelling was developed by Wold in 1981 [28], and majority of researchers have referred to it as a pivot point of regression models. The following section looks at the common quantitative models for specific types of fruit. Hereon, examples of studies that developed quantitative models for stone fruit and nuts (**Table 1**), berries and aggregate fruit (**Table 2**) and pome fruit (**Table 3**) are reviewed.

Fruit	Assessed quality parameter(s)	NIR mode used	Spectral range	Vis-NIRS models developed	Reference
Almond	Amygdalin content	Diffuse reflectance mode	888–1795 nm	PLS	[29]
Date	TSS, moisture content and colour	Reflectance	285–1200 nm	PCR	[30]
Jaboticaba	Total anthocyanin content	Reflectance	714–2500 nm	iSPA-PLS, PLS and GA-PLS	[25]
Mango	TSS, firmness, TA and rind pitting index	Reflectance	700–1100 nm	PLS	[31]
Olives	Fat content, moisture and free acidity	Reflectance	380–1690 nm	PLS and LS-SVM	[32]
Peach	Days before decay	Reflectance	900–2500 nm	PLS, LS-SVM and MFRG	[33]
Plums	SSC, TA, juice pH, TSS/TA and firmness	Interactance	500–1010 nm	PLS	[34]

LS-SVM, least squares support vector machine; MFRG, multiple fitting regression based on Gaussian fitting function; PLS, partial least squares regression; PCA-LDA, principal component analysis-linear discriminant analysis; SPA-LDA, successive projection algorithm-linear discriminant analysis; GA-LDA, genetic algorithm-linear discriminant analysis; PCR, principal component regression.

Table 1.
 Application of Vis-NIRS for assessing quality parameters of stone fruits or nuts.

Fruit	Assessed quality parameters	NIR mode used	Spectral range	Vis-NIRS models developed	Reference
Blackberries, wild blueberries, raspberries, redcurrants and strawberries	Total phenolic compounds and antioxidant activity	Reflectance	904–1699 nm	PLS	[35]
<i>Citrullus colocynthis</i>	Total polyphenol content	Absorbance	700–2500 nm	PLS	[36]
Mandarins and oranges	Mass, colour, fruit diameter, firmness, pericarp thickness and juice mass	Reflectance	1600–2400 nm	MWPLS	[26]
Mulberry	SSC	Reflectance	400–2500 nm	PLS	[19]
Pineapple	Nitrate level	Interactance	600–1200 nm	PLS	[37]
Strawberry	TSS and pH	Reflectance	10,494–3673 cm ⁻¹	SIMPLS	[38]
Strawberry	TSS	Interactance	4000–10,000 cm ⁻¹	iPLS and MWPLS	[27]
Tomato	Firmness	Reflectance	500–1700 nm	PLS	[34]
Watermelon	Lycopene, β-carotene and TSS	Reflectance	900–1700 nm	PLS	[8]

PLS, partial least squares regression; SIMPLS, soft independent modelling partial least squares regression; iPLS, interval partial least squares; MWPLS, moving window partial least squares.

Table 2.
Application of Vis-NIRS for assessing quality of berry or aggregate fruit.

Fruit	Assessed quality parameters	NIR mode used	Spectral range	Vis-NIRS models developed	Reference
Apple	SSC	Interactance	500–1100 nm	PLS	[39]
Loquat	Moisture content	Reflectance	750–2500 nm	PLS	[40]
Pears	TSS	Reflectance	710–930 nm	PLS	[41]
Pears	SSC	Reflectance	930–2548 nm	PLS	[42]
Pears	SSC and firmness	Absorbance	500–1010 nm	PLS and MLR	[43]
Persimmon	Astringency and tannin contents	Interactance and transmittance	600–1100 nm	PLS	[44]
Wax jambu	Total phenolic compound content	Interactance	1000–2400 nm	PLS	[45]

PLS, partial least square regression; MLR, multiple linear regression.

Table 3.
Application of Vis-NIRS for assessing quality of pome fruit.

Fruit	Classification parameter	NIR mode used	Spectral range	Vis-NIRS models developed	Reference
Almond	Amygdalin content	Interactance	888–1795 nm	LDA, QDA and PLS-DA	[28]
Hazelnuts	Regions and cultivars	Transmittance	650–4000 cm^{-1}	PCA, LDA and PLS-DA	[47]
Almond nuts	Concealed damage	Reflectance	1125–2153 nm	PLS-DA	[48]
Jaboticaba	Cultivars	Reflectance	1000–2500 nm	PCA-LDA, SPA-LDA and GA-LDA	[49]
Macadamia nuts	Variety	Reflectance	11,544–3952 cm^{-1}	PCA-LDA and GA-LDA	[50]
Peach	Cultivars	Reflectance	800–2600 nm	PCA, UVE-PLS and SPA	[39]
Pine nuts	Geographic origin	Reflectance	400–2500 nm	PLS-DA	[51]

LDA, linear discriminant analysis; QDA, quadratic discriminant analysis; PCA, principal component analysis; PLS-DA, partial least squares regression discriminant analysis; UVE-PLS, uninformative variable elimination based on partial least squares; PCA, principal component analysis; SPA, successive projection algorithm; PCA-LDA, principal component analysis-linear discriminant analysis; GA-LDA, genetic algorithm-linear discriminant analysis.

Table 4.
Application of Vis-NIRS for classification of stone fruit and nuts.

Fruit	Classification parameter	NIR mode used	Spectral range	Vis-NIRS models developed	Reference
Blackberries, wild blueberries, raspberries, redcurrants and strawberries	Total phenolic compounds and antioxidant activity	Reflectance	904–1699 nm	PCA	[35]
Citrus	Firmness	Reflectance	400–1750 cm^{-1}	Raman signal	[52]
Mulberry leaf	Pesticide residue	Reflectance	390–1050 nm	PLS-DA	[53]
Nectarine	Variety	Reflectance	360–1795 nm	LDA and PLS-DA	[28]
Strawberry	Organic and conventionally grown fruit	Reflectance	12,500–3600 cm^{-1}	PLS-DA	[38]
Tomato fruit	Ripeness	Interactance	400–1000 nm	PLS-DA	[54]
Tomato fruit	Lycopene content	Reflectance	275–1150 nm	PLS-DA	[55]

LDA, linear discriminant analysis; PCA, principal component analysis; PLS-DA, partial least squares regression discriminant analysis.

Table 5.
Applications of Vis-NIRS for classification of berry or aggregate fruit.

Fruit	Classification parameter	NIR mode used	Spectral range	Vis-NIRS models developed	Reference
Apples	Cultivars	Reflectance	4000–10,000 cm ⁻¹	Fuzzy linear discriminant analysis and fuzzy c-means clustering	[56]
Apples	Bitter pit	Reflectance	971.2–1142.8 nm	QDA and SVM	[57]
Apples	Bitter pit	Reflectance	935–2500 nm	Spectral pattern recognition	[58]
Apples	Cultivars	Reflectance	1000–2500 nm	PCA	[59]
Apples	Separating organic and inorganic fruit	Reflectance	900–1700 nm	Spectral pattern recognition and PLS-DA	[60]
Apples	Internal browning	Reflectance	740–1040 nm	Spectral pattern recognition	[61]
Chinese quince fruit	Varieties	Reflectance	1000–2500 nm	LDA, QDA and SVM	[62]
Persimmon fruit	Fruit origin	Reflectance	740–2700 nm	PCA and LS-SVM	[63]

LDA, linear discriminant analysis; QDA, quadratic discriminant analysis; PCA, principal component analysis; PLS-DA, partial least squares regression discriminant analysis; SVM, support vector machine; PCA, principal component analysis.

Table 6.
Application of Vis-NIRS for classification of pome fruit.

3.2 Classification models

Most fruit growers classify their crop into different quality classes in order to state their selling price and target different markets. Fruit destined for a local market may not be at the same level of quality as fruit destined for exports to international markets. Fruit can be sorted based on their maturity level, colour, origin, size and other characteristics of interest to consumers. This necessitates an effective way of classifying many fruits at short period of time. The Vis-NIRS technique has been shown to have an ability to assess a minimum of three fruits per second [46], which is way faster than the potential of a human panel normally used on commercial scales. The following tables exemplify the studies that demonstrated the ability of Vis-NIRS to classify stone fruit and nuts (**Table 4**), berry and aggregate fruit (**Table 5**) and pome fruit (**Table 6**). Notably, researchers have an extended freedom of choice in selecting classification models compared with quantification models. However, partial least square discriminant analysis (PLS-DA) and linear discriminant analysis (LDA) are the commonly used models for fruit. Discriminant analyses use a principal component analysis (PCA) for extracting, compressing and screening multivariate data such as spectra. The PCA technique employs a mathematical procedure that transforms a set of response variables into a set of non-correlated variables called principal components. PCA produces linear combinations of variables that are useful descriptors or even predictors of some particular structure in the data matrix [64]. Although typically used for spectral data, different classification models can also be used for mapping data matrix of any type.

4. Current status of spectroscopy application on fruits

4.1 Vis-NIRS application on fresh fruit

There are a great number of studies demonstrating the capability of Vis-NIRS to accurately assess biochemical and physical quality parameters of fruit. The commonly assessed compounds of fresh fruit include sugar contents, acidity, juice pH, pectin, firmness, etc. because of their direct link with being referred to as sorting categories [9]. Secondary factors of quality such as bruising, scars and other disorders are not commonly assessed. However, some studies have assessed factors indirectly associated with fruit quality such as postharvest disorders. The ability of Vis-NIRS to assess invisible internal disorders such as brown heart disorder of pears has been demonstrated [65]. Magwaza et al. [66] demonstrated the ability of Vis-NIRS to detect rind breakdown disorder of mandarins. The detection of presymptomatic attributes leading to disorders has also been demonstrated successfully on fresh fruit. Ncama et al. [67] demonstrated the ability of Vis-NIRS to detect susceptibility of fresh grapefruit to rind pitting disorder occurring in postharvest storage. The extent of Vis-NIRS application has been reported from the stable laboratory-based instruments, portal instruments and in sorting lines. The most fascinating studies were those that demonstrated the ability of Vis-NIRS to assess the quality of fruit in motion on sorting lines. Salguero-Chaparro and Peña-Rodríguez [32] successfully quantified the contents of fats, free acidity and moisture of intact olives using a system mounted on the conveyor belt. Such studies were a clear demonstration of the period at which commercial fruit growers should adopt the Vis-NIRS technique for sorting their fruit.

4.2 The application of Vis-NIRS on secondary products from fruits

Studies demonstrating the ability of Vis-NIRS on assessing quality of slices of fresh fruit are common. The importance of monitoring their quality can be associated to their altered respiration rate which may result to degradation of their quality at an elevated rate. Fruits have hard sheet-like peels that regulate their respiration and protect the flesh from carbon dioxide that leads to development of the browning pigments. It is for this reason that careful quality management is crucial after removing the exocarp of fruit.

Dried fruits have little biological activities occurring during their storage. As such, they have extended life span compared to fresh fruit. Their low biological activities only necessitate the determination of parameters associated to edibility such as taste and flavour only once immediately after the drying process. When fruits are dried, their taste parameters are nearly fixed. After the drying stage, the necessary factors to analyse are the protective substances such as biochemical compounds related with antifungal or antibacterial activities if their quality is also threatened by infections. On the other hand, juices and wines are judged by holding true to the manufacturer's flavour. This therefore calls for each and every bottle to hold similar characteristics to keep a trusting trade with customers. It is not the flavour-related parameters that require rapid assessment using Vis-NIRS but secondary metabolites associated to flavour such as phenolic compounds, vitamins, chloride, sulphate and mineral contents [68, 69]. The maturity stage (alcohol strength) of wines during fermentation can increase the accuracy of management. Rapid determination of titratable acidity of apple wine using Vis-NIRS during the fermentation process was demonstrated by Peng et al. [70].

Wine ageing in wooden barrels is aligned with improved final sensory profile and, therefore, price of purchase. It is for this reason that the process used during wine ageing needs to be traceable for insurance of trustworthy trading standards. Basalekou et al. [71] demonstrated the ability of Vis-NIRS to discriminate different wines based on variety, type of barrel and ageing time. Magdas et al. [72] demonstrated rapid discrimination of wines based on variety, vintage and geographic origin. The shelf life of wines and juices may also be predicted inversely by determination of fermentation and adulteration compounds. The common spectra acquisition mode used on liquid fruit product is the transmittance mode. This is due to the uniformity of the liquid texture which does not deflect radiation throughout the sample. The light that is not absorbed by the liquid is then reported to a spectrometer as an absorbance spectrum. Fourier transform Raman spectroscopy method is the common type of spectra collected [73, 74]. However, Teixeira dos Santos et al. [69] revealed a better suitability of mid-infrared spectroscopy (87.7% of correct predictions) over near-infrared (60.4%) and Raman spectroscopy (60.8%) on classifying wines based on geographic origin.

5. Future perspectives

There are a lot of studies that demonstrated the ability of assessing quality of fruit by application of Vis-NIRS. The application of Vis-NIRS has been tested and approved on many varieties of fruit from different geographic conditions. Different data collection, pre-processing and chemometric analysis methods and different kinds of prediction models have been developed and demonstrated to accurately assess fruit quality. The next research step in this field is very hard to point out. Arguably, it is the right time to consider Vis-NIRS as an ordinary method of assessing quality parameters of fruit. Studies with an objective of demonstrating the application of Vis-NIRS with different modes, on different fruit or fruit cultivars, or using different chemometric methods and selecting the best method are no longer contributing any novelty of interest in research. Such experiments are most relevant to technicians who want to calibrate spectrometers for use in commercial lines but not as research investigations.

Significant recent research reports on demonstrating new application methods and new chemometric techniques or developing new types of models. To our knowledge, no report has defied the accuracy of PLS models. The reports then become unnecessary from the application point of view. As long as the ordinary PLS model or its modified forms are able to obtain 97% prediction accuracy on analysing TSS [75, 76], they are better than using the destructive reflectometer technique. As long as PLS models can obtain 90% accuracy on analysing total phenolic compounds [77, 78], they are better than the use of procedures based on protocols involving the use of chemicals and sophisticated laboratory equipment. Illustrating ways of increasing the accuracy of PLS models is of course important, but it does not contribute any novelty in the research. Vis-NIRS has been demonstrated in online systems [32], which should have been a signal that it is no longer new and can be a commonly used technique. The only novelty of intrigue to technicians would be developing models that hold 100% accuracy, which is also not astonishing because Vis-NIRS models are assessed based on predicting reference values of a parameter that is assessed by destructive techniques. Destructive techniques may have had errors and inaccuracies that arose from a non-calibrated human potency. Vis-NIRS can accurately predict incorrect reference data and create a precise model with incorrect calibration.

6. Conclusion

The research world has greatly demonstrated the potential of Vis-NIRS application for assessing quality of fruit. But the technique is still not common on commercial lines. The Vis-NIRS scarcity on commercial lines could be associated to the expensive prices of the spectrometers compared to weighing scales. As such, most supermarkets may choose to use the mass of fruit to determine the purchase price although not accurate since a big fruit does not give a warrant of a satisfying flavour. The fresh horticultural produce industry is one of the few food industries that do not indicate the nutritional characteristics of their product. Most processed food stuff has a table of contents of carbohydrates, fats, vitamins, etc. indicated on their containers. Customers nowadays are willing to pay extra prices for high nutritious fruit [9]. The nutritional information of fruit could be easily indicated if the Vis-NIRS technique is adapted in the market. Therefore, trustworthy trade relationship could be easily achieved since the biochemical components of fruit could be associated with the purchasing price. Buying the instrument is a once-off expense that will improve the industry for as long as there is no other superior technology invented. The next step in research should focus on gathering information or reasons that result to distributors and end market sellers not willing to adapt using Vis-NIRS. Teaching the public about Vis-NIRS is necessary because most people are not scientists and may not understand the safety of applying radiation on their food. It should be remembered that some people believe that biotechnology used to produce genetically modified organisms is a source of toxic food escalating diseases such as cancer [79].

Conflict of interest

Khayelihle Ncama obtained financial support from the Citrus Academy and National Research Foundation for scarce skills. Lembe S. Magwaza received NRF grant for y-rated researchers (Grant No. 112101).

Author details


Khayelihle Ncama^{1*}, Lembe S. Magwaza², Asanda Mditshwa² and Samson Z. Tesfay²

1 Department of Crop Science, North West University, Mmabatho, South Africa

2 Discipline of Crop and Horticultural Science, University of KwaZulu-Natal, Scottsville, South Africa

*Address all correspondence to: khae.ncama@gmail.com

IntechOpen

© 2018 The Author(s). Licensee IntechOpen. This chapter is distributed under the terms of the Creative Commons Attribution License (<http://creativecommons.org/licenses/by/3.0>), which permits unrestricted use, distribution, and reproduction in any medium, provided the original work is properly cited. 

References

- [1] Ncama K, Magwaza LS, Mditshwa A, Tesfay SZ. Plant-based edible coatings for managing postharvest quality of fresh horticultural produce: A review. *Food Packaging and Shelf Life*. 2018;**16**:157-167. DOI: 10.1016/j.fpsl.2018.03.011
- [2] Mditshwa A, Magwaza LS, Tesfay SZ, Mbili N. Postharvest quality and composition of organically and conventionally produced fruits: A review. *Scientia Horticulturae*. 2017;**216**:148-159. DOI: 10.1016/j.scienta.2016.12.033
- [3] Shewfelt RL. Measuring quality and maturity. In: *Postharvest Handling*. 3rd ed. Athens, Georgia, USA: Food Science and Technology, University of Georgia; 2014. pp. 387-410. DOI: 10.1016/B978-0-12-408137-6.00014-4
- [4] Xu R, Takeda F, Krewer G, Li C. Measure of mechanical impacts in commercial blueberry packing lines and potential damage to blueberry fruit. *Postharvest Biology and Technology*. 2015;**110**:103-113. DOI: 10.1016/j.postharvbio.2015.07.013
- [5] Jiménez MR, Rallo P, Suárez MP, Rapoport HF, Morales-Sillero A, Lerma LC. Assessment of quantitative parameters for evaluating impact bruising structural damage in olive fruit tissue. *Scientia Horticulturae*. 2017;**224**:293-295. DOI: 10.1016/j.scienta.2017.06.027
- [6] Ribera-Fonseca A, Noferini M, Jorquera-Fontena E, Rombolà AD. Assessment of technological maturity parameters and anthocyanins in berries of cv. Sangiovese (*Vitis vinifera* L.) by a portable Vis/NIR device. *Scientia Horticulturae*. 2016;**209**:229-235. DOI: 10.1016/j.scienta.2016.06.004
- [7] Wang Z, Walsh KB, Verma B. On-tree mango fruit size estimation using RGB-D images. *Sensors*. 2017;**17**(12):2738. DOI: 10.3390/s17122738
- [8] Tamburini E, Costa S, Rugiero I, Pedrini P, Marchetti MG. Quantification of lycopene, β -carotene, and total soluble solids in intact red-flesh watermelon (*Citrullus lanatus*) using on-line near-infrared spectroscopy. *Sensors*. 2017;**17**(4):746. DOI: 10.3390/s17040746
- [9] Lin H, Ying Y. Theory and application of near infrared spectroscopy in assessment of fruit quality: A review. *Sensors & Instruments in Food Quality*. 2009;**3**:130-141. DOI: 10.1007/s11694-009-9079-z
- [10] Kader AA. *Postharvest Technology of Horticultural Crops*. California: University of California Agriculture and Natural Resources; 2002. pp. 535, Vol. 3311
- [11] Nicolai BM, Beullens K, Bobelyn E, Peirs A, Saeys W, Theron KI, et al. Nondestructive measurement of fruit and vegetable quality by means of NIR spectroscopy: A review. *Postharvest Biology and Technology*. 2007;**46**(2):99-118. DOI: 10.1016/j.postharvbio.2007.06.024
- [12] Coombe BG. The development of fleshy fruits. *Annual Review of Plant Physiology*. 1976;**27**(1):207-228. DOI: 10.1146/annurev.pp.27.060176.001231
- [13] Guthrie JA, Liebenberg CJ, Walsh KB. NIR model development and robustness in prediction of melon fruit total soluble solids. *Australian Journal of Agricultural Research*. 2006;**57**(4): 411-418. DOI: 10.1071/AR05123
- [14] Lammertyn J, Peirs A, De Baerdemaeker J, Nicolai B. Light penetration properties of NIR radiation in fruit with respect to non-destructive quality assessment. *Postharvest Biology and Technology*. 2000;**18**(2):121-132. DOI: 10.1016/S0925-5214(99)00071-X

- [15] MacDaniels LH. Morphology of the Apple and Others Pome Fruits. Ithaca, New York: Cornell University, Agricultural Experiment Station; 1940
- [16] Knee M. Pome fruits. In: Biochemistry of Fruit Ripening. Dordrecht: Springer; 1993. pp. 325-346. DOI: 10.1007/978-94-011-1584-1_11
- [17] Martínez-Gómez P, Sánchez-Pérez R, Dicenta F. Fruit development in almond for fresh consumption. Journal American Pomological Society. 2008;**62**(2):82
- [18] Rapoport HF, Pérez-López D, Hammami SBM, Agüera J, Moriana A. Fruit pit hardening: Physical measurement during olive fruit growth. Annals of Applied Biology. 2013;**163**(2):200-208. DOI: 10.1111/aab.12046
- [19] Hui Y, Cheng G, Dandan D, Xia L, Li L, Mengxing L, et al. Establishment of partial least square regression model for determination of soluble solid content in mulberry fruit by handheld near infrared spectrometer. Science of Sericulture. 2016;**6**:020
- [20] Minasny B, McBratney A. Why you don't need to use RPD. Pedomtron. 2013;**33**:14-15
- [21] Chang CW, Laird DA, Mausbach MJ, Hurburgh CR. Near-infrared reflectance spectroscopy-principal components regression analyses of soil properties. Soil Science Society of America Journal. 2001;**65**:480-490. DOI: 10.2136/sssaj2001.652480x
- [22] Jamshidi B, Minaei S, Mohajerani E, Ghassemian H. Reflectance Vis/NIR spectroscopy for nondestructive taste characterization of Valencia oranges. Computers and Electronics in Agriculture. 2012;**85**:64-69
- [23] Wold S, Trygg J, Berglund AH. Some recent developments in PLS modeling. Chemometrics and Intelligent Laboratory Systems. 2001;**58**(2):131-150
- [24] De Jong S, Phatak A. Partial least squares regression. Recent advances in total least squares techniques and errors-in-variables modelling. Philadelphia: Society of Industrial Applied Mathematics; 1997. pp. 25-36
- [25] Mariani NCT, de Almeida Teixeira GH, de Lima KMG, Morgenstern TB, Nardini V, Júnior LCC. Vis-NIRS and iSPA-PLS for predicting total anthocyanin content in Jaboticaba fruit. Food Chemistry. 2015;**174**:643-648. DOI: 10.1016/j.foodchem.2014.11.008
- [26] Torres I, Pérez-Marín D, De la Haba MJ, Sánchez MT. Developing universal models for the prediction of physical quality in citrus fruits analysed on-tree using portable Vis-NIRS sensors. Biosystems Engineering. 2017;**153**:140-148. DOI: 10.1016/j.biosystemseng.2016.11.007
- [27] Chen H, Liu Z, Cai K, Xu L, Chen A. Grid search parametric optimization for FT-NIR quantitative analysis of solid soluble content in strawberry samples. Vibrational Spectroscopy. 2018;**94**:7-15. DOI: 10.1016/j.vibspec.2017.10.006
- [28] Cortés V, Blasco J, Aleixos N, Cubero S, Talens P. Visible and near-infrared diffuse reflectance spectroscopy for fast qualitative and quantitative assessment of nectarine quality. Food and Bioprocess Technology. 2017;**10**(10):1755-1766. DOI: 10.1007/s11947-017-1943-y
- [29] Cortés V, Talens P, Barat JM, Lerma-García MJ. Potential of NIR spectroscopy to predict amygdalin content established by HPLC in intact almonds and classification based on almond bitterness. Food Control. 2018;**91**:68-75. DOI: 10.1016/j.foodcont.2018.03.040
- [30] Alhamdan AM, Atia A. Non-destructive method to predict Barhi dates quality at different stages of maturity utilising near-infrared (NIR)

- spectroscopy. *International Journal of Food Properties*. 2018;**20**:1-10. DOI: 10.1080/10942912.2017.1387794
- [31] Rungpichayapichet P, Mahayothee B, Nagle M, Khuwijitjaru P, Müller J. Robust Vis-NIRS models for non-destructive prediction of postharvest fruit ripeness and quality in mango. *Postharvest Biology and Technology*. 2016;**111**:31-40. DOI: 10.1016/j.postharvbio.2015.07.006
- [32] Salguero-Chaparro L, Peña-Rodríguez F. On-line versus off-line Vis-NIRS analysis of intact olives. *LWT—Food Science and Technology*. 2014;**56**(2):363-369. DOI: 10.1111/jfpe.12593
- [33] Huang Y, Lu R, Chen K. Prediction of firmness parameters of tomatoes by portable visible and near-infrared spectroscopy. *Journal of Food Engineering*. 2018;**222**:185-198. DOI: 10.1016/j.jfoodeng.2017.11.030
- [34] Li M, Lv W, Zhao R, Guo H, Liu J, Han D. Non-destructive assessment of quality parameters in 'Foriar' plums during low temperature storage using visible/near infrared spectroscopy. *Food Control*. 2017;**73**:1334-1341. DOI: 10.1016/j.foodcont.2016.10.054
- [35] Gajdoš Kljusurić J, Mihalev K, Bečić I, Polović I, Georgieva M, Djaković S, et al. Near-infrared spectroscopic analysis of total phenolic content and antioxidant activity of berry fruits. *Food Technology and Biotechnology*. 2016;**54**(2):236-242. DOI: 10.17113/ftb.54.02.16.4095
- [36] Rizvi TS, Mabood F, Ali L, Al-Broumi M, Al Rabani HK, Hussain J, et al.. Application of NIR spectroscopy coupled with PLS regression for quantification of total polyphenol contents from the fruit and aerial parts of *Citrullus colocynthis*. *Phytochemical Analysis*. 2018;**29**(1): 16-22. DOI: 10.1002/pca.2710
- [37] Srivichien S, Terdwongworakul A, Teerachaichayut S. Quantitative prediction of nitrate level in intact pineapple using Vis-NIRS. *Journal of Food Engineering*. 2015;**150**:29-34. DOI: 10.1016/j.jfoodeng.2014.11.004
- [38] Amodio ML, Ceglie F, Chaudhry MMA, Piazzolla F, Colelli G. Potential of NIR spectroscopy for predicting internal quality and discriminating among strawberry fruits from different production systems. *Postharvest Biology and Technology*. 2017;**125**:112-121. DOI: 10.1016/j.postharvbio.2016.11.013
- [39] Guo W, Gu J, Liu D, Shang L. Peach variety identification using near-infrared diffuse reflectance spectroscopy. *Computers and Electronics in Agriculture*. 2016;**123**:297-303. DOI: 10.1016/j.compag.2016.03.005
- [40] Li LL, Wang HX, Ling P, Ji SG. Application of near-infrared spectroscopy in determination of moisture content in *Eriobotrya japonica*. *Chinese Journal of Experiments in Traditional Medicine Formulae*. 2013;**19**:104-107
- [41] Choi JH, Chen PA, Lee B, Yim SH, Kim MS, Bae YS, et al. Portable, non-destructive tester integrating VIS/NIR reflectance spectroscopy for the detection of sugar content in Asian pears. *Scientia Horticulturae*. 2017;**220**:147-153. DOI: 10.1016/j.scienta.2017.03.050
- [42] Li J, Tian X, Huang W, Zhang B, Fan S. Application of long-wave near infrared hyperspectral imaging for measurement of soluble solid content (SSC) in pear. *Food Analytical Methods*. 2016;**9**(11):3087-3098. DOI: 10.1007/s12161-016-0498-2
- [43] Wang J, Wang J, Chen Z, Han D. Development of multi-cultivar models for predicting the soluble solid content and firmness of European pear (*Pyrus communis* L.) using portable Vis-NIR

- spectroscopy. *Postharvest Biology and Technology*. 2017;**129**:143-151. DOI: 10.1016/j.postharvbio.2017.03.012
- [44] Noypitak S, Terdwongworakul A, Krisanapook K, Kasemsumran S. Evaluation of astringency and tannin content in 'Xichu' persimmons using near infrared spectroscopy. *International Journal of Food Properties*. 2015;**18**(5):1014-1028. DOI: 10.1080/10942912.2014.884577
- [45] Viegas TR, Mata AL, Duarte MM, Lima KM. Determination of quality attributes in wax jambu fruit using Vis-NIRS and PLS. *Food Chemistry*. 2016;**190**:1-4. DOI: 10.1016/j.foodchem.2015.05.063
- [46] Bellon V, Vigneau JL, Sévila F. Infrared and near-infrared technology for the food industry and agricultural uses: On-line applications. *Food Control*. 1994;**5**(1):21-27. DOI: 10.1016/0956-7135(94)90129-5
- [47] Manfredi M, Robotti E, Quasso F, Mazzucco E, Calabrese G, Marengo E. Fast classification of hazelnut cultivars through portable infrared spectroscopy and chemometrics. *Spectrochimica Acta Part A: Molecular and Biomolecular Spectroscopy*. 2018;**189**:427-435. DOI: 10.1016/j.saa.2017.08.050
- [48] Rogel-Castillo C, Boulton R, Opastpongkarn A, Huang G, Mitchell AE. Use of near-infrared spectroscopy and chemometrics for the non-destructive identification of concealed damage in raw almonds (*Prunus dulcis*). *Journal of Agricultural and Food Chemistry*. 2016;**64**(29):5958-5962. DOI: 10.1021/acs.jafc.6b01828
- [49] Costa RC, Junior LCC, Morgenstern TB, de Almeida Teixeira GH, de Lima KMG. Classification of Jaboticaba fruits at three maturity stages using Vis-NIRS and LDA. *Analytical Methods*. 2016;**8**(11):2533-2538. DOI: 10.1039/C5AY03212A
- [50] Carvalho LC, Morais CL, Lima KM, Leite GW, Oliveira GS, Casagrande IP, et al. Using intact nuts and near infrared spectroscopy to classify Macadamia cultivars. *Food Analytical Methods*. 2017;**1**:1-10. DOI: 10.1007/s12161-017-1078-9
- [51] Loewe V, Navarro-Cerrillo RM, García-Olmo J, Riccioli C, Sánchez-Cuesta R. Discriminant analysis of Mediterranean pine nuts (*Pinus pinea* L.) from Chilean plantations by near infrared spectroscopy (Vis-NIRS). *Food Control*. 2017;**73**:634-643. DOI: 10.1016/j.foodcont.2016.09.012
- [52] Nekvapil F, Brezestean I, Barchewitz D, Glamuzina B, Chiş V, Pinzaru SC. Citrus fruits freshness assessment using Raman spectroscopy. *Food Chemistry*. 2018;**242**:560-567. DOI: 10.1016/j.foodchem.2017.09.105
- [53] Lu XZ, Jun SUN, Ning YANG, Zhang JL. Discrimination of absence or presence of pesticide residue in mulberry leaf using VIS-NIR hyperspectral imaging and Plsda. *DEStech Transactions on Engineering and Technology Research (icca)*. Gyeongju, Korea: International Conference on Control and Automation (ICCA 2016); 2016. DOI: 10.12783/dtetr/icca2016/5996. ISBN: 978-1-60595-329-8
- [54] Zhu Q, He C, Lu R, Mendoza F, Cen H. Ripeness evaluation of 'sun bright' tomato using optical absorption and scattering properties. *Postharvest Biology and Technology*. 2015;**103**:27-34. DOI: 10.1016/j.postharvbio.2015.02.007
- [55] Clément A, Dorais M, Vernon M. Nondestructive measurement of fresh tomato lycopene content and other physicochemical characteristics using visible-NIR spectroscopy. *Journal of Agricultural and Food Chemistry*. 2008;**56**(21):9813-9818. DOI: 10.1021/jf801299r

- [56] Wu X, Wu B, Sun J, Yang N. Classification of apple varieties using near infrared reflectance spectroscopy and fuzzy discriminant C-means clustering model. *Journal of Food Process Engineering*. 2017;**40**(2). DOI: 10.1111/jfpe.12355
- [57] Kafle GK, Khot LR, Jarolmasjed S, Yongsheng S, Lewis K. Robustness of near infrared spectroscopy based spectral features for non-destructive bitter pit detection in “honey crisp” apples. *Postharvest Biology and Technology*. 2016;**120**:188-192
- [58] Jarolmasjed S, Espinoza CZ, Sankaran S. Near infrared spectroscopy to predict bitter pit development in different varieties of apples. *Journal of Food Measurement and Characterization*. 2017;**11**(3): 987-993. DOI: 10.1007/s11694-017-9473-x
- [59] Eisenstecken D, Panarese A, Robatscher P, Huck CW, Zanella A, Oberhuber M. A near infrared spectroscopy (Vis-NIRS) and chemometric approach to improve apple fruit quality management: A case study on the cultivars “Cripps pink” and “Braeburn”. *Molecules*. 2015;**20**(8):13603-13619. DOI: 10.3390/molecules200813603
- [60] Song W, Wang H, Maguire P, Nibouche O. Differentiation of organic and non-organic apples using near infrared reflectance spectroscopy—A pattern recognition approach. In: *Sensors*. 2016 IEEE; 2016. pp. 1-3
- [61] Vanoli M, Rizzolo A, Grassi M, Spinelli L, Verlinden BE, Torricelli A. Studies on classification models to discriminate ‘Braeburn’ apples affected by internal browning using the optical properties measured by time-resolved reflectance spectroscopy. *Postharvest Biology and Technology*. 2014;**91**:112-121. DOI: 10.1016/j.postharvbio.2014.01.002
- [62] Shao W, Li Y, Diao S, Jiang J, Dong R. Rapid classification of Chinese quince (*Chaenomeles speciosa* Nakai) fruit provenance by near-infrared spectroscopy and multivariate calibration. *Analytical and Bioanalytical Chemistry*. 2017;**409**(1):115-120. DOI: 10.1007/s00216-016-9944-7
- [63] Khanmohammadi M, Karami F, Mir-Marqués A, Garmarudi AB, Garrigues S, De La Guardia M. Classification of persimmon fruit origin by near infrared spectrometry and least squares-support vector machines. *Journal of Food Engineering*. 2014;**142**:17-22. DOI: 10.1016/j.jfoodeng.2014.06.003
- [64] Cozzolino D, Cynkar WU, Shah N, Smith P. Multivariate data analysis applied to spectroscopy: Potential application to juice and fruit quality. *Food Research International*. 2011;**44**(7):1888-1896. DOI: 10.1016/j.foodres.2011.01.041
- [65] Wang M, Feng X. Progress on near-infrared non-destructive testing technology of pears. *Journal of Food Safety and Quality*. 2014;**5**(3):681-690. DOI: j.foodsq.20143147415
- [66] Magwaza LS, Opara UL, Cronje PJ, Landahl S, Nieuwoudt HH, Mouazen AM, et al. Assessment of rind quality of ‘Nules Clementine’ mandarin fruit during postharvest storage: 2. Robust Vis/Vis-NIRS PLS models for prediction of physico-chemical attributes. *Scientia Horticulturae*. 2014;**165**:421-432. DOI: 10.1016/j.scienta.2013.09.050
- [67] Ncama K, Tesfay SZ, Fawole OA, Opara UL, Magwaza LS. Non-destructive prediction of ‘Marsh’ grapefruit susceptibility to postharvest rind pitting disorder using reflectance Vis/NIR spectroscopy. *Scientia Horticulturae*. 2018;**231**:265-271. DOI: 10.1016/j.scienta.2017.12.028

- [68] Teixeira dos Santos TA, Pascoa RNMJ, Porto PALS, Cerdeira AL, Lopes JA. Application of Fourier-transform infrared spectroscopy for the determination of chloride and sulfate in wines. *LWT-Food Science and Technology*. 2016;**67**:181-186. DOI: 10.1021/jf001196p
- [69] Teixeira dos Santos CA, Páscoa RNMJ, Sarraguça MC, Porto PALS, Cerdeira AL, González-Sáiz JM, et al. Merging vibrational spectroscopic data for wine classification according to the geographic origin. *Food Research International*. 2017;**102**:504-510. DOI: 10.1016/j.foodres.2017.09.018
- [70] Peng B, Ge N, Cui L, Zhao H. Monitoring of alcohol strength and titratable acidity of apple wine during fermentation using near-infrared spectroscopy. *LWT—Food Science and Technology*. 2016;**66**:86-92. DOI: 10.1016/j.lwt.2015.10.018
- [71] Basalekou M, Pappas C, Tarantilis P, Kotseridis Y, Kallithraka S. Wine authentication with Fourier transform infrared spectroscopy: A feasibility study on variety, type of barrel wood and ageing time classification. *International Journal of Food Science and Technology*. 2017;**52**:1307-1313. DOI: 10.1111/ijfs.13424
- [72] Magdas DA, Guyon F, Feher I, Pinzaru SC. Wine discrimination based on chemometric analysis of untargeted markers using FT-Raman spectroscopy. *Food Control*. 2018;**85**:385-391. DOI: 10.1016/j.foodcont.2017.10.024
- [73] Martin C, Bruneel J, Guyon F, Médina B, Jourdes M, Teissedre P, et al. Raman spectroscopy of white wines. *Food Chemistry*. 2015;**181**:235-240. DOI: 10.1016/j.foodchem.2015.02.076
- [74] Mandrile L, Zeppa G, Giovannozzi AM, Rossi AM. Controlling protected designation of origin of wine by Raman spectroscopy. *Food Chemistry*. 2016;**211**:260-267. DOI: 10.1016/j.foodchem.2016.05.011
- [75] Liu C, Yang SX, Deng L. A comparative study for least angle regression on NIR spectra analysis to determine internal qualities of navel oranges. *Expert Systems with Applications*. 2015;**42**(22):8497-8503. DOI: 10.1016/j.eswa.2015.07.005
- [76] Ncama K, Tesfay SZ, Opara UL, Fawole OA, Magwaza LS. Non-destructive prediction of 'Valencia' orange (*Citrus sinensis*) and 'Star Ruby' grapefruit (*Citrus × paradisi* Macfad) internal quality parameters using Vis/NIRS. In: VIII International Postharvest Symposium: Enhancing Supply Chain and Consumer Benefits-Ethical and Technological 1194; 2016. pp. 1119-1126
- [77] Mora-Ruiz ME, Reboredo-Rodríguez P, Salvador MD, González-Barreiro C, Cancho-Grande B, Simal-Gándara J, et al. Assessment of polar phenolic compounds of virgin olive oil by NIR and mid-IR spectroscopy and their impact on quality. *European Journal of Lipid Science and Technology*. 2017;**119**(1). DOI: 10.1002/ejlt.201600099
- [78] Genisheva Z, Quintelas C, Mesquita DP, Ferreira EC, Oliveira JM, Amaral AL. New PLS analysis approach to wine volatile compounds characterization by near infrared spectroscopy (NIR). *Food Chemistry*. 2018;**246**:172-178. DOI: 10.1016/j.foodchem.2017.11.015
- [79] Bredahl L. Determinants of consumer attitudes and purchase intentions with regard to genetically modified food—results of a cross-national survey. *Journal of Consumer Policy*. 2001;**24**(1):23-61. DOI: 10.1023/A:1010950406128

IR-Spectroscopy of Radiation-Stimulated Processes of Adsorption, Radiolysis, and Hydrogenation on the Surface of Metals in Contact with Hydrocarbons

Nushaba Gadzhieva

Abstract

This chapter presents the results of IR spectroscopic studies of radiation-stimulated heterogeneous processes of adsorption, radiation-chemical decomposition (radiolysis) of hydrocarbons on the metal surface, and radiative hydrogenation of these surfaces under the action of gamma radiation. It deals with the spectrokinetic regularities, their features, and the mechanisms of radiation-stimulated adsorption and radiolysis of hydrocarbons in heterogeneous metal-hydrocarbon systems, in particular in heterogeneous Al (Be)-n-hexane systems, using reflection-absorption IR spectroscopy (IRRAS). The role of intermediate surface-active decomposition products in the process of heterogeneous radiolysis of hydrocarbons is discussed, as well as the influence of the surface relief of the metal in the dynamics of the change in the decomposition process on the rate of formation and the yield of final products of radiolysis.

Keywords: reflection-absorption IR spectroscopy, metal (Al, Be), hydrocarbons (n-hexane), gamma radiation, radiation-stimulated adsorption, radiolysis, hydrogenation

1. Introduction

At present, the development of radiation materials science; radiation catalysis; nuclear, space, and laser technology and nanotechnology; and technologies using radiation and high-energy particles has led to the formation of a new promising direction—radiation-heterogeneous processes (RHP) in contact with various phases. Obtaining a package of experimental data and information on the study of RHP using complex physical-chemical methods, including spectroscopic methods, also opens up new opportunities for solving a number of problems on the surface of metals and oxides. The activated metal surface accelerates the radiation-chemical decomposition of paraffins and increases the efficiency of hydrogen production in the radiolysis of hydrocarbons. At the same time, surface adsorption of paraffins significantly influences the course of the radiation-heterogeneous decomposition

process and, therefore, the yield of radiolysis products. In the literature, there are a number of experimental and theoretical studies devoted to the study of the interaction and activation of paraffins on the surface of metals [1–4].

However, until now, the problems associated with the adsorption of hydrocarbons on the radiation-modified surface of metals have not been studied sufficiently [5–8]. In fact, there are no data on the radiation-chemical decomposition of hydrocarbons on the surface of metals and the radiation hydrogenation of these surfaces under the influence of gamma radiation. This chapter presents the results of work on IR spectroscopic studies of radiation-stimulated heterogeneous processes of adsorption, radiolysis, and hydrogenation on the surface of metals in contact with hydrocarbons [5–17].

2. Objects and methods of research

2.1 Objects

Metal plates of aluminum (Al) and beryllium (Be) reactor materials having a smooth polished surface with a high reflection coefficient ($R = 0.88 + 0.05$) in the middle IR region ($\lambda = 2.2\text{--}25\ \mu\text{m}$) were used and investigated [9, 10]. As the hydrocarbon adsorbate, the authors selected unsaturated pairs of n-hexane ($\text{n-C}_6\text{H}_{14}$), the purification and adsorption of which are described in detail in [10, 11]. The formation of gaseous decomposition products—molecular hydrogen and hydrocarbons—was monitored chromatographically and spectroscopically. IR absorption spectra of gaseous hydrocarbons were obtained in a gas cuvette with an optical path length of $\sim 1\ \text{m}$. Radiation-chemical yields of these products have been determined [12]. The heterosystem Al (Be)/ads.n-hexane was irradiated with γ -quanta on an isotope ^{60}Co source with dose rates $d\Phi_\gamma/dt = 0.80$ and $1.03\ \text{Gy/s}$ at room temperature. The absorbed dose was $\Phi_\gamma = 0.5\text{--}120\ \text{kGy}$.

2.2 Method of IR reflection-absorption spectroscopy (IRRAS)

Molecular vibrational spectroscopy of substances in various aggregate states has long and firmly established itself as a method for studying their structure, properties, and all kinds of transformations in external interactions. Similar information on the adsorbed state of molecular systems would be of great value. However, it is not possible to mechanically transfer to it the whole arsenal of experimental, theoretical, and calculated methods of vibrational spectroscopy. In the experimental plan, the main difficulty is that a useful optical signal turns out to be small and, in the end, one must deal with a very poor signal-to-noise ratio, since a small number of molecules (at the level of one monomolecular layer) participate in the absorption, emission, or scattering events.

In the IR range, for measurement of the vibrational spectra of thin films on metals with a nanosized scale, the most promising are methods in which the probe electric field has a maximum intensity on a smooth surface of the metal or very close to it. This condition is satisfied when the grazing angle effect is applied to the metal in the IR reflection-absorption spectroscopy (IRRAS) method [18]. The advantage of this method is the wide range of wavelengths available for investigation. One of the most important conditions for successful application of methods of vibrational spectroscopy is a wide range of the spectrum, usually $200\text{--}4000\ \text{cm}^{-1}$ —the area of the “fingerprint” of the overwhelming number of molecular systems, where most of the vibrational frequencies fall. In this respect, the IRRAS method seems to be the most wide-range and practical than the method of surface electromagnetic wave spectroscopy (SEW), which has high sensitivity. Therefore, in obtaining the spectra

of the reflection of oxides in the region of lattice vibrations, in studying radiation-heterogeneous adsorption processes, in the transformation of water and hydrocarbon molecules, and in studying the processes of oxidation and hydrogenation of aluminum and beryllium metals in contact with water and n-hexane. The choice of this method is due to the fact that it has already proved itself as a noncontact non-destructive optical probing method in the study of adsorbed molecules and oxide films on metal surfaces. The IRRAS method allows one to simultaneously obtain complete information about some chemical stages of radiation-heterogeneous transformations in metal-water, metal-hydrocarbon systems, the formation of adsorption—and catalytically active surface functional groups, and also to trace the formation of oxide and hydride films during oxidation and hydrogenation metal.

According to the theory of IRRAS [18], the efficiency of the interaction of infrared radiation with a smooth metal surface is achieved with incidence close to a sliding (i.e., close to 90°) and with p-polarization. This method is sensitive to the components of the dipole moments of vibrational transitions in thin films perpendicular to the metal surface.

The IR reflection spectra at the drop of linearly polarized radiation on the sample at an angle close to the sliding angle $\varphi = 88^\circ$ were measured at room temperature by means of a special reflecting device (Shimadzu, Japan), adapted to Specord 75 IR spectrophotometer, as well as Harrick prefixes. The optical scheme of the prefix of reflection with the angle of incidence of rays near 88° collected on the base of the attachment “Harrick” is shown in **Figure 1**. Mirror 1 sent a beam of radiation to the surface of sample 2 (for the axial beam $\varphi_0 = 88^\circ \pm 0.5^\circ$). Narrow mirrors 3 and 4 of a special shape, as well as screen 7, provided passage through the prefix to only those rays for which the angle of incidence on the sample lay in the interval $\varphi_0 - 1^\circ < \varphi < \varphi_0 + 1^\circ$. The screens in front of mirror 2, which were not shown in the figure, made it possible to illuminate a part of the sample surface occupied by the film and located between two horizontal dashed lines.

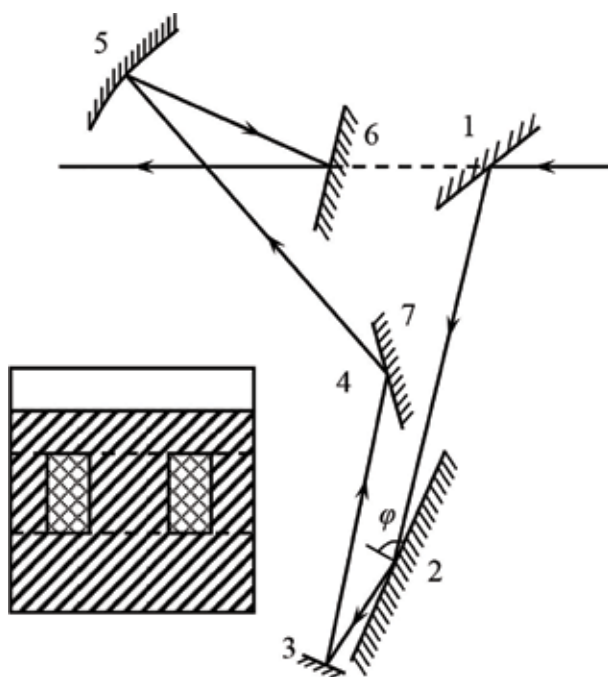


Figure 1. Optical scheme of the attachment of reflection: 1,4,6 - flat mirrors, 5 - concave mirror, 7 - screen, φ - angle of incidence of radiation on the sample. The inset shows the sample used.

After reflection from the rotary mirror 6, the radiation was directed to the detector (receiver). At $\varphi = 88^\circ$, the rays reflected from the entire illuminated surface of the sample were captured. When using a reflection attachment, polarizers in the form of Al gratings were placed in both channels of the spectrophotometer on plates of KRS-5 with a polarization degree of 99%, which transmitted radiation polarized parallel to the plane of incidence of radiation on the sample. Another hand-held ZnS polarizer was also used. The IR reflection spectra at the drop of linearly polarized radiation on the sample at an angle close to the sliding ($\varphi = 88^\circ$) were measured in the region of wavenumbers $\nu = 3400\text{--}650\text{ cm}^{-1}$ at room temperature. The optical densities of the absorption bands were determined from $D = -\lg(R/R_0)$. According to this formula, the optical densities D and D_0 of the bands of stretching vibrations C—H and Me—H of adsorbed n-hexane (D_0 —optical density in the initial sample, D —in the processed samples) were calculated and their ratios D/D_0 were determined [18].

3. Radiation-stimulated adsorption of n-hexane on the surface of aluminum and beryllium

In this section, we present and discuss the results of experimental studies devoted to the spectroscopic study of radiation-stimulated adsorption of hydrocarbons, in particular n-hexane, on the surface of reactor materials—metal plates of aluminum and beryllium. To this end, the authors used the IR reflection-absorption spectroscopy method and developed a special vacuum optical cell that takes into account the specifics of conducting radiation studies. Let's consider some important aspects of this IR research, which in our opinion are the most interesting.

IR absorption spectra of n-hexane in the stretching vibration region of CH adsorbed on the dehydroxylated aluminum surface at room temperature are presented in **Figure 2a** (curve 1) [8, 10]. As can be seen from the figure, the adsorption of n-hexane on the aluminum surface is accompanied by the formation of a number of absorption bands (a.b.): narrow ones at $\nu_{\max} = 2950$ and 2920 cm^{-1} , weak at 2900 and 2880 cm^{-1} and intense wide at 2680 cm^{-1} . The narrow bands are close in position to the bands characteristic of $\nu(\text{CH})$ in the spectra of n-C₆H₁₄ in the gas phase [19], which allows them to be attributed to physically adsorbed n-hexane. An

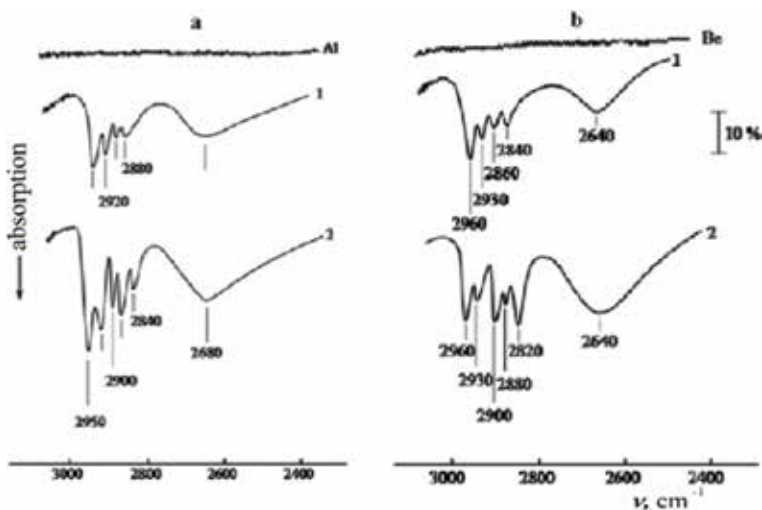


Figure 2. IR absorption spectra of n-hexane adsorbed on the surface of aluminum (a) and beryllium (b): 1—initial and 2— γ -irradiated at $\Phi_\gamma = 10\text{ kGy}$, $T = 300\text{ K}$, $P = 20\text{ Pa}$.

asymmetric broad band with a maximum at 2680 cm^{-1} is attributed to the vibration of one of the C—H bonds in the n-C₆H₁₄ molecule perturbed by the surface centers of aluminum. The unusually low frequency of oscillations, as well as the relatively high intensity and width, indicates a strong perturbation of n-hexane molecules upon adsorption. The complex to which this a.b. object belongs is not stable and is destroyed by evacuation at room temperature. This allows us to classify this band as n-hexane adsorbed in molecular form.

The formation of a molecular complex was theoretically proved in the framework of an ab initio quantum chemical calculation of the profile of the potential energy of dissociative methane adsorption on the Ni surface and was experimentally established when studying its adsorption on metallic surfaces (Fe, Ni, Pt) [20]. Weak a.b. with maxima at 2900 and 2880 cm^{-1} indicate a slight dissociative adsorption of n-hexane on the Al surface, which is associated with even lower concentrations of such forms than for H-bound complexes, especially at a relatively low interaction temperature.

When studying the adsorption of n-hexane on preliminarily γ -irradiated aluminum samples, we found that starting from certain values of the irradiation dose ($\Phi_\gamma = 10\text{ kGy}$) at room temperature, strong dissociative chemisorption is observed (**Figure 2a**, curve 2). It occurs as a result of the interaction of n-hexane with surface-active centers formed under the action of γ -quanta in aluminum. This is evidenced by the increase and redistribution of the intensities of a.b. at 2900 and 2880 cm^{-1} , as well as the appearance in the IR spectrum of a new a.b. with a maximum at 2840 cm^{-1} . The observed absorption bands apparently belong to the stretching vibrations of the CH bonds of the fragments CH₃, C₂H₅, etc. bound by aluminum (aluminum alkyls) [6–8, 10].

The dissociative adsorption is also confirmed by the appearance in the region of $2000\text{--}1700\text{ cm}^{-1}$ of bands with frequencies of 1920 , 1830 , and 1760 cm^{-1} of Al—H bonds in the IR spectrum, which are related to surface aluminum hydrides [3, 4]. The formation of hydrides in the interaction of n-hexane with aluminum is consistent with the hydride mechanism of interaction of metals with hydrocarbons [4, 6–8].

In order to reveal the spectrokinetic regularities of radiation-stimulated adsorption of n-hexane on the aluminum surface, the kinetic adsorption curves, that is, the dependence of the changes in the relative optical densities of the D/D₀ bands of the molecularly and dissociatively adsorbed n-hexane forms on the absorbed dose of irradiation, were studied. The spectra are shown in **Figure 3a**. As can be seen from **Figure 3a** (curve 1), the kinetic feature of radiation-stimulated chemisorption consists of a certain initial induction period at $\Phi_\gamma \leq 5\text{ kGy}$, related to the healing of biographical defects, the linear region at $2 \leq \Phi_\gamma \leq 25\text{ kGy}$, caused by the generation of adsorption active centers and the adsorption of additional n-C₆H₁₄ molecules at these centers, as well as from the stationary saturation region occurring at $\Phi_\gamma > 25\text{ kGy}$.

Apparently, under the action of γ -radiation in aluminum, new active surface states are generated, whose density increases with increasing γ -radiation dose in aluminum, and the probability of their interaction with adsorbed n-hexane molecules increases, which causes their dissociation. At the same time, the kinetic curve of molecularly adsorbed n-hexane is characterized by two regions: in the region $5 \leq \Phi_\gamma \leq 10\text{ kGy}$, formation is observed, and at $\Phi_\gamma > 10\text{ kGy}$, the molecular H-complex decays (**Figure 3a**, curve 2). The presence of activated dissociative chemisorption in the region $5 \leq \Phi_\gamma \leq 25\text{ kGy}$ is also confirmed by the course of the kinetic curve obtained for surface aluminum hydrides (**Figure 3b**).

Thus, in the region of absorbed dose $5 \leq \Phi_\gamma \leq 25\text{ kGy}$, activated dissociative chemisorption is detected, which is explained both by an increase in the number of centers of activated adsorption due to surface-excited states of aluminum with

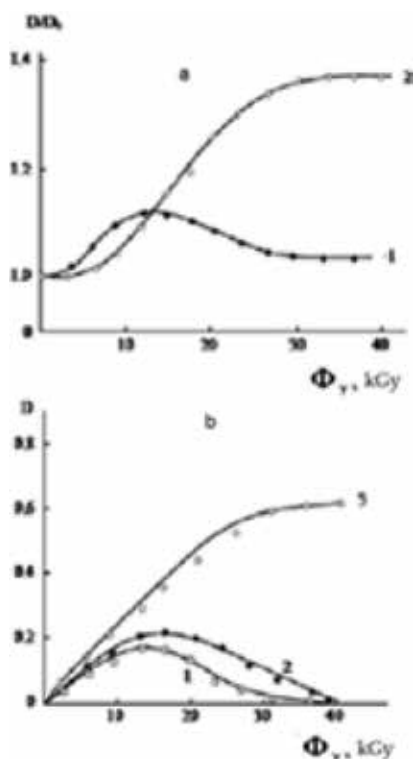


Figure 3.

(a) Dependences of the relative optical densities of the bands molecularly (1) and dissociative (2) adsorbed *n*-hexane from the absorbed γ -irradiation dose in the Al/ads.*n*-hexane heterosystem: $\nu_{\max} = 2680$ (1) and 2880 cm^{-1} (2). (b) Dependences of the optical densities of the absorption bands of aluminum surface hydrides on the absorbed dose of γ -irradiation: $\nu_{\max} = 1920$ (1b), 1830 (2b) and 1760 cm^{-1} (3b).

increasing γ -radiation dose and by decomposition of H-bound complexes as a result of energy transfer excitation to *n*-hexane molecules. Activated adsorption of *n*-hexane was also observed on the nickel surface [1, 20], and according to [1, 21], dissociative adsorption of methane on metals is usually activated. Similar results were also obtained in the study of the radiation-stimulated adsorption of *n*-hexane on the beryllium surface. The observed narrow bands refer to physically adsorbed *n*-hexane. The asymmetric broad band with a maximum at 2640 cm^{-1} is attributed to the vibration of one of the C—H bonds in the $\text{n-C}_6\text{H}_{14}$ molecule perturbed by the surface centers of beryllium. The unusually low frequency of oscillations, and also the relatively high intensity and width ($\nu_{1/2} = 50 \text{ cm}^{-1}$) indicate a strong perturbation of *n*-hexane molecules during adsorption. This band refers to *n*-hexane adsorbed in the molecular form. Weak a.b. with peaks at 2860 and 2840 cm^{-1} indicate a slight dissociative adsorption of *n*-hexane on the Be surface. When studying the adsorption of *n*-hexane on preirradiated beryllium samples, it was established that starting from certain values of the irradiation dose ($\Phi_\gamma = 10 \text{ kGy}$), strong dissociative chemisorption is observed at room temperature (**Figure 2b**, curve 2). It occurs as a result of the interaction of *n*-hexane with surface-active centers formed under the action of γ -quanta in beryllium. This is evidenced by the appearance in the IR spectrum of new a.b. with maxima at 2860 and 2820 cm^{-1} . The observed absorption bands seem to refer to stretching vibrations of the C—H bonds of the fragments CH_3 , C_2H_5 , etc., associated with beryllium (beryllium alkyls) [14, 15]. The dissociative adsorption is also

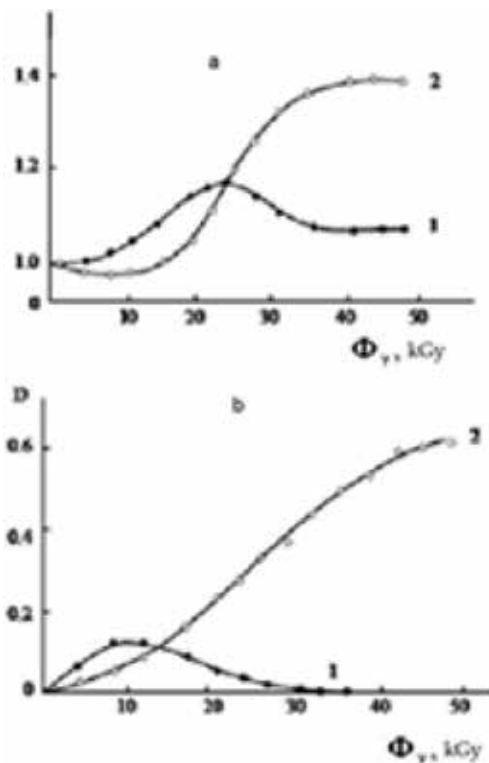


Figure 4.

Dependence on the absorbed dose of gamma irradiation in the Be-adsorbed n-hexane system of the relative optical densities of the bands molecularly (1) and dissociatively (2) adsorbed n-hexane (a) and optical densities of absorption bands of surface beryllium hydrides (b): $\nu_{max} = 2640$ (1a), 2880 (2a), 1790 (1b), and 1740 cm^{-1} (2b).

confirmed by the appearance in the IR spectrum in the $2000\text{--}1700\text{ cm}^{-1}$ region of bands with frequencies of 1790 and 1740 cm^{-1} , which relate to the Be—H bonds of surface beryllium hydrides [14, 15]. The kinetic curves of radiation-stimulated adsorption of n-hexane on the beryllium surface have also been studied in [14] (Figure 4). It was found that the kinetic feature of radiation-stimulated chemisorption consists of a certain initial induction period at $\Phi_\gamma \leq 10$ kGy, a linear region at $10 \leq \Phi_\gamma \leq 25$ kGy, and also from a stationary saturation region at $\Phi > 25$ kGy. Apparently, the generation of new active surface states under the action of γ -radiation in beryllium, the density of which increases with increasing dose of γ -radiation in beryllium, and the probability of their interaction with adsorbed n-hexane molecules, which causes their dissociation. At the same time, the kinetic curve of molecularly adsorbed n-hexane is characterized by two regions. It is seen that the kinetic feature of radiation-stimulated adsorption in the $5 \leq \Phi_\gamma \leq 10$ kGy region is observed, and at $\Phi_\gamma > 10$ kGy, the molecular H-complex decays (Figure 4a, curve 2). The presence of activated dissociative chemisorption in the region $5 \leq \Phi_\gamma \leq 25$ kGy is also confirmed by the kinetic curve obtained for surface beryllium hydrides (Figure 4b).

Thus, in the region of absorbed dose $5 \leq \Phi_\gamma \leq 10$ kGy, activated dissociative chemisorption is detected, which is explained both by an increase in the number of centers of activated adsorption due to surface excited beryllium states with increasing dose of γ -radiation and by decomposition of H-bound complexes as a result of transmission excitation energy to n-hexane molecules.

4. Radiation-chemical transformation (radiolysis) of n-hexane on the surface of aluminum and beryllium

In this section, some aspects of IR spectroscopic studies of the radiation-chemical transformation of n-hexane on the surface of aluminum and beryllium at room temperature are made to determine the role of surface intermediate-active particles and their products in the dynamics of changes in the radiolysis process.

The IR spectra of the reflection of the Al/ads.n-hexane heterosystem before (curve 1) and after the action of γ -quanta (curves 2–4) at room temperature in the frequency range $\nu = 3500\text{--}650\text{ cm}^{-1}$ are shown in **Figure 5**. Changes in the spectra were observed in both the region of stretching (**Figure 5a**) and deformation vibrations of C—H (**Figure 5b**). It is seen that in the unirradiated heterosystem after the adsorption of n-hexane on the aluminum surface in the stretching vibration region of CH there is an appearance of absorption bands (a.b.) indicating the occurrence of three forms of adsorption: physical adsorption (narrow bands at $\nu_{\max} = 2950$ and 2920 cm^{-1}), the molecular form of adsorption (intense broad band at 2680 cm^{-1}), and insignificant dissociative chemisorption (weak bands at 2900 and 2880 cm^{-1}) (**Figure 5a**, curve 1). The flow of three forms of adsorption is also confirmed by the formation of a number of bands in the region of deformation vibrations of C—H with maxima at $\nu_{\max} = 1540, 1480, 1460, 1400,$ and 1360 cm^{-1} (**Figure 5b**, curve 1).

Irradiation of the Al/ads.n-hexane heterosystem by γ -quanta at $\Phi_{\gamma} = 10\text{ kGy}$ leads to the formation of additional a.b. in the spectra. (**Figure 5a** and **b**, curves 2), which indicates the radiation-chemical decomposition of n-hexane on the Al surface. Radiolysis of n-hexane in the Al/ads.n-hexane system in the stretching vibration region of C—H (ν_{CH}) is accompanied by the disappearance of the a.b. at 2950 and 2920 cm^{-1} , a decrease in the intensity of the broad band at 2680 cm^{-1} and its narrowing and

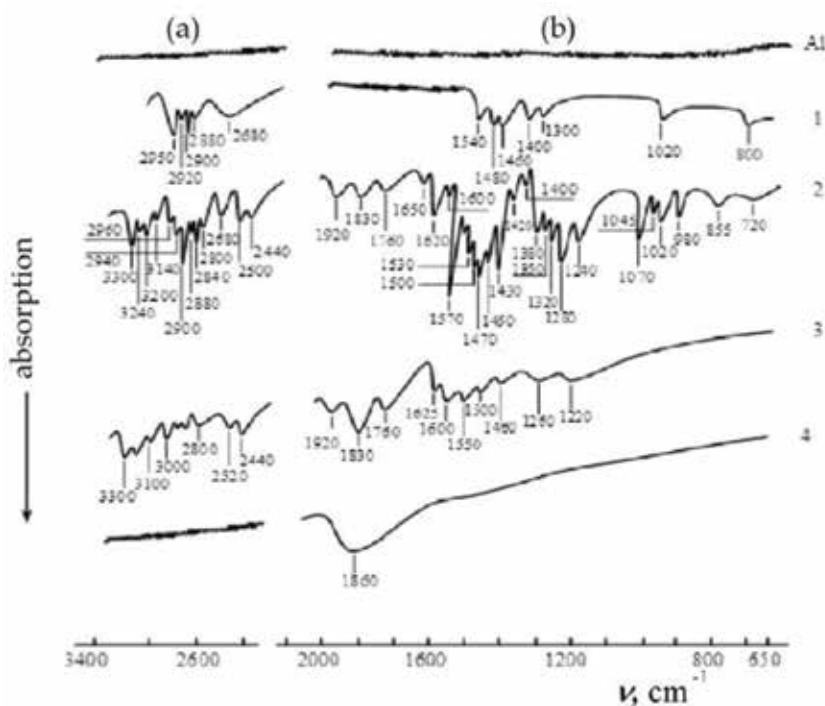


Figure 5. IR absorption spectra of the Al/ads.n-hexane system: 1—initial, 2–4—after γ -radiolysis at $\Phi_{\gamma} = 10$ (2), 20 (3), and 30 kGy (4).

the appearance of a series of narrow bands at 2960, 2940, 2900, 2880, 2840, and 2800 cm^{-1} , and also comparatively broad at 2520 and 2440 cm^{-1} bands indicating the formation of surface aluminum alkyls and molecular complexes (**Figure 5a**, curve 2). The observed new narrow a.b. at 2980–2780 cm^{-1} are associated with the formation of adsorbed C_1 – C_5 hydrocarbons, and relatively broad bands at 2500–2400 cm^{-1} are possibly due to heavier than n-hexane hydrocarbons [19, 22–27]. The formation of aluminum alkyls is also confirmed by the presence in the spectrum of a.b. in the regions of planar and out-of-plane deformation vibrations of δ_{CH} relatively narrow with maxima at –1470, 1450, 1430, 1420, 1400, 1380, and wide at 855 and 720 cm^{-1} (**Figure 5b**, curve 2). A weak broad band at 720 cm^{-1} refers to the pendular vibrations of the CH_2 group, which are not connected with the skeleton vibrations and is characteristic of long paraffin chains of the type $\text{—(CH}_2\text{)}_n\text{—}$ ($n \geq 4$) [25–27].

As a result of the decomposition of n-hexane in the Al/n-hexane system, various olefins, mainly trans-ethylene, propylene, butylene-1, hexene-1, and trans-hexene-3, are formed similarly to homogeneous radiolysis. This is evidenced by a.b. with maxima at 1650, 1620, 1600, 1570, and 1530 cm^{-1} , characterizing the stretching vibrations $\nu_{\text{C=C}}$ in the π -complexes of these adsorbed olefins with the Al^{3+} cation predominantly by the octahedral coordination of Al atoms [26–30] (**Figure 5b**, curve 2). The appearance of a number of a.b. in the regions of stretching ν_{CH} ($\nu \sim 3140$ – 3075 cm^{-1}), planar ($\nu \sim 1350$ – 1200 cm^{-1}), and out-of-plane ($\nu \sim 1100$ – 950 cm^{-1}) strain δ_{CH} vibrations of CH containing $=\text{CH}_2$ and $=\text{CH—}$ groups is one of the main criteria for proving the formation of olefins on the surface of π -complexes [26, 27]. In this case, a.b. with peaks of 1320 and 1280 cm^{-1} are attributed to the plane deformation vibrations ν_1 and ν_2 of two different symmetry classes, and a.b. with maxima of 980 cm^{-1} —the out-of-plane deformation vibration of $=\text{CH}$ disubstituted ethylene (trans) [10, 26, 27]. The formation of π -complexes of olefins is also confirmed by the presence of a.b. with maxima at 3300, 3240, and 3200 cm^{-1} in the overtone coupling region $\nu_{\text{C=C}}$ (**Figure 5a** and **b**, curve 2) [26, 27].

With an increase in the γ -radiation dose Φ_γ up to 20 kGy, the spectra are transformed: the intensities of some a.b. associated with adsorbed hydrocarbons and olefins decrease, indicating that they are partially decomposed (**Figure 5a** and **b**, curve 3). Partial decomposition of olefins is accompanied by their dissociative adsorption and the formation of π -allyl complexes on the aluminum surface [26]. A further increase in the value of Φ_γ to 30 kGy leads to a complete decomposition of hydrocarbons and olefins (curve 4). In addition, an interesting fact was discovered, consisting in an increase in the intensities of a.b. associated with the formation of surface hydrides. At irradiation doses up to 10 kGy, bands with frequencies of 1920, 1830 and 1760 cm^{-1} appear in the IR spectrum in the region 2000–1700 cm^{-1} , which refer to Al—H [2–4]. With an increase in the dose of γ -irradiation up to 20 kGy, the intensities of these a.b. increase, which indicates the accumulation of hydrogen in the form of its hydrides (**Figure 5b**, curves 2, 3). A further increase in the value of Φ_γ to 40 kGy is accompanied by the formation of aluminum hydride Al—H_3 stable at room temperature (a.b. with a maximum at 1830 cm^{-1}) (**Figure 5b**, curve 4) [10]. As follows from IR spectroscopy, the radiolysis of n-hexane in the γ -irradiated Al/n-hexane heterosystem is accompanied by the formation of intermediate decomposition products—surface aluminum alkyls, π -complexes of olefins and aluminum hydrides (**Table 1**).

The main end products of decomposition are gaseous hydrocarbons and molecular hydrogen, the formation of which was monitored by spectroscopic and chromatographic methods. IR absorption spectra of gaseous hydrocarbon products of n-hexane radiolysis in the region of out-of-plane deformation vibrations of C—H are shown in **Figure 6a**. It can be seen that for small values of the absorbed dose of γ -irradiation ($\Phi_\gamma = 10 \text{ kGy}$) in the Al/n-hexane system, a.b. with maxima at 830, 800, 785, 770, 750, and 720 cm^{-1} (**Figure 6a**, curve 1), whose location and

Sample	Surface aluminum alkyls (ν cm^{-1})	Surface π -complexes of olefins (ν , cm^{-1})	Surface hydrides (ν , cm^{-1})
Al/ads.n-hexane	2960, 2940, 2900, 2880, 2840, and 2800 (region of stretching vibrations C—H), 2520 and 2440 Narrow bands 1470, 1450, 1430, 1420, 1380 (region of planar and nonplanar deformation of the vibrations δ_{CH}), broad 855 and 720	1650, 1620, 1600, 1570, and 1530 (C = C bond) 3300, 3240, and 3200 (overtone coupling region C = C) $\nu \sim 3140\text{--}3075$ (the stretching vibration region ν_{CH}) $\nu \sim 1350\text{--}1200$ and $\nu \sim 1100\text{--}950$ (the region of planar and out-of-plane deformation δ_{CH} vibrations of C—H containing = CH ₂ and = CH— groups)	1920, 1830 (stable form AlH ₃), 1760

Table 1.
Spectroscopic assignment of intermediate products of radiolysis of *n*-hexane on the aluminum surface.

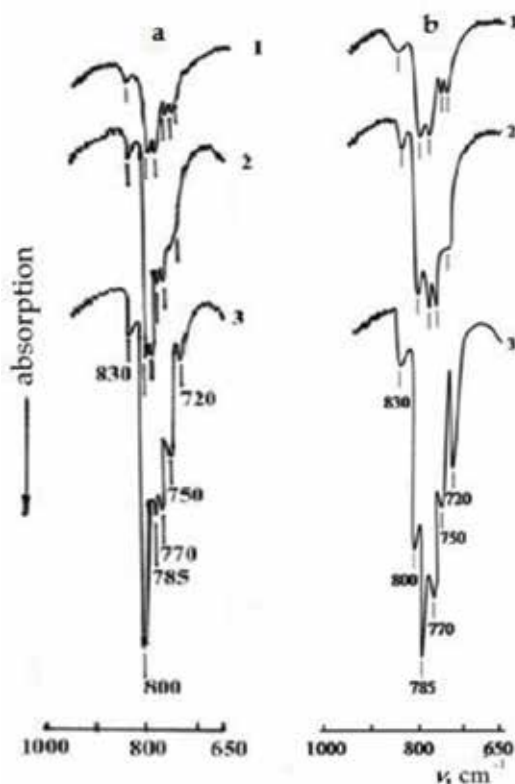


Figure 6.
IR spectra of the absorption of gaseous hydrocarbon products of *n*-hexane radiolysis on the surface of Al (a) and Be (b) in the region of out-of-plane deformation vibrations of CH at doses of gamma irradiation $\Phi_\gamma = 10$ (1), 20 (2), and 30 kGy (3).

half-width allows them to be assigned to C₁–C₅ hydrocarbons in the gas phase [19]. With an increase in the absorbed dose of Φ_γ to 30 kGy, the intensities of these bands are redistributed and increased (curves 2–3), and a further increase in Φ_γ to 40 kGy does not lead to appreciable changes in the spectrum. Comparison of dose changes in the absorption spectra of intermediate and final hydrocarbon products of the

decomposition of n-hexane in the γ -irradiated Al/ads.n-hexane system, which occur as a function of the absorbed dose of γ -irradiation, shows that they have an antibatic character. According to the chromatographic analysis, the total radiation-chemical yield of hydrocarbons $\Sigma G(C_1-C_5)$ is 0.36 molecule/100 eV. The kinetic regularity of the accumulation of molecular hydrogen in the radiolysis of n-hexane in the Al/ads.n-C₆H₁₄ system was studied in [10]. Based on the kinetic curve of H₂ accumulation, the rate of the radiative formation of H₂ is determined and the radiation-chemical yield of molecular hydrogen $G_{\text{ads}}(H_2)$ in the Al/ads.n-hexane heterosystem is calculated, taking into account the total absorbed radiation dose of gamma quanta, which is $G_{\text{ads}}(H_2) = 29.6$ molecule/100 eV. It should be noted that the yield of hydrogen for a homogeneous phase (in the absence of aluminum) is $G(H_2) = 5.2$ molecule/100 eV [29–31].

A comparison of $G_{\text{ads}}(H_2)$ and $G(H_2)$ under identical conditions indicates the radiation-catalytic activity of aluminum during the decomposition of n-hexane. Similar results were obtained with the radiation-chemical transformation of n-hexane on the surface of beryllium at room temperature. Radiolysis of n-hexane in the presence of beryllium is accompanied by the formation of intermediate decomposition products-surface beryllium hydrides, beryllium alkyls, and π -olefin complexes (Table 2).

The variety of products of n-hexane radiolysis is a consequence of the formation of highly reactive radicals upon irradiation of hydrocarbons. Thus, the formation of higher hydrocarbons in the radiolysis of n-C₆H₁₄ is due to the appearance of a number of alkyl radicals that combine with each other to form C₇H₁₆, or n-hexane or C₇H₁₆, and give products of more complex composition. The main end products of decomposition are gaseous hydrocarbons and molecular hydrogen. IR absorption spectra of gaseous hydrocarbon products of n-hexane radiolysis on the beryllium surface in the region of extraplane deformation vibrations of C—H are presented in Figure 6b.

According to the chromatographic analysis, the total radiation-chemical yield of hydrocarbons $\Sigma G(C_1-C_5)$ is 0.28 molecule/100 eV. The kinetic regularity of the accumulation of molecular hydrogen in the radiolysis of n-hexane in the system Be/ads.n-C₆H₁₄ [14, 15] has been studied. Based on the kinetic curve of H₂ accumulation, the rate of the radiative formation of H₂ is determined and its activation energy is calculated, which is $E_a \approx 4.5$ kC/mol. According to the calculation, the radiation-chemical yield of molecular hydrogen is $G_{\text{ads}}(H_2)$ in the heterosystem Be/ads.n-C₆H₁₄, taking into account the total absorbed radiation dose of γ -quanta, is $G_{\text{ads}}(H_2) = 24.8$ molecule/100 eV. It should be noted that the yield of hydrogen for a homogeneous

Sample	Surface beryllium alkyls (ν, cm^{-1})	Surface π -complexes of olefins (ν, cm^{-1})	Surface hydrides (ν, cm^{-1})
Be/ads. n-hexane	2960, 2930, 2900, 2880, 2840, 2820 (region of stretching vibrations C—H), 2520 and 2420 narrow bands 1468, 1450, 1430, 1415, 1400, 1370 (region of planar, out-of-plane deformation vibrations δ_{CH}), broad bands 855 and 720 cm^{-1}	1660, 1610, 1580, 1565, 1550, 1530 (C = C bond) 3300, 3840, 3200 and 3140 (overtone region C = C) $\nu(3140-3050)$ (region stretching vibrations ν_{CH}) $\nu(2140-3050)$ $\nu(1060-950)$ (region of planar, out-of-plane deformation vibrations of C—H containing = CH ₂ and = CH groups)	1790, 1740 (stable form BeH ₂)

Table 2.
 Spectroscopic assignment of intermediate products of radiolysis of n-hexane on the surface of beryllium.

phase (in the absence of beryllium) is $G(\text{H}_2) = 5.2$ molecule/100 eV. A comparison of $G_{\text{ads}}(\text{H}_2)$ and $G(\text{H}_2)$ under identical conditions indicates the radiation-catalytic activity of beryllium and aluminum during the decomposition of n-hexane.

A comparative analysis of the studies shows that gamma irradiation of aluminum (beryllium)/ads.n-hexane heterosystems with γ -quanta in the region of absorbed dose of $5 < \Phi_\gamma \leq 50$ kGy leads to a radiation-chemical decomposition of n-C₆H₁₄. In contrast to the homogeneous phase, the radiolysis of n-hexane in the presence of aluminum and beryllium is accompanied by the formation of intermediate products of decomposition of surface aluminum and beryllium hydrides, aluminum (beryllium) alkyls, and π -complexes of olefins. The authors revealed the limits of doses of complete radiolysis of n-hexane, below which its partial decomposition occurs, and at higher levels, a stationary saturation region sets in. The kinetics of the accumulation of molecular hydrogen has been studied and its radiation-chemical yields, which constitute the are determined $G_{\text{ads}}(\text{H}_2) = 24.8$ (in the presence of Be) and 29.6 molecule/100 eV (in the presence of Al), respectively.

In the heterogeneous radiolysis of n-hexane in contact with a metal, γ -quanta are exposed to both n-hexane and metal [28–30]. Since metals are a core of positive ions immersed in an electron gas, excitation and ionization produced by radiation in them create only defects that arise during elastic collisions [28, 29]. Such defective centers are the radiation-induced active states S^* (ions, localized charges, etc.), whose density on the surface of metals with thin oxide films is much larger compared to the surface of metals (Al, Be) with continuous oxide layers. The interaction of the active surface states of S^* and the release of secondary electrons from the metal under the action of γ -radiation ($Me \xrightarrow{\gamma} S^*, e_s$) with n-hexane lead to the excitation of its molecules by n-C₆H₁₄* (ads). In the surface-active states of S^* , the excitation of n-hexane molecules is carried out through complexation stages with further transfer of excitation energy to the molecules of n-C₆H₁₄.

5. Radiation-stimulated hydrogenation of the surface of aluminum and beryllium in contact with n-hexane

The study of radiation-stimulated hydrogenation of the surface of metals in contact with hydrocarbons is of interest from the point of view of the development of radiation-heterogeneous catalysis processes [29, 30]. The identification of the mechanisms and kinetic regularities of the formation of hydride layers at the initial stage of the process is necessary to solve the problems of radiation embrittlement of metals and alloys, as well as the production of molecular hydrogen by its accumulation in the form of hydrides [23, 24, 29, 30].

In this section, the features of the radiation-stimulated hydrogenation of the surface of aluminum and beryllium contacting with n-hexane are exposed under the action of gamma irradiation at room temperature.

Radiation-chemical conversion of n-hexane in the Al-n-hexane heterosystem takes place at an absorbed dose of $\Phi_\gamma > 0.5$ kGy and is accompanied by the formation of aluminum hydrides, which is confirmed by the appearance and IR reflection spectra in the bands $\nu = 2000\text{--}1500$ cm⁻¹ of the absorption bands 1920, 1830, and 1760 cm⁻¹, related to the Al—H bonds (**Figure 7a**, curve 1). The formation of hydrides in the interaction of n-hexane with aluminum occurs via the hydride mechanism of interaction of metals with hydrocarbons [3, 4] according to which in the first stage of the reaction after orientation of n-hexane molecules on the aluminum surface and mutual polarization of molecular and atomic layers at the aluminum/ads.n-hexane interface, a new metal-hydrogen bond is formed, and a new chemical compound, the hydride, appears on the surface of the metal. The formation

of various types of hydrides is associated with different coordination numbers of a coordinative unsaturated aluminum atom [2–4]. **Figure 6a** shows the change in the bands of Al—H stretching vibrations as a function of the contact time τ of aluminum with n-hexane under radiation exposure ($T = 300 \text{ K}$, $d\Phi_\gamma/dt = 0.80 \text{ Gy/s}$). Increasing the contact time from 10 min to 40 h (absorbed dose of 0.5 and 120 kGy, respectively) leads to the transformation of spectra accompanied by the redistribution of the intensities of these bands and their fusion and the formation of aluminum hydride in a more stable form of Al—H₃ ($\nu = 1830 \text{ cm}^{-1}$) at room temperature (curves 2–4). According to [2–4], the frequencies of stretching vibrations of Al—H₃ are in the region of 1850–1770 cm^{-1} , while the intensity increases by almost an order of magnitude and the half-width $\nu_{1/2}$ by 3.6 times (from 50 to 180 cm^{-1}).

A similar picture is also observed when the bands of stretching vibrations of Be—H are varied as a function of the contact time τ of beryllium with n-hexane under radiation action ($T = 300 \text{ K}$, $d\Phi_\gamma/dt = 0.80 \text{ Gy s}$). Increase in the contact time from 10 min to 40 h is accompanied by the transformation of hydride bands and the formation of beryllium hydride in the stable form of Be—H₂ ($\nu = 1740 \text{ cm}^{-1}$) (**Figure 7b**, curves 2–4). In this case, the intensity increases almost by ~ 4 , and the half-width $\nu_{1/2}$ by ~ 2.2 times. The observed increase in $\nu_{1/2}$ for the vibration bands of Al—H and Be—H in hydride layers is due to the inhomogeneous broadening caused by the effect of γ -irradiation.

It is known that irradiation leads to the nucleation and growth of defects such as dislocation loops and pores and stimulates diffusion processes, initiating the effect

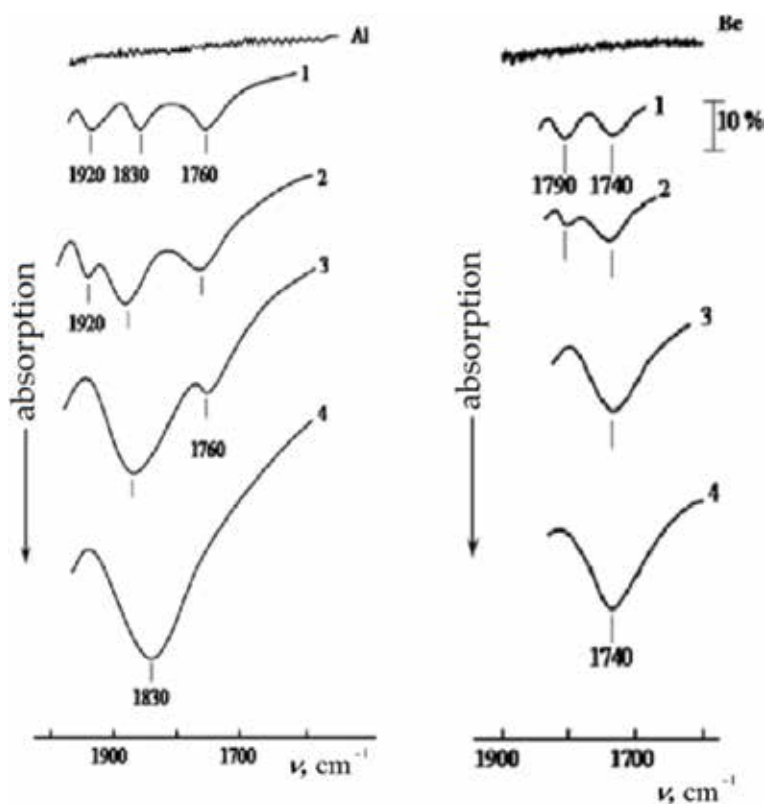


Figure 7. The change of the bands of stretching vibrations of Al—H and Be—H on the dependence of contact time τ of aluminum (a) and beryllium (b) with n-hexane under radiation action τ : 10 min (1), 5 h (2), 20 h (3), and 40 h (4). ($T = 300 \text{ K}$, $d\Phi_\gamma/dt = 0.80 \text{ Gy/s}$).

of segregation of impurities and/or the appearance of new phases, the formation of which in conventional thermal conditions is impossible. Thus, it can be argued that in the general case, irradiation initiates the creation of microstructural inhomogeneities in the metal [32], which possibly lead to broadening of the Al—H and Be—H vibration bands of the hydride layers obtained by radiation hydrogenation of Al and Be in contact with n-hexane.

It should be noted that the probability of formation of MeC precipitates on the surface of Al and Be plates contacting with n-hexane in the region of the absorbed dose $\Phi_\gamma \leq 120$ kGy is small. Therefore, in the IR reflection spectra, it was not possible to detect the absorption bands of the skeleton vibration of Al (Be)—C bonds [33]. With the purpose of experimental confirmation of the role of hydrogen nanoclusters (accumulations) during defect formation on the metal surface during their interaction by substances under the action of gamma radiation, a microscopic study of the aluminum surface after radiative hydrogenation was carried out.

Figure 8a and **b** shows 3D AFM images of surfaces of aluminum plates up to (a) and after hydrogenation at an absorbed dose of $\Phi_\gamma = 120$ kGy. The surface of the original Al plate with a thin natural oxide film ($d = 3.6$ nm) is characterized by a high degree of density defect (a). Hydrogenation of aluminum leads to the formation of hydride phase islands on its surface and the formation of a continuous hydride layer with a thickness $d \sim 450$ nm as a result of the introduction of H^+ ions and their migration into the volume either from a defective surface or from internal traps along the grain boundaries. In the 3D images of hydrogenated aluminum, the areas indicating carbon nanotube-like formations are clearly distinguished [7, 21].

The yields of hydrogen accumulated in the form of aluminum and beryllium hydrides have also been determined. To this end, the kinetics of hydrogen desorption by aluminum and beryllium at a temperature of $T = 423$ K was studied by the method of [6, 7]. The yields of H_2 are found to be 0.12 molecule/100 eV for aluminum and 0.07 molecule/100 eV for beryllium. The experimental results obtained once again testify to the high ability of aluminum to accumulate hydrogen in the form of its hydride. It should be noted that the development of systems related to storage and generation of hydrogen for autonomous power plants based on oxygen-hydrogen fuel cells in efficiency (27 g components per 1 g of hydrogen) is inferior to aluminum only to systems with lithium hydride and lithium metal. This shows that one of the promising methods is the radiation-chemical reduction of hydrogen from water by metallic aluminum.

IR spectroscopic studies revealed that hydrogen was partially accumulated in the form of Al (Be) hydride [6, 7, 16] upon radiolysis of n-hexane on the surface of aluminum and beryllium metals. The dynamics of formation of the hydride layer shows that the process of radiation-stimulated hydrogenation at room temperature

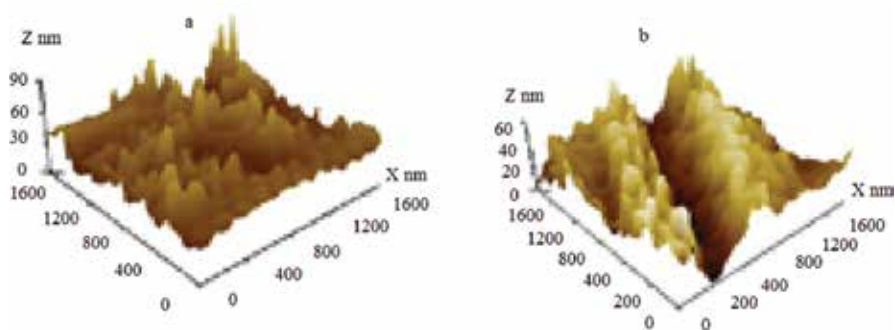


Figure 8. 3D images of the surface of the initial (a) and hydrogenated (b) aluminum samples.

on the surface of these metals, contacting with n-hexane, with γ -irradiation in the absorbed dose range of 0.5–120 kGy has a multistage nature. IR spectroscopic data are in good agreement with the results of electrophysical measurements [11, 12]. In works on electrophysical measurements, it was shown that the transition from the first stage to the latter is accompanied by a decrease in the electrical conductivity of aluminum and beryllium by several times and by an order of magnitude increase in the thickness of the resulting hydride layer. The growth of the electrical resistivity of metals at the last stage is explained by the formation of a subsurface layer of dissolved hydrogen that dissipates the conduction electrons and the formation of defects in the structure of metals.

6. The influence of the surface relief of aluminum on the processes of radiolysis of n-hexane

As noted above, the problems associated with the occurrence of radiation processes in a heterogeneous metal-hydrocarbon system have not been studied sufficiently; there are also no experimental data on the effect of the state of the metal surface on the course of radiation-heterogeneous processes of paraffin decomposition. Most metals are usually characterized by the presence of thin protective oxide films on their surface, the passivation of which is disturbed under the condition of increased radiation. This leads to a change in the surface state of metals and significantly affects the course of radiation-heterogeneous processes of paraffin decomposition [5–17]. In the nanostructured surface of metals, the mechanisms and rates of radiation-chemical transformations change—local charges and their distribution, ionization energies and electron affinity, conformations and reactivity; new “forced” reactions appear; and many other anomalies are found [34–35]. The process of radiolysis of n-hexane on the surface of previously radiation-oxidized aluminum plates containing thin oxide films of various thickness to reveal the role of Al nanostructured surface in the dynamics of the decomposition process and its influence on the rate of formation and on the yield of final products of radiolysis is considered in [9, 11]. The kinetics of the accumulation of molecular hydrogen during the decomposition of n-hexane on the surface of Al in a relationship with the growth of oxide films was studied.

Nanostructuring of the Al surface was created by preliminary oxidation of aluminum plates in contact with water under the action of γ -radiation at room temperature by the method of [17]. This involved the modification of the metal surface and the formation of a nanostructured oxide coating with an unusual property. 3D AFM-images of these surfaces are shown in **Figure 9**. Radiation-oxidized plates of Al contained oxide films with a thickness of 8–600 nm on the surface [5].

The kinetics of the accumulation of molecular hydrogen in the radiolysis of n-hexane in radiation-oxidized Al/ads.n-hexane systems at room temperature has been studied. Based on the kinetic curves of H_2 accumulation shown in **Figure 10**, the rates of formation and radiation-chemical yields of molecular hydrogen are determined. The radiation-chemical yields of H_2 are calculated in two ways [31].

For comparison with the homogeneous phase and the characteristics of the radiation-catalytic activity, the values of the radiation-chemical yield of H_2 - $G_{ads}(H_2)$ (H_2) are calculated, taking into account the energy absorbed by the substance subjected to radiolysis (n-hexane) and the entire system of $G_{total}(H_2)$. Comparison of the values of $G_{ads}(H_2) = 21.4$ – 127.2 molecule/100 eV in the heterogeneous radiolysis of n- C_6H_{14} with a value of $G(H_2) = 5.2$ molecule/100 eV for the homogeneous phase (in the absence of aluminum) under identical conditions of our experiments indicates radiation-catalytic activity of aluminum during the decomposition of

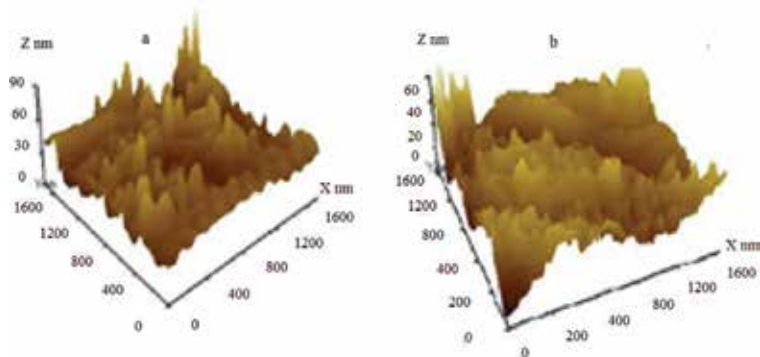


Figure 9. 3D images of radiation-oxidized surfaces of aluminum with thickness $d = 8$ (a) and 600 nm (b).

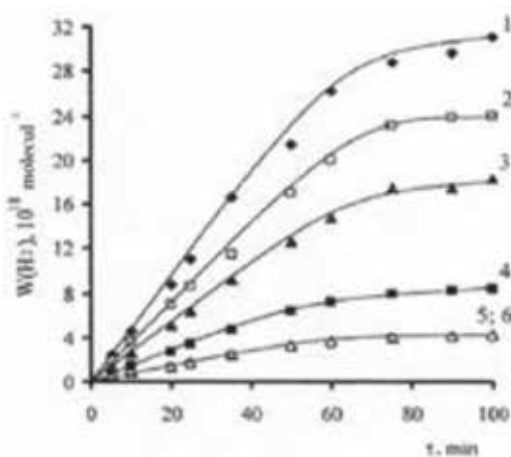


Figure 10. Kinetics of accumulation of molecular hydrogen on radiation-oxidized aluminum surfaces containing oxide films with a thickness of 8 (1), 40 (2), 80 (3), 200 (4), 400 (5), and 600 nm (6).

n-hexane. The energy efficiency of converting the energy of ionizing radiation to the energy of molecular hydrogen is characterized with the aid of $G_{\text{total}}(\text{H}_2)$, and therefore, in the future, their values are used in the discussion.

The dependence of the rate of formation of molecular hydrogen $W(\text{H}_2)$ in the radiolysis of n- C_6H_{14} in radiation-oxidized Al/ads.n-hexane systems on the thickness of oxide films on the aluminum surface is shown in **Figure 11**. As can be seen from **Figure 11**, this dependence has an exponential character. The decrease in the thickness (d) of oxide films by ~ 2 orders of magnitude (from 600 to 8 nm) is accompanied by an increase in the rate of formation of molecular hydrogen $W(\text{H}_2)$ by ~ 7 times (from 1.1 to $7.6 \cdot 10^{15} \text{ g}^{-1} \text{ s}^{-1}$). In this case, the value of the yield of molecular hydrogen $G_{\text{total}}(\text{H}_2)$ increases from 4.3 to 8.2 molecule/100 eV. An abrupt increase in the value of the rate of formation of H_2 is observed in the region of small thicknesses ($d = 8\text{--}80 \text{ nm}$), where the surface of aluminum shows comparatively high catalytic activity. A further increase in the thickness of oxide films from 80 to 600 nm leads to a monotonic decrease in the rate of formation of molecular hydrogen.

The effect of the topography of the powder surface on the rate of its oxidation and on the yield of molecular hydrogen was also found by the authors of [36, 37] in the oxidation of compact and porous beryllium and beryllium powder by steam. It was found that the interaction of compact and porous beryllium with water vapor

under certain conditions of experiments and oxidation states, the growth of the rate constant acquires the character of a jump and the yield of molecular hydrogen increases by an order of magnitude. The results obtained are explained with the dynamic instability of the oxide layer structure on the surface of compact and porous beryllium and the change in the relief surface area of the “recess-protrusion” type [36]. A direct evidence of the role of the nanostructured surface of Al containing oxide films of various thicknesses in the process of n-hexane decomposition in the heterogeneous system of radiation-oxidized Al/ads.n-hexane is the AFM data. **Figure 9** shows the AFM images of surfaces of radiation-oxidized aluminum containing oxide films of different thicknesses (a, b). Comparison of the images shows that the surface of Al containing thin oxide films ($d = 8 \text{ nm}$) is characterized by its high defectiveness (**Figure 9a**).

It is known that at room temperature, the interaction of oxygen with aluminum produces clusters with a small number of atoms [38, 39] and there are more than 10 complexes on the surface of Al, differing not only in localization sites but also in structure and electronic structure. As a rule, such complexes coexist even at sufficiently high degrees of filling of the surface and interact with each other. Complexes with the greatest reactivity play the role of active centers in heterogeneous catalysis [35]. The presence of such complexes on the surface of Al in the initial stages of its oxidation is confirmed by the registration of multi-quantum vibrational transitions of oxygen clusters using scanning tunneling microscopy and topographic images [35], as well as the results of RTL studies [15, 17]. Depending on the size and shape of the oxygen nanoclusters, the specific surface energy of aluminum also changes [38]. The presence of a hydroxyl cover also contributes to an increase in the adsorption of n-hexane on the oxidized aluminum surface, since OH groups are active adsorption centers [39]. Further oxidation of aluminum leads to the formation of oxide islands on its surface and the formation of a continuous intrinsic oxide layer

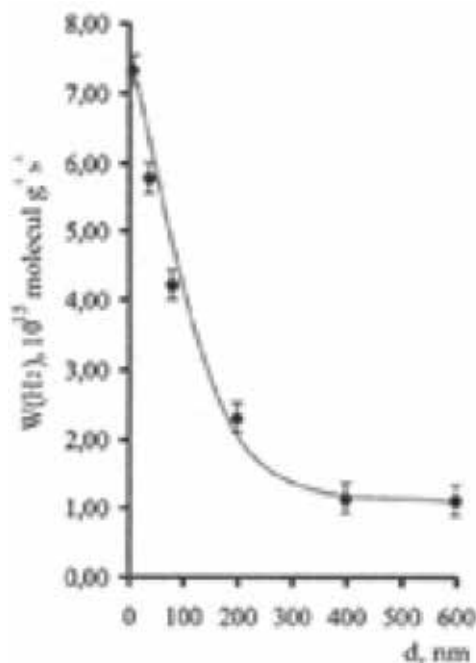


Figure 11. Dependence of the rate of formation of molecular hydrogen upon the radiolysis of n-hexane in systems of radiation-oxidized aluminum/ads.n-hexane from the thickness of oxide films on the Al surface.

($d \sim 80\text{--}600\text{ nm}$) as a result of introduction of oxygen atoms and migration of oxygen hole centers to the volume either from a defective surface or from internal traps along grain boundaries (**Figure 9b**). Depending on the degree of oxidation of the aluminum surface, its adsorption capacity with respect to n-hexane will vary.

The surface of Al containing thin oxide films in comparison with the surface with continuous oxide layers is characterized by a greater adsorption capacity. These processes are most effective if the thicknesses of oxide films are commensurable with the values of the mean free path of charge carriers (electrons and holes) in the metal and oxide, and the total energy transfer absorbed by the adsorbent (Al–Al₂O₃) to surface adsorbed n-hexane molecules is determined, which causes its decomposition by the recombination mechanism [27, 29].

7. Conclusion

This chapter presents the results of IR spectroscopic studies (IR reflection-absorption spectroscopy) of radiation-stimulated heterogeneous processes of adsorption, radiation-chemical decomposition (radiolysis) of hydrocarbons on the metal surface, and the radiation hydrogenation of these surfaces under the action of gamma radiation. The role of intermediate surface-active decomposition products in the process of heterogeneous radiolysis of hydrocarbons is discussed, as well as the influence of the surface relief of the metal in the dynamics of the change in the decomposition process on the rate of formation and the yield of final products of radiolysis. The chapter deals with the spectrokinetic regularities, their features, and the mechanisms of radiation-stimulated adsorption and radiolysis of hydrocarbons in heterogeneous metal-hydrocarbon systems, in particular in heterogeneous Al (Be)-n-hexane systems first time. It is shown that n-hexane absorption in Al (Be) surface happens by the molecular and dissociative mechanisms. It has been found that the decomposition of excited n-hexane molecules upon their radiolysis on the surface of aluminum and beryllium metals is accompanied by the formation of active intermediate decomposition products that can interact with the surface-active states of metals and form their hydrides, alkyls, and π -complexes of olefins. The final decomposition products are hydrocarbons and molecular hydrogen (H₂). It is shown that during the radiolysis of n-hexane on the surface of Al and Be metals, hydrogens are partially accumulated in the form of their hydrides.

Thanks

I am grateful to Melikova S.Z., PhD, for the rendered help at registration of work.

Author details

Nushaba Gadzhieva
Institute of Radiation Problems of the National Academy of Sciences of Azerbaijan,
Baku, Azerbaijan

*Address all correspondence to: nushaba6@mail.ru

IntechOpen

© 2018 The Author(s). Licensee IntechOpen. This chapter is distributed under the terms of the Creative Commons Attribution License (<http://creativecommons.org/licenses/by/3.0>), which permits unrestricted use, distribution, and reproduction in any medium, provided the original work is properly cited. 

References

- [1] Kislyuk MU. Diffusion of adsorbed gases on metal surfaces. *Kinetics and Catalysis*. 1998;**39**:246-263
- [2] Hara M, Domen K, Kato M, et al. Observation of an alkyl complex formed by CH₂ with an Al(111) surface. *Journal of the Chemical Society, Chemical Communications*. 1990:1717-1718
- [3] Hara M, Domen K, Onishi T, et al. Desorption of an aluminum hydride from hydrogen adsorbed on an Al(111) surface. *The Journal of Physical Chemistry*. 1991;**95**:6-7
- [4] Hara M, Domen K, Onishi T, et al. The formation and desorption of aluminum hydride from hydrogen adsorbed aluminum surfaces. *Surface Science*. 1991;**242**:459-463
- [5] Gadzhieva NN, Rimikhanova AN, Garibov AA. Features of radiation-stimulated adsorption of n-hexane on the aluminum surface. *The Journal of Physical Chemistry*. 2007;**81**:915-918
- [6] Gadzhieva NN, Rimikhanova AN. Radiation-stimulated hydrogenation of the aluminum surface in contact with n-hexane. *Journal of Physics and Chemistry of Materials Processing*. 2007;**6**:27-31
- [7] Gadzhieva NN, Rimikhanova AN. Radiation-stimulated hydrogenation of aluminum in contact with n-hexane. In: *Materials of the X International Conference "Physical and chemical processes in Inorganic Materials" (PCP-10)*; 10-12 October 2007; Kemerovo. 2007. pp. 26-28
- [8] Gadzhieva NN. Radiochemical conversion of n-hexane on the aluminum surface. In: *Materials of the X International Conference "Physical and Chemical Processes in Inorganic Materials" (PCP-10)*; 10-12 October 2007; Kemerovo. 2007. pp. 23-25
- [9] Gadzhieva NN. Effect of nanostructured aluminum surface on n-hexane radiolysis processes. In: *Materials of the International Conference "Perspectives of peaceful use of nuclear energy" dedicated to the 40th Anniversary of the Institute of Radiation Problems of NASA*; 3-4 November 2009; Baku. 2009. pp. 50-52
- [10] Gadzhieva NN. A study of the radiation-chemical transformation of n-hexane on the surface of aluminum. *Russian Journal of Physical Chemistry A*. 2010;**8**:785-790. DOI: 10.1134/s0036024410040308
- [11] Gadzhieva NN. Effect of nanostructural surface of radiation-oxidized aluminum on radiolytic processes in n-hexane. *Protection of Metals and Physical Chemistry of Surface*. 2010;**46**:222-226
- [12] Gadzhieva NN. Investigation of the formation of oxide nanostructures on the surface of aluminum under radiation exposure. In: *Theses of the 8th International Conference "Nuclear and Radiation Physics"*; 20-23 September 2011; Almaty, Kazakhstan. 2011. p. 60
- [13] Gadzhieva NN. Infrared spectroscopy study of radiation-chemical transformation of n-hexane on a beryllium surface. *Optics and Spectroscopy*. 2017;**123**:21-25. DOI: 10.1134/s0030400X17070098
- [14] Gadzhieva NN. Infrared spectroscopy study of radiation-induced adsorption of n-hexane on a beryllium surface. *Optics and Spectroscopy*. 2017;**123**:26-29. DOI: 10.1134/s0030400X17070098
- [15] Gadzhieva NN, Magerramov AM. Radiothermoluminescence of oxides nanostructures on surfaces of radiation-oxidized aluminum and beryllium. *Optics and Spectroscopy*.

2018;**124**:323-327. DOI: 10.1134/
s0030400X180.30104

[16] Gadzhieva NN. Features of radiation-stimulated hydrogenation of an aluminum surface. *Journal of Surface Investigation: X-Ray, Synchrotron and Neutron Techniques*. 2018;**12**:516-519. DOI: 10.1134/s1027451018030096

[17] Gadzhieva NN. Study of formation of oxide nanostructures on the surface of radiation-oxidated aluminum. *Materials Science: Materials Review (MS:MR)*. 2018;**1**:1-6

[18] Greenler RG. Reflection method for obtaining the infrared spectrum of a thin layer on a metal surface. *Journal of Chemical Physics*. 1969;**50**:1963-1968

[19] Sverdlov LM, Kovner MA, Krainov EP. *The Vibrational Spectra of Polyatomic Molecules*. Moscow: Nauka; 1970. 269p

[20] Avdeev VI, Zhidomirov GM. Theoretical analysis of the reaction of decomposition of methane on the surface of Ni (100). *Kinetics and Catalysis*. 1994;**35**:225-231

[21] Roshchina TM. Adsorption phenomena and surface. *SOJ*. 1998;**40**:59-63

[22] Davydov AA, Budneva AA. The study of the adsorption of hydrocarbons on oxide catalysts by IR spectroscopy. XX. Spectra of diffuse scattering of paraffin's adsorbed on simple oxides. *Kinetics and Catalysis*. 1995;**36**:781-786

[23] Kotov AG, Gromov VV. *Radiation Physics and Chemistry of Heterogeneous Systems*. Moscow: Energoatomizdat; 1988. 232p

[24] Strelko VV, Kabakchi AM, editors. *Radiation-Chemical Processes in Heterogeneous Systems on the Basis of Dispersed Oxides*. Moscow: Power Publishing; 1981. 120p

[25] *Infrared Spectra of Complex Molecules*. Per. with Engl. Moscow: Izd. II; 1963. 590 p.

[26] Davydov AA. *IR Spectroscopy in the Chemistry of the Surface of Oxides*. Novosibirsk: Science; 1984. 256p

[27] Davydov AA. *Molecular Spectroscopy of Oxide Catalysts*. Germany; Wiley VCH: Verlag Gm BH. 2004. 586p

[28] Akkerman AF, Grudsky MY, Smirnova BB. *Secondary Electron Radiation in Solids under the Action of γ -Quanta*. Moscow: Energoizdat; 1986. 168 p

[29] Garibov AA. Regularities of energy transfer in the processes of radiation-catalytic decomposition of substances on the surface of oxide and metal oxide systems. In: *Abstract of the Doctor of Science in Chemistry*. Baku; 1995. 50p

[30] Agayev TN. Radiation-catalytic processes of hydrogen production from water and hydrocarbons and the influence of structural materials on their kinetic parameters. In: *Abstract of the Dissertator Chem. Sciences*. Baku; 2015. 42p

[31] Pikayev AK. *Modern Radiative Chemistry. Radiolysis of Gases and Liquids*. Moscow: Nauka; 1986. 433p

[32] Platonov PA, Tursunov IE, Levit VI. Influence of microstructural inhomogeneities and gas impurities on the physicochemical properties of stainless steels. *Questions of Atomic Science and Technology. A Series of Physics of Radiation Damage and Radiation Material Science*. 1987;**40**:65-79

[33] Guseva MI, Gureev VM, Danelyan LS, et al. Investigation of the properties of mixed Be + C layers on beryllium. *Surface: X-ray, Synchrotron and Neutron Studies*. 2006;**3**:19-32

[34] Dalidchik FI, Grishin MV, Kovalevsky SA. Another nonequilibrium vibrational distribution of nanoparticles. *Letters in the ZhETF*. 1997;**65**:306-312

[35] Dalidchik FI, Kovalevsky SA, Shub BR. Scanning tunnel vibrational spectroscopy of single surface complexes and detection of single electron spins. *Uspekhi Khimii*. 2001;**70**:715-729

[36] Davydov DA. The formation and degradation of oxide films on beryllium. *Questions of Atomic Science and Technology*. 2010;**2**:39-49

[37] Davydov DA, Biryukov AY, Holotova OV, et al. Some studies of beryllium and the development of beryllium elements of thermonuclear reactors. 2006. Available from: <http://itertu.ru/vant>

[38] Zhukovsky YF, Smirnov EP, Lokenbach AL. Quantum-chemical description of the interaction of water molecules with metallic aluminum. Cluster model of surface water dimer. *The Journal of Physical Chemistry*. 1990;**64**:230-235

[39] Garibov AA, Velibekova GZ, Agayev TN, et al. Radiation-heterogeneous processes in contact aluminum with water. *Chemistry of High Energies*. 1992;**26**:235-238

Application of Infrared Spectroscopy in Catalysis: Impacts on Catalysts' Selectivity

Patricia Concepción

Abstract

Catalysis plays an important role in sustainable chemistry, enabling the development of more efficient processes by minimizing the consumption of energy and reducing the generation of by-products. The design of efficient catalysts is a key point in this respect, where spectroscopy confers fundamental knowledge at the molecular scale. Among the different spectroscopies, infrared (IR) spectroscopy is of great interest, enabling information about the nature of active species and the reaction mechanism, leading to precise structure-activity correlations, which are a key point in the design of new catalysts. Moreover, the dynamic behavior of the catalysts under working conditions can be also monitored by IR spectroscopy, where structural modifications of working catalysts have strong repercussion in catalysis. In this chapter, interesting examples will be discussed, related to industrial relevant processes, like Fischer-Tropsch synthesis, ethylene oligomerization, synthesis of aniline from nitrocompounds, and the dehydration of aldoximes to nitriles.

Keywords: catalysis, Fischer-Tropsch, ethylene, nitrobenzene, aldoximes, CO

1. Introduction

One of the greatest challenges in the current chemical industry is the development of high-efficient processes with increased selectivity and reduced generation of by-products. This has motivated extensive research in the last years focused on the use of alternative renewable feedstocks and on the development of less energetic reaction pathways or radically new chemical processes [1]. Catalysis plays an important role in defining new eco-efficient processes, where improvements in catalyst design and in catalytic reactor engineering are key elements that have to be linked to each other. The rational development of catalysts with enhanced catalytic performance relies on a fundamental knowledge of the catalytic process encompassing the reaction mechanism, rate-limiting reaction step, and the nature of active sites of the catalyst, where spectroscopy and theoretical studies are key aspects [2, 3]. Among the different types of spectroscopies, infrared (IR) spectroscopy is one of the most powerful techniques for the characterization of catalytic systems. This is easily demonstrated by the high number of studies found in the literature focused on the characterization of catalysts involved in industrial relevant processes [4–8]. In recent years, thanks to the technological advances allowing enhanced spectral (signal/noise level), temporal (rapid scan and step scan), and

spatial (IR microscopy) resolution, with cutting-edge values in the μs and μm range, respectively, and by the development of new catalytic IR cells enabling transient studies in the μs range [9], a lot of interest has emerged in studying the catalyst under conditions resembling those encountered in catalysis, i.e., under “in situ” or “operando” conditions [10, 11]. In addition, extensive effort is being placed in coupling IR spectroscopy to other spectroscopies (UV–Vis, EXAFS, AP-XPS) [12, 13], expanding the information obtained for a given catalytic system. In the present chapter, the application of IR spectroscopy in catalysis is described providing interesting examples to illustrate how IR spectroscopy allows accurate characterization of catalyst surface sites and the identification of active sites in working catalysts enabling to establish structure-activity correlations, being this key point in the design of new catalysts. Moreover, the analysis of the reaction mechanism and rate-determining reaction steps by means of time- and temperature-resolved IR spectroscopy will also be discussed. Some examples related to relevant industrial processes like Fischer-Tropsch synthesis, ethylene oligomerization, dehydration of aldoxime compounds to their corresponding nitriles, and hydrogenation of nitrobenzene to aniline or azobenzene will be provided in order to illustrate the great potential of IR spectroscopy in the field of catalysis.

2. IR spectroscopy in catalyst characterization

IR spectroscopy provides detailed molecular information of the nature of adsorbed species on a catalyst surface, their interaction strength, and evolution under controlled atmospheres and temperatures. Using specific probe molecules, it allows to extract relevant information of the nature of surface sites on a catalyst, such as acid, base, and redox sites, surface defects, and the dynamic behavior of those sites under reaction conditions. Moreover, thermodynamic data such as entropy and enthalpy of molecular adsorption on a specific surface site [14, 15] and kinetic data can be accurately obtained. Altogether and comparing the IR data with macro-kinetic catalytic data, it assists in defining precise structure-activity correlations on a working catalyst, which is crucial in new catalyst designs. On the other hand, IR spectroscopy can be applied under a diverse set of environments: in air, in vacuum or in the presence of reactants under controlled low pressure, at cryogenic or high temperatures, and under more relevant catalytic conditions, including gases at atmospheric or even at higher pressures (20–30 bar) and liquids, allowing catalyst research to be performed under a wide range of reaction conditions. In the following sections, the application of IR spectroscopy in catalysis, especially in unraveling the nature of surface sites, discerning those who acts as active sites, and determining the reaction mechanism and rate-limiting step, will be discussed through selected illustrative examples.

2.1 Determination of the nature of surface sites

The surface of industrial catalysts is quite complex, comprising sites of different natures such as Brønsted (H^+) acid sites, Lewis acid and base sites, transition metals with redox properties, and surface defects. Due to this huge number of sites, it is sometimes hard to get information about the intrinsic properties of the surface sites present in a working catalyst and, more importantly, to identify those who are involved in the catalytic process, called active sites. In this direction, IR spectroscopy with the aid of probe molecules has been proven as a very powerful characterization technique. Such probe molecules interact with specific surface sites resulting in a shift of their characteristic vibrational mode providing information

about the chemical properties of the surface site (i.e., oxidation state, coordination, and chemical environment) and in the case that the adsorption coefficient of the corresponding IR mode is known, allowing their quantification. Many probe molecules are reported in the literature enabling information of specific aspects of the catalyst surface [16–18]. The choice of an appropriate molecule is a crucial point in the surface characterization, and often the combined use of several molecules is required for a comprehensive knowledge of the catalyst surface sites. Perhaps, the most widely known application of probe molecules in IR spectroscopy is related to the identification and quantification of acid sites (Lewis and Brønsted) in a catalyst [19, 20]. Several base molecules have been used for that purpose, where weak bases like H₂, N₂, CO, and NO have been proven as very sensitive to the local environment and oxidation state of the surface site [21, 22], while strong bases, like pyridine and ammonia, are less sensitive but very specific to the presence of Brønsted acid sites [23, 24]. The use of other probe molecules, like acetonitrile, alcohols, and thiols, has also been reported [25]. In this direction, an interesting example with important industrial repercussion is the search of efficient catalysts for the elimination of NO_x emissions, where the selective catalytic reduction (SCR) of NO_x with ammonia (NH₃-SCR) or hydrocarbons (HC-SCR) is today one of the most efficient technologies. In this context, Cu-exchanged zeolites have shown interesting catalytic performance, where the identification of the nature of copper species is clue but highly challenging due to the coexistence of many different species such as isolated Cu²⁺, Cu⁺, Cu(OH)⁺, dimeric [Cu-O-Cu], sub-nanometric Cu_xO_y clusters, and/or CuO and Cu₂O aggregates [26–28]. Despite the massive number of investigations on these systems, there is still controversy about the nature of active sites, mainly due to the wide range of catalysts explored in the literature containing a mixture of multiple copper sites. Therefore, one way to overcome the complexity of many industrial catalysts is to try to design catalysts containing well-defined uniform sites and use them as model systems in both catalytic and spectroscopic studies. Following this hint, Cu-exchanged zeolites with uniform isolated sites (Cu-SAPO-34 and Cu-SSZ-13) have been prepared in our group by a hydrothermal synthetic approach [29–31]. Both catalysts show high activity and stability in the NH₃-SCR reaction, making them interesting candidates for the investigation of active sites in the SCR reaction. IR spectroscopy of CO and NO adsorption as probe molecules, combined with theoretical modeling of the vibrational frequencies, has allowed precise identification of Cu²⁺/Cu⁺ species located either in the 8-ring or 6-ring of the zeolite structure, as well as the identification of Cu-O-Cu dimeric species, resolving some of the controversy in the assignation of IR band frequencies present in the literature and establishing the role of isolated Cu²⁺/Cu⁺ ions as active sites in the NH₃-SCR [32].

Among the different types of industrial catalysts, metal-based catalysts containing noble metals like Pt, Pd, and Rh and non-noble metals like Ni, Co, and Ru are used in many industrial processes. The catalytic activity and selectivity of this class of catalysts are strongly influenced by their particle size and morphology, electronic state of surface metal atoms, and metal interfaces or heterojunctions in the metal particle, where a comprehensive knowledge of these parameters is essential in understanding their catalytic performance. To achieve that, the combination of several spectroscopic tools is strongly required, being IR of CO as probe molecule of great interest. Based on the shift of the $\nu(\text{C}\equiv\text{O})$ frequency, metal particles exhibiting different facets like the (111) (100) (110) crystallographic planes, as well as the presence of undercoordinated metal atoms located in steps and corners of the metal particle, can be easily detected [33, 34]. For example, by combining IR of CO as probe molecule with theoretical vibrational simulations obtained by the density functional theory (DFT) method, gold atoms of different natures have been

investigated in supported gold nanoparticle catalysts. Specifically, gold atoms with different coordination degrees (for instance, in the edge and corners of the particle), electron density (for instance, Au^{δ+} atoms located in the perimeter of the gold particle in close contact with the support), and oxidation state (Au³⁺, Au⁺ and Au⁰) have been accurately defined [35].

Finally, the characterization of surface base sites in a catalyst using IR spectroscopy of probe molecules (like CO₂, trichloromethane, acetylene, and pyrrole) is less studied, mainly due to the complexity of some of the probe molecules when adsorbed on the catalyst surface [17, 36]. For example, CO₂ adsorption on basic surface sites leads to several types of carbonate species which hinder accurate identification of surface base properties [37].

2.2 Determination of the nature of active sites: structure-activity correlation

The main challenge in spectroscopy, and specifically in IR spectroscopy, is to differentiate the catalytic active sites which are directly involved in the reaction mechanism, from the rest of sites normally present on the surface of working catalysts. Only in this case, it is possible to define accurate structure-activity correlations, which allows to direct the synthesis of new catalysts. Identification of active sites is not always straightforward and requires a multidisciplinary approach, combining surface characterization with catalytic data and, if possible, with theoretical calculations. In the following subsections, we will provide some examples of our work where active sites have been accurately identified.

2.2.1 Nature of active sites in the dehydration of aldoximes to nitriles on heterogeneous ceria catalysts

Nitriles are precursors for a wide range of organic products like carboxylic acids, amines, ketones, and amides. The most efficient route for the synthesis of nitriles is the dehydration of aldoximes that can easily be obtained from the corresponding aldehydes. Homogeneous catalytic systems such as Pd(II) complexes with a phosphino-oxime ligand [38], Co(II)Cl₂ [39], Ga(OTf)₃ [40], and Fe(ClO₄)₃ [41] are employed with interesting performance but presenting important limitations such as catalyst recovery, use of hazardous organic solvents, and long reaction time. Therefore, a lot of attention is paid in developing alternative heterogeneous catalysts. Among the different heterogeneous catalysts reported in the literature [42, 43], nanocrystalline ceria (nCeO₂) stands as a very promising catalyst in the dehydration of a variety of aldoximes (including alkyl and cycloalkyl aldoximes) to the corresponding nitriles at moderate temperature (149°C) with yields around 80–97% [44]. The catalyst shows good stability and recyclability after several uses. While both acid and basic sites are discussed in the literature for aldoxime dehydration, there is no clear understanding about the role of each of them in the reaction mechanism. In order to shed light into the participation of acid and base sites in the reaction mechanism, we performed a detailed IR study on nCeO₂ compared with other catalysts (CeO₂, MgO, Al₂O₃, and TiO₂). The different catalysts are studied in the dehydration of 4-methoxybenzaldehyde oxime, where the initial reaction rate follows the order nCeO₂ > MgO > Al₂O₃ > CeO₂ > TiO₂. Surface characterization is done using CO and CHCl₃ as probe molecules. Based on the IR spectra of CO adsorption (**Figure 1A**), the acid strength of the different catalysts (being proportional to the red ν(C≡O) shift) can be ranked in the order Al₂O₃ > TiO₂ > MgO > nCeO₂ > CeO₂, while the number of surface acid sites (peak area normalized by the catalyst surface area), called surface acid density, follows a different order CeO₂ > TiO₂ > nCeO₂ > Al₂O₃ > MgO. In the same way, based on the

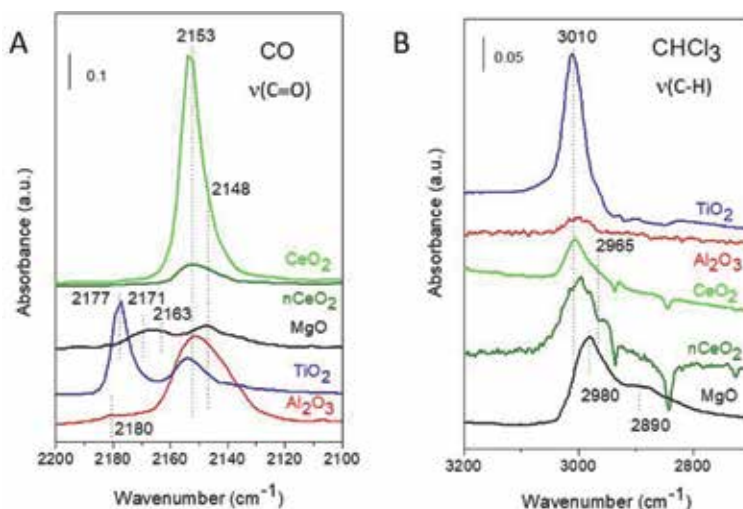
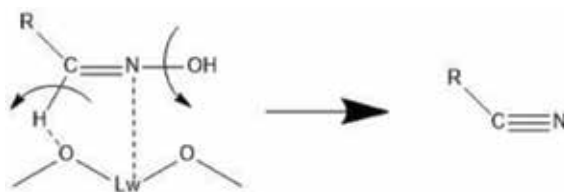


Figure 1. (A) IR spectra of CO adsorption at saturation coverage on the different catalysts. (B) IR spectra of CHCl₃ adsorption at saturation coverage on the same catalysts. All spectra are normalized to sample weight.

IR spectra of CHCl₃ adsorption (**Figure 1B**), the basic strength (being proportional to the blue $\nu(\text{C-H})$ shift) can be ranked in the order MgO > nCeO₂ > CeO₂ > TiO₂ > Al₂O₃. The same order can be applied for the surface base density.

Once the catalyst acid and base sites are established, the “in situ” dehydration of propionaldehyde oxime is studied by IR spectroscopy in order to understand how the presence of those sites influences the reactivity of the samples. The observed IR red shift of both $\nu\text{C}=\text{N}$ (from 1640 cm⁻¹ in the gas phase to 1646 cm⁻¹ on nCeO₂ and 1667 cm⁻¹ on Al₂O₃) and $\nu\text{N-OH}$ vibrations (1028 cm⁻¹ in the gas phase to 1037 cm⁻¹ on nCeO₂ and 1051 cm⁻¹ on Al₂O₃), suggests a mechanism for which the activation of propionaldehyde oxime involves an N-bond complex to a surface Lewis acid site increasing in that way the C=N and N-OH bond strength [45], followed by N-OH bond elimination and C-H cleavage with subsequent water and nitrile formation (**Scheme 1**). This differs to the conventional oxidative dehydration mechanism (i.e., interaction of the oxygen of the oxime with Lewis acid sites) for which a blue shift of both vibrations would be expected [45].

In addition, notice that in general the shift in the IR vibration of an adsorbed molecule reflects the degree of bond activation which is proportional to their catalytic reactivity. However, such a correlation is not found in this case, where the observed shift of the N-OH vibration is proportional to the sample acid strength, but doesn't match to the catalyst activity. Thus, Lewis acid sites, while being involved in the reaction mechanism, seems not to be a determinant factor for the catalytic activity. On the contrary, considering that both nCeO₂ and MgO samples, with the highest basic strength, are the most active catalysts, surface basicity should



Scheme 1. Proposed mechanism for the dehydration of aldoximes to nitriles on metal oxide heterogeneous catalysts.

play a decisive role in the reaction mechanism. Basic sites are involved in the C-H bond cleavage, which from the IR and catalytic studies can be proposed as the rate-limiting step of the reaction. In conclusion, both Lewis acid sites and basic sites are involved in the reaction mechanism, being Lewis acid sites involved in the adsorption of the oxime, while strong basic sites are required for C-H activation.

In this way, combining IR data with catalytic data, the highest catalytic activity of the nCeO₂ can be ascribed to an appropriate number of surface acid sites enabling the activation of the oxime and strong basic sites favoring C-H cleavage. While similar strong basic sites are present on MgO, the lower surface density of acid sites explains its lower activity than nCeO₂. Moreover, owing to the basic character of both nCeO₂ and MgO, desorption of the nitrile from the catalyst surface is favored avoiding secondary reactions and enhancing catalyst stability.

2.2.2 Nature of active sites in ethylene oligomerization reaction

Ethylene oligomerization is an interesting chemical route of industrial importance for the production of linear and branched higher olefins. Those olefins, depending on their carbon number, show several applications, for example, comonomers in polyethylene industry (C₄–C₆), as plasticizer alcohols (C₈–C₁₀), as synthetic lubricants (C₁₀–C₁₂), in the detergent industry (C₁₂–C₁₆), and as lube oil components or in surfactant manufacture (C₁₆–C₁₈). Industrially, the process takes place in liquid phase using homogeneous transition metal complexes as catalysts and alkyl aluminum compounds as activators [46]. Owing to the limitations of the actual industrial process, such as difficulty to separate the catalyst from oligomers, increase of operational cost, and broad carbon number distribution of products, the search of alternative heterogeneous solid catalysts is very interesting from both economic and environmental points of view. In this sense, nickel loaded on acidic aluminosilicates such as zeolites and amorphous mesoporous supports has attracted great attention as efficient and environmentally friendly heterogeneous catalysts for ethylene oligomerization, although they suffered from catalyst deactivation with time of stream (TOS) [47]. Recently, our group developed a bifunctional catalyst comprised of Ni loaded on nanocrystalline zeolite HBeta (Ni-HBeta) with high catalytic activity and stability during the oligomerization process [48]. Ethylene conversions of ~90% at 2.5 wt% Ni loading in the Ni-HBeta catalyst under conventional reaction conditions (T = 120°C, P_{tot} = 35 bar, P_{C₂H₄} = 26 bar, WHSV = 2.1 h⁻¹) are obtained without apparent signs of deactivation within 1–9 h TOS. Despite the high promising features displayed by Ni-based catalysts, the nature of active sites (isolated Ni⁺ and/or Ni²⁺) remained under debate, being subject of intense research studies in the last years [49–52]. To this aim, catalytic studies with high temporal resolution in the earliest stage of the reaction monitored by a combined gas chromatograph (GC) and mass spectrometry (MS) analysis technique and coupled with “in situ” IR-CO surface titration spectroscopic studies are performed in our group in order to identify the nature of the active Ni sites for ethylene oligomerization in the Ni-HBeta catalyst [53]. Catalysts with different nickel loadings (1, 2.5, 5, and 10 wt%) are studied. Specification of the nature of nickel sites monitored by IR of CO as probe molecule shows in all samples isolated Ni²⁺ cations in ion exchange positions of the zeolite and isolated Ni²⁺ interacting with silanol groups of internal defects (hydroxyl nests) or stacking faults of the nanocrystalline beta zeolite. Indeed, the IR-CO spectra of the activated 5wt%Ni-HBeta catalyst show IR bands at 2214 and 2207 cm⁻¹ assigned to carbonyls of isolated Ni²⁺ ion exchange cations [51, 54] and an IR band at 2196 cm⁻¹ attributed to isolated Ni²⁺ interacting with silanol groups [55], in addition to IR bands at 2175, 2164, 2156, and 2143, 2131 cm⁻¹

attributed to CO interacting with Brønsted acid sites, aluminols, silanols, and physically adsorbed CO, respectively (**Figure 2**).

Interestingly, independent of the nickel loading in the Ni-HBeta sample, the time-resolved GC-MS catalytic studies performed in a low-dead-volume catalytic setup, working at 1 bar, 120°C, and WHSV of 33 h⁻¹ (**Figure 3A**), show a significant loss of ethylene conversion in parallel to a decrease in the butene concentration at the very early reaction stage (first 10 min) before achieving pseudo-steady-state activity at TOS of 30 min. The short time frame where the initial loss of activity occurs prevents their detection in a conventional high-pressure reactor setup, where all catalysts are shown to remain stable up to 9 h TOS. Coupled to the catalytic studies, IR studies at the same experimental conditions are performed using a low-volume IR catalytic cell. The “in situ” IR ethylene oligomerization reaction is stopped at different stages of the reaction (10 s, 8 min, 30 min, and 70 min) and the nature of Ni sites titrated by IR of CO as probe molecule. Since all catalysts displayed similar trends, the 5wt%Ni-HBeta catalyst is taken as representative in the following discussion. After “in situ” reaction with ethylene in the IR catalytic cell, a sharp reduction in the intensity of the IR bands related to the isolated Ni²⁺ ions is noticed even after only 10s of reaction (**Figure 3B**). The decrease in intensity is particularly significant for the higher frequency bands at 2214 and 2207 cm⁻¹ related to the ion exchanged Ni²⁺ ions with stronger Lewis acid character, while that at 2196 cm⁻¹ of less acidic isolated Ni²⁺ interacting with silanol groups is much less affected; meanwhile, Brønsted acid sites at 2175 cm⁻¹ are also considerably reduced in intensity. In addition, dicarbonyl Ni⁺ bands at 2138 and 2095 cm⁻¹ [56] are clearly detected at low CO coverage since the very early reaction stage, increasing in intensity during the course of the reaction (spectra not shown).

Linking the IR and GC-MS data (**Figure 3C**), Ni⁺ ions cannot be considered as active site since the intensity of the IR bands of Ni⁺ ions increases with reaction time, while the catalytic activity decreases. Despite this, a clear parallelism between

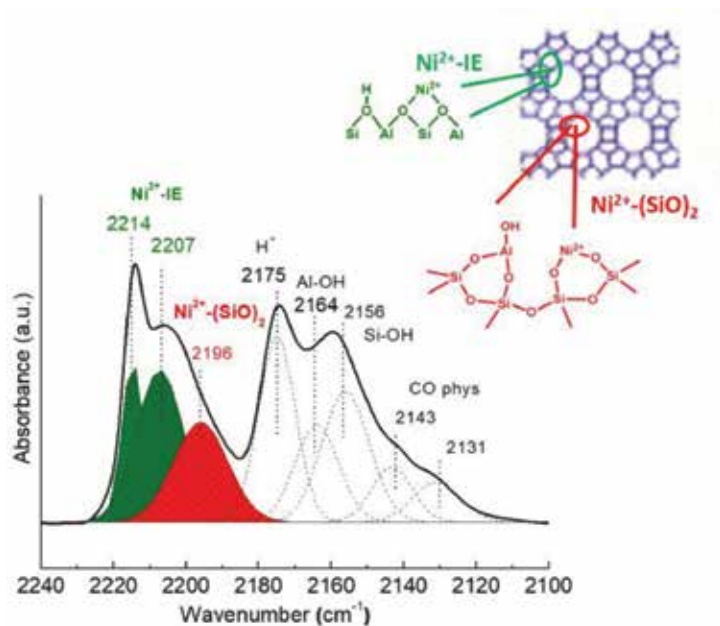


Figure 2. IR spectra of CO adsorption at saturation coverage and at -175°C on the 5wt%Ni-HBeta sample activated in N₂ flow (20 ml/min) at 300°C for 3 h.

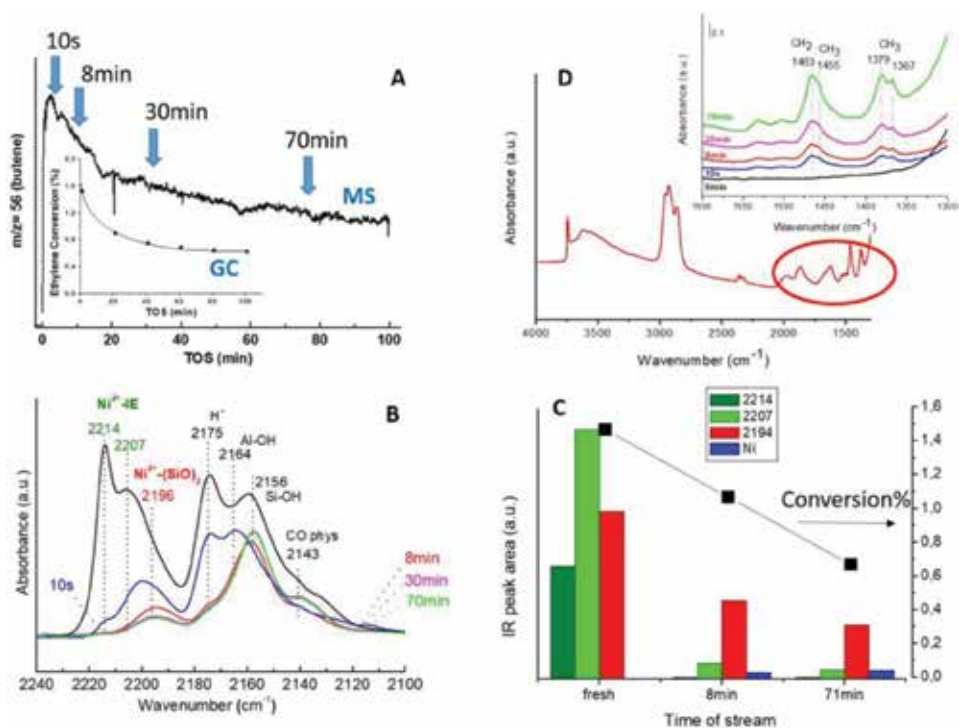


Figure 3. (A) Time-resolved GC–MS analysis in the ethylene oligomerization reaction performed at 1 bar and 120°C on the 5wt%Ni-HBeta sample. The arrows correspond to the reaction stages where surface titration by IR–CO is performed. (B) IR spectra of CO adsorption at -175°C and at saturation coverage on the 5wt%Ni-HBeta sample stopped at selected reaction times. (C) Evolution in the concentration of the different nickel sites in the working 5wt%Ni-HBeta sample and their correlation with catalytic data (conversion). (D) The “in situ” IR spectra under ethylene oligomerization reaction at 1 bar and 120°C and at different TOS highlighting hydrocarbon formation.

the reduction in intensity of the IR bands of isolated Ni^{2+} ions and the initial decline in ethylene conversion rate is observed, implying that the two phenomena should be closely related. Significantly, while isolated ion exchange Ni^{2+} ions (IR bands at 2214 and 2207 cm^{-1}) become almost totally blocked in the first seconds of the reaction, Ni^{2+} ions interacting with silanol groups (IR band at 2196 cm^{-1}) remain accessible under reaction conditions and can accordingly be considered as the true catalytic active sites under steady-state conditions. The blocking of the most acid Ni^{2+} and Brønsted acid sites under reaction conditions is due to irreversibly adsorbed hydrocarbons formed from the very early stages of reaction as detected in the “in situ” IR spectra (Figure 3D). In conclusion, these results highlight the importance of nickel sites of intermediate Lewis acid strength in order to design efficient ethylene oligomerization catalysts.

2.2.3 Nature of active sites in the Fischer-Tropsch reaction

The Fischer-Tropsch (FT) reaction has gained renewed interest in the last years as an alternative route to produce high-quality liquid fuels from alternative sources to petroleum, such as natural gas, coal, and biomass [57]. In the FT process, cobalt-based catalysts have preferentially been employed due to their high stability, low activity for the competitive reverse water gas shift reaction (WGSR), and high selectivity to long-chain n-paraffins compared to alternative catalysts based on

iron [58]. Due to the interest in this process, a lot of research has been devoted to prepare novel catalysts with improved catalytic behavior. One conventional way to improve the catalytic activity is increasing the metal dispersion (i.e., decreasing particle size), but unexpectedly a low reaction rate and a low selectivity to the desired long-chain hydrocarbons have been observed in the FT process when decreasing the cobalt particle size below 8–9 nm [59, 60]. This trend differs from the classical structure sensitivity behavior, and the reason behind has been a long-lasting debate in the literature. Particularly, the presence of unreduced Co species due to the lower reducibility of small Co nanoparticles and the reoxidation of Co sites under reaction conditions in highly dispersed catalysts [60–64] have been the most widely discussed issues. In order to understand this nonclassical particle size-dependent activity, cobalt nanoparticles with a homogenous particle size distribution from 5.6 to 10.4 nm are prepared in our laboratory using a reverse micellar synthesis procedure and deposited onto a surface-silylated ITQ-2 delaminated pure silica zeolite [65]. As reference, a Co/SiO₂ catalyst with Co particle size of 141 nm is also studied. The metal loading in all samples is 10 wt%. The high reducibility of the catalysts and their homogeneous particle size distribution make them ideal candidates as model systems for investigating the aforementioned catalytic behavior. Spectroscopic studies combined with catalytic studies under FT conditions (P = 20 bar and T = 220°C) are performed. In the catalytic studies, the intrinsic catalytic activity (TOF) decrease with decreasing Co particle size from 10.4 to 5.6 nm remains constant for particle sizes above 10.4 nm, according to the literature. The evolution of the cobalt sites under FT reaction conditions is nicely followed in the “in situ” IR studies performed at ambient pressure under syngas flow and at increasing temperatures (25–220°C) (**Figure 4**). All samples show similar trend, where at 25°C two IR bands at 2048 cm⁻¹ associated with linearly CO adsorbed on fcc Co⁰ sites [66] and at 1625 cm⁻¹ due to adsorbed water are observed. Increasing the temperature to 150 and 200°C, there are no bands observed in the Co-carbonyl region, probably due to a complete blockage of the surface sites and due to CO dissociation and the growth of adsorbed H_xC intermediate species. Indeed, a band at 612 cm⁻¹ is observed in the low-frequency range, associated with adsorbed oxygen atoms (i.e., Co-O) [67]. Finally, increasing the temperature to

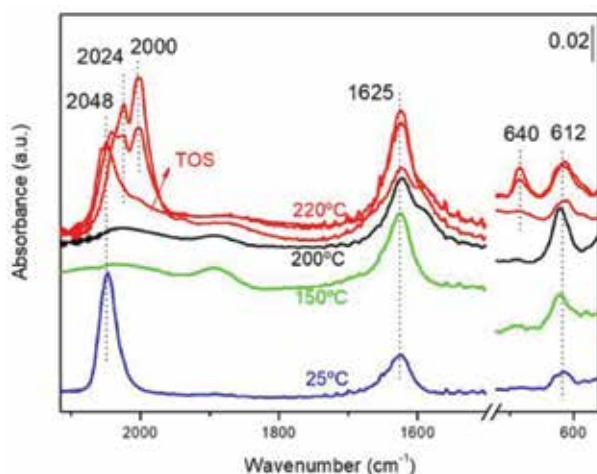


Figure 4. FTIR spectra of the Co/ITQ-2 sample with 10.4 nm Co particle size under FT reaction conditions at 1 bar and at 25, 150, 200, and 220°C. Each spectrum is recorded after 45 min at each temperature. At 220°C the IR spectra are recorded at 120, 210, and 240 min time on stream (TOS).

220°C, Co-carbonyls are rapidly restored, due to desorption of reaction intermediate species leaving free cobalt metal sites for CO adsorption. Concomitantly, a progressive shift in the Co-carbonyl IR band is observed from 2048 cm^{-1} to 2024 and 2000 cm^{-1} with increasing reaction time at 220°C, where the 2024 and 2000 cm^{-1} IR bands are related to unsaturated or low coordinated cobalt surface sites located in defect sites or on more open crystallographic cobalt planes [68, 69]. Being this shift in the IR bands irreversible, it is ascribed to cobalt surface reconstruction from an fcc structure to a more open crystallographic structure, the last one behaving as the true active site under working conditions [65]. Notice the parallel appearance of an IR band at 642 cm^{-1} ascribed to cobalt-carbon species [70, 71] which provides the first experimental evidence for the role of carbon atoms in promoting surface reconstruction of the cobalt particle under FT conditions, in agreement to previous DFT calculations [72].

Notoriously, on the sample with the smallest Co particle size (5.6 nm) and lower catalytic activity (**Figure 5A**), a band at 2060 cm^{-1} , not observed on the other samples, is detected in the “in situ” IR spectra (**Figure 5B**). This band, already observed in their reduced state prior to FT reaction, increases in intensity under FT conditions and has been ascribed to $\text{Co}^{\delta+}$ sites in the cobalt-support interface [73]. While those interface sites are majority in particles of small size, their increase under FT reaction conditions results from morphological changes in the small cobalt nanoparticle, as already detected by HRTEM, where a flattening of the cobalt particle is observed after FT reaction, enhancing the amount of metal interface sites. Since the electropositive character of the $\text{Co}^{\delta+}$ sites inhibits CO dissociation, a higher amount of these sites turn out in a lower FT activity, explaining in that way the lower FT catalytic activity observed at small Co particle sizes. This result is interesting from a fundamental point of view explaining the nonclassical particle size-dependent FT activity and more importantly from a scientific point of view, highlighting the dynamism of catalysts under reaction condition and their impact on their catalytic performance, which has been underestimated in many studies. In this context, thanks to the recent development of advances of the spectroscopic tools with “in situ” capabilities, a lot of progress has been done in this direction, not only in the FT reaction but also in other catalytic processes, revealing a highly dynamic behavior of the catalysts at working conditions [74, 75].

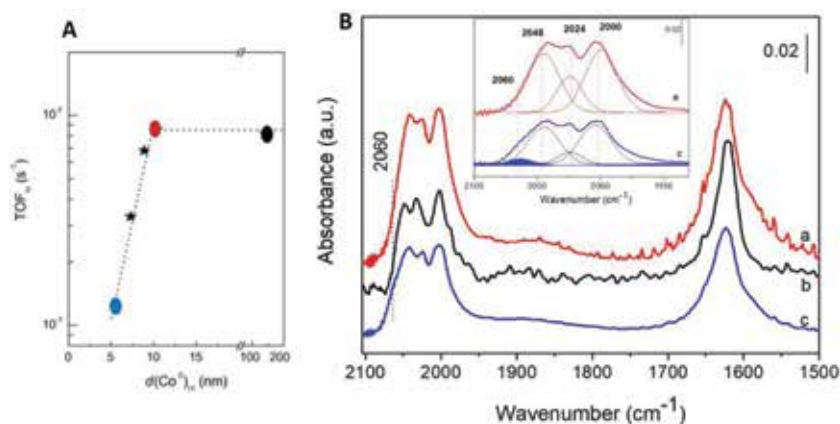


Figure 5.

(A) Variation of the turnover frequency (TOF) in FT at 220°C and 20 bar with the cobalt particle size. (B) IR spectra after 4 h on stream in FT (220°C, 1 bar) for (a) Co-ITQ-2 with 10.4 nm Co particle size, (b) Co/SiO₂ with 141 nm Co particle size, and (c) Co-ITQ-2 with 5.6 nm Co particle size samples. In the inset the deconvolution of the Co-carbonyl region highlighting the presence of the 2060 cm^{-1} IR band.

2.3 Determination of reaction mechanism and rate-limiting reaction step

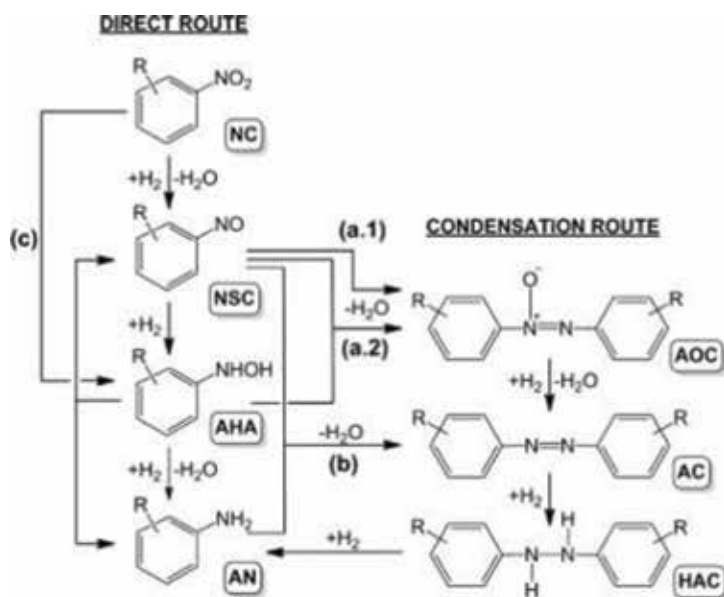
Besides the characterization of catalyst surface sites, the identification of reaction intermediate species and reaction mechanism in a catalytic process is of great interest. It allows to define the rate-limiting reaction step, which coupled to a fundamental knowledge of the nature of active sites involved in each elementary step, enables a rational design of industrial catalysts. However, due to the transient nature of reaction intermediates, differentiating them from other species present in the catalyst but not being involved in the catalytic process (called as spectators) is often difficult. Ways to do it are following the evolution of surface species during time- and temperature-resolved IR experiments and combining the IR data with catalytic data obtained either “in situ” in coupled GC–MS analysis or in “ex situ” studies. The same can be done performing pressure-dependent IR studies. Next, an example will be presented that is supported by temperature-resolved IR studies, and different reaction mechanisms are established depending on the catalyst properties.

2.3.1 Hydrogenation of nitroaromatics on supported gold catalysts

Experiments performed in our laboratory have shown that under the same reaction conditions ($T = 120^{\circ}\text{C}$, $P = 4$ bar H_2 , $[\text{Au}] = 1\%$ mol, Nitrobenzene = 0.25 M), Au nanoparticles of 2.5–3.5 nm particle size deposited on ceria (Au/CeO_2) and on titania (Au/TiO_2) display different selectivities in the hydrogenation of nitrobenzene. Thus, aniline is predominately formed on Au/TiO_2 (~90% selectivity at 97% conversion), while azobenzene (~99% selectivity at 100% conversion) is formed on the Au/CeO_2 catalyst [76]. Both aniline and azobenzene are valuable intermediates in the industrial production of pharmaceuticals, agrochemicals, pigments, dyes, and food additives, conferring high interest in the possibility to tune in a rational way the selectivity to the desired product by modifying the nature of the catalyst. If one considers the general reaction scheme proposed by Haber to reduce nitroaromatics (**Scheme 2**), it seems that the different catalytic performance of both Au/TiO_2 and Au/CeO_2 catalysts has to be related to a different reaction route (direct route versus condensation route), but the question is why both catalysts follow different reaction paths, and why in the case of the condensation route aniline is not formed as the final product. In order to answer this question, IR studies combined with micro-kinetic studies have been performed on both catalysts.

2.3.1.1 IR studies of the hydrogenation of nitrobenzene on Au/TiO_2 catalysts

The hydrogenation of nitrobenzene is followed by IR on the Au/TiO_2 catalysts performing temperature-dependent studies. In the IR spectra (**Figure 6A**), simultaneous to the consumption of nitrobenzene (IR bands at 1523 cm^{-1}), nitrosobenzene ($1483, 1475\text{ cm}^{-1}$), phenylhydroxylamine (1489 cm^{-1}), and aniline (1495 cm^{-1}) are formed [77, 78]. The micro-kinetic data IR displayed in **Figure 6B** shows a low surface concentration of nitrosobenzene and a high amount of phenylhydroxylamine. Being phenylhydroxylamine an intermediate compound (see **Scheme 2**), its high surface concentration indicates a low hydrogenation rate to aniline and the coexistence of an additional parallel direct reaction path of phenylhydroxylamine formation starting from nitrobenzene in which nitrosobenzene formation is circumvented (**Figure 6C**). These results and the absence of IR bands of azoxy and/or azocompounds help to propose a direct hydrogenation route. Moreover, it is shown that the low surface concentration of nitrosobenzene during nitrobenzene hydrogenation is clue in this reaction path.



Scheme 2.

Reaction pathways in the hydrogenation of nitrocompounds to anilines. NC = nitrocompound, NSC = nitroso compound, AHA = aromatic hydroxylamine, AN = aniline, AOC = azoxy compound, AC = azo compound, HAC = hydrazo compound [76].

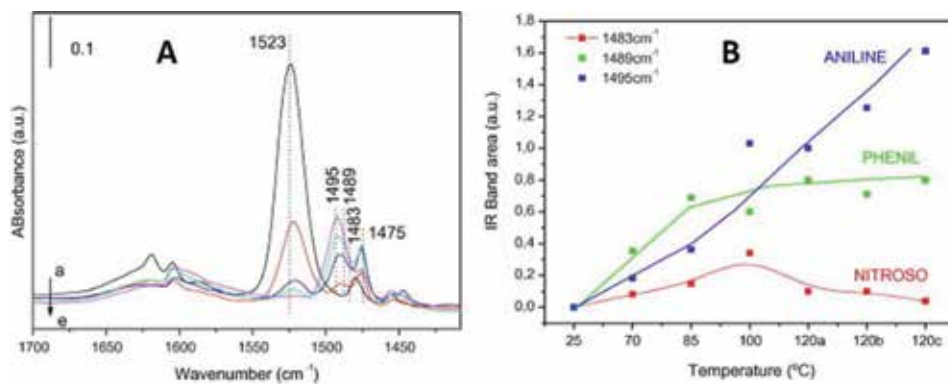


Figure 6.

(A) IR spectra in the hydrogenation of nitrobenzene on Au/TiO₂ catalyst at (a) 25°C, (b) 70°C, (c) 85°C, (d) 100°C, and (e) 120°C (0.5 mbar NB and 8 mbar H₂). (B) Evolution of the IR surface reaction intermediates species with temperature. (C) Proposed reaction path.

This is confirmed by additional IR experiments where the surface coverage of nitrosobenzene on the Au/TiO₂ catalyst is modified and the evolution of surface species under hydrogenation conditions monitored. Thus, at low surface coverage, a fast hydrogenation of nitrosobenzene to phenylhydroxylamine is observed,

followed by further hydrogenation to aniline, whereas at high nitrosobenzene coverage, azoxybenzene is mainly formed [76].

2.3.1.2 IR studies of the hydrogenation of nitrobenzene on Au/CeO₂ catalysts

In the temperature-dependent nitrobenzene hydrogenation IR studies performed on the Au/CeO₂ catalyst, nitrobenzene (IR bands at 1509 and 1343 cm⁻¹) disappears slowly, followed by nitrosobenzene formation (1540, 1491, and 1398 cm⁻¹) (**Figure 7A**). Nitrosobenzene is stabilized on the catalyst surface until 100°C, temperature at which azoxybenzene (IR bands at 1546, 1372, and 1357 cm⁻¹) is formed. Increasing temperature to 120°C azobenzene (IR bands at 1303 and 1566 cm⁻¹) is formed, showing a maximum at 21 min of reaction and then starting to decrease. This is associated to desorption of azobenzene to the gas phase, avoiding in that way a progressive hydrogenation to aniline and explaining the high selectivity to azobenzene displayed by the Au/CeO₂ catalyst [76]. These results are in line with a condensation route favored by an accumulation of nitrosobenzene on the catalyst surface. Moreover, previous IR results show a very fast reactivity of nitrosobenzene with phenylhydroxylamine, even at 25°C, giving azoxybenzene. Based on it, the surface accumulation of nitrosobenzene in the hydrogenation of nitrobenzene on the Au/CeO₂ catalyst, the absence of phenylhydroxylamine in the IR spectra, and the onset of azoxybenzene formation at 100°C indicate that the hydrogenation rate of nitrosobenzene to phenylhydroxylamine is low, being this the rate-limiting step. In conclusion, from these results, the different reaction pattern observed on the Au/CeO₂ catalysts is related to the stabilization of nitrosobenzene on the CeO₂ surface, which is ascribed to their basic properties compared to the TiO₂ as support.

Accordingly, these results show that it is possible to modulate the selectivity in the one-step nitroaromatic hydrogenation by adjusting the catalyst properties modulating in that way the concentration of nitrosobenzene on the catalyst surface.

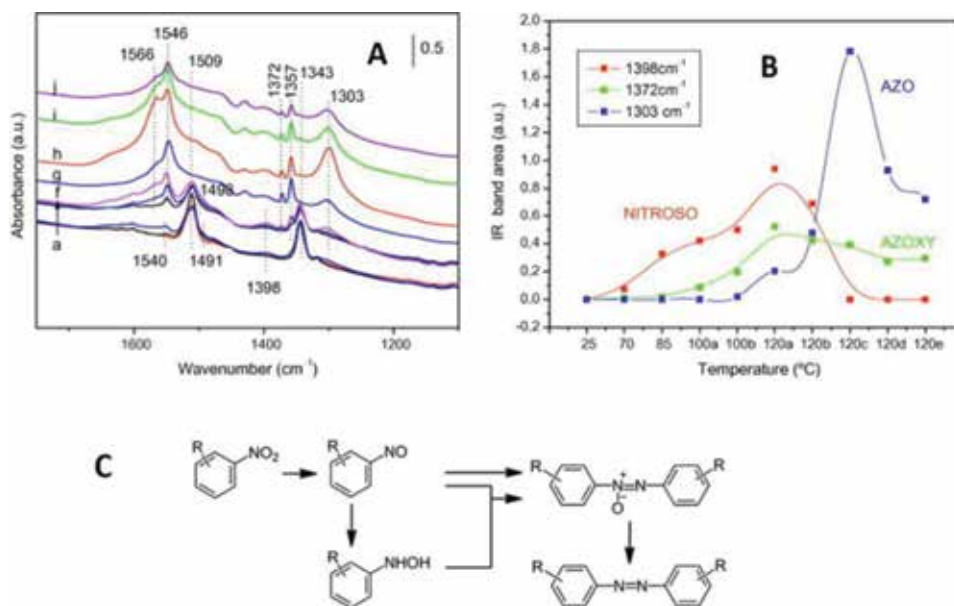


Figure 7. (A) IR spectra in the hydrogenation of nitrobenzene on Au/CeO₂ catalyst at (a) 25°C, (b) 70°C, (c) 85°C, (d) 100°C 10 min, (e) 100°C 30 min, (f) 120°C 7 min, (g) 120°C 17 min, (h) 120°C 21 min, (i) 120°C 26 min, and (j) 120°C 46 min (0.5 mbar NB and 8 mbar H₂). (B) Evolution of the IR surface reaction intermediates species with temperature. (C) Proposed reaction path.

3. Conclusion

IR spectroscopy has been shown as a very powerful technique in the field of catalysis, enabling important information difficult to obtain with other techniques. Thus, surface sites and active species can be properly analyzed, which combined with the analysis of the reaction mechanism and the rate-limiting step are key points to direct the synthesis of catalysts with improved selectivity. Moreover, the dynamism of catalyst surfaces under reaction conditions monitored by IR spectroscopy has been highlighted, a fact usually underestimated but with strong repercussion on the catalytic performance.

Acknowledgements

PC thanks the financial support of the Spanish government “Severo Ochoa Program” (SEV-2016-0683).

Conflict of interest


There is no conflict of interest in this publication.

Author details

Patricia Concepción
Instituto de Tecnología Química, Universitat Politècnica de València-Consejo Superior de Investigaciones Científicas (UPV-CSIC), Valencia, Spain

*Address all correspondence to: pconcepc@upvnet.upv.es

IntechOpen

© 2018 The Author(s). Licensee IntechOpen. This chapter is distributed under the terms of the Creative Commons Attribution License (<http://creativecommons.org/licenses/by/3.0>), which permits unrestricted use, distribution, and reproduction in any medium, provided the original work is properly cited. 

References

- [1] Centi G, Perathoner S. Catalysis and sustainable (green) chemistry. *Catalysis Today*. 2003;77:287-297
- [2] Corma A, Serna P, Concepción P, Calvino JJ. Transforming nonselective into chemoselective metal catalysts for the hydrogenation of substituted nitroaromatics. *Journal of the American Chemical Society*. 2008;130:8748-8753. DOI: 10.1021/ja800959g
- [3] Boronat M, Concepción P. Combined theoretical and spectroscopic mechanistic studies for improving activity and selectivity in heterogeneous catalysis. *Catalysis Today*. 2017;285:166-178. DOI: 10.1016/j.cattod.2016.11.048
- [4] Zaera F. New advances in the use of infrared adsorption spectroscopy for the characterization of heterogeneous catalytic reactions. *Chemical Society Reviews*. 2014;43:7624-7663. DOI: 10.1039/c3cs60374a
- [5] Bordiga S, Lamberti C, Bonino F, Travert A, Thibault-Starzyk F. Probing zeolites by vibrational spectroscopies. *Chemical Society Reviews*. 2015;44:7262-7341. DOI: 10.1039/c5cs00396b
- [6] Ryczkowski J. IR spectroscopy in catalysis. *Catalysis Today*. 2001;68:263-381. DOI: 10.1016/S0920-5861(01)00334-0
- [7] Peri JB. Infrared spectroscopy in catalytic Research. In: Anderson JR, Boudart M, editors. *Catalysis. Catalysis (Science and Technology)*. Vol. 5. Berlin, Heidelberg: Springer; 1984. pp. 171-220. DOI: 10.1007/978-3-642-93247-2_3
- [8] Vimont A, Thibault-Starzyk F, Daturi M. Analysing and understanding the active sites by IR spectroscopy. *Chemical Society Reviews*. 2010;39:4928-4950. DOI: 10.1039/B919543M
- [9] Meunier FC. The design and testing of kinetically- appropriate operando spectroscopic cells for investigating heterogeneous catalytic reactions. *Chemical Society Reviews*. 2010;39:4602-4614. DOI: 10.1039/B919705M
- [10] Foster AJ, Lobo RF. Identifying reaction intermediates and catalytic active sites through in situ characterization techniques. *Chemical Society Reviews*. 2010;39:4783-4793. DOI: 10.1039/C0CS00016G
- [11] Eli S, Weckhuysen BM. Infrared and Raman imaging of heterogeneous catalysts. *Chemical Society Reviews*. 2010;39:4615-4625. DOI: 10.1039/C0CS00064G
- [12] Bentrup U. Combining in situ characterization methods in one set-up: Looking with more eyes into the intricate chemistry of the synthesis and working of heterogeneous catalysts. *Chemical Society Reviews*. 2010;39:4718-4730. DOI: 10.1039/B919711G
- [13] Newton MA, Von Beek W. Combining synchrotron-based X-ray techniques with vibrational spectroscopies for the in situ study of heterogeneous catalysts: A view from a bridge. *Chemical Society Reviews*. 2010;39:4845-4863. DOI: 10.1039/B919689G
- [14] Gribov EN, Cocina D, Spoto G, Bordiga S, Ricchiardi G, Zecchina A. Vibrational and thermodynamic properties of Ar, N₂, O₂, H₂ and CO adsorbed and condensed into (H,Na)-Y zeolite cages as studied by variable temperature IR spectroscopy. *Physical Chemistry Chemical Physics*. 2006;8:1186-1196. DOI: 10.1039/B513367J
- [15] Arean CO, Delgado MR, Bibiloni GF, Bludský O, Nachtigall P. Variable-temperature IR spectroscopic and theoretical studies on CO₂ adsorbed in

- zeolite K-FER. *Chemphyschem.* 2011;**12**: 1435-1443. DOI: 10.1002/cphc.201000995
- [16] Knözinger H, Huber S. IR spectroscopy of small and weakly interacting molecular probes for acidic and basic zeolites. *Journal of the Chemical Society, Faraday Transactions.* 1998;**94**:2047-2059. DOI: 10.1039/A802189I
- [17] Lavalley JC. Infrared spectrometric studies of the surface basicity of metal oxides and zeolites using adsorbed probe molecules. *Catalysis Today.* 1996;**27**:377-401. DOI: 10.1016/0920-5861(95)00161-1
- [18] Davydov A. *Molecular Spectroscopy of Oxide Catalyst Surfaces.* Hoboken, NJ: John Wiley&Sons, Inc.; 2003. ISBN 0-417-98731-X
- [19] Busca G. Spectroscopic characterization of the acid properties of metal oxide catalysts. *Catalysis Today.* 1998;**41**:191-206. DOI: 10.1016/S0920-5861(98)00049-2
- [20] Lercher JA, Gründling C, Eder-Mirth G. Infrared studies of the surface acidity of oxides and zeolites using adsorbed probe molecular. *Catalysis Today.* 1996;**27**:353-376. DOI: 10.1016/0920-5861(95)00248-0
- [21] Zecchina A, Scarano D, Bordiga A, Ricchiardi G, Spoto G, Geobaldo F. IR studies of CO and NO adsorbed on well characterized oxide single microcrystals. *Catalysis Today.* 1996;**27**(3-4):403-435. DOI: 10.1016/0920-5861(95)00202-2
- [22] Bordiga S, Regli L, Cocina D, Lamberti C, Bjørgen M, Lillerud KP. Assessing the acidity of high silica chabazite H-SSZ-13 by FTIR using CO as molecular probe: Comparison with H-SAPO-34. *The Journal of Physical Chemistry. B.* 2005;**109**:2779-2784. DOI: 10.1021/jp045498w
- [23] Daniell W, Topsoe NY, Knözinger H. An FTIR study of the surface acidity of USY zeolites: Comparison of CO, CD₃CN and C₅H₅N probe molecules. *Langmuir.* 2001;**17**(20):6233-6239. DOI: 10.1021/la010345a
- [24] Kondo JN, Nishitani R, Yoda E, Yokoi T, Tatsumi T, Domen K. A comparative IR characterization of acid sites on HY zeolite by pyridine and CO probes with silica-alumina and γ -alumina references. *Physical Chemistry Chemical Physics.* 2010;**12**:11576-11586. DOI: 10.1039/C0CP00203H
- [25] Morterra C, Mentrui MP, Cerrato G. Acetonitrile adsorption as an IR spectroscopic probe for surface acidity/basicity of pure and modified zirconias. *Physical Chemistry Chemical Physics.* 2002;**4**:676-687. DOI: 10.1039/B109047J
- [26] Giordanino F, Vennestrom PN, Lundegaard LF, Stappen FN, Mossin S, Beato P, Bordiga S, Lamberti C. Characterization of Cu-exchanged SSZ-13: A comparative FTIR, UV-VIS, and EPR study with Cu-ZSM-5 and Cu- β with similar Si/Al and Cu/Al ratios. *Dalton Transactions.* 2012;**42**(35): 1274-12761. DOI: 10.1039/c3dt50732g
- [27] Wang D, Zhang L, Kamasamudram K, Epling WS. In situ -DRIFT study of selective catalytic reduction of NO_x by NH₃ over Cu-exchanged SAPO-34. *ACS Catalysis.* 2013;**3**:871-881. DOI: 10.1021/cs300843k
- [28] Borfecchia E, Lomachenko KA, Giordanino F, Falsig H, Beato P, Soldatov AV, Bordiga S, Lamberti C. Revisiting the nature of Cu sites in the activated Cu-SSZ-13 catalyst for SCR reaction. *Chemical Science.* 2015;**6**: 548-563. DOI: 10.1039/c4sc02907k
- [29] Martínez-Franco R, Moliner M, Franch C, Kustov A, Corma A. Rational direct synthesis methodology of very active and hydrothermally stable Cu-SAPO-34 molecular sieves for the SCR

- of NO_x. *Applied Catalysis B: Environmental*. 2012;**127**:273-280. DOI: 10.1016/j.apcatb.2012.08.034
- [30] Martínez-Franco R, Moliner M, Concepcion P, Thogersen JR, Corma A. Synthesis, characterization and reactivity of highly hydrothermally stable Cu-SAPO-34 materials prepared by "one pot" processes. *Journal of Catalysis*. 2014;**314**:73-82. DOI: 10.1016/j.jcat.2014.03.018
- [31] Martínez-Franco R, Moliner M, Thogersen JR, Corma A. Efficient one-pot preparation of Cu-SSZ-13 materials using cooperative OSDAs for their catalytic application in the SCR of NO_x. *ChemCatChem*. 2013;**5**:3316-3323. DOI: 10.1002/cctc.201300141
- [32] Concepción P, Boronat M, Millán R, Moliner M, Corma A. Identification of distinct copper species in Cu-CHA samples using NO as probe molecule. A combined IR spectroscopic and DFT study. *Topics in Catalysis*. 2017;**60**: 1653-1663. DOI: 10.1007/s11244-017-0844-7
- [33] Concepción P, Corma A, Silvestre-Albero J, Franco V, Chane-Ching JY. Chemoselective hydrogenation catalysts: Pt on mesostructure CeO₂ nanoparticles embedded within ultrathin layers of SiO₂ binder. *Journal of the American Chemical Society*. 2004;**126**:5523-5532. DOI: 10.1021/ja031768x
- [34] Yudanov IV, Sahnoun R, Neyman KM, Rösch N, Hoffmann J, Schauer mann S, et al. CO adsorption on Pd nanoparticles: Density functional and vibrational spectroscopy studies. *Journal of Physical Chemistry*. 2003;**107**:255-264. DOI: 10.1021/jp022052b
- [35] Boronat M, Concepción P, Corma A. Unravelling the nature of gold surface sites by combining IR spectroscopy and DFT calculations. Implications in *Catalysis. Journal of Physical Chemistry C*. 2009;**113**:16772-16784. DOI: 10.1021/jp905157r
- [36] Bosch E, Huber S, Weitkamp J, Knözinger H. Adsorption of trichloro- and trifluoromethane in Y-zeolites as studied by IR spectroscopy and multinuclear solid-state NMR. *Physical Chemistry Chemical Physics*. 1999;**1**: 579-584. DOI: 10.1039/A808296K
- [37] Köck EM, Kogler M, Bielz T, Klötzer B, Penner S. In situ FT-IR spectroscopic study of CO₂ and CO adsorption on Y₂O₃, ZrO₂, and Ytria-stabilized ZrO₂. *The Journal of Physical Chemistry. C, Nanomaterials and Interfaces*. 2013;**117**: 17666-17673. DOI: 10.1021/jp405625x
- [38] Menéndez-Rodríguez L, Tomás-Mendivil E, Francos J, Nájera C, Crochet P, Cadierno V. Palladium (II) complexes with a phosphino-oxime ligand: Synthesis, structure and applications to the catalytic rearrangement and dehydration of aldoximes. *Catalysis Science & Technology*. 2015;**5**: 3754-3761. DOI: 10.1039/C5CY00413F
- [39] Tamilselvan P, Basavaraju YB, Sampathkumar E, Murugesan R. Cobalt (II) catalyzed dehydration of aldoximes: A highly efficient practical procedure for the synthesis of nitriles. *Catalysis Communications*. 2009;**10**(5):716-719. DOI: 10.1016/j.catcom.2008.11.025
- [40] Yan P, Batamack P, Prakash GKS, Olah GA. Gallium (III) triflate catalyzed dehydration of aldoximes. *Catalysis Letters*. 2005;**101**:141-143. DOI: 10.1007/s10562-005-4880-8
- [41] Behbahani FK, Heravi MM, Oskooie HA. Highly efficient dehydration of aldoximes in the presence of Fe(ClO₄)₃ as catalyst. In: Taylor JC, editor. *Advances in Chemistry Research*. Vol. 7. 1st quartier. New York: Nova Science Publishers, Hauppauge; 2011. pp. 253-257. ISBN: 978-1-61761-898-7

- [42] Rapeyko A, Climent MJ, Corma A, Concepción P, Iborra S. Postsynthesis-treated iron-based metal-organic frameworks as selective catalysts for the sustainable synthesis of nitriles. *ChemSusChem*. 2015;**8**:3270-3282. DOI: 10.1002/cssc.201500695
- [43] Choi E, Lee C, Na Y, Chang S. [RuCl₂(p-cymene)]₂ on carbon: An efficient, selective, reusable, and environmentally versatile heterogeneous catalyst. *Organic Letters*. 2002;**4**(14):2369-2371. DOI: 10.1021/ol0260977
- [44] Rapeyko A, Climent MJ, Corma A, Concepción P, Iborra S. Nanocrystalline CeO₂ as a highly active and selective catalyst for the dehydration of aldoximes to nitriles and one-pot synthesis of amides and esters. *ACS Catalysis*. 2016;**6**:4564-4575. DOI: 10.1021/acscatal.6b00272
- [45] Sirijaraensre J, Limtrakul J. Structures and mechanism of the dehydration of benzaldoxime over Fe-ZSM-5 zeolites: A DFT study. *Structural Chemistry*. 2013;**24**(4):1307-1318. DOI: 10.1007/s11224-012-0161-5
- [46] Mc Guinness D. Olefin oligomerization via metallacycles: Dimerization, trimerization, tetramerization, and beyond. *Chemical Reviews*. 2011;**111**(3):2321-2341. DOI: 10.1021/cr100217q
- [47] Lallemand M, Finiels A, Fajula F, Hulea V. Catalytic oligomerization of ethylene over Ni-containing dealuminated Y zeolites. *Applied Catalysis A: General*. 2006;**301**:196-201. DOI: 10.1016/j.apcata.2005.12.019
- [48] Martínez A, Arribas MA, Concepción P, Moussa S. New bifunctional Ni-H-beta catalysts for the heterogeneous oligomerization of ethylene. *Applied Catalysis A: General*. 2013;**467**:509-518. DOI: 10.1016/j.apcata.2013.08.021
- [49] Agirrezabal-Telleria I, Iglesia E. Stabilization of active, selective, and regenerable Ni-based dimerization catalysts by condensation of ethene within ordered mesoporous. *Journal of Catalysis*. 2017;**352**:505-514. DOI: 10.1016/j.jcat.2017.06.025
- [50] Tanaka M, Itadani A, Kuroda Y, Iwamoto M. Effect of pore size and nickel content of Ni-MCM-41 on catalytic activity for Ethene dimerization and local structures of nickel ions. *Journal of Physical Chemistry C*. 2012;**116**:5664-5672. DOI: 10.1021/jp2103066
- [51] Moussa S, Arribas MA, Concepción P, Martínez A. Heterogeneous oligomerization of ethylene to liquids on bifunctional Ni-based catalysts: The influence of support properties on nickel speciation and catalytic performance. *Catalysis Today*. 2016;**277**: 78-88. DOI: 10.1016/j.cattod.2015.11.032
- [52] Andrei RD, Popa MI, Fajula F, Hulea V. Heterogeneous oligomerization of ethylene over highly active and stable Ni-ALSBA-15 mesoporous catalysts. *Journal of Catalysis*. 2015;**323**:76-84. DOI: 10.1016/j.jcat.2014.12.027
- [53] Moussa S, Concepción P, Arribas MA, Martínez A. Nature of active sites and initiation mechanism for ethylene oligomerization on heterogeneous Ni-beta catalysts. *ACS Catalysis*. 2018;**8**: 3903-3912. DOI: 10.1021/acscatal.7b03970
- [54] Mihaylov M, Hadjiivanov K. FTIR study of CO and NO adsorption and coadsorption on Ni-ZSM-5 and Ni/SiO₂. *Langmuir*. 2002;**18**:4376-4383. DOI: 10.1021/la015739g
- [55] Hadjiivanov K, Mihaylov M, Klissurski D, Stefanov P, Abadjieva N, Vassileva E, Mintchev L. Characterization of Ni/SiO₂ catalysts prepared by successive deposition and reduction of Ni²⁺ ions. *Journal of*

- Catalysis. 1999;**185**:314-323. DOI: 10.1006/jcat.1999.2521
- [56] Penkova A, Dzwigaj S, Kefirov R, Hadjiivanov K, Che M. Effect of the preparation method on the state of nickel ions in BEA zeolites. A study by Fourier transform infrared spectroscopy of adsorbed CO and NO, temperature reduction, and X-ray diffraction. *Journal of Physical Chemistry C*. 2007; **111**(24):8623-8631. DOI: 10.1021/jp071927p
- [57] Dry ME. The Fischer-Tropsch process-commercial aspects. *Catalysis Today*. 1990;**6**(3):183-206. DOI: 10.1016/0920-5861(90)85002-6
- [58] Iglesia E. Design, synthesis, and use of cobalt-based Fischer-Tropsch synthesis catalysts. *Applied Catalysis A: General*. 1997;**161**:59-78. DOI: 10.1016/S0926-860X(97)00186-5
- [59] Reuel RC, Bartholomew CH. Effects of support and dispersion on the CO hydrogenation activity/selectivity properties of cobalt. *Journal of Catalysis*. 1984;**85**:78-88. DOI: 10.1016/0021-9517(84)90111-8
- [60] Martínez A, López C, Márquez F, Díaz I. Fischer-Tropsch synthesis of hydrocarbons over mesoporous Co/SBA-15 catalysts: The influence of metal loading, cobalt precursor, and promoters. *Journal of Catalysis*. 2003; **220**(2):486-499. DOI: 10.1016/S0021-9517(03)00289-6
- [61] Khodakov AY, Griboval-Constant A, Bechara R, Zholobenko VL. Pore size effects in Fischer-Tropsch synthesis over cobalt-supported mesoporous Silicas. *Journal of Catalysis*. 2002; **206**(2):230-241. DOI: 10.1006/jcat.2001.3496
- [62] Kim DJ, Dunn BC, Cole P, Turpin G, Ernst RD, Pugmire RJ, Kang M, Kim JM, Eyring EM. Enhancement in the reducibility of cobalt oxides on a mesoporous silica supported cobalt catalyst. *Chemical Communications*. 2005:1462-1464. DOI: 10.1039/b417536k
- [63] Bezemer GL, Bitter JH, Kuipers HP, Oosterbeek H, Holeywijn JE, Kapteijn F, Van Dillen AJ, De Jong KP. Cobalt particle size effects in the Fischer-Tropsch reaction studied with carbon nanofiber supported catalysts. *Journal of the American Chemical Society*. 2006; **128**(12):3956-3964. DOI: 10.1021/ja058282w
- [64] Barbier A, Tuel A, Arcon I, Kodre A, Martin GA. Characterization and catalytic behaviour of Co/SiO₂ catalysts: Influence of dispersion in the Fischer-Tropsch reaction. *Journal of Catalysis*. 2001;**200**(1):106-116. DOI: 10.1006/jcat.2001.3204
- [65] Prieto G, Martínez A, Concepción P, Moreno-Tost R. Cobalt particle size effects in Fischer-Tropsch synthesis: Structural and in situ spectroscopic characterisation on reverse micelle-synthesised Co/ITQ-2 model catalysts. *Journal of Catalysis*. 2009;**266**:129-144. DOI: 10.1016/j.jcat.2009.06.001
- [66] Song D, Li J, Cai Q. In situ diffuse reflectance FTIR study of CO adsorbed on a cobalt catalyst supported by Silia with different pore sizes. *Journal of Physical Chemistry C*. 2007;**11**: 18970-18979. DOI: 10.1021/jp0751357
- [67] Hu Z, Mo L, Feng X, Shi J, Wang Y, Xie Y. Synthesis and electrochemical capacitance of sheet-like cobalt hydroxide. *Materials Chemistry and Physics*. 2009;**114**:53-57. DOI: 10.1016/j.matchemphys.2008.07.073
- [68] Prieto G, Concepción P, Murciano R, Martínez A. The impact of pre-reduction thermal history on the metal surface topology and site-catalytic activity of Co/SiO₂ Fischer-Tropsch catalysts. *Journal of Catalysis*. 2013;**302**: 37-48. DOI: 10.1016/j.jcat.2013.02.022

- [69] Rygh LES, Nielsen CJ. Infrared study of CO adsorbed on a Co/Re/ γ -Al₂O₃-based Fischer-Tropsch catalyst. *Journal of Catalysis*. 2000;**194**(2): 401-409. DOI: 10.1006/jcat.2000.2955
- [70] Anson CE, Powell DB. The metal-carbide stretching frequencies in the clusters [M₅C(CO)₁₅] (M=Ru, Os) and their derivatives as an aid to cluster structure determination. *Journal of Molecular Structure*. 1987;**159**:11-17. DOI: 0022-2860/87
- [71] Lavrentiev V, Abe H, Yamamoto S, Naramoto H, Narumi K. Formation of promising Co-C nanocompositions. *Surface and Interface Analysis*. 2003;**35**: 36-39. DOI: 10.1002/sia.1489
- [72] Ciobica IM, Van Santen RA, Van Berge PJ, Van de Loosdrecht J. Adsorbate induced reconstruction of cobalt surfaces. *Surface Science*. 2008; **602**(1):17-27. DOI: 10.1016/j.susc.2007.09.060
- [73] Rygh LES, Ellestad OH, Klæboe P, Nielsen CJ. Infrared study of CO adsorbed on Co/ γ -Al₂O₃ based Fischer-Tropsch catalysts; semi-empirical calculations as a tool for vibrational assignments. *Physical Chemistry Chemical Physics*. 2000;**2**:1835-1846. DOI: 10.1039/B000188K
- [74] Moliner M, Gabay JE, Kliewer CE, Carr RT, Guzman J, Casty GL, Serna P, Corma A. Reversible transformation of Pt nanoparticles into single atoms inside high-silica chabazite zeolite. *Journal of the American Chemical Society*. 2016; **138**(48):15743-15750. DOI: 10.1021/jacs.6b10169
- [75] Liu L, Zakharov DN, Arenal R, Concepción P, Stach EA, Corma A. Evolution and stabilization of subnanometric metal species in confined space by in situ TEM. *Nature Communications*. 2018;**9**:574-584. DOI: 10.1038/s41467-018-03012-6
- [76] Combata D, Concepción P, Corma A. Gold catalysts for the synthesis of aromatic azocompounds from nitroaromatics in one step. *Journal of Catalysis*. 2014;**311**:339-349. DOI: 10.1016/j.jcat.2013.12.014
- [77] Boronat M, Concepción P, Corma A, González S, Illas F, Serna P. A molecular mechanism for the chemoselective hydrogenation of substituted nitroaromatics with nanoparticles of gold on TiO₂ catalysts: A cooperative effect between gold and the support. *Journal of the American Chemical Society*. 2007;**129**(51):16230-16237. DOI: 10.1021/ja076721g
- [78] Richner G, Van Bokhoven JA, Neuhold YM, Makosch M, Hungerbühler K. In situ infrared monitoring of the solid/liquid catalyst interface during the three-phase hydrogenation of nitrobenzene over nanosized Au on TiO₂. *Physical Chemistry Chemical Physics*. 2011;**13**: 12463-12471. DOI: 10.1039/C1CP20238C



Edited by Marwa El-Azazy

Delving into Infrared Spectroscopy: Principles, Advances and Applications, and with basic knowledge of IR spectroscopy, will provide the reader with a synopsis of fundamentals and groundbreaking advances in the field. Readers will see a variety of MIR applications and difficulties encountered, especially in an industrial environment. Competency in FT-IR spectroscopy in biomedical research and early-stage diagnosis of obesity is shown. Challenges associated with VIS-NIR applications are shown through application of the technique in assessing quality parameters of fruits. Moreover, IR spectroscopic studies of radiation-stimulated processes, and the influence of using IR in developing an ideal catalyst and hence an efficient catalysis process, are discussed. The impact of coupling multivariate data analysis techniques to IR is shown in almost every chapter.

Published in London, UK
© 2019 IntechOpen
© John Santarossa / iStock

IntechOpen

